

# **Predicting the Distribution of Acid Volatile Sulfide in Marine Sediment from Colour Analysis of Sediment Profile Images**

**Peter S. Wilson**

A thesis submitted to  
Auckland University of Technology  
in fulfilment of the requirements for the degree of  
Doctor of Philosophy (PhD)

2015

School of Applied Sciences  
Auckland University of Technology

# Abstract

Measuring the sediment content of acid volatile sulfides (AVS), one indicator of coastal ecosystem functioning and the remineralisation of organic matter, is laborious and therefore rarely considered in routine coastal monitoring. In this thesis, I further develop an approach presented by Bull and Williamson (2001) to estimate the in situ distribution of AVS in subtidal soft sediment from sediment-profile images. I then determine whether this approach is valid at multiple locations in the Hauraki Gulf, New Zealand and investigate sediment chemical properties that may affect the approach. Finally, I apply this approach to assess soft coastal sediment that had been organically enriched by a long-line mussel farm.

I first established a strong correlation ( $R^2 = 0.95$ ) between sediment AVS concentration (extracted by cold 1 M HCl) and the colour intensity of sediment collected at 12 m water depth off the eastern coast of Waiheke Island, New Zealand. I then used this AVS/colour correlation to estimate the distribution of AVS in the upper 20 cm of this sediment from sediment profile images. These images were obtained in situ with a lightweight imaging device consisting of a modified flatbed scanner housed inside a watertight acrylic tube (SPI-Scan™, Benthic Science Ltd.). I made two types of estimates from the acquired images: First, I obtained a vertical AVS concentration profile by averaging the colour intensities of horizontally aligned pixels. Second, I created a two-dimensional distribution plot of AVS concentration by assigning individual pixel colour intensities.

I determined whether this approach was valid at other locations by establishing an AVS/colour correlation at each of three locations in the Hauraki Gulf, New Zealand. The slopes of the fits that best described the data at each location were similar, however, the positions of the fits along the grey scale axis were offset. That is, the AVS/colour correlation was site specific and, consequently, combining the data from three locations did not produce an AVS/colour correlation that could accurately predict the sediment AVS concentration at all three locations. I suggested that the observed grey value offsets were caused by differences in the background colour of the sediment, that is, caused by sediment components other than AVS.

I investigated the sediment sulfur chemistry at these three locations to determine the cause of differences in the AVS/colour correlation between locations. Using a sequential extraction technique, I measured three pools of sedimentary sulfides: dissolved porewater sulfide, AVS, and sequentially extracted chromium reducible sulfide (CRS<sub>s</sub>). Dissolved porewater sulfides contribute to the total AVS concentration but not to the sediment colour. The constituents of CRS<sub>s</sub>, however, contribute to the sediment colour but not to the total AVS concentration.

The analysis revealed that the concentration of dissolved porewater sulfides was negligible. It also revealed that the relative proportions of AVS and CRS<sub>s</sub> were functions of sediment age. Sediment at greater depth in the sediment column contained greater proportions of CRS<sub>s</sub> than surficial sediment because it was older. Black mineral pyrite was the main constituent of CRS<sub>s</sub>. The transformation of pyrite from its precursors can take up to several years. Contrastingly, the minerals that primarily comprise AVS (mackinawite and greigite) form from their precursors over hours or days. I suggested that the reason for the non-linear AVS/colour correlation was because of a change in the relative proportions of AVS and CRS<sub>s</sub> with sediment depth.

The slope of the fit describing data from a site with a high AVS concentration and low CRS<sub>s</sub> concentration will be steep because the majority of the change in sediment

colour arises from a change in the concentration of AVS minerals. Contrastingly, the slope of the fit describing data from a site with a low AVS concentration and high CRS<sub>s</sub> concentration will be less steep because a change in sediment colour intensity will be largely from a change in the concentration of CRS<sub>s</sub> minerals, rather than AVS minerals.

Finally, I used this approach investigate temporal changes in the extent of the seafloor area underneath a New Zealand long-line mussel farm of elevated sediment AVS content. Such assessment requires accurate detection of the AVS footprint boundary. I demonstrated how to detect this boundary with sediment profile imagery.

I analysed 182 sediment profile images taken along three transects leading from approximately 50 m inside to 200 m outside the long-line mussel farm and found that the mean sediment colour intensity inside the farm boundary was almost 1.5 times lower than that of the sediment away from the farm. Segmented regression analysis of the combined colour intensity data revealed a breakpoint in the trend of increasing grey values with increasing distance from the farm at  $56 \pm 13$  m ( $\pm 95\%$  confidence interval of the breakpoint) outside the mussel farm. Mapping of grey value data with ArcMap (ESRI, ArcGIS) indicated that the extent of the AVS footprint is a function of water column depth; organic particles disperse further in a deeper seawater column.

I conclude that for soft coastal sediment, the described sampling and data analysis techniques may provide a rapid and reliable supplement to existing benthic surveys that assess environmental effects of marine farms or other organic enrichment sources.



# Table of Contents

List of Figures	vi
List of Tables	xiii
Attestation of Authorship	xvi
Acknowledgements	xvii
<b>1 Introduction</b>	<b>1</b>
1.1 Coastal particulate organic matter . . . . .	3
1.1.1 Sources of particulate organic matter . . . . .	3
1.1.2 Settlement through the water column . . . . .	9
1.1.3 Deposition of organic matter on the seafloor . . . . .	13
1.1.4 Influence of benthic fauna on the distribution of sedimentary sulfides . . . . .	17
1.2 Sulfate reducing bacteria . . . . .	19
1.3 Acid volatile sulfide . . . . .	23
1.3.1 Sources of AVS . . . . .	25
1.4 Sediment-profile imagery (SPI) . . . . .	32
1.4.1 Image analysis . . . . .	34
1.4.2 Ecological indices . . . . .	36
1.4.3 Redox potential discontinuity (RPD) . . . . .	42
1.4.4 Colour correlations . . . . .	44
1.4.5 Modifications to SPI instruments . . . . .	47
1.5 Research questions . . . . .	52
<b>2 Estimating the in situ distribution of acid volatile sulfides from sediment pro- file images</b>	<b>54</b>
2.1 Introduction . . . . .	54
2.2 Methods . . . . .	59
2.2.1 Calibration: correlating AVS content and colour intensity . . . . .	60
2.2.2 Application: in situ SPI analysis . . . . .	65
2.3 Results . . . . .	69
2.3.1 Calibration: correlating AVS content and colour intensity . . . . .	69
2.3.2 Application: in situ SPI and analysis . . . . .	71
2.4 Discussion . . . . .	72
<b>3 Assessing the suitability of the sediment AVS/colour correlation at three sites in the Hauraki Gulf, New Zealand</b>	<b>80</b>

3.1	Introduction . . . . .	80
3.2	Methods . . . . .	82
3.2.1	Sediment collection . . . . .	82
3.2.2	Sediment analysis . . . . .	83
3.2.3	Statistical analyses . . . . .	86
3.3	Results . . . . .	87
3.3.1	Sediment characteristics . . . . .	87
3.3.2	Site-specific AVS/colour correlations . . . . .	87
3.3.3	Pooled-data AVS/colour correlation . . . . .	89
3.3.4	Converting AVS concentration units . . . . .	91
3.4	Discussion . . . . .	94
3.4.1	Differences in the AVS/colour correlation at different locations . . . . .	94
3.4.2	Assessing the suitability of an AVS/colour correlation established from multiple sites . . . . .	97
<b>4</b>	<b>Sediment sulfur chemistry</b>	<b>98</b>
4.1	Introduction . . . . .	98
4.2	Methods . . . . .	102
4.2.1	Sediment collection . . . . .	103
4.2.2	Sequential extraction . . . . .	104
4.2.3	AVS extraction conditions . . . . .	111
4.2.4	Statistical analyses . . . . .	112
4.3	Results . . . . .	113
4.3.1	Sequential extraction . . . . .	113
4.3.2	Extraction methods . . . . .	119
4.4	Discussion . . . . .	123
4.4.1	Relative proportion of sulfide pools at different locations and sediment depths . . . . .	123
4.4.2	Effects of CRS <sub>s</sub> on the AVS/colour correlation . . . . .	125
4.4.3	Effect of increasing acid strength on the AVS/colour correlation . . . . .	126
<b>5</b>	<b>Assessing the sulfide footprint of mussel farms with sediment profile imagery: a New Zealand trial</b>	<b>129</b>
5.1	Introduction . . . . .	129
5.2	Methods . . . . .	133
5.2.1	In situ SPI survey . . . . .	133
5.2.2	SPI analyses . . . . .	136
5.2.3	Statistical analyses . . . . .	138
5.2.4	Colour intensity mapping . . . . .	138
5.3	Results . . . . .	139
5.4	Discussion . . . . .	145
<b>6</b>	<b>Conclusion</b>	<b>149</b>
6.1	Recommendations for further work . . . . .	154
	<b>References</b>	<b>157</b>
	<b>Appendices</b>	<b>171</b>

# List of Figures

1.1	Biogeochemical cycling of particulate organic matter, dissolved organic matter, and dissolved inorganics in the oceans. The dominant pathways that contribute to sedimentation are highlighted in blue. Modified from Libes (2009). . . . .	4
1.2	Chemical equations for the major pathways by which organic matter degrades in the marine environment. The different electron acceptors are shown in the bold headings. Organic matter is represented by the formula $(\text{CH}_2\text{O})_{106}(\text{NH}_3)_{16}(\text{H}_3\text{PO}_4)$ . The grey bars and values on the right show the calculated energy return from each pathway. Modified from Schulz and Zabel (2006); original data from Froelich et al. (1979). . . . .	12
1.3	Representation of organic matter flux from the ocean surface to the sea-floor. Zones of productivity are indicated by the hashed areas and an indication of the relative change in the rate of carbon flux by depth is shown by the solid black line. From Schulz and Zabel (2006). . . . .	13
1.4	Generalised species–abundance–biomass curves illustrating the changes in the benthos along a decreasing organic enrichment gradient. Modified from Pearson and Rosenberg (1978). . . . .	16
1.5	Simplified illustration of the sulfate reducing bacteria metabolism. The black lines show that the majority of energy from the inputs (organic compounds and sulfur/sulfate) is conserved in the outputs ( $\text{CO}_2$ and $\text{H}_2\text{S}$ ). The red lines show that a minor fraction of the input energy is used by the organism for cellular function. Image from Rabus, Hansen, and Widdel (2013). . . . .	21
1.6	Illustration of AVS component interactions in marine sediment. The components outside the black box are not included in the AVS definition but are important sources or products in the sulfur cycle. Arrows indicate dominant reaction directions and two arrow-headed lines indicate reversible reactions. Polysulfide is shown in grey because it may be a minor contributor to AVS. Note that reactions with solid iron (oxyhydr)oxides are not shown. Image from Rickard and Morse (2005). . . . .	25
1.7	Molecular structure diagrams of the mineral mackinawite. (A) The single unit, and (B) the packing structure. Sulfur atoms are yellow, and iron atoms are orange. The cube frame in (B) indicates the extent of the repeating unit. X-ray crystal data from Lennie, Redfern, Schofield, and Vaughan (1995). . . . .	27

1.8	Molecular structure diagrams of the mineral greigite. (A) The single unit, and (B) the packing structure. Sulfur atoms are yellow, and iron atoms are orange. The cube frame in (B) indicates the extent of the repeating unit. X-ray crystal data from Skinner, Erd, and Grimaldi (1964).	28
1.9	Molecular structure diagrams of the mineral pyrite. (A) The single unit, and (B) the packing structure. Sulfur atoms are yellow, and iron atoms are orange. The cube frame in (B) indicates the extent of the repeating unit. X-ray crystal data from Brostigen and Kjekshus (1969).	29
1.10	Illustration of the first published SPI instrument, which was used by Rhoads and Young (1970). (A) Side view showing the Nikonos (Nikon) underwater camera and flash attached to a water-filled acrylic pyramid. The narrow end of the pyramid was painted black to decrease light backscatter. (B) Cross-section view of the instrument. Reproduced from Germano, Rhoads, Valente, Carey, and Solan (2011).	33
1.11	Illustration of the first vessel-deployed SPI instrument, which was used by Rhoads and Cande (1971). Image reproduced from Germano et al. (2011).	34
1.12	Visual representation of the indicators that are identified in a sediment-profile image and used in the OSI succession model (Rhoads & Germano, 1982). (A) The response over time to a physical disturbance, and (B) the response over distance from a point source of pollution.	36
1.13	Visual representation of the BHQ index by Nilsson and Rosenberg (1997). The upper panel shows example sediment profile images that have been assigned different stages of the index, ranging from highly oxidised sediment at Stage 3, to heavily affected and anoxic sediment in Stage 0. The lower panel shows the species–abundance–biomass curve presented Pearson and Rosenberg (1978) from which the index was developed. Image from Nilsson and Rosenberg (2000).	37
1.14	Examples of benthic successional stages that can be defined from a sediment-profile image using the OSI. (A) Stage 1: dense assemblage of small tube-dwelling polychaetes. (B) Stage 2: dominated by tube-dwelling amphipods ( <i>Ampelisca abdita</i> Mills, 1964). (C) Stage 3: dominated by infaunal deposit feeders. The presence of such feeders is inferred from feeding pockets, which are indicated by arrows. Image from Germano et al. (2011), original image from Rhoads and Germano (1982).	39
1.15	Modified sediment profile imagery instrument, Dynamic SPI (DySPI), developed by Blanpain et al. (2009). (1) Motorised winch, (2) camera housing, (3) cutting blade, (4) transparent imaging window. Image modified from Blanpain et al. (2009).	48
1.16	Modified sediment profile imagery device, SPIScan, designed by Patterson, Kennedy, O'Reilly, and Keegan (2006). The prism comprises a computer flatbed scanner modified to be waterproof and have a cutting edge to penetrate the sediment. The air reservoir is required to equalize the pressure inside the prism with the external water pressure. Image modified from Patterson et al. (2006).	49

1.17	A rotational sediment profile imagery instrument, SPI-Scan (Benthic Science Ltd.) deployed in New Zealand coastal waters. (1) Rope to raise and lower the instrument, (2) electrical tether that connects the instrument to a computer on the boat, (3) electronic component housing, (4) transparent acrylic tube that penetrates the sediment and houses the scan head. . . . .	51
2.1	A visual representation of the hue, saturation, intensity (HSI) colour model. The three rings in each layer illustrate the effect of changing saturation. The outer ring has 100% saturation, followed by 60% and 20% saturation towards the centre. Hue is described using degrees, where red is 0°, green is 120°, and blue is 240°. The larger middle layer has an intensity of 50% and the layers above and below have intensities of 75 and 25, respectively. . . . .	58
2.2	Location of the study site in Awakiriapa Bay, Waiheke Island, New Zealand. The extent of the mussel farm is denoted by the black hatched area and the star indicates the location of the sediment core collection. . . .	61
2.3	An example image of homogenised soft, subtidal sediment and a colour calibration strip on a flatbed scanner. The shaded area was used to measure the average sediment colour intensity. The white asterisks show the location of air bubbles that were excluded from the measurement. . . . .	63
2.4	A prototype sediment profile imaging device (SPI-Scan™, Benthic Science Ltd.) used in this study to acquire sediment profile images. (A) Electrical tether that connects the device to a 24 V power source and a computer on the surface; (B) scanner electronics housing; (C) scan head; (D) frame. . . . .	66
2.5	(A and C) Two example sediment profile images obtained with the SPI-Scan in March 2013 from Awakiriapa Bay, Waiheke Island, New Zealand. Small black and white bars on the scale to the right of each image are 1 mm; the larger bars are 10 mm. The images are overlaid with vertical AVS concentration ( $[AVS]$ , $\mu\text{mol g}^{-1}$ wet weight) profiles derived from image analysis; error bars for AVS concentration are too small to be seen. (B and D) Two-dimensional AVS distribution plots derived from the images A and C, respectively. . . . .	68
2.6	A scatter plot showing the relationship between the sediment AVS concentration ( $\mu\text{mol g}^{-1}$ wet weight) and the colour intensity of soft, subtidal sediment (upper 9 cm) collected from Awakiriapa Bay, Waiheke Island, New Zealand. A colour intensity of 0 is black, and that of 100 is white. The solid line is a quadratic fit through all points ( $[AVS] = 0.002 \times \text{GREY}^2 - 0.525 \times \text{GREY} + 28.392$ , $R^2 = 0.93$ , $n = 117$ ); the 95% confidence interval of the fit is denoted by the grey shaded area. . . .	70
2.7	Cropped sediment profile image obtained with the SPI-Scan instrument from Awakiriapa Bay, Waiheke Island, New Zealand, in June 2013. This example shows a burrow that can invalidate automated image analysis. The small marks on the right hand scale are 1 mm, and the larger marks, 10 mm. . . . .	74

- 2.8 Cropped sediment profile image obtained with the SPI-Scan instrument from Awakiriapa Bay, Waiheke Island, New Zealand, in June 2013 and the derived false-colour AVS distribution image. This example shows the effects of the sediment surface losing contact with the scanner tube, allowing surficial sediment to fall in between the scanner tube and the sub-surface sediment, which invalidates image analysis. The small marks on the right hand scale are 1 mm, and the larger marks, 10 mm. . . . . 75
- 2.9 A scatter plot showing the linear relationship between the sediment AVS concentration ( $\mu\text{mol g}^{-1}$  dry weight) and the colour intensity of soft, subtidal sediment (upper 9 cm) collected from Awakiriapa Bay, Waiheke Island, New Zealand. A colour intensity of 0 is black, and that of 100 is white. The solid line is a linear fit through all points ( $[\text{AVS}] = -0.424 \times \text{GREY} + 39.32$ ,  $R^2 = 0.91$ ,  $n = 117$ ); the 95% confidence interval of the fit is denoted by the grey shaded area. The dashed line shows the fit for the data from Bull and Williamson (2001) with the equation  $[\text{AVS}] = -0.342 \times \text{GREY} + 38.4$ . . . . . 77
- 3.1 Locations of the three sediment-sampling sites in the Hauraki Gulf, New Zealand (black circles). The beige polygons indicate the boundaries of mussel farms in the region. Data from Land Information New Zealand and Waikato Regional Council. . . . . 83
- 3.2 Scheme used sample subtidal marine sediments collected in acrylic tubes. 84
- 3.3 The relationship between acid volatile sulfide concentration (wet weight) and sediment colour intensity at three mussel farms in the Hauraki Gulf, New Zealand. A colour intensity of 0 is black, and that of 100 is white. Each solid line is a linear fit through that sites data points and the shaded area indicates the 95% confidence interval of the fit. . . . . 88
- 3.4 Pooled AVS concentration and sediment colour intensity data from three sampled sites — Awakiriapa Bay, Wilson Bay, and Te Kouma — in the Hauraki Gulf, New Zealand. AVS concentrations are presented per gram wet sediment. The solid black line denotes a linear fit through all data points and the dashed lined denotes a quadratic fit through all data points. The grey shaded area indicates the 95% confidence interval of each fit. . . . . 89
- 3.5 Comparison of AVS concentrations measured in sediment samples and AVS concentrations estimated from the sediment colour intensity of the samples using the pooled-data correlation equation. The black line indicates the line of best fit through the data ( $R^2 = 0.86$ ) and the grey shading denotes the 95% confidence interval of the fit. The dotted line denotes a 1:1 relationship, that is, where the estimated AVS concentration is equal to the measured AVS concentration. . . . . 91

3.6	Difference between AVS concentrations measured in the laboratory and AVS concentrations estimated using the equation of the linear fit that best described the pooled-data (measured AVS concentration – estimated AVS concentration). A positive value indicates that the estimated AVS concentration is lower than the measured AVS concentration. A value of zero (indicated by the dashed horizontal line) indicates that the measured AVS concentration was the same as the AVS concentration estimated from sediment colour intensity. The grey box and black horizontal lines denote the lower, middle, and upper quartiles of the data. The range of values is indicated by the vertical lines. Individual values are overlaid as semi-transparent black circles. Outliers (deemed to be 1.5 times the interquartile range) are shown as black circles. . . . .	92
3.7	The relationship between acid volatile sulfide concentration (dry weight) and sediment colour intensity at three mussel farms in the Hauraki Gulf, New Zealand. The intensity of black is 0 and that of white is 100. Each solid line is a linear fit through the data points of one site and the shaded area indicates the 95% confidence interval of the fit. . . . .	93
3.8	An illustration of the process for converting AVS concentration from $\mu\text{mol g}^{-1}$ wet sediment to $\mu\text{mol g}^{-1}$ dry sediment. The left hand column shows the process for sediment with 20% water content whereas the right hand column shows the process for sediment with 50% water content. . . . .	96
4.1	Visual representation of the sulfide components in marine sediment (top row). The grey shaded areas denote the sulfide pools as used in this study and the components that comprise each pool. . . . .	99
4.2	Schematic diagram showing the laboratory equipment setup for extracting chromium reducible sulfides from marine sediment. The acidic chromium(II) chloride solution converts sedimentary mineral sulfides into hydrogen sulfide gas ( $\text{H}_2\text{S}$ ), which is carried to the zinc acetate trapping solution by the carrier gas, argon (Ar). . . . .	107
4.3	A Jones reductor made using a zinc/mercury amalgam in a burette to reduce chromium(III) chloride ( $\text{CrCl}_3$ , blue) to chromium(II) chloride ( $\text{CrCl}_2$ , green). The flow speed of the $\text{CrCl}_2$ solution was increased using gentle suction and collected in a Büchner flask (not shown). . . . .	108
4.4	Sediment colour intensity–AVS concentration correlation at three sites in the Hauraki Gulf, New Zealand. AVS was extracted using 1 M HCl. The colour intensity of black is 0 and that of white is 100. Each coloured line is a quadratic fit that best describes the data for each site. The 95% confidence interval for each fit is shown by the grey shaded area. . . . .	114
4.5	Relationships between sediment colour intensity and sulfide concentration for three sites in the Hauraki Gulf, New Zealand. . . . .	115
4.6	Relationship between sediment colour intensity and the total reduced sulfide concentration for three sites in the Hauraki Gulf, New Zealand. TRS is the sum of the acid volatile sulfide (AVS) and sequentially extracted chromium reducible sulfide ( $\text{CRS}_s$ ) fractions. . . . .	116

- 4.7 Sediment acid volatile sulfide (AVS) and sequentially extracted chromium reducible sulfide (CRS<sub>s</sub>) concentrations from three sampled sites in the Hauraki Gulf, New Zealand. The boxes show the upper, middle, and lower quartile of the data. Black vertical lines indicate the range of the data. Outliers (1.5 times the interquartile range) are plotted separately as black points. The overlaid semi-transparent points are the individual measured sulfide concentrations. The mean is indicated by the white circle. . . . . 117
- 4.8 Mean sediment concentrations of acid volatile sulfide (AVS, left), chromium reducible sulfide (CRS<sub>s</sub>, middle), and grey value (right) by depth for three sampled sites in the Hauraki Gulf, New Zealand ( $n = 8$ ). Error bars show the 95% confidence interval of the mean. . . . . 119
- 4.9 Mean ratio of acid volatile sulfide (AVS) to sequentially extracted chromium reducible sulfide (CRS<sub>s</sub>) concentration from three sites in the Hauraki Gulf, New Zealand ( $n = 8$ ). A low ratio indicates a greater proportion of CRS<sub>s</sub>. Sediment depth is the average depth of the analysed sediment slice. Error bars show the 95% confidence interval of the mean. 120
- 4.10 Correlations between sediment colour intensity and AVS concentration for three different acid extraction methods. Sediment from Awakiriapa Bay, Waiheke Island, New Zealand was extracted in 6 M HCl + SnCl<sub>2</sub>, 0.5 M H<sub>2</sub>SO<sub>4</sub> + TiCl<sub>3</sub>, or 1 M HCl. The best fit through the data for each method is denoted by the solid lines and the 95% confidence interval for each fit is shown by the grey shaded area. . . . . 121
- 4.11 Difference in the amount of AVS extracted from marine sediment when using 6 M HCl and 1 M HCl. The line of best fit through the data is indicated by the black line and the 95% confidence interval of the fit is indicated by the grey shading. Difference =  $-0.05 \times \text{grey} + 5.87$ ,  $p < 0.001$ ,  $R^2 = 0.31$ . . . . . 122
- 5.1 Location of the long-line mussel farm in Awakiriapa Bay, Waiheke Island, New Zealand. The hashed area indicates the long-line mussel farm. Each black symbol represents one sediment profile image taken along one of three transects. . . . . 134
- 5.2 An example in situ profile image of sediment beneath the mussel farm in Awakiriapa Bay, Waiheke Island, New Zealand. The small and large black and white bars on the right hand side indicate 1 and 10 mm. Colour references are used for colour calibration of the digital image. . . . 135
- 5.3 Example sediment profile images showing the range of sediment colours in Awakiriapa Bay, Waiheke Island, New Zealand. The left image was obtained outside the farm, 48 m north of the northern farm boundary, and the middle image and right images were obtained inside the farm, 35 and 57 m south of the northern farm boundary. The small and large black bars are 1 and 10 mm. . . . . 136



- 5.4 Two methods for selecting the area of interest for image analysis. The grey-scale images were derived from a full colour image by extracting the colour intensity channel in the HSI colour space. A, a rectangle starting approximately 1 cm from the sediment surface; B, a polygon that follows the contour of the sediment surface, starting approximately 1 cm below the sediment surface. The small and large black bars are 1 and 10 mm. . . . . 137
- 5.5 Sediment AVS concentrations along three transects crossing the northern boundary of a mussel farm in Awakiriapa Bay, Waiheke Island, New Zealand. AVS concentrations were predicted from measured sediment colour intensities using the previously established AVS/colour correlation (Chapter 2). AVS concentrations inside the grey area were derived from grey values within the range of grey values included in the AVS/colour intensity correlation; AVS concentrations outside of this grey area were extrapolated using the correlation equation. . . . . 140
- 5.6 Segmented regression analysis. A segmented regression model identified the distance from the northern farm boundary at which the colour intensities of the sediment in Awakiriapa Bay, Waiheke Island, New Zealand started to decrease when heading towards the farm. The analysis was performed on data combined from the three transects (A) and separately for each transect (B–D). The grey shaded area shows the 95% confidence interval of the model and the vertical grey dashed line denotes the mussel farm boundary. Negative distances indicate points within the farm, that is, south of the northern farm boundary. . . . . 142
- 5.7 Sediment colour intensity footprint of the Awakiriapa Bay mussel farm, Waiheke Island, New Zealand. A local polynomial interpolation model (ArcMap) extrapolated the colour intensity of the sediment imaged along three transects (black symbols) to map the sediment colour intensity in the shaded area. Sediment colour intensity is correlated to AVS concentration (Bull and Williamson (2001), Chapter 2). The hashed area denotes the mussel farm. The dashed line 56 m north of the northern farm boundary denotes the edge of the mussel farm AVS footprint, as identified from segmented regression analysis of sediment colour intensity data. . . . . 144

## List of Tables

1.1	Suggested trophic states for the coastal environment based on the supply of organic carbon by Nixon (1995). . . . .	7
1.2	Currently recognised genera of sulfate reducing bacteria (Rabus et al., 2013). . . . .	20
1.3	Equations for the metabolic pathways of sulfate reducing bacteria. The final column shows the Gibbs free energy of the reaction under standard conditions: pH 7, 25 °C, and 1 bar partial pressure. From Jørgensen (2006). . . . .	22
1.4	Extraction efficiencies of commonly used AVS extraction methods on synthetically prepared mackinawite, greigite, and pyrite, and mineral pyrite. Data from Cornwell and Morse (1987). . . . .	32
1.5	Direct measurements and visual estimates that can be made from a sediment-profile image as summarised by Germano et al. (2011). . . . .	35
1.6	Sediment-profile image derived parameters and their assigned index values used to calculate the organism–sediment index (OSI) score of an image. . . . .	40
1.7	Sediment-profile image derived parameters and their associated values used to assign the image a Benthic Habitat Quality (BHQ) score. BHQ = A + B + C. The BHQ value can range between 0 and 15. From Nilsson and Rosenberg (1997). . . . .	41
2.1	Comparison of three major colour spaces used to numerically represent colour. The final column shows an example of how to define the blue square using the different colour spaces. . . . .	57
2.2	Colour assignments used to produce a false-colour image from a grey scale sediment profile image. . . . .	67
2.3	Results of a linear and a quadratic model for the correlation between AVS concentration and sediment colour intensity. The BIC adds a penalty value for each parameter in the model and returns a log-likelihood value; a lower BIC value indicates a better fit. . . . .	70
3.1	Sediment particle sizes (% volume) and median size (µm), as determined by laser particle size analysis from three sampled sites in the Hauraki Gulf, New Zealand. Water content and organic matter are the average values from 40 separately measured sediment subsamples with the standard error of the mean shown in parentheses. Particle size classifications are based on the Wentworth Scale. The site locations are shown in Figure 3.1 . . . . .	87

3.2	Equations for the linear fits that best describe the AVS/colour correlation for three sites in the Hauraki Gulf, New Zealand. AVS concentrations were presented per gram wet sediment. The data are presented in Figure 3.3. . . . .	88
3.3	Equations for the linear and quadratic fits that describe the relationship between AVS concentration and sediment colour intensity. AVS concentrations were presented per gram wet sediment and per gram dry sediment. The BIC value in the final column indicates the maximum log-likelihood value of the model; a smaller value indicates a better fit. . . . .	90
3.4	Full factorial ANCOVA to investigate difference in slopes of the fits that best describe the data presented in Figure 3.7. AVS concentration (dry weight) = Grey + Site, $R^2 = 0.94$ . . . . .	93
3.5	Equation terms and $R^2$ value for the fits through the data presented in Figure 3.7. AVS concentrations are presented per gram dry sediment. . . . .	93
4.1	Extraction efficiencies of commonly used AVS extraction methods on synthetically prepared mackinawite, greigite, and pyrite, and mineral pyrite. Data from Cornwell and Morse (1987). . . . .	100
4.2	Sulfur recovery from various sulfur sources using a reduced chromic acid extraction technique (Canfield, Raiswell, Westrich, Reaves, & Berner, 1986). . . . .	101
4.3	Granulometric analyses and mean sediment water and organic content. Mean diameters of sediment particles at the three sample sites by % volume. 10% of the distribution is below $d(0.1)$ , 50% of the distribution is below $d(0.5)$ , the median of the volume distribution, and 90% of the distribution is below $d(0.9)$ . The volume weighted mean (Mean) is the diameter of a sphere that has the same volume as the measured particle. Detailed results presented in Appendix A. . . . .	104
4.4	Amount of N,N-dimethyl- <i>p</i> -phenylenediamine sulfate (diamine) and ferric chloride ( $\text{FeCl}_3 \cdot 6 \text{H}_2\text{O}$ ) dissolved into 500 mL of 50% HCl in deionised water (Cline, 1969). This mixed diamine reagent was used to determine the concentration of sulfide in the zinc acetate trapping solution from the reduced chromium extraction of marine sediment. The two higher concentration ranges require dilution of the sample after the colour has developed. A dilution factor of 2:25 means 2 mL of sample diluted with 23 mL deionised water. . . . .	110
4.5	Terms for the quadratic fits that best describe the correlation between sediment colour intensity and AVS concentration at three sites in the Hauraki Gulf, New Zealand. The data and fits are displayed in Figure 4.4. . . . .	114
4.6	ANCOVA results to determine whether grey value (Grey) and the site (Site) are significant predictors for AVS concentration [AVS] from three locations in the Hauraki Gulf, New Zealand. Linear model: $[\text{AVS}] = (\text{Grey} + \text{Grey}^2) + \text{Site} + (\text{Grey} + \text{Grey}^2):\text{Site}$ ; $R^2 = 0.95$ . . . . .	114
4.7	Summary of ANOVAs to determine differences in the AVS and $\text{CRS}_s$ concentrations between the sites Awakiriapa Bay (AB), Wilson Bay (WB), and Te Kouma (TK). Post-hoc Tukey contrasts are presented in the final column for $p < 0.05$ . . . . .	118

4.8	Mean AVS and CRS <sub>s</sub> concentrations and the mean AVS:CRS <sub>s</sub> ratios at three sites in the Hauraki Gulf, New Zealand. The 95% confidence interval of the mean is shown in parentheses; $n = 40$ . . . . .	118
4.9	Full factorial ANCOVA model used to determine whether different combinations of acids and concentrations (Method) extracted different amount of AVS from marine sediment (AVS concentration = [Grey + Grey <sup>2</sup> ] + Method + [Grey + Grey <sup>2</sup> ]:Method). Grey value was used as the covariate. The $R^2$ of the model was 0.93. . . . .	122
4.10	Quadratic model terms and the $R^2$ values for the fits that best describe the correlation between sediment colour intensity and AVS concentration for three different AVS extraction methods. The data and fits are displayed in Figure 4.10. . . . .	122
5.1	Parameters for the local polynomial interpolation model in ArcMap (ESRI ArcGIS, version 10.2). Measured sediment colour intensities along three transects running across the boundary of the mussel farm in Awakiriapa Bay, Waiheke Island, New Zealand were extrapolated over an area extending from ~50 m inside the northern farm boundary to ~200 m north of the farm boundary. . . . .	139
5.2	Extent of the Awakiriapa Bay mussel farm colour intensity footprint. The extent of the mussel farm footprint was determined by segmented regression analysis for each transect individually, and for the combined set of sediment colour intensity data. . . . .	141
5.3	ANCOVA used to investigate differences in the colour intensity of sediment along three transects across the Awakiriapa Bay mussel farm boundary, Waiheke Island, New Zealand. Overall includes all data points for each transect, Inside farm and Outside farm include data points for distances <0 and >0 m from the northern farm boundary. Where the result was significant ( $p > 0.05$ ), I used a Tukey posthoc contrast to determine ranking. The model equation was: Grey = Distance + Transect. . . . .	141
5.4	Full factorial ANCOVA used to investigate the effect of Distance from the farm boundary, Transect, and Depth on the colour intensity of the sediment inside the farm (distance <0 m from the farm boundary). . . . .	143
5.5	Mean water depth and mean sediment colour intensity for each of three transects within the mussel farm. The final column indicates the number of samples that were averaged. . . . .	143

## Attestation of Authorship

I hereby declare that this submission is my own work and that, to the best of my knowledge and belief, it contains no material previously published or written by another person (except where explicitly defined in the acknowledgements), nor material which to a substantial extent has been submitted for the award of any other degree or diploma of a university or other institution of higher learning.

Signed \_\_\_\_\_

Date \_\_\_\_\_

# Acknowledgements

This thesis is a result of much more than the work I alone conducted over the past few years. I will be forever grateful for the incredible support that many offered me during this time. I will do my best to acknowledge those who supported me below, however, there will be people I miss out and I want you to know that your help was no less appreciated.

Firstly, thank you to my supervisor Kay Vopel for your continual input and honing of my work. It has been a long process but your attention to detail and persistence never faulted. We made it!

To my colleagues in WL, I am fortunate to have worked with such a great group of people whom I can call good friends. Jarrod, Paul, Tim, Becs, Steph, and Emma, through sheer force of will and volume of coffee, we will all succeed. Thanks also to Matt, Severine, and Clara for helping me out when diving.

Dylan, you were by my side for the majority of the time it took me to get through this PhD, and for this, you should be commended for your patience while hearing my complaints and your encouragement when I thought all hope was lost. You were a consistent motivator and one of the main reasons I made it to the end. Thank you.

Finally, the biggest thank you to my family. I'm incredibly lucky to have family that I can always count on. Thank you to my grandparents who have all been cheering me on from the sideline. Emma, Ryan, Jack, and Eve, thank you for sharing your house

with me for a time and always being willing to lend a hand. Mum and Dad, I can't thank you enough for your support on all levels.

To you all, arohanui.

# Chapter 1

## Introduction

The central theme of this research was inspired by Bull and Williamson (2001) who published a correlation between the colour of soft, subtidal, coastal sediment and its acid volatile sulfide (AVS) content. AVS forms in marine sediments as a result of the microbial degradation of organic matter. Here, I present the development of this correlation into a technique that can be used to assess and monitor the effects of organic enrichment on soft coastal sediments.

The AVS/colour correlation established by Bull and Williamson (2001) was best described by a linear function, with an  $R^2$  value of 0.62. The authors suggested that minimising sediment colour and AVS concentration measurement errors may result in a stronger correlation. To address this, I will assess whether I can improve the AVS/colour correlation by modifying the methods for acquiring sediment profile images, measuring the sediment colour, and measuring sediment sulfide concentration.

Bull and Williamson (2001) established an AVS/colour correlation based on samples from a subtidal location in the Whau Estuary, Auckland, New Zealand. It is unknown whether this correlation changes in different locations. To explore this uncertainty, I will investigate the AVS/colour correlation of sediment at multiple sites in the Hauraki Gulf, New Zealand.



If the AVS/colour correlation differs at each location, it is important to understand why such differences occur. Many different sedimentary components contribute to sediment colour and AVS concentration; it will be important to identify the specific chemical species that contribute to these sedimentary properties so that reasons for differences between sites can be investigated. AVS comprises multiple sulfide minerals and the relative proportions of such minerals may differ between sites, which is likely to have an effect on the AVS/colour correlation.

To place the development of a technique to assess and monitor the effects of organic enrichment in context, I will first review and discuss the processes that lead to the deposition of particulate organic matter on the seafloor: primary production, eutrophication, which may increase primary production, and marine farming. Before deposition, organic matter settles through the water column and undergoes degradation via multiple processes. After deposition, organic matter is then further degraded both physically and chemically. The chemical processes are mediated by bacteria, and therefore, I will briefly describe these bacteria and the processes by which they degrade organic matter.

One of the main products of the microbially mediated degradation of organic matter is hydrogen sulfide ( $\text{H}_2\text{S}$ ).  $\text{H}_2\text{S}$  readily reacts with iron in the sediment to form dark iron sulfide minerals. I will discuss the formation of these minerals and how organic matter deposition rates affect their concentrations. I will also briefly discuss how AVS can be extracted from marine sediments.

Because AVS minerals are coloured, they are visible in sediment-profile images. Sediment-profile images can be acquired in situ using underwater devices. This technique is known as sediment profile imagery (SPI). I will discuss how SPI has developed over time, and how it has been applied to assess the effects of physical disturbances and organic enrichment on ecosystem functioning. Finally, I will explore how SPI has been used to detect changes in sediment colour and relate these changes to specific chemical components in the sediment.

## 1.1 Coastal particulate organic matter

### 1.1.1 Sources of particulate organic matter

#### Primary production

The majority of particulate organic matter in the coastal environment is generated by primary producers, predominantly phytoplankton, microphytobenthos, macroalgae, and some bacteria. Steinacher et al. (2010) estimated the total annual primary production by photosynthetic planktonic organisms in the modern world to be in the order of  $20\text{--}50 \times 10^9$  tons of carbon per year. These organisms require sunlight to photosynthesise and are therefore limited to the surface layer in the ocean. This layer is called the euphotic zone and its lower boundary is defined as the depth at which only 1% of the surface photosynthetically active radiation (PAR) remains (Kirk, 1994). The thickness of this layer can range from  $<1$  m in turbid coastal areas to 200 m in the open ocean.

Figure 1.1 illustrates the biogeochemical cycle of carbon in the ocean. Phytoplankton mediate the processes that introduce dissolved inorganics (carbon and nutrients) into the marine environment as they are the only organisms in the water column able to utilise these inorganics. In the sediment, benthic microphytes are also able to utilise dissolved inorganics. Organic matter is transferred around the marine food web by the feeding activities of heterotrophs such as bacteria, protozoans, and animals.

Dissolved organic matter is made available to other organisms when it is exuded or leaks from living cells, or when the living cells die. There is no unified particle size to differentiate between dissolved and particulate organic matter, however, commonly  $0.4 \mu\text{m}$  is used (Loring & Rantala, 1992). Particles  $<0.4 \mu\text{m}$  are classified as dissolved organic matter, and those  $>0.4 \mu\text{m}$  are classified as particulate organic matter. The cell walls of dead phytoplankton are broken down by various enzymes and the organic nutrients become available for use by other organisms. Phytoplankton are also eaten

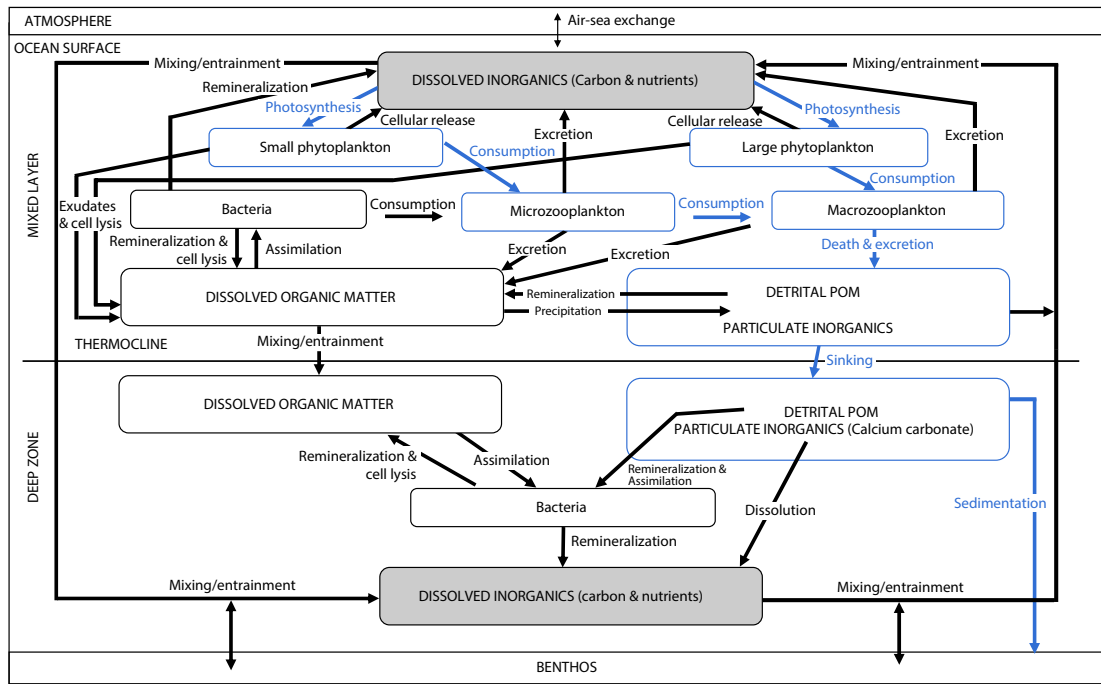
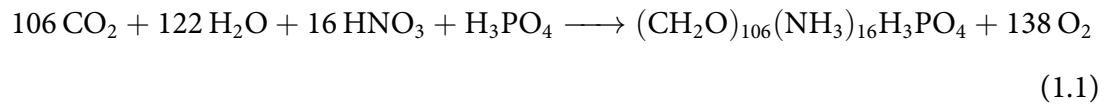


**Figure 1.1:** Biogeochemical cycling of particulate organic matter, dissolved organic matter, and dissolved inorganics in the oceans. The dominant pathways that contribute to sedimentation are highlighted in blue. Modified from Libes (2009).

by zooplankton and larger marine organisms, which transfers the accumulated nutrients to higher trophic levels of the food web.

Particulate organic matter forms predominantly by the following three processes: (1) assimilation of inorganic nutrients by phytoplankton, (2) assimilation of dissolved organic matter by heterotrophic microorganisms, and (3) precipitation and coagulation of dissolved organic matter to form colloids.

The elemental composition of marine plankton in all the world's oceans is relatively constant. It has a ratio of C:N:P of 106:16:1, and this is called the Redfield ratio (Redfield, 1934). Redfield proposed  $C_{106}(H_2O)_{106}(NH_3)_{16}PO_4$  as an ideal formula for a hypothetical "phosphorylated amino-carbohydrate" molecule that represents average planktonic organic matter. The author proposed that such a molecule formed as a result of photosynthesis via the following reaction:



This reaction illustrates that phytoplankton photosynthesis requires inorganic nitrogen  $\text{HNO}_3$  and phosphorus  $\text{H}_3\text{PO}_4$  in addition to carbon dioxide and water. In the ocean, nitrogen and phosphorus occur in much lower concentrations than the other reactants, and therefore, their concentrations are often the limiting factor for this reaction.

Pytoplankton is a term used to describe a wide range of pelagic photoautotrophs, so it might be expected that the C:N:P ratio of some species in this group deviate from the Redfield ratio. Quigg et al. (2003) identified statistically significant differences among the C:N:P ratios of different eukaryotic phyla and superfamilies cultured in the laboratory. Klausmeier, Litchman, Daufresne, and Levin (2004) also found differences between phytoplankton species using numerical modelling techniques and found that the Redfield N:P ratio of 16 is not a 'universal optimum' for phytoplankton, but instead represents an average of the species-specific ratios in the marine environment.

Geider and Roche (2002) collated data on marine phytoplankton published in the literature to determine the range of C:N:P ratios measured in the marine environment. Their analysis revealed N:P ratios in algae and cyanobacteria ranging from 5–100, which deviate greatly from the Redfield ratio. Low ratios were observed when phosphate was in great excess of inorganic nitrogen, whereas higher ratios were observed when inorganic nitrogen was in great excess of phosphate. Thus, the C:N:P ratio of marine phytoplankton is a factor of both species composition and the relative proportion and concentration of phosphate and inorganic nitrogen.

The water column isn't the only place where primary production occurs. Illuminated marine sediments contain benthic microphytes in the upper few millimetres, including unicellular eukaryotic algae and cyanobacteria. In coastal waters, benthic microphytes

contribute significantly to primary production; they can dominate the productivity in intertidal habitats (Joint, 1978; Varela & Penas, 1985), but are generally less productive than water column primary producers in subtidal habitats (Cahoon, Beretich, Thomas, & McDonald, 1993; Cahoon & Cooke, 1992; MacIntyre & Cullen, 1996).

Organic matter, both dissolved and particulate, that is generated in situ is referred to as autochthonous. Organic matter can also be generated externally, such as on the land, and transported into the coastal environment, in which case it is referred to as allochthonous. Prahl, Ertel, Goni, Sparrow, and Eversmeyer (1994) investigated carbon isotope ratios to determine the proportion of terrestrial organic matter in marine sediments (water depth 55–136 m) off the coast of Washington state and found that up to 60% of the organic matter was of terrestrial origin. The authors also found that the terrestrial contribution to sediment organic matter decreased with increasing water depth and distance from the coast. They found that ~30% of the organic matter in continental slope sediments (water depth 387–1004 m) was terrestrially derived, and <15% in basin sediments (water depth 1885–2617 m).

Sikes, Uhle, Nodder, and Howard (2009) similarly used carbon isotopes to identify the origin of surface sediments in the Hauraki Gulf, New Zealand. Sediment was collected from water depths ranging from 28–335 m and showed a similar pattern to that of Prahl et al. (1994). The study revealed that terrestrial sediment made up 56–60% of the total sediment composition at most of the sites. Sediment from the greatest water depth and furthest from the shore still comprised 40–45% terrestrial sediment. Both studies show the substantial contribution of terrestrially derived sediment in marine-dominated coastal environments and how readily such sediment is transported offshore.

Nitrogen and phosphorus support the abundance and biomass of primary producers. An increase in these nutrients, under the right conditions, can result in an increase in primary productivity, and therefore, organic matter deposition in the marine environment. Such increase in nutrients is referred to as eutrophication. Although

eutrophication doesn't directly contribute to the production of organic matter, the effects of eutrophication, including increased biomass of primary producers, do contribute. For this reason, I briefly discuss eutrophication in the following section.

### Coastal eutrophication

The term eutrophication is commonly used to refer to the increase in the input of nutrients, primarily nitrogen and phosphorous, into a water body. Nixon (1995) suggested that the definition should be more general, in that it refers to an increase in organic carbon. This is because nitrogen and phosphorous are not the only species that determine the available nutrient concentration. Nixon suggested that eutrophication should be defined as “an increase in the rate of supply of organic carbon to an ecosystem”. Such increased rate could arise from either autochthonous or allochthonous carbon. With this definition, Nixon went on to suggest four trophic states in the coastal environment based on the supply of organic matter, which I present in Table 1.1.

**Table 1.1:** Suggested trophic states for the coastal environment based on the supply of organic carbon by Nixon (1995).

	Organic carbon supply (g C m <sup>-2</sup> y <sup>-1</sup> )
Oligotrophic	<100
Mesotrophic	100–300
Eutrophic	301–500
Hypertrophic	>500

Nixon (1995) emphasised that the definition of eutrophication and the trophic state classification system were intended to be neutral, that is, there was no implication that one state was more desirable than another, or that eutrophication per se would result in an undesirable system. In fact, the natural state of most coastal marine environments ranges from oligotrophic to eutrophic (Richardson & Jørgensen, 2013). “Natural eutrophication” occurs regularly in coastal upwelling regions, such as the

north-western coast of Africa (Huntsman & Barber, 1977) and the eastern Gulf of California (Lluch-Cota, 2000). In such regions, strong offshore winds displace surface water away from the coast. The nutrient-poor surface water is then replaced by the upwelling of nutrient-rich deep water into the euphotic zone.

Coastal managers are interested in identifying the extent of eutrophication that is caused by anthropogenic activities. Such activities include land clearing, the use of fertiliser, the discharge of human and animal waste, and burning fossil fuels (Nixon, 1995). Richardson and Jørgensen (2013) note that in popular and scientific literature, the term eutrophication is often misused to include the effects of nutrient enrichment, whereas, the formal definition of eutrophication only encompasses the increased supply of nutrients to a system. Nixon (1995) suggests that the major driving force behind anthropogenic inputs of nitrogen and phosphorous in the marine environment is our need to satisfy human nutritional demands. The majority of this input arises from fertilisers that are applied to agricultural areas and subsequently wash into waterways.

One of the first and most visible effects of increased supply of nitrogen and phosphorous into the coastal environment is the rapid growth of aquatic macrophytes. The amount of light and inorganic nutrients are the key factors for phytoplankton growth and the extent of growth is dependent on whichever of these is the limiting factor. Generally, inorganic nutrients are the limiting factor in the coastal environment. The decomposition of organic matter provides inorganic nutrients, which is why an increase in organic matter can result in increased growth of aquatic macrophytes.

### **Marine farming**

Large amounts of particulate organic matter are generated by the intensive cultivation of fish in the form of faeces and uneaten food (Ye, Ritz, Fenton, & Lewis, 1991). The input of nutrient-rich feed can alter the chemistry of the water column and the

sediment beneath and surrounding the farm. For example, the oxygenation of the water column decreased to as little as 35% saturation within 3 m of a salmon farm on the western Scottish coast (Brown, Gowen, & McLusky, 1987). The entire sediment, including the surface layer and the sediment–water interface, was reducing beneath the farm and to a distance of 11 m from the farm boundary. Increased organic matter deposition on the seafloor can impede oxygen diffusion into the underlying sediment. Additionally, the degradation of organic matter is an oxygen-consuming process. The combination of these effects can result in the absence of oxygen in the underlying sediment, also known as anoxia. Anoxic conditions can decrease the diversity of the benthic faunal assemblage (Gray, Wu, & Or, 2002; Pearson & Rosenberg, 1978).

Mussel farms deposit less organic matter than fish farms because mussels do not require supplementary feed. They produce faeces and pseudofaeces (mucus wrapped particles excreted by the mussel, which could not be digested), which increase the rate of sedimentation to the seafloor beneath and surrounding such farms (e.g., Callier, McKindsey, & Desrosiers, 2007; Danovaro, Gambi, Luna, & Mirto, 2004).

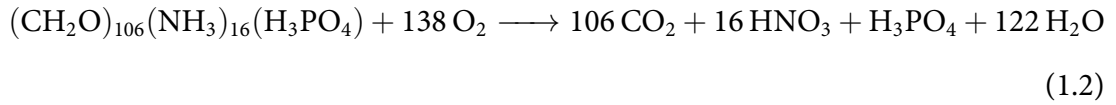
Investigations on the effects of long-line mussel farms on the benthic ecosystem have revealed a wide range of scenarios, from no detectable difference between inside and outside the farm (Crawford, Macleod, & Mitchell, 2003; Danovaro et al., 2003), to the replacement of macrofauna, such as bivalves and urchins, with opportunistic polychaetes underneath the farm as a result of increased organic matter deposition (Mattsson & Lindén, 1983; Stenton-Dozey, Probyn, & Busby, 2001).

### **1.1.2 Settlement through the water column**

Particulate organic matter is partially mineralised as it sinks through the water column (Glud, Gundersen, Jørgensen, Revsbech, & Schulz, 1994; Wenzhöfer & Glud, 2002). Mineralisation is the process of converting organic carbon into inorganic carbon, which can be used by phytoplankton. The mineralisation of Redfield's idealised



planktonic organic matter can be represented stoichiometrically as:



Particle dispersal, sinking velocity, and mineralisation are three parameters that determine the quantity of organic matter that settles through the water column before being deposited on the seafloor.

Stokes' law can be used to describe the sinking velocity ( $v_s$ ,  $\text{m s}^{-1}$ ) of an ideal spherical particle in a viscous fluid:

$$v_s = \frac{(\rho_2 - \rho_1) \times g \times D^2}{18\eta} \quad (1.3)$$

where  $\rho_2$  and  $\rho_1$  are the densities of the particle and the water ( $\text{g cm}^{-3}$ ),  $g$  is the acceleration due to gravity ( $\text{m s}^{-2}$ ),  $D$  is the particle diameter (cm), and  $\eta$  is the dynamic viscosity of the water ( $\text{g cm}^{-1} \text{ s}^{-1}$ ).

This equation demonstrates that smaller, less dense particles sink slower than larger particles. Most organic matter particles are not spherical, however, and will sink slower than an ideal sphere because of increased friction.

For example, Giles and Pilditch (2004) quantified the sinking velocities of faeces and pseudofaeces (biodeposits) of the mussel *Perna canaliculus*. They found that mussels on a “natural seawater” diet, produced faecal pellets that sank  $0.9\text{--}4.3 \text{ cm s}^{-1}$ , and pseudofaeces that sank  $0.5\text{--}2.2 \text{ cm s}^{-1}$ . The shape of the faeces was cylindrical and that of the pseudofaeces was amorphous. Sinking velocities for both deposits increased logarithmically with the particle width, not length for the cylindrical faeces pellet, as the particles descended in an orientation that created the least friction. Particles are subject to oxidation and degradation during their time in the water column. The rate of oxidation and degradation can be used by modellers to determine how much organic matter remains undegraded and is deposited on the seafloor.

The euphotic zone is a highly productive area of the coastal region and a large proportion of organic matter that settles through the water column is degraded in this zone before it reaches the seafloor. For example, Hedges, Clark, and Cowie (1988) measured up to 60% less organic carbon at 60 m water depth than in the upper water layers using sediment traps in Dabob Bay, Washington. The degradation of such large amounts of organic matter increases the oxygen demand of the water column. If this demand is higher than the oxygen supply into the water column, the oxygen concentration in the water column decreases, resulting in hypoxia or anoxia. In the absence of oxygen, organic matter degradation continues via anaerobic pathways that use alternative electron acceptors.

### **Anaerobic degradation**

Oxygen is used as an electron acceptor in the degradation process. Alternatively, other chemical species can act as electron acceptors, but their concentrations and potential energy returns vary widely (Figure 1.2).

In the absence of oxygen, anaerobic microorganisms can decompose organic matter using manganese(IV), nitrate, iron(III), or sulfate as the electron acceptor. The concentration of iron and manganese in the water column are typically too low for microorganisms to oxidise significant amounts of organic matter using these electron acceptors; however, these electron acceptors play an important part in marine sediments and I will discuss them later.

The results of sediment trap studies indicate that less than 50% of total organic matter produced by primary production is deposited on the seafloor in coastal areas, and this amount decreases to less than 1% in the deep sea (Martin, Knauer, Karl, & Broenkow, 1987; Suess, 1980). Organic matter is rapidly consumed in the water column, as it is the only chemical source of energy for heterotrophs. As a result of this consumption, not all particulate organic matter settling through the water column reaches the

<b>Dissolved oxygen</b>	
$(\text{CH}_2\text{O})_{106}(\text{NH}_3)_{16}(\text{H}_3\text{PO}_4) + 138 \text{ O}_2 \longrightarrow$ $106 \text{ CO}_2 + 16 \text{ HNO}_3 + \text{H}_3\text{PO}_4 + 122 \text{ H}_2\text{O}$	-3190 kJ mol <sup>-1</sup>
<b>Manganese-oxides</b>	
$(\text{CH}_2\text{O})_{106}(\text{NH}_3)_{16}(\text{H}_3\text{PO}_4) + 236 \text{ MnO}_2 + 472 \text{ H}^+ \longrightarrow$ $236 \text{ Mn}^{2+} + 106 \text{ CO}_2 + 8 \text{ N}_2 + \text{H}_3\text{PO}_4 + 366 \text{ H}_2\text{O}$	-3090 kJ mol <sup>-1</sup>
<b>Nitrate</b>	
$(\text{CH}_2\text{O})_{106}(\text{NH}_3)_{16}(\text{H}_3\text{PO}_4) + 84.8 \text{ HNO}_3 \longrightarrow$ $106 \text{ CO}_2 + 42.4 \text{ N}_2 + 16 \text{ NH}_3 + \text{H}_3\text{PO}_4 + 148.4 \text{ H}_2\text{O}$	-2750 kJ mol <sup>-1</sup>
<b>Iron-oxides</b>	
$(\text{CH}_2\text{O})_{106}(\text{NH}_3)_{16}(\text{H}_3\text{PO}_4) + 212 \text{ Fe}_2\text{O}_3 + 848 \text{ H}^+ \longrightarrow$ $424 \text{ Fe}^{2+} + 106 \text{ CO}_2 + 16 \text{ NH}_3 + \text{H}_2\text{PO}_4 + 530 \text{ H}_2\text{O}$	-1410 kJ mol <sup>-1</sup>
<b>Sulfate</b>	
$(\text{CH}_2\text{O})_{106}(\text{NH}_3)_{16}(\text{H}_3\text{PO}_4) + 53 \text{ SO}_4^{2-} \longrightarrow$ $106 \text{ CO}_2 + 16 \text{ NH}_3 + 53 \text{ S}^{2-} + \text{H}_3\text{PO}_4 + 106 \text{ H}_2\text{O}$	-380 kJ mol <sup>-1</sup>
<b>Methane fermentation</b>	
$(\text{CH}_2\text{O})_{106}(\text{NH}_3)_{16}(\text{H}_3\text{PO}_4) \longrightarrow 53 \text{ CO}_2 + 53 \text{ CH}_4 + 16 \text{ NH}_3 + \text{H}_3\text{PO}_4$	-350 kJ mol <sup>-1</sup>

**Figure 1.2:** Chemical equations for the major pathways by which organic matter degrades in the marine environment. The different electron acceptors are shown in the bold headings. Organic matter is represented by the formula  $(\text{CH}_2\text{O})_{106}(\text{NH}_3)_{16}(\text{H}_3\text{PO}_4)$ . The grey bars and values on the right show the calculated energy return from each pathway. Modified from Schulz and Zabel (2006); original data from Froelich et al. (1979).

seafloor. Figure 1.3 illustrates the organic matter flux and productivity from the upper water column to burial in the sediment.

Anaerobic degradation can also occur inside organic matter particles suspended in fully oxygenated seawater. Jørgensen (1977a) investigated this phenomenon and found that 50–200 µm large sediment pellets contained internal anaerobic microniches. The chemical environment within microniches were reducing and contained sulfate-reducing (*Desulfovibrio* spp.) and sulfide oxidizing (*Beggiatoa* spp.) bacteria. Within these microniches, bacteria produced  $\text{H}_2\text{S}$ , which diffused out into the surrounding oxidising environment where it was rapidly oxidised. Reduced microniches occur in organic matter when the rate of oxygen supply from the

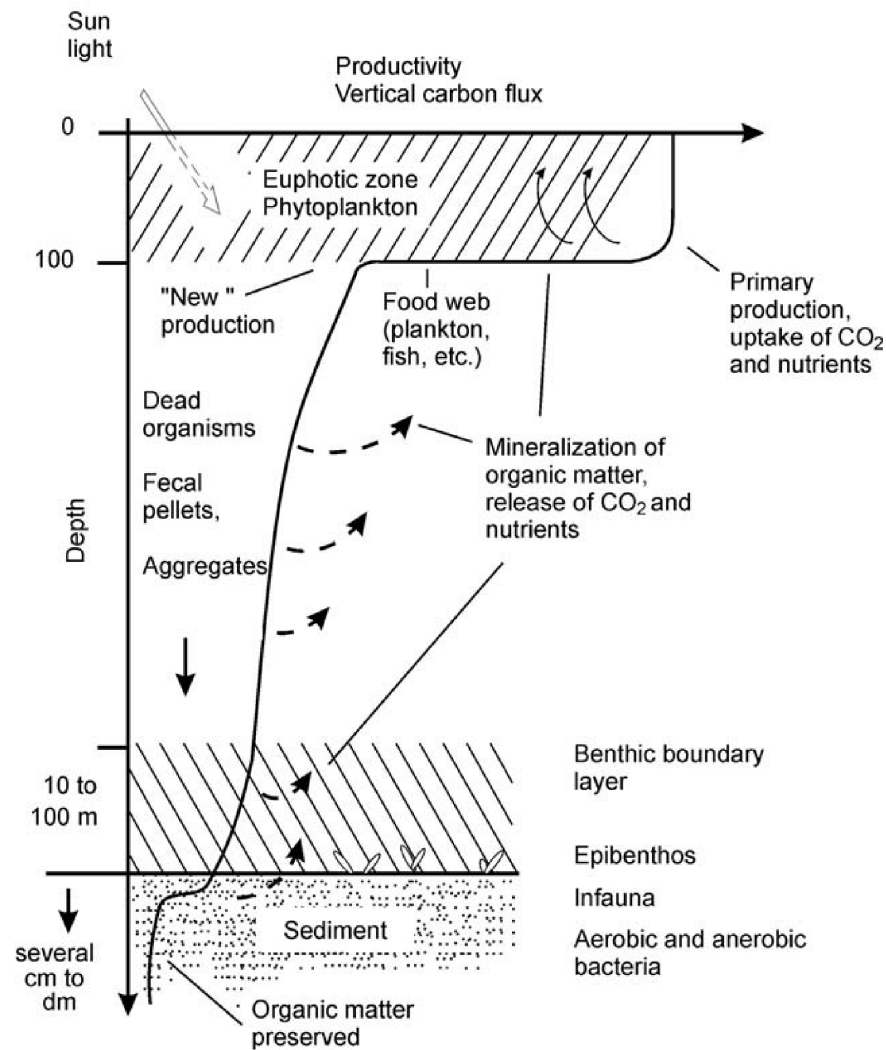


**Figure 1.3:** Representation of organic matter flux from the ocean surface to the seafloor. Zones of productivity are indicated by the hashed areas and an indication of the relative change in the rate of carbon flux by depth is shown by the solid black line. From Schulz and Zabel (2006).

surrounding seawater via diffusion is slower than the rate of oxygen consumption due to the microbial degradation of organic matter.

### 1.1.3 Deposition of organic matter on the seafloor

#### Benthic organic matter degradation

Organic matter that is deposited on coastal sediments undergoes degradation by physical and chemical pathways. The first conceptual organic degradation model was proposed by Froelich et al. (1979) and Figure 1.2 presents the dominant pathways by

which organic matter degradation occurs. Most deposited organic matter is mineralised by microbes (mostly bacteria and archaea), but some of it is consumed by benthic fauna (Fenchel, King, & Blackburn, 2012). Only a small part of the organic matter that is eaten by animals is utilised by their digestive system. In addition to digestion, the shredding or chewing of organic matter increases the exposed particle surface, which increases the potential rate of microbial degradation (Aller, 1994; Fenchel et al., 2012).

The oxidation of organic matter provides energy to many microorganisms aided by an oxidising agent, the most favourable being oxygen (Jørgensen & Kasten, 2006). In cohesive sediments, oxygen is typically transported from the overlying water into the sediment by molecular diffusion or as a result of biological activity. Oxygen is typically depleted within a few millimetres of the surface in organically enriched sediments because diffusion is slow and the oxygen concentration in seawater is relatively low ( $\sim 200 \mu\text{mol L}^{-1}$ ). Below this thin oxic zone, anaerobic prokaryotes use alternative electron acceptors to decompose the remaining organic matter (Bagarinao, 1992). In Danish coastal sediments, for example, less than 20% of organic matter may be oxidised with  $\text{O}_2$  as the electron acceptor (Canfield, Jørgensen, et al., 1993).

In order of decreasing energy, the electron acceptors used are:  $\text{O}_2 > \text{Mn}^{\text{IV}}$  (Mn oxides)  $> \text{NO}_3^- > \text{Fe}^{\text{III}}$  (Fe oxides)  $> \text{SO}_4^{2-} > \text{CH}_4$  (Froelich et al., 1979). Although the sulfate pathway returns one of the least amounts of energy, the concentration of sulfate in the water column dictates that sulfate reduction is the dominant pathway for organic matter degradation in coastal sediments (Bagarinao, 1992; Fenchel et al., 2012; Reeburgh, 1983; Thode-Andersen & Jørgensen, 1989). In seawater there is approximately two orders of magnitude more sulfate ( $\sim 25 \text{ mmol L}^{-1}$ ) than there is dissolved oxygen ( $\sim 0.2 \text{ mmol L}^{-1}$ ). Sulfate reduction is not, however, limited to anoxic sediment; it can occur simultaneously with oxic processes (Jørgensen & Bak, 1991). Jørgensen and Bak (1991) suggest that since the bacteria responsible for organic matter degradation can tolerate oxygen for extended periods of time ( $> 3$  hours; Cypionka, 1994), they may also carry out sulfate reduction in the presence of oxygen.

The authors alternatively suggest that the bacteria carry out sulfate reduction within anoxic and reducing microenvironments. The product of organic matter degradation via the sulfate pathway is hydrogen sulfide  $\text{H}_2\text{S}$ .

The produced  $\text{H}_2\text{S}$  is highly reactive and air-sensitive. It readily reacts with metals in the sediment to form more stable sulfide minerals. I discuss such sulfide minerals in more detail in section 1.3.1.

### **Effects of deposition on the benthos**

In the coastal environment, only the upper few millimetres of the sediment is oxidising. Oxygen penetration depth is controlled by the rate of oxygen diffusion into the sediment from oxygenated bottom water and the rate of oxygen consumption by chemical and biologically mediated reactions (Revsbech, Jørgensen, & Blackburn, 1980). An additional factor that influences sediment oxygen penetration depth is the rate of supply of organic matter. Van Duyl, Kop, Kok, and Sandee (1992) investigated the effects of organic matter deposition on sediment oxygen penetration by adding known amounts of organic matter to sediment cores in a laboratory and found that that oxygen penetration into the sediment was dependent on the rate of organic matter supply. If the rate of oxygen consumption is higher than the rate of oxygen diffusion, the underlying sediment can become hypoxic or anoxic.

### **Effects to the benthos**

Pearson and Rosenberg (1978) presented generalised species–abundance–biomass curves that illustrate observed changes to the benthos along a gradient of decreasing organic input (Figure 1.4). The authors described that in a non-enriched environment, benthic macrofaunal communities typically consist of many species and have a high biomass, but each species only has a moderate number of individuals. The area closest to a large source of organic matter is usually void of macrofauna. The number of species increases further away from the organic matter source, but initially the species

present are small, resilient, opportunistic species such as polychaetes. The ecotone is the point at which the benthic composition transitions from a high abundance of few species, to a more stable composition of low abundance of many species, including larger macrofauna.

Coastal managers are often interested in the composition of the benthic faunal communities and how these change over time when assessing the impacts of organic enrichment.

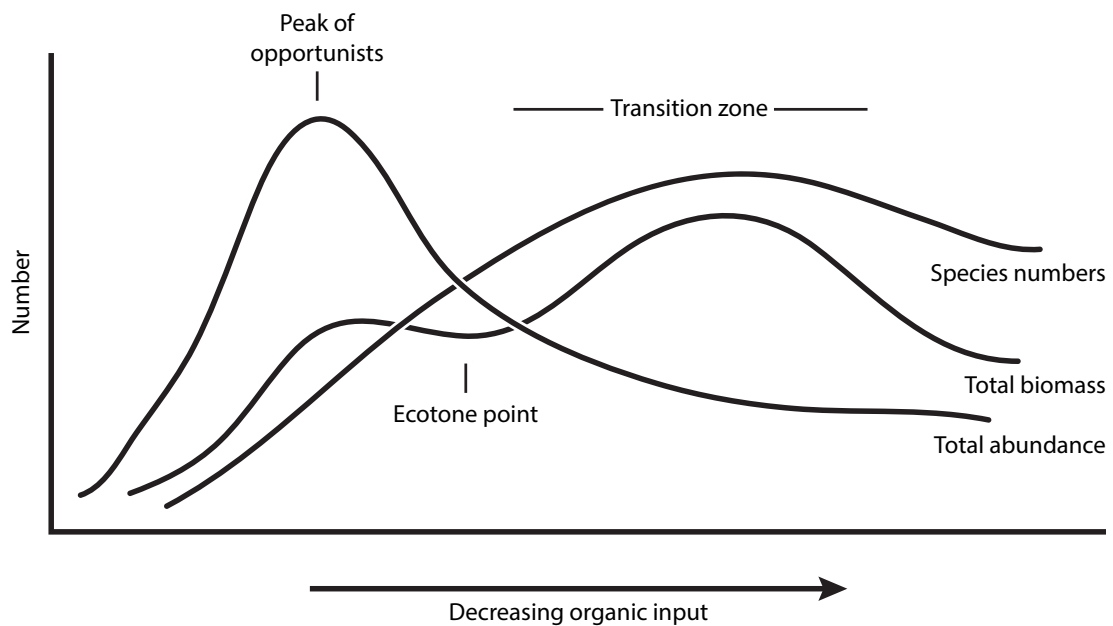


**Figure 1.4:** Generalised species–abundance–biomass curves illustrating the changes in the benthos along a decreasing organic enrichment gradient. Modified from Pearson and Rosenberg (1978).

The benthic community structure can change in response to organic matter enrichment over small spatial scales. For example, Callier et al. (2007) investigated the benthos between the lines of a long-line mussel farm in 5–7 m water depth off the eastern Canadian coast and identified the dominant species to be two polychaetes, *Polydora ciliata* (Johnston, 1838) and *Capitella capitata* (Fabricius, 1780). Directly beneath the hanging lines, however, *P. ciliata* was absent and *C. capitata* was 12 times more abundant than between the lines. The distance between the two sampling points was 10 m. The authors suggest that this indicates a shift from an intermediately enriched environment between the lines of the farm to a greatly enriched environment directly beneath the lines. The polychaete *C. capitata* has some resistance to sulfide

toxicity and hypoxia, which can explain their presence in an organically enriched environment (Diaz & Rosenberg, 1995).

Following the Pearson-Rosenberg model, an increase in organic matter causes a decrease in species richness.

Chamberlain, Fernandes, Read, Nickell, and Davies (2001), for example, reported lower species diversity beneath, and up to 40 m away from, a long-line mussel farm in southwest Ireland. The authors described species diversity using the Shannon–Wiener diversity index, where a value approaching 0 indicates one dominant species. Beneath the farm, the Shannon–Wiener diversity index decreased to 1.5, from 2.5 at a distance 60 m away from the farm, which indicates a decrease in species diversity beneath the farm. Beneath this farm, there was an increase in the proportion of the polychaete *Ophryotrocha hartmanni* Huth, 1933. This species alone accounted for 63% of the total counted fauna, whereas this species was present at much lower abundances at sampling sites further from the farm. The authors attribute the decrease in species diversity beneath the farm to the increase in organic carbon and nitrogen supplied from the overlying farm.

Contrastingly, Wong and O'Shea (2011) identified an increase in species richness and abundance beneath a mussel farm in the Hauraki Gulf, New Zealand. The authors suggest the increase was attributed to the added structure of fallen mussel shells that other species could attach to, rather than a preference for the higher organic matter content.

#### **1.1.4 Influence of benthic fauna on the distribution of sedimentary sulfides**

In addition to diffusion of solutes over the sediment–water interface, the activities of bioturbating macrofauna influence the distribution of sedimentary sulfides in coastal marine sediments. Specifically, their physical reworking of sediment when moving



across the sediment surface and creating burrows and tubes, and irrigating these burrows and tubes by pumping oxygenated water (Kristensen et al., 2012).

To constrain the scope of my research, I focus on the chemical aspects that influence sedimentary sulfides, rather than the effect of bioturbating macrofauna. I do, however, briefly discuss their main effects in this section.

One of the more obvious effects of bioturbating macrofauna is the movement of particles as they move along the sediment surface and create burrows and tubes. This process transports particles from an anoxic environment deeper in the sediment to an oxic environment closer towards the sediment–water interface. Reduced sulfides transported into oxic environments will, over time, be reoxidised.

Typically, oxygen only diffuses a number of millimetres in shallow coastal sediments, compared to centimetres in deeper oceanic sediments (Glud et al., 1994). The burrows and tubes created by benthic macrofauna considerably increase the surface area available for diffusion to occur and at depths greater than if solutes diffused solely from the sediment–water interface (Fenchel, 1996; Kristensen, 1984). This greater surface area and deeper penetration of oxygen creates a thicker oxic layer than in sediment lacking bioturbating macrofauna. The effect of this is that the majority of reduced sulfides will occur deeper in the sediment below the thickened oxic boundary.

Furthermore, when oxygenated water is pumped from the bottom water around the burrows and tubes, it reacts with the oxygen sensitive organic matter that was previously in anoxic environment (Kristensen, 2000). This additional oxidation increases the overall rate of organic matter degradation within the sediment, and thus the production of  $\text{H}_2\text{S}$ .

## 1.2 Sulfate reducing bacteria

Bacteria play an important part in marine biogeochemical cycling. They are responsible for mediating a large number of redox processes that result in the degradation of organic matter, such as those previously discussed under ‘anaerobic degradation’. Bacteria accelerate the reaction rate of these processes through enzymatic catalysis at a rate up to  $10^{20}$ -fold faster than the non-catalysed reaction (Jørgensen, 2006).

There are currently 32 recognised genera of sulfate reducing bacteria (Table 1.2). They have a diverse morphology, ranging from spherical to multicellular gliding filaments and can be found in environments with temperatures ranging from  $<0^{\circ}\text{C}$  in the Arctic (Knoblauch, Sahm, & Jørgensen, 1999), to  $>100^{\circ}\text{C}$  by hydrothermal vents (Jørgensen, Isaksen, & Jannasch, 1992). Although this group of bacteria is called sulfate reducing bacteria, many can also use sulfite ( $\text{SO}_3^{2-}$ ) or thiosulfate ( $\text{S}_2\text{O}_3^{2-}$ ) as alternative electron acceptors, which are also reduced to sulfide (Rabus et al., 2013). Additionally, there are species belonging to the domain Archaea that are sulfate-reducers, however, I will focus on bacteria in this section.

Sulfate reducing bacteria conserve some of the energy from the degradation of organic matter to fuel their cellular function, such as growth and division, synthesis of macromolecules, transport of solutes across the cell membrane, secretion, and movement. They couple the degradation process to the formation of a proton ( $\text{H}^+$ ) gradient across the cell membrane. This proton gradient is similar to that of a battery; however, protons are stored inside the cell, rather than electrons. I present a simplified illustration of the sulfate reducing bacteria metabolism in Figure 1.5.

Sulfate reducing bacteria can metabolise sulfate via many pathways (Table 1.3). The Gibbs’ free energy ( $\Delta G^0$ ), shown in the final column, represents the net energy produced (negative) or consumed (positive) from the reaction under standard conditions. The standard conditions are pH 7,  $25^{\circ}\text{C}$ , and 1 bar partial pressure of gases. These are the conditions used to standardise the laboratory-derived values,

**Table 1.2:** Currently recognised genera of sulfate reducing bacteria (Rabus et al., 2013).

Genus	Morphology	Optimum temperature (°C)	Electron acceptors used in addition to $\text{SO}_4^{2-}$
<i>Desulfovibrio</i>	Vibrio	30–38	$\text{SO}_3^{2-}$ , $\text{S}_2\text{O}_3^{2-}$ , fumarate
<i>Desulfomicrobium</i>	Oval or rod	28–37	$\text{SO}_3^{2-}$ , $\text{S}_2\text{O}_3^{2-}$
<i>Desulfobulbus</i>	Oval	28–39	$\text{SO}_3^{2-}$ , $\text{S}_2\text{O}_3^{2-}$ , $\text{NO}_3^-$
<i>Desulfobacter</i>	Oval or vibrio	28–32	$\text{SO}_3^{2-}$ , $\text{S}_2\text{O}_3^{2-}$
<i>Desulfobacterium</i>	Oval	20–35	$\text{S}_2\text{O}_3^{2-}$
<i>Desulfococcus</i>	Sphere	28–36	$\text{SO}_3^{2-}$ , $\text{S}_2\text{O}_3^{2-}$
<i>Desulfosarcina</i>	Oval (forms aggregates)	33	$\text{SO}_3^{2-}$ , $\text{S}_2\text{O}_3^{2-}$
<i>Desulfomonile</i>	Rod	37	$\text{SO}_3^{2-}$ , $\text{S}_2\text{O}_3^{2-}$ , benzoate
<i>Desulfonema</i>	Multicellular filaments	30–32	$\text{SO}_3^{2-}$ , $\text{S}_2\text{O}_3^{2-}$
<i>Desulfobotulus</i>	Vibrio	34	$\text{SO}_3^{2-}$
<i>Desulfoarculus</i>	Vibrio	35–39	$\text{SO}_3^{2-}$ , $\text{S}_2\text{O}_3^{2-}$
<i>Desulfotomaculum</i>	Straight or curved rod, sporulates	30–38, 50–65 (thermophilic)	$\text{S}_2\text{O}_3^{2-}$ , fumarate
<i>Desulfosporosinus</i>	Straight or curved rod, sporulates	30–37	$\text{S}_2\text{O}_3^{2-}$
<i>Thermodesulfovibrio</i>	Vibrio	65	$\text{SO}_3^{2-}$ , $\text{S}_2\text{O}_3^{2-}$
<i>Thermodesulfobacterium</i>	Rod	65–70	$\text{S}_2\text{O}_3^{2-}$
<i>Thermodesulforhabdus</i>	Rod	60	$\text{SO}_3^{2-}$
<i>Desulfacinum</i>	Oval	60	$\text{SO}_3^{2-}$ , $\text{S}_2\text{O}_3^{2-}$
<i>Desulforhopalus</i>	Oval	18–19	$\text{SO}_3^{2-}$ , $\text{S}_2\text{O}_3^{2-}$
<i>Desulforhabdus</i>	Rod	37	$\text{SO}_3^{2-}$ , $\text{S}_2\text{O}_3^{2-}$
<i>Desulfonatronovibrio</i>	Vibrio	37	$\text{SO}_3^{2-}$ , $\text{S}_2\text{O}_3^{2-}$
<i>Desulfonatronum</i>	Vibrio	37–40	$\text{SO}_3^{2-}$ , $\text{S}_2\text{O}_3^{2-}$
<i>Desulfohalobium</i>	Rod	37–40	$\text{SO}_3^{2-}$ , $\text{S}_2\text{O}_3^{2-}$ , $\text{S}^0$
<i>Desulfofustis</i>	Rod	28	$\text{SO}_3^{2-}$ , $\text{S}^0$
<i>Desulfocella</i>	Vibrio	34	—
<i>Desulfocapsa</i>	Rod	20–30	—
<i>Desulfobacca</i>	Oval	37	$\text{SO}_3^{2-}$ , $\text{S}_2\text{O}_3^{2-}$
<i>Desulfuromusa</i>	Rod	30	$\text{S}^0$ , $\text{NO}_3^-$ , fumarate, DMSO <sup>*</sup> , Fe(III)-citrate
<i>Desulfospira</i>	Curved rod	26–30	$\text{SO}_3^{2-}$ , $\text{S}_2\text{O}_3^{2-}$ , $\text{S}^0$
<i>Desulfobacula</i>	Rod	28	No data
<i>Desulfofrigus</i>	Rod	10	$\text{SO}_3^{2-}$ , $\text{S}_2\text{O}_3^{2-}$ , Fe(III)-citrate
<i>Desulfofaba</i>	Rod	7	$\text{SO}_3^{2-}$ , $\text{S}_2\text{O}_3^{2-}$
<i>Desulfotalea</i>	Rod	10	$\text{SO}_3^{2-}$ , $\text{S}_2\text{O}_3^{2-}$ , Fe(III)-citrate

\* DMSO = Dimethyl sulfoxide  $[(\text{CH}_3)_2\text{SO}]$

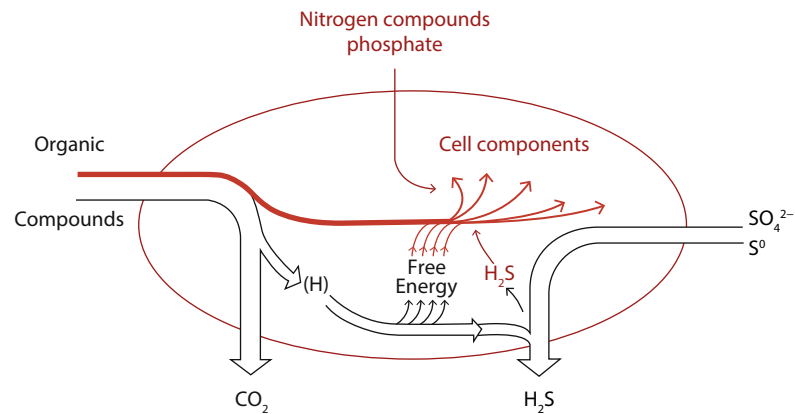


**Figure 1.5:** Simplified illustration of the sulfate reducing bacteria metabolism. The black lines show that the majority of energy from the inputs (organic compounds and sulfur/sulfate) is conserved in the outputs ( $\text{CO}_2$  and  $\text{H}_2\text{S}$ ). The red lines show that a minor fraction of the input energy is used by the organism for cellular function. Image from Rabus et al. (2013).

however, actual environmental conditions (pH, temperature, etc.) are usually different to these conditions, and therefore, the reactions will have different energy returns.

Such difference in conditions may increase or decrease the free energy of each reaction. Generally, reactions will only proceed if the energy return is greater than  $\sim 20 \text{ kJ mol}^{-1}$  as this is approximately the energy required to form the energy-carrying molecule adenosine triphosphate (ATP; Hoehler, Alperin, Albert, & Martens, 1998). An organism can only conserve some of the energy from a reaction if ATP can be formed.

Under standard conditions, the disproportionation of elemental sulfur requires more energy that it produces, and therefore, should not occur (Table 1.3); however, when  $\text{HS}^-$  is readily removed and consumed by other sedimentary processes, this reaction produces a net gain in energy as the equilibrium of the reaction is shifted further to the right hand side of the equation (Cypionka, 1994).

The major factors that control the rate of bacterial sulfate reduction are the amount of deposited organic matter on the seafloor and its reactivity, assuming that the overlying water is oxygenated. To identify the limiting factors of sulfate reduction, Boudreau and Westrich (1984) controlled the dissolved porewater sulfate concentration in marine sediment cores from Long Island Sound, USA, and found that the sulfate reduction rate only reduced at very low concentrations ( $< 3\text{--}4 \text{ mmol L}^{-1}$ ).

**Table 1.3:** Equations for the metabolic pathways of sulfate reducing bacteria. The final column shows the Gibbs free energy of the reaction under standard conditions: pH 7, 25 °C, and 1 bar partial pressure. From Jørgensen (2006).

Pathway and stoichiometry	$\Delta G^0$ (kJ mol <sup>-1</sup> )
<i>Reduction of sulfur compounds</i>	
$\text{SO}_4^{2-} + 4 \text{H}_2 + \text{H}^+ \longrightarrow \text{HS}^- + 4 \text{H}_2\text{O}$	-155
$\text{SO}_3^{2-} + 3 \text{H}_2 + \text{H}^+ \longrightarrow \text{HS}^- + 3 \text{H}_2\text{O}$	-175
$\text{S}_2\text{O}_3^{2-} + 4 \text{H}_2 \longrightarrow 2 \text{HS}^- + 3 \text{H}_2\text{O}$	-179
$\text{S}^0 + \text{H}_2 \longrightarrow \text{HS}^- + \text{H}^+$	-30
<i>Incomplete sulfate reduction</i>	
$\text{SO}_4^{2-} + 2 \text{H}_2 + \text{H}^+ \longrightarrow \text{S}_2\text{O}_3^{2-} + 5 \text{H}_2\text{O}$	-65
<i>Disproportionation</i>	
$\text{S}_2\text{O}_3^{2-} + \text{H}_2\text{O} \longrightarrow \text{SO}_4^{2-} + \text{HS}^- + \text{H}^+$	-25
$4 \text{SO}_3^{2-} + \text{H}^+ \longrightarrow 3 \text{SO}_4^{2-} + \text{HS}^-$	-236
$4 \text{S}^0 + 4 \text{H}_2\text{O} \longrightarrow \text{SO}_4^{2-} + 3 \text{HS}^- + 5 \text{H}^+$	33
<i>Oxidation of sulfur compounds</i>	
$\text{HS}^- + 2 \text{O}_2 \longrightarrow \text{SO}_4^{2-} + \text{H}^+$	-794
$\text{HS}^- + \text{NO}_3^- + \text{H}^+ + \text{H}_2\text{O} \longrightarrow \text{SO}_4^{2-} + \text{NH}_4^+$	-445
$\text{SO}_3^{2-} + 2 \text{O}_2 + \text{H}_2\text{O} \longrightarrow \text{SO}_4^{2-} + 2 \text{H}^+$	-976
$\text{SO}_3^{2-} + \frac{1}{2} \text{O}_2 \longrightarrow \text{SO}_4^{2-}$	-257

Alternatively, Westrich and Berner (1984) studied the sulfate reduction rate in sediment from the same site but manipulated the amount of organic matter in the sediment. The authors identified a first-order relationship between the concentration of organic matter and the sulfate reduction rate, that is, the sulfate reduction rate increased linearly with an increased concentration of organic matter. They also identified that the organic matter could be divided into two fractions, a highly reactive fraction and a non-reactive fraction. Fresh plankton was collected for the experiment as the organic matter source by towing a net behind a boat in Long Island Sound. The sample comprised a variety of diatoms, predominantly the genus *Leptocylindrus* Cleve, 1889 (60–70%). The non-reactive fraction made up ~35% of the organic matter and was not degraded during the two years in which the experiment ran. The authors suggest that such fraction may still be degradable, but on a much longer timescale that couldn't be investigated during their experiment.

The studies by Boudreau and Westrich (1984) and Westrich and Berner (1984) show that the bacterial sulfate reduction rate of organic matter in coastal sediments

increases with increasing sediment organic matter content as long as the concentration of dissolved porewater sulfate is  $>3 \text{ mmol L}^{-1}$ .

### 1.3 Acid volatile sulfide

In aqueous environments,  $\text{H}_2\text{S}$  formed during the microbially mediated degradation of organic matter dissociates into the hydrosulfide anion ( $\text{HS}^-$ ) and the bisulfide anion ( $\text{S}^{2-}$ ); the proportion of these three species is pH dependant (Morse, Millero, Cornwell, & Rickard, 1987).  $\text{H}_2\text{S}$  and  $\text{HS}^-$  are the most important forms in marine environments and  $\text{S}^{2-}$  has no significant activity.

The overall rate of sedimentary sulfate reduction responds to the rate of organic particle deposition, that is, the supply of sulfide to coastal sediment increases with its organic carbon supply (Berner, 1978; Brückert, 1998; Cornwell & Sampaou, 1995; Dahlbäck & Gunnarsson, 1981; Oenema, 1990; Y. I. Sorokin & Zakuskina, 2012). Approximately 80% (Canfield, Thamdrup, & Hansen, 1993) to 90% (Hansen, Ingvorsen, & Jørgensen, 1978; Jørgensen, 1982) of the sulfide is re-oxidised, mostly through microbial activity. The remaining sulfide reacts to form more thermodynamically stable forms such as the minerals mackinawite ( $\text{FeS}$ ), greigite ( $\text{Fe}_3\text{S}_4$ ), and pyrite ( $\text{FeS}_2$ ), which are responsible for the black colour of coastal sediments (Berner, 1964a; Goldhaber & Kaplan, 1980; Jørgensen, 1977b). Most of these sulfides convert back to  $\text{H}_2\text{S}$  when treated with acid and are collectively known as acid volatile sulfide (AVS).

Berner (1964a) defined AVS as the sedimentary sulfur that is extracted by  $1 \text{ mol L}^{-1}$   $\text{HCl}$ , including porewater sulfides and metastable iron sulfide minerals such as mackinawite and greigite but excluding the more stable pyrite. I. I. Sorokin, Giovanardi, Pranovi, and Sorokin (1999) consider AVS to be one of the most important environmental quality indicators, and while initially developed to gain

insight into early diagenetic processes, it has been more commonly used in the last few years as an indicator of sediment metal toxicity.

Sulfides bind with many trace metals present in marine sediment, limiting their activity and bioavailability (H. E. Allen, Fu, & Deng, 1993; Ankley, 1996). Trace metal bioavailability is the degree and rate at which the trace metal is absorbed by living organisms, which may have adverse effects on the organism depending on the metal, the chemical form of the metal, and the concentration. The process of sulfides binding with metals alters the chemical form of the metal and can decrease its bioavailability. Di Toro et al. (1990) found that when the concentration of AVS exceeded the concentration of cadmium, very low concentrations of cadmium were detected in the sediment porewater. The authors observed low toxicity from cadmium in the amphipods *Rhepoxynius hudsoni* Barnard & Barnard, 1982 and *Ampelisca abdita* Mills, 1964, even though the total concentration of cadmium should have been above their threshold. Di Toro et al. (1992) conducted a similar experiment using nickel and made the same observations. The authors then suggested that AVS concentration may be a suitable indicator of bioavailability for a range of cationic metals, including cadmium, copper, nickel, lead, and zinc. They hypothesised that the metals would not be bioavailable so long as the molar concentration of sulfide was higher than the sum of the concentration of metals (Cooper & Morse, 1998; Di Toro et al., 1992). Therefore, measuring AVS in addition to cationic metals could be used as an indicator for potential metal bioavailability.

Treating marine sediments with acid also extracts cationic metals. The metals that are extracted during this treatment are known as simultaneously extractable metals (SEM). Metal bioavailability can be estimated using the ratio of AVS:SEM (H. E. Allen et al., 1993).



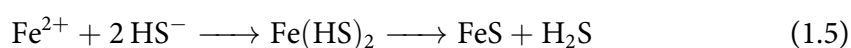


minerals occur as nanoparticles. X-ray powder diffraction (XRPD) and scanning electron microscopy (SEM) are two of the most commonly used techniques for determining mineral composition but they have shown to be ineffective with minerals of this type (Morse & Cornwell, 1987). Despite the lack of direct observation, the general assumption is that AVS is predominantly comprised of mackinawite and greigite minerals (Rickard & Morse, 2005).

### Mackinawite

Mackinawite is one of the major constituents of black sedimentary iron sulfides (Morse et al., 1987). It is kinetically the first iron sulfide to form in low-temperature aqueous systems (Morse & Rickard, 2004). In response to the difficulty of detecting mackinawite in marine sediments using common techniques, Berner (1964c) synthesised the mineral in a laboratory by precipitating  $\text{Fe}^{2+}$  salts with  $\text{S}^{2-}$  so that he could make suitable measurements. He found that in the structure of mackinawite, each iron atom is coordinated to four other iron atoms in the same plane (Figure 1.7). Each iron atom is also coordinated to four sulfur atoms which sit above and below the plane of iron atoms and are in a tetrahedral geometry around the iron atom. This structure forms layers. Iron(II) monosulfides have been given many names throughout the literature, including hydrotroilite, kansite, precipitated FeS, amorphous FeS, and disordered mackinawite; further study of these minerals revealed that they all have the same tetragonal structure and are most likely all mackinawite (Rickard & Morse, 2005).

Equations for the two competing mechanisms that form mackinawite are shown below:



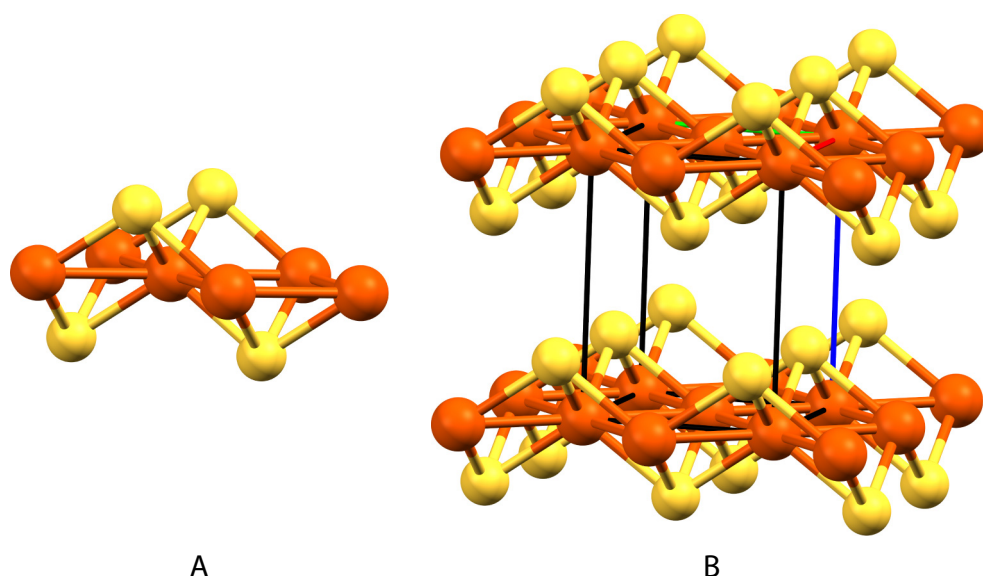


**Figure 1.7:** Molecular structure diagrams of the mineral mackinawite. (A) The single unit, and (B) the packing structure. Sulfur atoms are yellow, and iron atoms are orange. The cube frame in (B) indicates the extent of the repeating unit. X-ray crystal data from Lennie et al. (1995).

Rickard (1995) proposed that the  $\text{HS}^-$  pathway involves the formation of a complex,  $\text{Fe}(\text{HS})_2$ , which slowly condenses to form  $\text{FeS}$ .

### Greigite

Greigite is assumed to be one of the major constituents of AVS (Rickard & Morse, 2005). It has the stoichiometry  $\text{Fe}_3\text{S}_4$  and a cubic arrangement (Figure 1.8). Mineral greigite is not completely soluble in  $\text{HCl}$ , therefore, the actual concentration of the mineral may be underestimated in standard, 1 M  $\text{HCl}$  acid extractions.

Lennie et al. (1997) demonstrated that greigite can form as a result of a solid state reaction from mackinawite. In a solid state reaction, the reactants do not dissolve in a solvent before reacting. This is in contrast to the typical formation of minerals in aqueous reactions, of which there have been no reports for greigite.

### Pyrite

The limiting factor in pyrite formation in the marine environment is the availability of reactive iron minerals (Berner, 1984; Gagnon, Mucci, & Pelletier, 1995). One of the

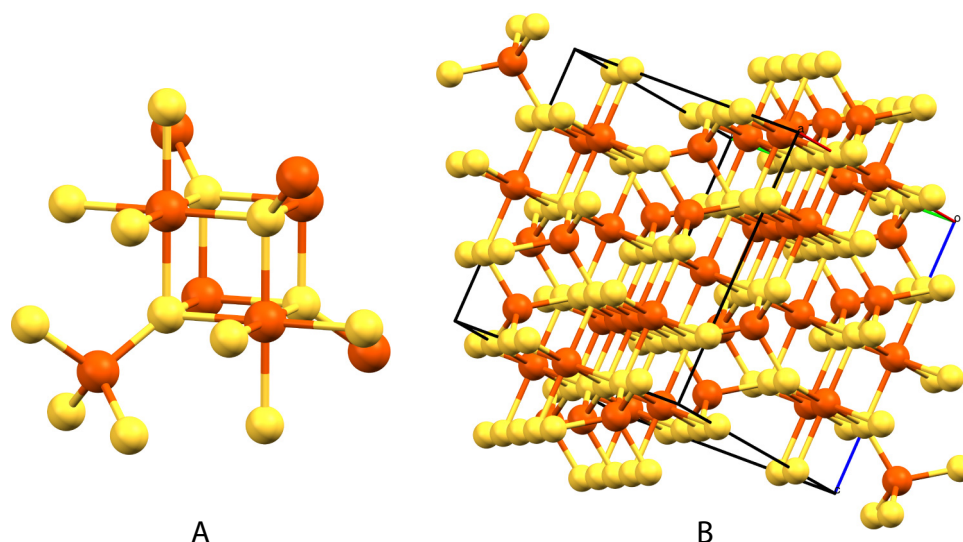


**Figure 1.8:** Molecular structure diagrams of the mineral greigite. (A) The single unit, and (B) the packing structure. Sulfur atoms are yellow, and iron atoms are orange. The cube frame in (B) indicates the extent of the repeating unit. X-ray crystal data from Skinner et al. (1964).

first proposed mechanisms for the production of pyrite involved the formation of “intermediate” metastable iron sulfides such as mackinawite and greigite. Later studies revealed that pyrite can also form in the absence of these metastable minerals (Luther III, 1991; Rickard, 1995, 1997; Rickard & Luther III, 1997). In the molecular structure of pyrite, each iron atom is coordinated to six sulfur atoms in an octahedral arrangement (Figure 1.9). Each sulfur atom is coordinated to three iron atoms, and one sulfur atom in a tetrahedral arrangement.

The overall reaction for pyrite ( $\text{FeS}_2$ ) formation can be written as:



where  $\text{S}^0$  is elemental sulfur. Rickard and Morse (2005) described and summarised pyrite formation theories in terms of kinetics and discussed how this process is much more complicated than the equation implies. The probability of a chemical reaction taking place decreases rapidly with increasing number of molecules required to react simultaneously. At ambient temperatures, elemental sulfur is present as  $\text{S}_8$ ; this modifies the equation to:

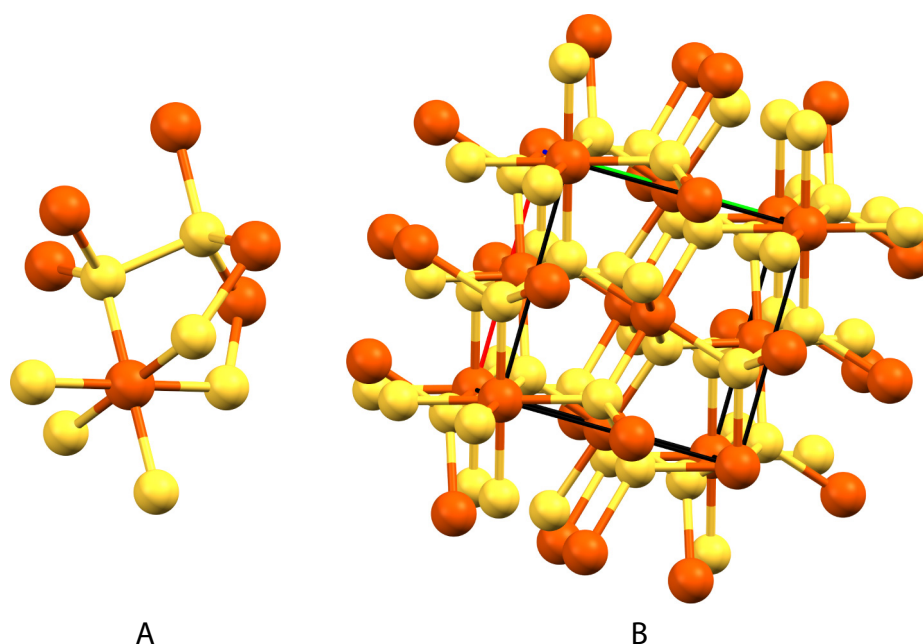
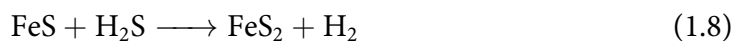


**Figure 1.9:** Molecular structure diagrams of the mineral pyrite. (A) The single unit, and (B) the packing structure. Sulfur atoms are yellow, and iron atoms are orange. The cube frame in (B) indicates the extent of the repeating unit. X-ray crystal data from Brostigen and Kjekshus (1969).



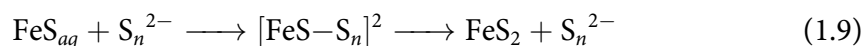
Nine molecules are required to interact simultaneously for this reaction to occur, which is highly improbable. Alternative mechanisms have been presented that instead use  $\text{H}_2\text{S}$  (Butler & Rickard, 2000; Rickard, 1997; Rickard & Luther III, 1997, 2007) and polysulfides (Luther III, 1991; Rickard, 1975) in the reaction to produce pyrite.

*The  $\text{H}_2\text{S}$  mechanism:*



This mechanism occurs in all reported formations of pyrite in the marine environment (Rickard & Morse, 2005). Rickard (1997) and Rickard and Luther III (1997) identified a rate limiting step in this reaction that involved the formation of the intermediate  $[\text{Fe} - \text{S} \longrightarrow \text{SH}_2]$ . This intermediate facilitates the oxidation of  $\text{S}^{2-}$  to  $\text{S}^-$ , which is required for the reaction to proceed.

*The polysulfide mechanism:*



where  $[\text{FeS}-\text{S}_n]^2$  is a reaction intermediate. Luther III (1991) developed this mechanism based on the idea that since pyrite itself is a polysulfide, a polysulfide must be involved in the reaction. In a voltammetric study, Theberge and Luther III (1997) identified that the FeS involved in the reaction was an aqueous cluster, rather than dissolved FeS. Both of these mechanisms were confirmed by the isotopic study conducted by Butler, Böttcher, Rickard, and Oldroyd (2004).

### **Dissolved sulfur species**

The dissolved sulfur species are generally a minor fraction of the AVS pool in iron-rich sediments, but cannot be ignored. They are more transient than the solid species, having short turnover times in the sulfur cycle of 1–5 days; in contrast, pyrite has a turnover time of about 10 years (Jørgensen, 1977b).

The main dissolved species include  $\text{H}_2\text{S}$ ,  $\text{HS}^-$ , and  $\text{Fe}_x\text{HS}_y$ . Theberge and Luther III (1997) identified aqueous FeS clusters using square wave voltammetry, and found them to comprise a series of compounds with the formula  $\text{Fe}_x\text{HS}_y$ , where  $x$  and  $y$  range from 2 to 150. They are involved in the formation of iron sulfide minerals, including mackinawite and greigite, and are one of the most important dissolved species that contribute to AVS, after  $\text{H}_2\text{S}$  and  $\text{HS}^-$  (Rickard & Morse, 2005).

Polysulfides is a collective term for dissolved sulfur species that have the formula  $\text{S}_n^{2-}$  (sulfanes) or  $\text{HS}_n^-$  (hydrosulfanes). Polysulfides can form in the presence of oxygen, for this reason, the concentration of polysulfides measured in the laboratory is likely to be higher than in the original sample unless samples are processed in an anoxic environment. Such increase in concentration occurs as the samples are often exposed to small amounts of oxygen during sampling and analysis (Rickard & Morse, 2005).

Because of the typically low concentration of polysulfides (Rickard & Morse, 2005), they are unlikely to contribute substantially to the total dissolved AVS pool.

### **Sulfur bacteria**

Considering that the majority of sulfate reduction is mediated by sulfate reducing bacteria, it is possible that the bacteria themselves may contribute to the AVS pool. Rickard and Morse (2005) estimated the potential contribution of bacteria to AVS by assuming a concentration of  $10^6$  cells  $\text{mL}^{-1}$  and each cell containing 5% by volume of FeS. This equates to a contribution of  $\sim 1$  nmol S  $\text{g}^{-1}$  dry sediment, which is negligible for a typical AVS concentration in the micromole range.

### **Extracting AVS**

A variety of methods for extracting AVS have been adapted since the inception of the AVS concept, in particular, the concentration of the acid used, the type of acid used (HCl or  $\text{HNO}_3$ ), whether or not to use hot or cold acid, and whether or not to include  $\text{SnCl}_2$  or  $\text{TiCl}_2$  to reduce interference from  $\text{Fe}^{3+}$  by keeping the solution reducing (Rickard & Morse, 2005, and enclosed references).

The most commonly used methods do not quantitatively extract the dominant AVS minerals such as mackinawite and greigite. Pyrite is partially extracted when using hot 6 M HCl, which is required to quantitatively extract mackinawite and greigite (Rickard & Morse, 2005); extraction efficiencies for these methods are shown in Table 1.4.

Luther III (2005) recommended omitting reducing agents from the extraction, as these can dissolve sedimentary pyrite, and keeping the HCl concentration between 1–5 mol  $\text{L}^{-1}$ . These conditions could potentially underestimate the concentration of mineral sulfides as they do not quantitatively extract sulfur from mackinawite and greigite.

**Table 1.4:** Extraction efficiencies of commonly used AVS extraction methods on synthetically prepared mackinawite, greigite, and pyrite, and mineral pyrite. Data from Cornwell and Morse (1987).

Method	% mineral sulfur extracted			
	Mackinawite	Greigite	Synthetic pyrite	Mineral pyrite
1 M HCl	92	40–67	0	0
6 M HCl + SnCl <sub>2</sub>	100–102	63–75	4–10	0
0.5 M H <sub>2</sub> SO <sub>4</sub> + TiCl <sub>2</sub>	101	96–100	48–82	0
Hot 6 M HCl + SnCl <sub>2</sub>	100–101	93–100	97–100	2

## 1.4 Sediment-profile imagery (SPI)

SPI is an underwater technique for acquiring images of the sediment–water interface and underlying sediment. The term SPI is also used to describe the process of collecting sediment cores in acrylic tubes and photographing them on a boat or in the laboratory (e.g., Grizzle & Penniman, 1991; Wildish, Hargrave, MacLeod, & Crawford, 2003). Unless stated, further discussion will be on sediment profile images obtained with an underwater instrument that penetrates the sediment to takes a profile image.

The first published use of SPI was by Rhoads and Young (1970), where they obtained sediment-profile images with a handheld underwater camera attached to an acrylic housing that penetrated the sediment. The instrument consisted of a Nikonos 35-mm film camera and flash attachment (Nikon) mounted on a Plexiglas prism, which had a field of view of 18 × 21 cm (Figure 1.10). SCUBA divers manually pushed the instrument into the sediment and took the photograph. The authors developed the instrument to view the sediment–water interface and the upper few centimetres of sediment. This enabled them to observe the in situ effects of bioturbation on the sediment. Prior to this technique, such observations could only be made from collected sediment cores or from a surface-only perspective.

This instrument was operated by a SCUBA diver, which limited the depth and length of its deployment. In response to this limitation, Rhoads and Cande (1971) developed a larger instrument that could be used in deeper water for longer periods of time. This

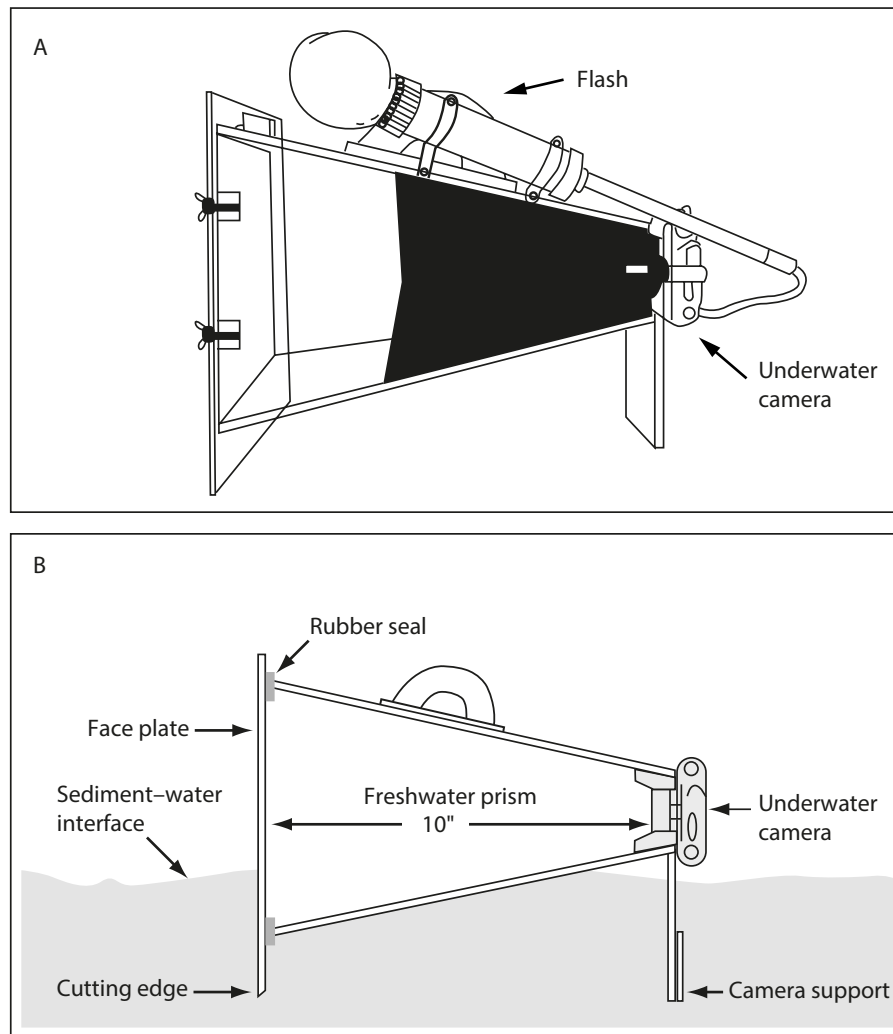


**Figure 1.10:** Illustration of the first published SPI instrument, which was used by Rhoads and Young (1970). (A) Side view showing the Nikonos (Nikon) underwater camera and flash attached to a water-filled acrylic pyramid. The narrow end of the pyramid was painted black to decrease light backscatter. (B) Cross-section view of the instrument. Reproduced from Germano et al. (2011).

instrument consisted of a metal frame supporting a wedge-shaped acrylic chamber, which reflected the sediment profile towards a film camera (Figure 1.11). Once the instrument had been lowered to the seafloor, a 58 kg weight pushed the prism into the sediment, penetrating approximately 10–20 cm into fine-grained (silt–clay) sediments. The camera took a photo before the instrument was moved to a new location.

The technology was known as remote ecological monitoring of the seafloor (REMOTS). REMOTS was trademarked in 1983, therefore, other sediment imaging technologies used an alternative name, sediment-profile imagery, SPI (Germano et al., 2011). REMOTS and SPI therefore describe the same methodology and can be used



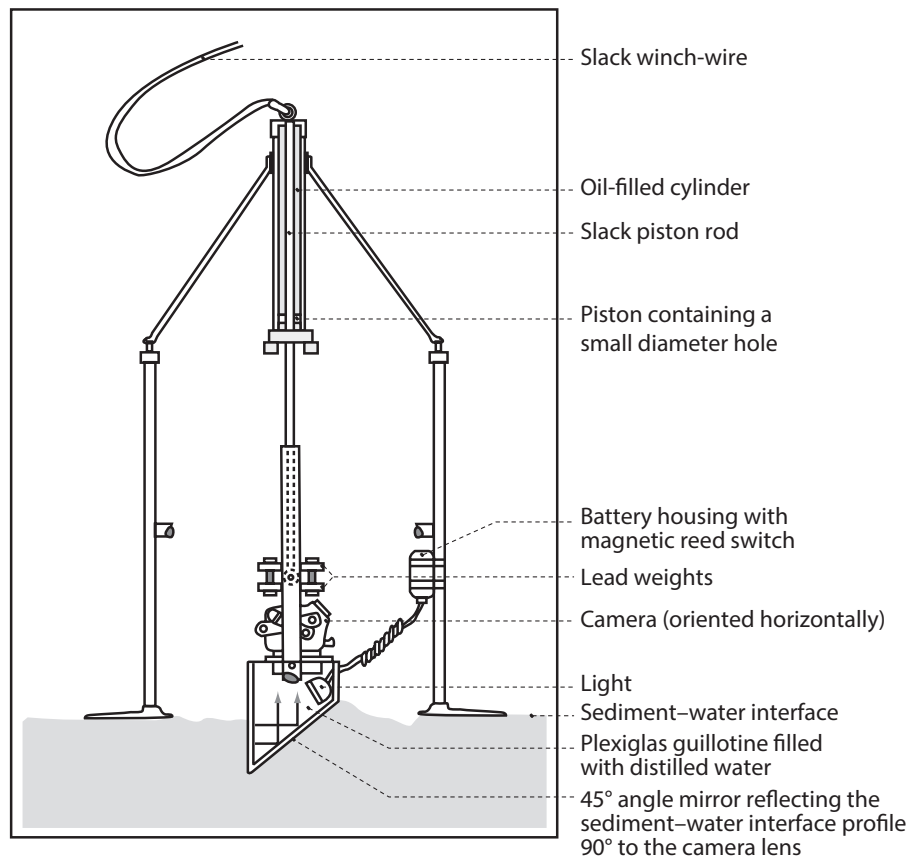


**Figure 1.11:** Illustration of the first vessel-deployed SPI instrument, which was used by Rhoads and Cande (1971). Image reproduced from Germano et al. (2011).

interchangeably; however, SPI appears to have become the more widely used acronym.

The camera used in the tethered instrument required film, which limited the number of images it could take to 12 or 24, depending on the film used. Modern versions of this instrument use digital single-lens reflect (SLR) cameras. The greatest advantage of using a digital SLR camera is that it is able to store thousands of high-resolution images. Alternatively, images can be sent directly to a computer on the surface-vessel via an attached cable or acoustic signal, providing near-instant images onboard.

#### 1.4.1 Image analysis

An analyst must inspect images individually using computer software to identify and measure the parameters in a sediment-profile image. Although images are analysed

using software, the current process is not fully automated or batch processed because the interpretation of the features requires in-depth knowledge of the sedimentary processes that result in such features. Germano et al. (2011) summarised the features that can be either directly measured or visually estimated from sediment-profile images (Table 1.5). The infaunal successional stage is derived from sediment features and benthic species that can be seen in the image.

**Table 1.5:** Direct measurements and visual estimates that can be made from a sediment-profile image as summarised by Germano et al. (2011).

Direct measurements	Visual estimates
<ul style="list-style-type: none"> <li>• Prism penetration depth</li> <li>• Presence and thickness of depositional layers</li> <li>• Depth of the oxidised surface layer (apparent redox potential discontinuity; aRPD)</li> <li>• Presence/absence of surface and subsurface biological features</li> </ul>	<ul style="list-style-type: none"> <li>• Sediment grain size major mode and range</li> <li>• Infaunal successional stage</li> </ul>

In the early 1980s, image analysis was done by tracing features on acetate film placed over enlarged black-and-white prints of each profile image (Germano et al., 2011). The analyst then measured the features and areas of interest on the traced and annotated film.

Assessing a sediment-profile image typically requires a person to manually identify sediment features. This identification is somewhat subjective. Romero-Ramirez, Grémare, Desmalades, and Duchêne (2013) developed the software SpiArcBase to semi-automate sediment-profile image analyses. After training the software with some example images, it is capable of identifying the sediment surface, the thickness of the oxidised surface layer, and some biogenic structures. This software may help to remove some of the subjectiveness in image analyses; however, it is no replacement for the interpretation of a skilled analyst.

Germano et al. (2011) stated that correctly interpreting sediment-profile images requires in-depth training and detailed knowledge of the complex biogeochemical

processes that are responsible for sediment colour and texture. Some of these processes are discussed in the following section.

### 1.4.2 Ecological indices

A number of ecological indices have been developed that use sediment profile image features and relate them to benthic ecosystem functioning. Indices provide a framework to quantify the status of the sediment based on chosen indicators. Pinto et al. (2009) comprehensively reviewed the currently used indices, however, I will only discuss the two that were developed specifically for use with sediment profile images. These are the organism–sediment index (OSI, Figure 1.12) and the benthic habitat quality index (BHQ, Figure 1.13).

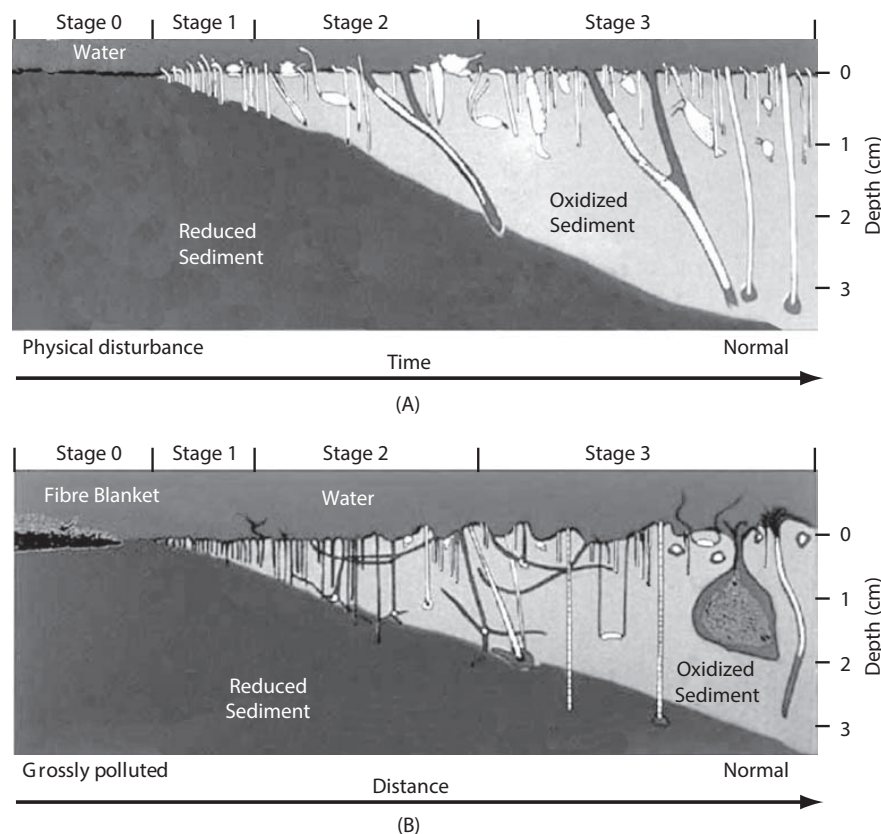


**Figure 1.12:** Visual representation of the indicators that are identified in a sediment-profile image and used in the OSI succession model (Rhoads & Germano, 1982). (A) The response over time to a physical disturbance, and (B) the response over distance from a point source of pollution.

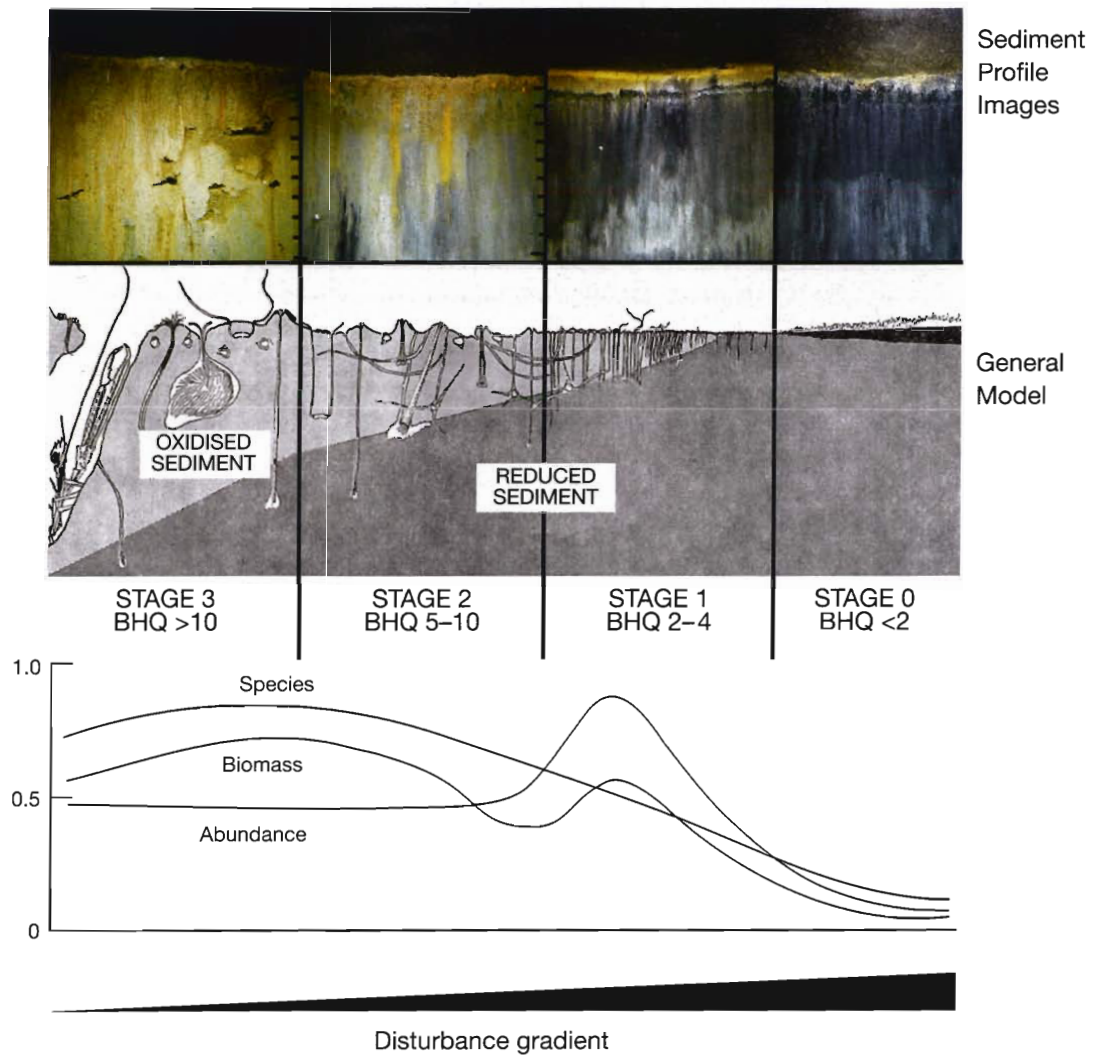


**Figure 1.13:** Visual representation of the BHQ index by Nilsson and Rosenberg (1997). The upper panel shows example sediment profile images that have been assigned different stages of the index, ranging from highly oxidised sediment at Stage 3, to heavily affected and anoxic sediment in Stage 0. The lower panel shows the species–abundance–biomass curve presented Pearson and Rosenberg (1978) from which the index was developed. Image from Nilsson and Rosenberg (2000).

### Organism–sediment index (OSI)

Rhoads and Germano (1986) attributed the lack of theory-based interpretation of images to the reluctant acceptance of SPI amongst other scientists in its first 10 years. The authors developed the OSI to address this issue. The OSI was one of the first ecological indices developed to use features identified from sediment-profile images. The authors' intent was to create a protocol that was supported by the theory of benthic succession in response to a physical disturbance or pollution. Such succession had been described by Johnson (1972) and Pearson and Rosenberg (1978).

The succession models described predictable changes in macrobenthic communities following a benthic disturbance, or along a pollution gradient. These changes were categorised into stages. Later, Rhoads and Boyer (1982) interpreted such models and stages and re-described the macrobenthic community changes in terms of how each modifies the observable physical and chemical sediment properties. The authors used a muddy subtidal site in Narragansett Bay, Rhode Island as a test site to obtain sediment-profile images and collect macrofaunal data from sediment cores. The observable features used to determine the successional stage are illustrated in Figure 1.12 and example sediment-profile images are shown in Figure 1.14.

Rhoads and Germano (1982) described the succession stages in terms of functional types rather than the presence of specific species or genera. This was so the model could be applied more broadly than the specific location it was developed. Such observations, however, were made in muddy sediments, and likewise, should be applied to muddy sediments.

The first successional stage is defined by the presence of small, opportunistic, tube-dwelling polychaetes or oligochaetes, or opportunistic bivalves such as *Mulinia lateralis* (Say, 1822). Such organisms are able to survive in heavily disturbed or polluted environments because most feed near or above the sediment surface and their tube walls or shells isolate them from the potentially toxic reduced solutes in the ambient porewater (Rhoads & Germano, 1982). Polychaetes and oligochaetes are able to colonise the sediment within a few days to weeks after a disturbance, reaching densities up to  $10^5$  individuals  $m^{-2}$  (Rhoads, McCall, & Yingst, 1978). These opportunistic organisms can have a substantial effect on the sediment because they pump oxygenated bottom water through their tubes. Oxygen from this pumped water then diffuses through the tube wall and begins to oxidise a thin layer of surrounding sediment (Aller, 1980).

As the upper sediment layers become oxygenated, infaunal deposit feeders colonise the sediment, replacing some, or the entire Stage 1 fauna. The progression of faunal

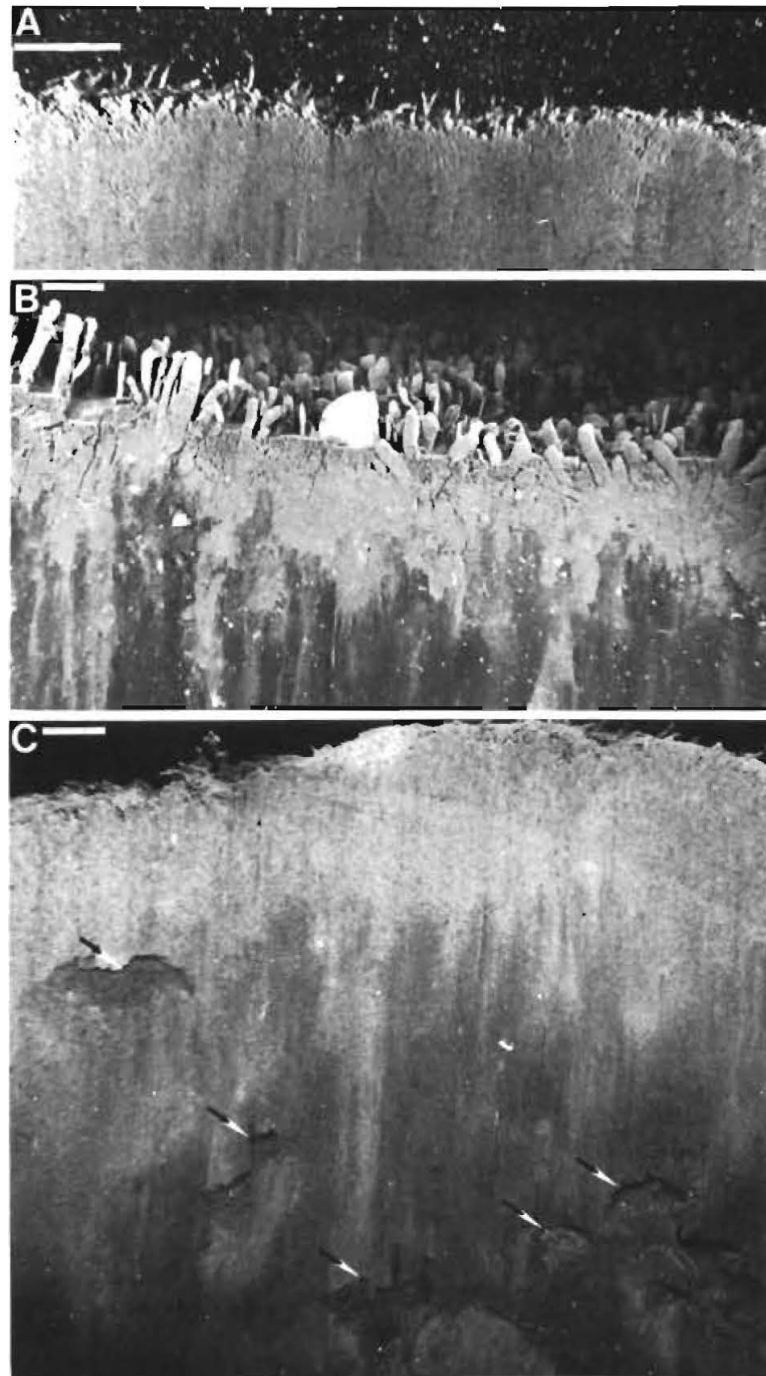


**Figure 1.14:** Examples of benthic successional stages that can be defined from a sediment-profile image using the OSI. (A) Stage 1: dense assemblage of small tube-dwelling polychaetes. (B) Stage 2: dominated by tube-dwelling amphipods (*Ampelisca abdita* Mills, 1964). (C) Stage 3: dominated by infaunal deposit feeders. The presence of such feeders is inferred from feeding pockets, which are indicated by arrows. Image from Germano et al. (2011), original image from Rhoads and Germano (1982).

replacement was arbitrarily divided into two stages: an intermediate (Stage 2) and an equilibrium (Stage 3) stage. The typical macrofauna present in Stage 2 are shallow-dwelling bivalves (e.g., *M. lateralis* and *Tellina agilis* Stimpson, 1857) and tube-dwelling amphipods (e.g., *Ampelisca abdita* Mills, 1964; see Figure 1.14).

The fauna of Stage 3 comprise tube-dwelling species (e.g., the polychaete family Maldanidae) as well as free moving species that create feeding burrows deeper in the sediment. Many of these species are deposit-feeders feeding on sub-surface material. They pump bottom-water into their burrows and/or rework the sediment displacing particles and porewater. This bioturbation oxygenates and homogenises the upper sediment layer.

The image derived successional stage is only one parameter required to calculate the OSI score. The other parameters and their scoring are shown below in Table 1.6.

**Table 1.6:** Sediment-profile image derived parameters and their assigned index values used to calculate the organism–sediment index (OSI) score of an image.

Chemical parameters		Biological parameters	
Mean aRPD depth (cm)	Index value	Successional stage	Index value
0	0	Azoic	−4
0–0.75	1	Stage 1	1
0.76–1.50	2	Stage 1–2	2
1.51–2.25	3	Stage 2	3
2.26–3.00	4	Stage 2–3	4
3.01–3.75	5	Stage 3	5
>3.75	6		
Methane present	−2	Secondary succession	5
No/low O <sub>2</sub>	−4		

OSI score = sum of chemical and biological parameters. Range: −10 to +11.

The OSI score can range from −10 to +11. The lowest values are given to sediments with low or no dissolved oxygen, no apparent macrofauna, and methane gas bubbles. The highest values are given to aerobic sediments that have a deep apparent redox potential discontinuity (aRPD) and show signs of larger macrofauna, including tubes, burrow, and feeding holes. A recently disturbed site or one that is exposed to some form of pollution or enrichment will have an OSI score <6.

## Benthic habitat quality (BHQ)

Nilsson and Rosenberg (1997) developed the BHQ so they could use SPI to assess spatial and temporal differences in a Swedish fjord-monitoring program. It differs from the OSI as specific features, such as, faecal pellets and organism-made tubes are each assigned values, which are then used to calculate the BHQ score (Figure 1.13, Table 1.7). Nilsson and Rosenberg (1997) deployed an instrument that consisted of two cameras, one to obtain the sediment-profile image and one to obtain an image of the seafloor. The BHQ index, therefore, uses a combination of sediment-surface and sediment-profile indicators. The BHQ score is used to infer the successional stage, which is in contrast to deriving the successional stage directly from image indicators and using the stage as a parameter in the OSI. The authors proposed that scoring features was a more objective method to determine the successional stage from a sediment-profile image.

**Table 1.7:** Sediment-profile image derived parameters and their associated values used to assign the image a Benthic Habitat Quality (BHQ) score.  $BHQ = A + B + C$ . The BHQ value can range between 0 and 15. From Nilsson and Rosenberg (1997).

A: Surface structures	Faecal pellets	1
	Tubes $\leq 2$ mm diameter	1
	or Tubes $> 2$ mm diameter	2
	Feeding pit or mound	2
B: Subsurface structures	Infauna	1
	Burrows (1–3)	1
	or Burrows ( $> 3$ )	2
	Oxic void at $\leq 5$ cm depth	1
	or Oxic void at $> 5$ cm depth	2
C: Mean aRPD depth (cm)	0	0
	0.1–1.0	1
	1.1–2.0	2
	2.1–3.5	3
	3.6–5.0	4
	$> 5$	5



### 1.4.3 Redox potential discontinuity (RPD)

One of the most common visual indicators measured in sediment profile images is the thickness of the oxidised sediment layer, which is indicated by the depth of the boundary between light and dark coloured sediment. This depth is known as the apparent redox potential discontinuity (aRPD). The depth of this discontinuity is a proxy for the boundary between oxidising and reducing conditions in the sediment. Iron forms  $\text{FeO}(\text{OH})$  in oxidised sediments, which is red-brown, and iron sulfides ( $\text{Fe}_x\text{S}_y$ ) form in reduced sediments, which range from dark-blue to black (Lyle, 1983). In some sediment, there is a visible grey/green layer, which indicates the zone where  $\text{Fe}^{3+}$  is reduced to  $\text{Fe}^{2+}$  (Lyle, 1983).

The depth of this transition from oxidising to reducing conditions can be measured accurately using redox potential electrodes; however, these electrodes typically have slow response times (>1 minute), which make measuring the redox potential time-consuming. The measurements are time-consuming because an analyst must measure a sediment redox potential (Eh) profile at sufficient resolution ( $\mu\text{m}$  to  $\text{mm}$ ) to identify the depth at which a steep change in Eh occurs.

A complicating factor is that not all sediments have a steep change in their Eh profile. For example, Fichez (1990) measured Eh profiles in sediment cores from the Mediterranean coast that had no change, or a gradual change with depth. Fichez sampled muddy sediments at the mouth of, and up to 100 m inside submarine caves in 15 m of water. The author detected a redox discontinuity in the sediment of the mouth of the cave; however, the sediment further inside the cave had high redox potentials throughout. Fichez attributed such observations to the rate of organic matter deposition on the sediments. The sediment at the mouth of the cave had a high oxygen demand as it received much organic matter. The rate of oxygen consumption was higher than the rate of oxygen supply, thus causing reducing conditions at depths >2 cm. Anoxic conditions were indicated by Eh values  $\leq 100$  mV. There was a lower rate of organic matter deposition inside the cave, and therefore, the sediments had much

lower oxygen demands. Degradation of the small amount of deposited organic matter occurred via aerobic processes, which resulted in a linear Eh profile, that is, no change with depth down to 15 cm.

The aRPD and the measured RPD do not always occur at the same depth in the sediment. For example, Rosenberg, Nilsson, and Diaz (2001) measured aRPD and RPD depths in subtidal sediment, and Diaz and Trefry (2006) in deep sea sediment, and found both measurements to agree. Gerwing, Gerwing, Drolet, Hamilton, and Barbeau (2013), however, repeated such comparison with intertidal sediments and found the aRPD and the RPD at significantly different depth.

Gerwing et al. (2013) explained that this difference occurred because redox electrodes measure the instantaneous redox potential at one point in the sediment, which can be highly dynamic, whereas, the sediment colour is a long-term average of the redox conditions. Teal, Parker, Fones, and Solan (2009) also identified a difference between the depth of the measured RPD and the aRPD and suggested that it was a result of recent infaunal bioturbation activity.

Accurate detection of the aRPD is often complicated by the presence of macrofaunal tubes and burrows causing its depth to vary up to several centimetres within the same sediment profile image (Rosenberg et al., 2001; Teal et al., 2009). Furthermore, redox conditions in surface sediment are subject to seasonal changes caused by, for example, sediment resuspension due to wave action or strong seawater currents, and deposition of algal-bloom derived organic matter.

Although the aRPD parameter is widely used in ecological indices and studies involving SPI, Germano et al. (2011) noted in their review of SPI that only five studies (Cicchetti et al., 2006; Diaz & Trefry, 2006; Mulsow, Krieger, & Kennedy, 2006; Rosenberg et al., 2001; Teal et al., 2009) had evaluated the relationships between image features and measurable sediment properties. These studies identified correlations between the depth of the aRPD and important environmental variables, such as bottom water dissolved oxygen concentration (Cicchetti et al., 2006), the depth of the

measured RPD (Diaz & Trefry, 2006; Mulsow et al., 2006), and the depth at which red- $\text{Fe}^{3+}$  is reduced to green- $\text{Fe}^{2+}$  (Teal et al., 2009). Germano et al. (2011) highlighted in their review that a key concept behind SPI analysis is that images need to be interpreted within the context of the ecosystem in which they were collected. That is, there must be an in-depth understanding of the benthos, which cannot be obtained from SPI, before an image can be correctly interpreted.

Despite the mentioned discrepancies and difficulties associated with the aRPD, Solan et al. (2003) have used sediment profile imaging (SPI) extensively for environmental assessments and concluded that it can be successfully used to make subjective generalisations of the overall redox chemistry. The authors suggested, however, that making specific statements about particular aspects of biogeochemistry was not possible from an image alone. Such generalisations can be useful to select areas for more in-depth analysis, such as faunal or chemical analyses.

#### 1.4.4 Colour correlations

Chemical analyses are often too expensive and time consuming to be included in routine monitoring. If the chemical species of interest correlated with an easily measured sediment property, this species could become a viable monitoring parameter. An alternative approach to traditional methods of image analysis is using the colour of the sediment to estimate the concentration of a coloured chemical species. This is in contrast to the previously discussed method of image interpretation, where image features were linked to benthic processes.

Bull and Williamson (2001) identified a relationship between the colour of estuarine sediments and two iron phases. Firstly, they found that the colour intensity of a sediment-profile image correlated with the AVS concentration ( $R^2 = 0.67$ ). Because AVS forms in response to organic matter deposition, its measurement can be useful for investigating the intensity of sedimentation and organic matter degradation. To the best of my knowledge, however, it is not used as a monitoring parameter because of its

laborious measurement. The authors achieved such correlation by vertically slicing subtidal estuarine sediment cores that were collected from Pakuranga Creek in Auckland, New Zealand. They photographed the sediments using film photography and arbitrarily subsampled portions of the exposed sediment for AVS analyses. The authors then correlated the mean colour intensity of the subsampled area from the sediment image with the measured AVS concentration. They found a linear relationship between these two parameters. These results demonstrated that it was possible to estimate the concentration of AVS from sediment profile images and they have provided a foundation for ideas and techniques developed throughout this thesis.

The second relationship that Bull and Williamson (2001) identified was between the colour saturation of a sediment-profile image the concentration of iron oxyhydroxide ( $\text{FeO}(\text{OH})$ ;  $R^2 = 0.62$ ).  $\text{FeO}(\text{OH})$  is olive-brown and is produced in oxic zones of the sediment. The authors were interested in  $\text{FeO}(\text{OH})$  because heavy metal ions readily adsorb to its surface and are incorporated into its structure. This makes it a potential indicator of metal bioavailability and toxicity, especially when used in conjunction with AVS measurements, another binding phase for metals.

Iron isn't the only element that has been correlated with sediment colour. Jakobsson et al. (2000) identified a relationship between sediment colour and the concentration of manganese. The colour relationship was more complex than the ones identified by Bull and Williamson, as it required multiple regressions using the red, green, and blue colour channels of the image. The authors created a linear model using the colour channels of the image and correlated this with the measured manganese oxide concentration from a ~7 m sediment core collected in the Arctic Ocean ( $R^2 = 0.75$ ). Peaks in the manganese concentration profile coincided with medium- to dark-brown coloured sediment, which the authors link to interglacial periods. The conditions during such periods raised the oxygen concentration in the bottom water, creating oxidising conditions that enhanced the precipitation of manganese. The authors used this relationship to obtain high-resolution profiles of manganese concentrations to

date the sediment. The greatest advantage of using sediment-profile image analysis in this study was that the authors were able to obtain many more data points for their ageing model from only 11 accurately measured samples.

Optical lightness is another sediment colour property that has been used by marine geologists and paleoceanographers. For example, Balsam, Deaton, and Damuth (1999) used it as a proxy for carbonate content in marine sediments. The authors measured the optical lightness of a subsampled sediment core using a UV-Vis spectrophotometer and reported the value as  $L^*$  from the CIE/ $L^*a^*b^*$  colour space. The three parameters in this colour space represent the lightness of the colour ( $L^*$ , where 0 is black, and 100 is white), its position between red and green ( $a^*$ ) and its position between yellow and blue ( $b^*$ ). The  $L^*$  value is related to the area beneath the spectral curve in the visible light region (400–700 nm). The authors then accurately determined carbonate content in the subsampled sediments using a vacuum gasometric technique by Jones and Kaiteris (1983). They noted that the sediment composition affected the strength of the correlation between optical lightness and carbonate content, such as the presence of iron oxides, oxyhydroxides, and organic matter.

Using optical lightness as a proxy for carbonate content was advantageous over the accurate method of analysing marine sediment carbonate content in this study as the authors were able to obtain a high resolution profile of carbonate content that would not have been possible otherwise. A second advantage is that using spectrophotometers to measure  $L^*$  is a non-destructive technique, which is important when assessing samples that cannot be sacrificed entirely, such as the cores in the authors study.

A commonality in these examples is that sediment colour correlations allow researchers to obtain many more data points than they could realistically measure using traditional methods. These image-predictions, however, are only valid once a correlation has been established at the site of interest.

### 1.4.5 Modifications to SPI instruments

Adapting SPI instruments for particular applications has resulted in additional features being added to the technology. Glud, Tengberg, Köhl, Hall, and Klimant (2001), for example, added a planar optode to the surface of the prism that penetrates the sediment. This enabled them to observe two-dimensional in situ oxygen distributions in addition to the colour profile image. The planar optode is coated with an oxygen-sensitive fluorescent dye. The dye is illuminated with high power LEDs and the emitted fluorescent light is measured. The intensity and length of the emission depend on the concentration of  $O_2$  that the dye is exposed to. Such emission can then be used to calculate the  $O_2$  concentration in the surrounding of the dye. The authors used this technology to gain further insight into variations in sediment  $O_2$  distributions and observe how benthic communities can affect such distributions. This technology can also be used to quantitatively measure how deep oxygen penetrates the sediment, rather than relying on the colour change of the sediment.

Solan et al. (2004) also used a fluorescent light source, however, the authors investigated the movement of particles due to bioturbation. They introduced dyed particles into the environment and used a camera to obtain a time-series of images to track the particle movement. Solan and co-workers used the term fluorescent SPI, or f-SPI to describe this technique. They deployed their instrument for 16 hours and recorded images every 10 minutes. The observations from this deployment allowed the authors to mathematically model the reworking and redistribution of the dyed sediment particles. The images revealed that the majority of particle movement was caused by the crab *Hyas araneus* (Linnaeus, 1758) as it moved and repositioned itself. Over the 16-hour period, the dyed particles were redistributed in a Gaussian- or biodiffusion-like manner, up to 1.6 cm deep in the sediment. The authors were able to observe, and most importantly, quantify, the displacement of particles by macrofauna using SPI in this study. Such displacement is well-known to marine researchers, but it is a difficult process to quantify.

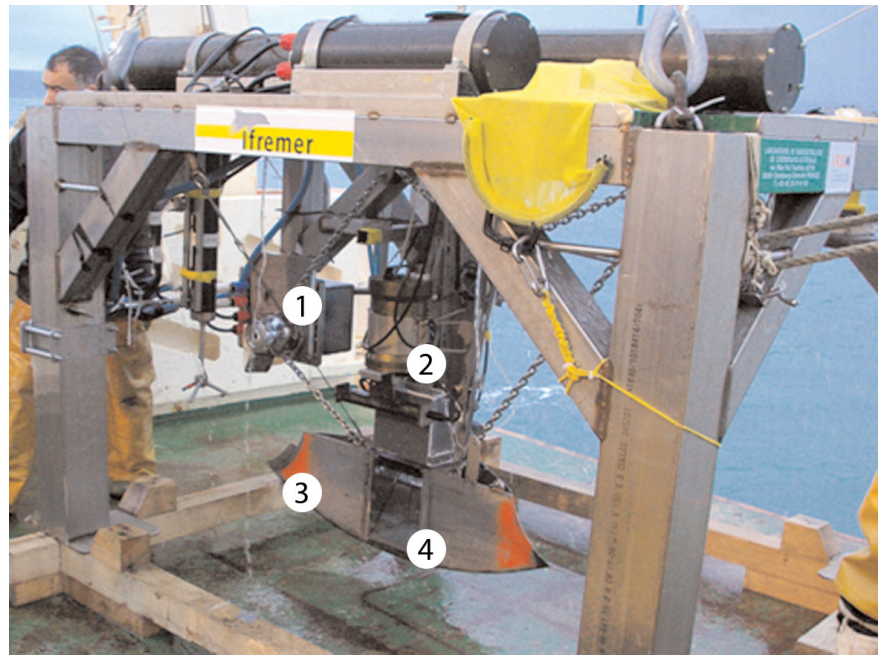


**Figure 1.15:** Modified sediment profile imagery instrument, Dynamic SPI (DySPI), developed by Blanpain et al. (2009). (1) Motorised winch, (2) camera housing, (3) cutting blade, (4) transparent imaging window. Image modified from Blanpain et al. (2009).

Blanpain et al. (2009) took an alternative approach to investigate particle movement using SPI; the authors modified their instrument to use a high-definition (HD) video camera instead of a film or digital camera so they could observe coarse grain sediment transport processes at the sediment–water interface (dynamic SPI, DySPI, Figure 1.15). The prototype instrument had a large bladed pendulum that sliced into the sediment to minimise the sediment–water interface disturbance. This is in contrast to the vertical pushing used by other SPI instruments. The sediment was illuminated with halogen lamps and the water column was illuminated by blue–green LEDs so that both could be observed. This was a large instrument that required a crane with a lifting capacity of ~1 tonne. The authors used software to analyse the video footage frame-by-frame to determine which particles had moved. They presented the instrument as a proof-of-concept and noted that this setup was ideal for investigating the effects of water currents on surface particles. In addition to minimising disturbance to the sediment–water interface, the bladed design also minimises flow disturbance when the instrument is oriented parallel to the flow direction.

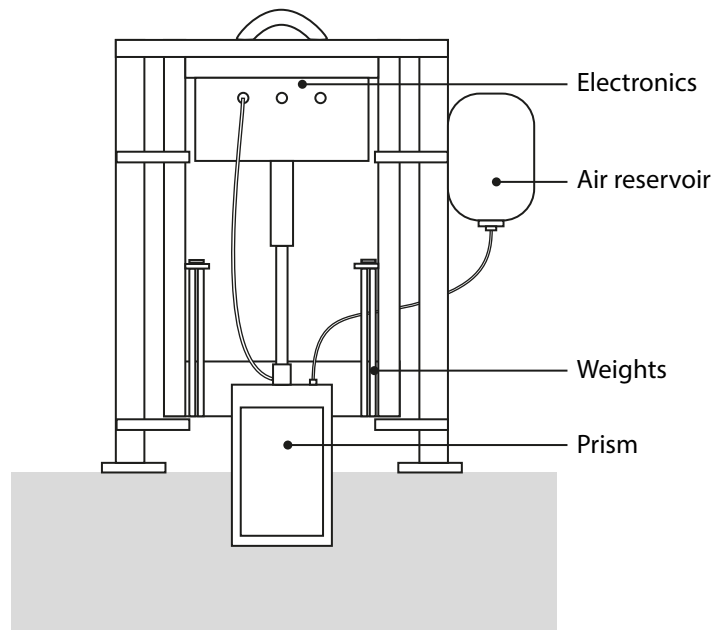


**Figure 1.16:** Modified sediment profile imagery device, SPIScan, designed by Patterson et al. (2006). The prism comprises a computer flatbed scanner modified to be waterproof and have a cutting edge to penetrate the sediment. The air reservoir is required to equalize the pressure inside the prism with the external water pressure. Image modified from Patterson et al. (2006).

The REMOTS-style instruments are large and heavy (>200 kg) and require a large vessel with a large lifting capacity to operate them. One of the reasons these instruments are so heavy is that they require much weight to push the prism far enough into the sediment to observe the sediment–water interface. A large prism requires a large amount of sediment to be displaced, and therefore, a large amount of force.

Patterson et al. (2006) designed a SPI instrument that addressed such sediment-displacement issue. The authors designed their instrument to incorporate a modified computer flatbed scanner, rather than a wedge-shaped prism (Figure 1.16).

The defining feature of this instrument is the modified prism component that penetrates the sediment. Unlike the wedge-shaped prism of the REMOTS-styled instruments (herein, digital SPI), the SPIScan prism is comprised of a computer flatbed scanner that had been modified to fit inside a stainless steel housing with a tempered-glass faceplate. Patterson et al. (2006) fit a nylon blade on the bottom of the



prism, cut at a 45° angle to aid sediment penetration. The width of the prism is 30 cm and the thickness is 4 cm, giving it a blade-like shape. Such design minimised the amount of sediment that needed to be displaced as the instrument was pushed into the sediment. This meant that less weight was required to push the instrument into the sediment than the equivalent digital SPI instrument. The weight of the instrument, however, was still high at 430 kg when loaded with the necessary weights. This was lighter than the digital SPI instrument the authors used for comparative measurements, which weighed 510 kg. Even though SPIScan weighed 80 kg less than the digital SPI instrument, it achieved 1.7 times greater penetration depth in the authors' study because of the prism design.

The greatest limitation of SPIScan is that it requires an air reservoir to equalise the pressure in the air-filled prism with the external water pressure. Patterson et al. (2006) briefly mention that in-house testing revealed that the electronics used in SPIScan would work in pressures up to 10 bar, which is the equivalent of 90–100 m water depth. In this study, however, the instrument was only used in 5–10 m water depth.

The authors note that another advantage of the SPIScan instrument was that it can be built on a budget of US\$5,000, plus labour. The low cost arises from the use of a readily available desktop scanner rather than an expensive digital SLR and prism setup. This makes SPI more accessible to individuals or research groups who cannot afford the larger digital SPI instruments.

Paavo (2007) also designed a SPI instrument that was based on a desktop flatbed scanner, however, this instrument was much smaller and lighter, weighing approximately 30 kg (SPI-Scan, Benthic Science Ltd.; Figure 1.17). SPI-Scan differs from the SPIScan developed by Patterson et al. (2006) in that the scan head moves in a circular motion inside an acrylic tube, rather than in a linear motion.

The volume of sediment that needs to be displaced for SPI-Scan to penetrate the sediment and acquire a profile image is less than the wedge-shaped prism instruments and this enables it to be much smaller and lighter and still penetrate the sediment to a

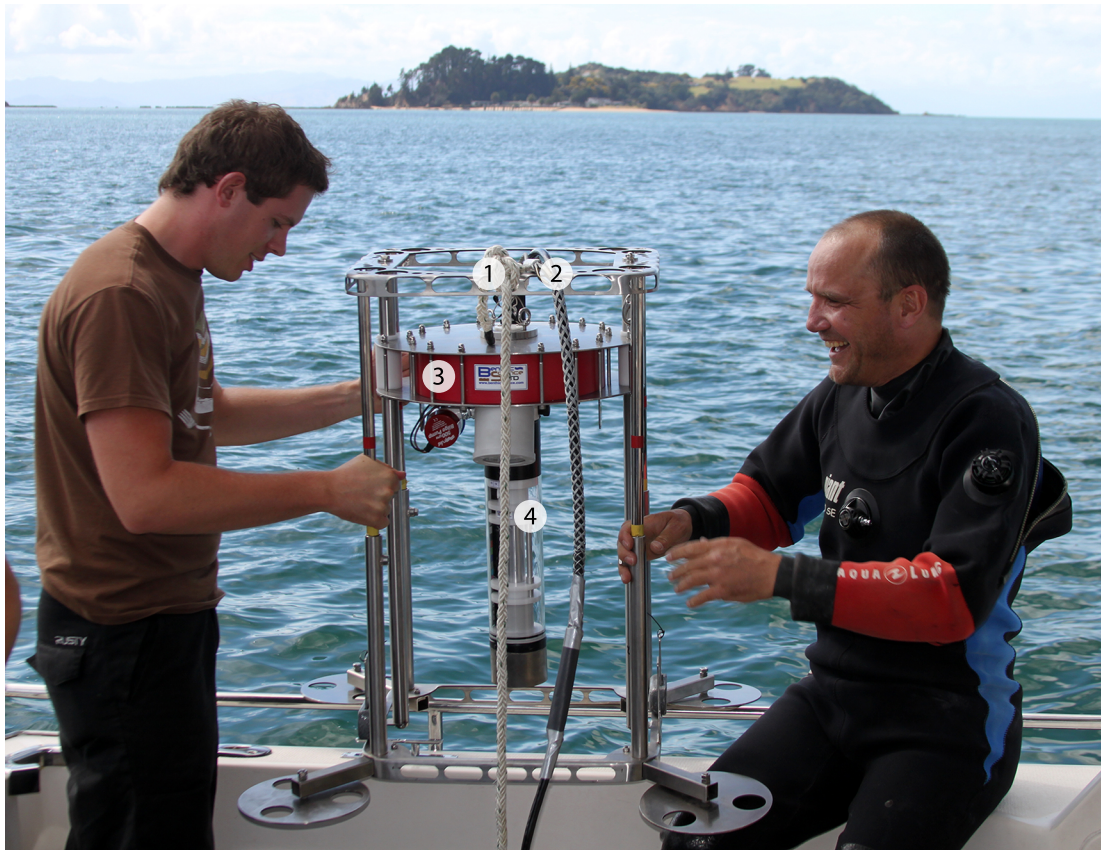


**Figure 1.17:** A rotational sediment profile imagery instrument, SPI-Scan (Benthic Science Ltd.) deployed in New Zealand coastal waters. (1) Rope to raise and lower the instrument, (2) electrical tether that connects the instrument to a computer on the boat, (3) electronic component housing, (4) transparent acrylic tube that penetrates the sediment and houses the scan head.

sufficient depth. The electrical components are contained in a larger elliptical body, mounted above the cylinder. The scanner moves along the inner surface of the cylinder over a horizontal distance of 120 mm to acquire a sediment image.

The image obtained by SPI-Scan is similar in its dimensions and resolution to a REMOTS-style instrument with a digital camera. Unlike the planar SPIScan, SPI-Scan doesn't require an air reservoir to equalise the internal pressure. The instrument is suitable for use in shallow coastal water (<30 m). This instrument has already been used for the assessment of mussel farms in New Zealand (e.g., Vopel & Funnell, 2006; Vopel, Giles, Budd, & Hart, 2007) and I used it exclusively throughout this research.

## 1.5 Research questions

In the following chapters, I describe the steps I have taken to explore evidence that sediment profile images are suitable for assessing the enrichment of coastal marine sediment with organic matter. More specifically, these chapters address the following research questions:

1. How do the techniques used to extract and measure AVS from marine sediments affect the AVS/colour correlation?
2. How do changes in these extraction techniques affect the ability to estimate AVS concentration from sediment colour intensity?
3. Does the correlation between sediment colour intensity and AVS concentration change at different locations, and if so, what causes these changes?
4. Which sulfide minerals are present in sediments in the Hauraki Gulf and how do they contribute to sediment colour?
5. How can this technique be developed into a tool for assessing the intensity of organic matter deposition in the coastal environment and detecting the 'footprint' of a long-line mussel farm?

I address the first research question in Chapter 2 by describing the use of alternative techniques to acquire sediment profile images in situ and measure sediment colour and sediment sulfide content. Bull and Williamson (2001) suggested that the AVS/colour correlation should be stronger than their results revealed. Using the previously mentioned new approaches, I assess whether it is possible to achieve a stronger correlation between sediment colour intensity and AVS concentration.

In Chapter 3, I investigate spatial differences in the AVS/correlation in the Hauraki Gulf. To date, Bull and Williamson (2001) have only published data on the AVS/colour correlation from one subtidal, estuarine location. For the purpose of developing this technique into a useful tool for assessing the intensity of organic matter deposition, it

is important to understand if the AVS/colour correlation differs between location and, if so, what causes these differences. I investigate such differences by establishing AVS/colour correlations at multiple locations in the Hauraki Gulf.

To further elucidate any identified spatial differences in the AVS/colour correlation, I investigate how the sediment chemistry may differ between locations in Chapter 4. More specifically, I investigate the sulfur species present in the studied sediments and compare the relative proportions of each of these species between sites. There are many sedimentary components that influence sediment colour. Identifying the composition of sulphur compounds and how changes in the relative proportions of these compounds might explain any spatial differences in the AVS/colour correlation. Another factor that influences AVS is the conditions used during the acid extraction. I investigate the effect of different AVS extraction methods on AVS concentration and the strength and shape of the AVS/colour correlation.

In Chapter 5, I demonstrate how SPI can be used to assess the intensity of organic matter deposition. To do so, I present a case study of a long-line mussel farm. I include an assessment of the AVS farm footprint to investigate spatial changes in the extent of the seafloor area of elevated sediment AVS content. Such assessment requires accurate detection of the AVS footprint boundary. I demonstrate how to detect this boundary with analyses of sediment colour intensity.

Finally, I present a synthesis of the findings from all chapters and present my conclusions from this research. I also present my recommendations for further work.

## Chapter 2

# Estimating the in situ distribution of acid volatile sulfides from sediment profile images

### 2.1 Introduction

Coastal sediments worldwide are affected by organic enrichment. Primary causes for this enrichment include eutrophication driven by anthropogenic loading of coastal waters with phosphorus and nitrogen (Cloern, 2001; Nixon, 1995; Rosenberg, Magnusson, & Nilsson, 2009) and deposition of organic matter via terrestrial runoff (Gray et al., 2002) and aquaculture (Holmer & Kristensen, 1994). The oxidation of the sediment organic matter provides energy to microorganisms aided by an oxidising agent (electron acceptor), the most energetically favourable being oxygen (Froelich et al., 1979). Because of transport limitations (diffusion in cohesive sediment) and low saturation concentration of oxygen in seawater, oxygen is typically depleted within a few millimetres from the surface of organically enriched sediment (Revsbech et al., 1980). Below this thin oxygenated zone, anaerobic bacteria use alternative electron acceptors to decompose organic matter (Bagarinao, 1992).

The abundance of sulfate ( $\text{SO}_4^{2-}$ ) in the water column dictates that the dominant pathway for organic matter degradation in organically enriched sediments is via sulfate reduction (Bagarinao, 1992; Thode-Andersen & Jørgensen, 1989), which leads to the production of  $\text{H}_2\text{S}$ . The rate of sedimentary sulfate reduction responds to the rate of organic particle deposition, that is, the supply of sulfide to coastal sediment increases with its organic carbon supply (Brüchert, 1998; Cornwell & Sarpou, 1995; Oenema, 1990; Y. I. Sorokin & Zakuskina, 2012). Approximately 80% (Canfield, Thamdrup, & Hansen, 1993) to 90% (Hansen et al., 1978; Jørgensen et al., 1992) of the sulfide is re-oxidised, mostly through microbial activity. The remaining sulfide reacts to form more thermodynamically stable forms such as the minerals mackinawite ( $\text{FeS}$ ), greigite ( $\text{Fe}_3\text{S}_4$ ), and pyrite ( $\text{FeS}_2$ ), which are responsible for the black colour of coastal sediments (Berner, 1964a; Goldhaber & Kaplan, 1980; Jørgensen, 1982). Most of these sulfides convert back to  $\text{H}_2\text{S}$  when treated with acid and are known as acid volatile sulfide (AVS).

In search of a rapid method for determining the sediment AVS content, Bull and Williamson (2001) tested a new laboratory approach to estimate the AVS content of estuarine sediment from sediment-profile images. They vertically sliced sediment cores, imaged the core section with film photography and studio lighting, and subsampled arbitrary points of the exposed section for AVS content. The authors developed the film and digitised the prints using a flatbed scanner. They then analysed the digitised images using computer software to obtain the mean grey value of the sediment where the subsamples were taken. The authors extracted and quantified AVS with an acid microdiffusion method and an ion-selective electrode (Williamson, Wilcock, Wise, & Pickmere, 1999). This method extracted sediment with 6 M HCl, and 10%  $\text{SnCl}_2$  to prevent oxidation from  $\text{Fe}^{3+}$ . The evolved  $\text{H}_2\text{S}$  was trapped in a disodium ethylenediamine tetra-acetic acid/NaOH/ascorbic acid buffer solution, which was contained in a smaller vial, housed inside the main extraction vessel. These techniques revealed a linear correlation ( $R^2 = 0.67$ ) between AVS concentration and sediment colour intensity.


Bull and Williamson (2001) suggested that the actual relationship between AVS concentration and sediment colour intensity was stronger than their data suggested. They gave three reasons for this suggestion: (1) Discrepancy between the sediment that was imaged and the sediment that was measured for AVS concentration. The authors sliced sediment cores and then photographed the cut surface. A sub-sample of sediment was then taken for AVS analysis that included the photographed sediment, and additional sub-surface sediment. Thus, sediment that was not photographed was used to determine the AVS concentration. (2) Uncertainty of quantifying sediment colour. The process by which Bull and Williamson (2001) quantified sediment colour consisted of multiple steps, each of which introduce some error; the largest variance likely occurring from the development of the film. (3) Other factors that contribute to sediment colour. The authors suggested that such factors include crystallinity and particle size, which affect light reflectance and scattering. Large particles scatter light at a smaller angles relative to the laser beam than small particles. Additionally, minor coloured phases that contribute to sediment colour, but are not AVS components, will weaken the correlation between sediment colour and AVS concentration. These factors will be present in all studied sediments, but the degree to which they influence sediment colouration is unknown. Using alternative techniques to quantify sediment colour and measure sediment AVS content may improve the predictive ability of the AVS concentration–sediment colour relationship.

The colour parameter that Bull and Williamson (2001) correlated with AVS concentration was colour intensity from the hue, saturation, and intensity colour model (HSI). There are many models for numerically representing colour; three major colour models that are used to describe sediment colours are RGB, HSI, and Munsell. I will present a brief overview of these three colour models, which Kuehni (2003) covers in much greater detail.

RGB is an additive model, that is, red, blue, and green light are added together at various levels to achieve the desired colour (Table 2.1). A specific colour is defined by three values, one for each colour channel ranging from 0–255. It is used widely for

computer monitors and TVs to produce their range of colours. The colour produced using a specific RGB value differs amongst the devices because not every device can produce the exact same “pure green”, for example. One shortcoming of this model is that it’s not able to define the entire colour spectrum that is visible to the human eye.

**Table 2.1:** Comparison of three major colour spaces used to numerically represent colour. The final column shows an example of how to define the blue square using the different colour spaces.

Colour space	Parameter	Parameter explanation	
RGB	Red	Each parameter can be assigned a value from 0–255 that indicates how much of each colour is included. The colour is black if all values are at zero, and white if all values are at 255.	60
	Green		190
	Blue		219
HSI	Hue	A value between 0 and 360 indicating the position on a colour wheel defining the principal hue, e.g., red (0), green (120), or blue (240).	191
	Saturation	A percent value between 0 and 100 that defines the “colourfulness” of the sample. A low saturation has a washed out or grey appearance.	68.8
	Intensity	A percent value that indicates the illumination of the sample, where 0 is dark and 100 is bright.	54.7
Munsell	Hue	The letter defines the principal hue: Red, Yellow, Green, Blue, and Purple. Between each principal hue is an intermediate hue, e.g., between red and yellow is YR. The number identifies its position on the colour wheel and can be between 0 and 10; 5B is primary blue, whereas 7.5B is heading toward blue-purple.	5B
	Value	A lightness value that ranges from 0 (black) to 10 (white).	7
	Chroma	A value representing the “purity” of a colour, which is similar to saturation in other models. This is a perceptual model so there is no upper limit on chroma. A low chroma is less pure and its appearance is washed out like a pastel colour.	8

The HSI colour model is an additive describes the same range of colours as RGB, but provides a more intuitive representation of colour. Since both RGB and HSI describe the same range of colours, no precision is lost converting between these models. The HSI model also achieves a closer agreement between the numeric colour change, and the colour change perceived by the human eye. The three values, hue, saturation, and intensity are used to define a specific colour, and the effect of changing these values can be seen in Figure 2.1.



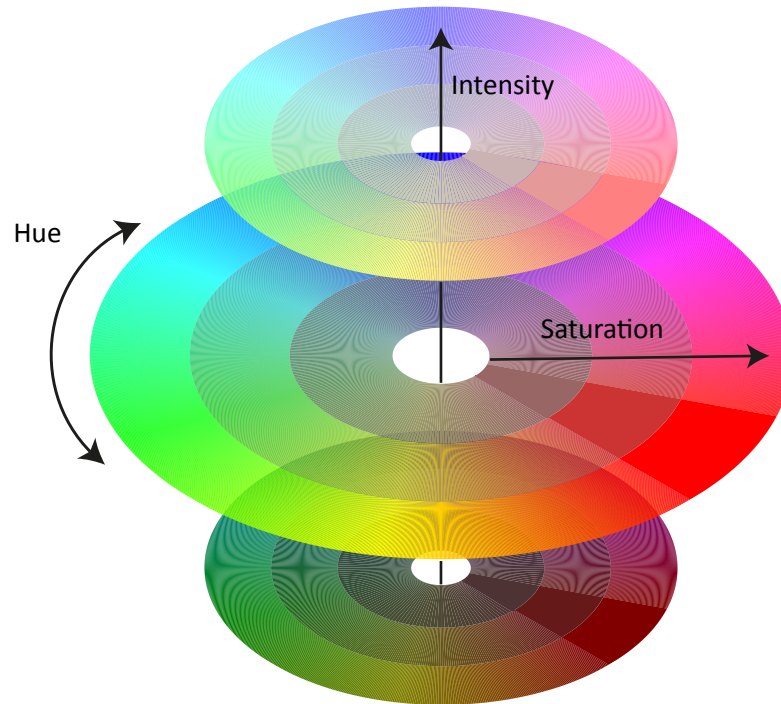


**Figure 2.1:** A visual representation of the hue, saturation, intensity (HSI) colour model. The three rings in each layer illustrate the effect of changing saturation. The outer ring has 100% saturation, followed by 60% and 20% saturation towards the centre. Hue is described using degrees, where red is 0°, green is 120°, and blue is 240°. The larger middle layer has an intensity of 50% and the layers above and below have intensities of 75 and 25, respectively.

Professor Albert H. Munsell developed the Munsell colour space to address the issue of perceptual uniformity. Munsell conducted research on people's response to colour changes and devised a colour model where the numeric change in the colour value was related to the change in colour perceived by the human eye. This additive colour space is able to define all colours that are visible to the human eye using three parameters: hue, value, and chroma. These three parameters have similar properties to the ones used by the HSI colour space. Munsell colours are typically defined by comparing the observed colour to a printed colour chart. Converting to and from the Munsell colour space can be difficult because there is no linear relationship between colour changes in the Munsell colour space and the colour change in any other colour space.

Conversions can be made based on tabulated data provided by Newhall, Nickerson, and Judd (1943), but this is not as precise as converting between other colour spaces, which can be achieved using simple formulas.

For the purpose of image analysis, the RGB and HSI colour spaces are sufficient as most scanner hardware record images in the RGB format. Even though more colours can be defined using the Munsell colour space than the RGB or HSI format, converting to the Munsell colour space has no advantage, as information lost during the scanning process cannot be regained. The concept of perceptual uniformity is not important for these analyses as the colour determination is performed by software, which is able to quantify colours more precisely than the human eye.

One opportunity to increase the strength of the AVS concentration–colour intensity correlation presented by Bull and Williamson (2001) lies in the choice of methods used to quantify AVS and sediment colour intensity. The authors expressed concern that the process of photographing the sediment, developing film, and digitising the film, introduced many opportunities for errors in colour reproduction.

Here, I explore this opportunity to develop an approach for the assessment of subtidal soft sediment. My first goal was to test if substituting laboratory film photography with digital imaging, and modifying the analytical method for sulfide quantification, resulted in a stronger correlation between sediment AVS content and colour intensity. My second goal was to demonstrate that an automated image analysing procedure can estimate the in situ distribution of AVS from images obtained with a lightweight sediment profile-imaging device (SPI-Scan™, Benthic Science Ltd.).

## 2.2 Methods

The following method is described in two distinct sections: (1) analysis of soft subtidal sediment in the laboratory to correlate sediment AVS concentration with colour intensity. This step is referred to as the calibration. (2) Application of the established AVS concentration–colour intensity correlation to sediment profile images, obtained in situ, to estimate the two-dimensional distribution of AVS.

### 2.2.1 Calibration: correlating AVS content and colour intensity

I collected seven cores of soft subtidal sediment using SCUBA from Awakiriapa Bay, Waiheke Island, New Zealand at a water depth of 12 m (Figure 2.2). The sample location was approximately 50 m north from the north-western corner of the mussel farm. I selected a location just outside the farm boundary to avoid the majority of dead mussel shells that accumulate on and in the sediment beneath and near the farm, while still being near enough to be exposed to elevated levels of organic matter from the farm. The tubes were pushed vertically into the sediment until two-thirds were filled with sediment and then sealed with stoppers on both ends to minimise sediment disturbance. The sediment-filled tubes were transported in a refrigerated box to the laboratory. In the laboratory, I removed the upper lids and immersed the tubes gently in a plastic container ( $1,444\text{ cm}^2 \times 54\text{ cm}$ ) filled with 48 cm (78 L) seawater, which was aerated with a bubble stone.

Within one week of collection, I sectioned one sediment core at a time at 5-mm intervals to a depth of 90 mm. The upper sediment section (0–5 mm) was discarded as it was disturbed during transport of the sediment cores. All other sediment slices were homogenised with a stainless steel spatula before removing  $4 \times \sim 1\text{ g}$  of sediment for AVS determination. The remaining homogenised sediment was distributed evenly for the determination of sediment colour intensity, water content, organic content, and particle size distribution. I processed each slice before cutting the next, keeping the air exposure of the sediment below 3 minutes. The effect of such exposure on the oxidation of AVS compounds is negligible (van Griethuysen, Gillissen, & Koelmans, 2002; Williamson et al., 1999).

Sediment water content was determined by weight loss after drying at  $90\text{ }^{\circ}\text{C}$  for 24 hours and organic content by weight loss after combusting in a  $400\text{ }^{\circ}\text{C}$  furnace for 6 h. Particle size was analysed with a laser-based particle analyser (Malvern Mastersizer 2000).

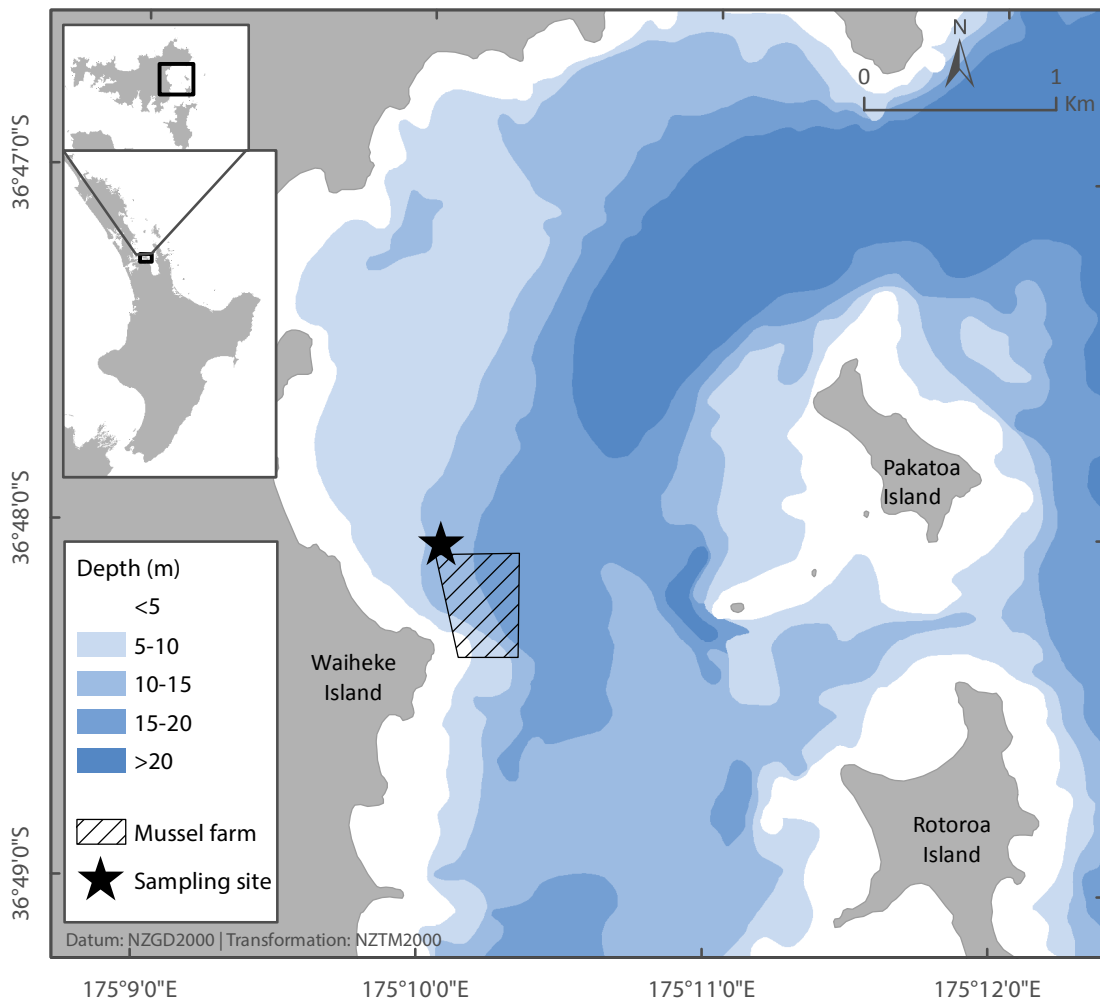


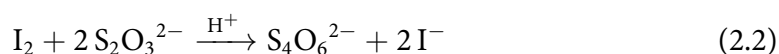
**Figure 2.2:** Location of the study site in Awakiriapa Bay, Waiheke Island, New Zealand. The extent of the mussel farm is denoted by the black hatched area and the star indicates the location of the sediment core collection.

### AVS determination

I added each of the four samples from a sediment slice (see above) into a 40 mL glass vial filled with 30 mL HCl (1 M, ACS grade) that was deoxygenated by purging with nitrogen for  $\geq 20$  minutes. The vial was closed with an airtight lid and briefly shaken. I weighed each HCl filled vial before and after adding sediment to determine the mass of sediment used in the extraction. I left the vials to stand while sectioning the remainder of the core. Sectioning one core was completed within one hour.

I used an amperometric  $\text{H}_2\text{S}$  microelectrode (Unisense A/S, 500- $\mu\text{m}$  tip diameter, response time  $\sim 1$  second) to measure the concentration of  $\text{H}_2\text{S}$  in the HCl extractant. The microelectrode was filled with a ferricyanide solution [ $\text{K}_3[\text{Fe}(\text{CN})_6]$ ] that reduced

to ferrocyanide ( $K_4[Fe(CN)_6]$ ) in the presence of  $H_2S$ , which diffused from the surrounding HCl extractant through the silicone membrane of the microelectrode tip (Jeroschewski, 1996; Kühl, Steuckart, Eickert, & Jeroschewski, 1998). The electrical current from the oxidation of the reduced ferrocyanide is linearly proportional to the concentration of  $H_2S$ . The microelectrode was calibrated with freshly prepared sulfide standards. To prepare the standards ranging from  $\sim 0$ – $800 \mu\text{mol S}^{2-} \text{ L}^{-1}$ , I added 0, 50, 100, and 250  $\mu\text{L}$  aliquots of a stock solution of  $\text{Na}_2\text{S} \cdot 9 \text{H}_2\text{O}$  (0.1 M) to 30 mL deoxygenated HCl (1 M). I measured the concentration of sulfide in the stock solution by iodometric titration with standard iodine (0.0125 M) and sodium thiosulfate (0.0125 M) solutions (Vogel, 1989). In this method, sulfide reacts with excess iodine in an acid solution (Equation 2.1), and the remaining iodine is titrated with sodium thiosulfate until colourless (Equation 2.2). The final endpoint was detected using a starch indicator.



I added 10 mL of the standardised iodine to a conical flask and acidified it with 1 mL of HCl (1 M). With swirling, I added 1 mL of the freshly made  $\text{Na}_2\text{S} \cdot 9 \text{H}_2\text{O}$  stock solution and then titrated with the standardised sodium thiosulfate solution until the solution was a light straw colour. I added three drops of 1% starch solution at this point and completed the titration until the solution was colourless.

### Colour analysis

I scanned each homogenised sediment sample with a flatbed scanner (CanoScan LiDE 100, Canon) at a resolution of 600 dpi ( $0.04 \text{ mm pixel}^{-1}$ ). The flatbed scanner illuminated the sediment with LEDs. A colour calibration strip was scanned alongside the sediment (shown in Figure 2.3).



**Figure 2.3:** An example image of homogenised soft, subtidal sediment and a colour calibration strip on a flatbed scanner. The shaded area was used to measure the average sediment colour intensity. The white asterisks show the location of air bubbles that were excluded from the measurement.

The resulting image was imported into the software *analySIS FIVE LS Research 3.3* (Olympus Soft Imaging Solutions) and stages of the colour analysis were automated using a macro. The first stage of the analysis normalises the image so that all images cover the same colour range. This colour range can change because of different lighting conditions such as light leaking through the sides of the scanner with a thick sample, or small differences resulting from the scanner's internal calibration. This can be corrected for by including a colour calibration strip in every scan. The macro to perform the normalisation is described and shown below:

1. The intensity channel of the sediment profile image was extracted as defined by the hue, saturation, and intensity (HSI) colour space, creating a grey scale image.
2. A  $4 \times 4$  pixel averaging filter was applied to the entire image to minimise the effects of noise and anomalies in the image.
3. The grey scale range of the image was adjusted linearly to cover the maximum available value range, that is, the black and white calibration squares at the

bottom of the image (Figure 2.3) were assigned values of 0 and 255 respectively. The brightest 2% and darkest 2% of the pixels were ignored during this step as some images contained artefacts that were brighter or darker than the calibration strip, voiding this step.

**Macro for Olympus analySIS FIVE LS Research to normalise images:**

```
ColorSeparationIntensity();
    Extract colour intensity channel

DefineNxN(1, 4);
    Define averaging filter, one pass 4 × 4 pixels

NxN(Op.Display, Op.Display);
    Apply averaging filter

OptimizeContrast(LowerOverflow:=2, UpperOverflow:=2);
    Discard brightest 2% and darkest 2% pixels and stretch the remaining values to use the entire grayscale range, 0–255
```

I then measured the average colour intensity values over the greatest image area possible, approximately 50 cm<sup>2</sup>, excluding anomalies such as air bubbles (see Figure 2.3).

### Data analysis

I applied a linear and a quadratic fit using colour intensity as the predictor parameter and AVS concentration as the response parameter to identify a correlation between these two variables (R version 3.0.2). I used colour intensity as the predictor parameter because the error associated with this measurement is very small; over 100,000 pixels are averaged to obtain the grey value, whereas only four measurements are averaged to obtain the AVS concentration. This configuration will produce the most representative regression using optimised least squares. I used ANCOVA to test whether the quadratic model described the data significant better than the linear model. I then used the Bayesian information criterion (BIC) to determine whether the linear or quadratic model was the most suitable (Schwarz, 1978). The BIC adds a penalty value for each parameter in the model and returns a log-likelihood value; a lower BIC value indicates a better fit.

### 2.2.2 Application: in situ SPI analysis

I used the laboratory established AVS–colour intensity correlation described above to estimate the in situ distribution of AVS by means of analyses of sediment profile images. I obtained sediment profile images by deploying a sediment-profile imaging device (SPI-Scan, Benthic Science Ltd., New Zealand, Figure 2.4) consisting of a modified consumer flatbed scanner (CanoScan LiDE 25, Canon; c.f. scanner used in the laboratory, CanoScan LiDE 100), housed inside a polycarbonate cylinder (8.5 cm diameter, 28 cm length). The electrical components are contained in a larger elliptical body ( $42 \times 30 \times 8$  cm, hereafter, electronics housing) attached to the top of the cylinder. The scanner moves along the inner surface of the cylinder over a horizontal distance of 120 mm to acquire a sediment image. A colour calibration strip, identical to the one used in the laboratory, is attached to the outside of the cylinder and included in every scan. The combined weight of the device and frame is  $\sim 30$  kg, making it considerably lighter than traditionally used sediment imaging devices such as REMOTS, which weighs  $>200$  kg (Rhoads & Cande, 1971; Rhoads & Germano, 1982; Rosenberg et al., 2001; Solan & Kennedy, 2002). The sediment penetration depth was adjusted by attaching 2–6 kg of weight to the electronics housing so that the sediment–water interface was approximately one-third of the distance from the top of the sediment profile image. An electrical tether connected the device to a 24 V power supply and a computer on the boat.

Sediment profile images were analysed using the same 3-step automated procedure used to analyse images of the sediment in the laboratory (see above). I excluded the upper 1 mm of sediment from the image analysis procedure to avoid any artefacts resulting from disturbance of sediment by the SPI instrument. An additional step was added to the macro to produce a false-colour image. The false-colour image was generated by assigning the grey value of each pixel to the corresponding AVS concentration with the previously derived correlation equation. AVS concentrations were grouped into  $1 \mu\text{mol g}^{-1}$  wet weight sediment ranges and assigned colours from



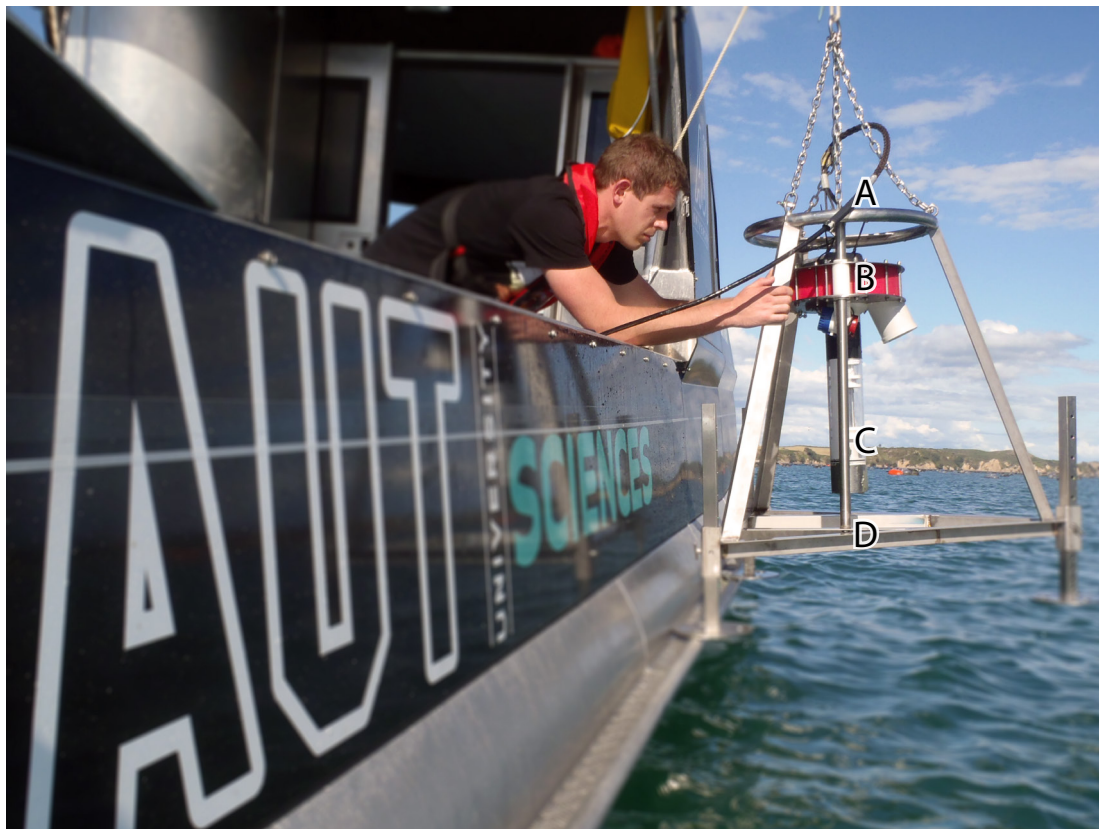


**Figure 2.4:** A prototype sediment profile imaging device (SPI-Scan™, Benthic Science Ltd.) used in this study to acquire sediment profile images. (A) Electrical tether that connects the device to a 24 V power source and a computer on the surface; (B) scanner electronics housing; (C) scan head; (D) frame.

green through to red for low to high concentrations (Table 2.2). I grouped concentrations  $>8 \mu\text{mol g}^{-1}$  together so detail in the lower concentration ranges wasn't lost by having too many colour graduations. The macro and colour assignment are shown below:

**Macro for Olympus analySIS FIVE LS Research to normalise an image and produce a false-colour image representing AVS concentration ranges:**

```
ColorSeparationIntensity();
```

*Extract colour intensity channel*

```
DefineNxN(1, 4);
```

*Define averaging filter, one pass  $4 \times 4$  pixels*

```
NxN(Op.Display, Op.Display);
```

*Apply averaging filter*

```
OptimizeContrast(LowerOverflow:=2, UpperOverflow:=2);
```

*Discard brightest 2% and darkest 2% pixels and stretch the remaining values to use the entire grayscale range, 0–255*









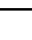
```
Op.Display = Op.Display + 1;
```

*Move image selection to the newly generated image*

```
imgLoadLUT(Op.Display, "AVS.Lut");
```

*Apply a look up table (LUT) to the grey scale image that assigns colours corresponding to AVS concentration ranges (colour assignments shown in Table 2.2)*

**Table 2.2:** Colour assignments used to produce a false-colour image from a grey scale sediment profile image.

AVS concentration range ( $\mu\text{mol g}^{-1}$ wet weight)	Grey value range	Assigned colour
0–1	86–100	 (RGB: 0, 104, 55)
1–2	79–85	 (RGB: 26, 152, 80)
2–3	73–78	 (RGB: 102, 189, 99)
3–4	68–72	 (RGB: 166, 217, 106)
4–5	63–67	 (RGB: 217, 239, 139)
5–6	59–62	 (RGB: 254, 224, 139)
6–7	55–58	 (RGB: 253, 174, 97)
7–8	51–54	 (RGB: 244, 109, 67)
>8	20–50	 (RGB: 215, 48, 39)

To generate a vertical AVS concentration profile (overlaid on Figure 2.5A and C), I defined a rectangular area in the sediment profile image, excluding anomalies such as air bubbles. The analySIS software then calculated the average grey value for every row of pixels within this area. Following this step, 40 rows were averaged, approximately 3.5 mm, to produce one data point. This step was used to reduce the number of data points in the profile. Finally, I converted the average grey values to AVS concentrations with the previously derived correlation equation.

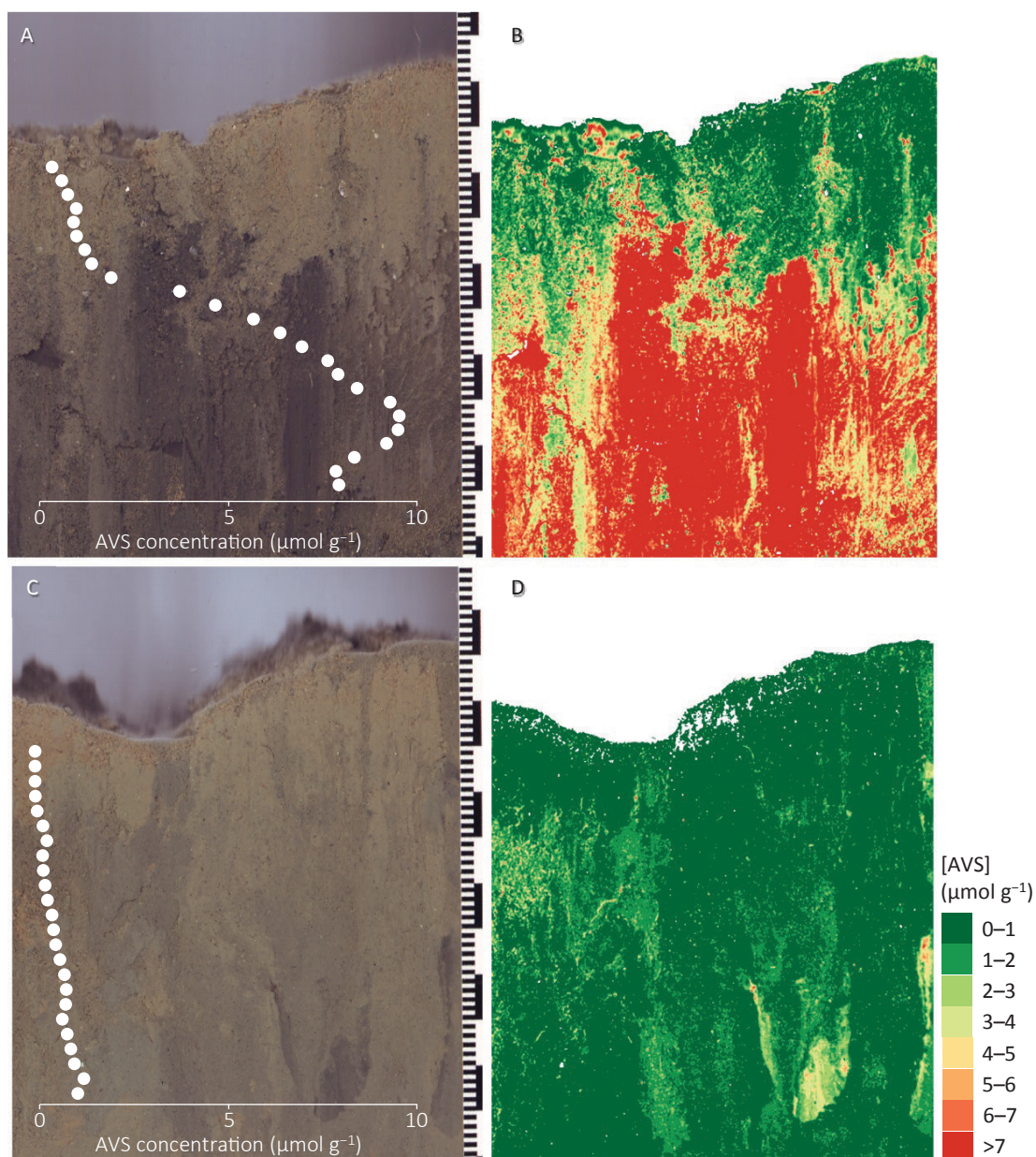


**Figure 2.5:** (A and C) Two example sediment profile images obtained with the SPI-Scan in March 2013 from Awakiriapa Bay, Waiheke Island, New Zealand. Small black and white bars on the scale to the right of each image are 1 mm; the larger bars are 10 mm. The images are overlaid with vertical AVS concentration ( $[\text{AVS}]$ ,  $\mu\text{mol g}^{-1}$  wet weight) profiles derived from image analysis; error bars for AVS concentration are too small to be seen. (B and D) Two-dimensional AVS distribution plots derived from the images A and C, respectively.

## 2.3 Results

### 2.3.1 Calibration: correlating AVS content and colour intensity

The mean sediment water content decreased from 75% in the upper layer to 65% at a depth of 9 cm and the mean organic matter content was  $6.3 \pm 0.9\%$  (dry weight, mean  $\pm$  SD,  $n = 54$ ). Particle size (% volume) analysis revealed that the upper 9 cm of the sediment comprised 9% clay, 73% silt, and 17% sand (based on the Wentworth scale; Appendix A).

The  $\text{H}_2\text{S}$  microelectrode responded linearly (minimum  $R^2 = 0.991$ ) to  $\text{H}_2\text{S}$  concentration. The measurement of one extract was completed in  $\sim 10$  seconds. The  $\text{H}_2\text{S}$  concentrations in the extract ranged from 4 to  $350 \mu\text{mol L}^{-1}$ , which corresponded to 0.14 to  $5.01 \mu\text{mol AVS g}^{-1}$  wet weight. Statistical outliers within the four replicate AVS measurements per sediment slice were identified with Grubb's outlier test and removed.

The colour intensity of the homogenised sediment from each slice was derived from the average grey value of  $\sim 200,000$  pixels (see Methods). The average 95% confidence interval of this measurement was  $\pm 0.006$  grey values.

A quadratic function best described the relationship between sediment AVS concentration and colour intensity (Figure 2.6, Table 2.3). This was revealed by a BIC value that was 23 values lower for the quadratic fit than it was for the linear fit. A BIC difference of 10 indicates that there is a 150:1 likelihood that the model with the lower score is the better fitting model (Raftery, 1995). In further support, the  $R^2$  value of the quadratic model ( $R^2 = 0.93$ ) was also higher than that of the linear model ( $R^2 = 0.92$ ). The average 95% individual confidence interval of the quadratic model was  $\pm 0.2 \mu\text{mol AVS g}^{-1}$  wet weight.

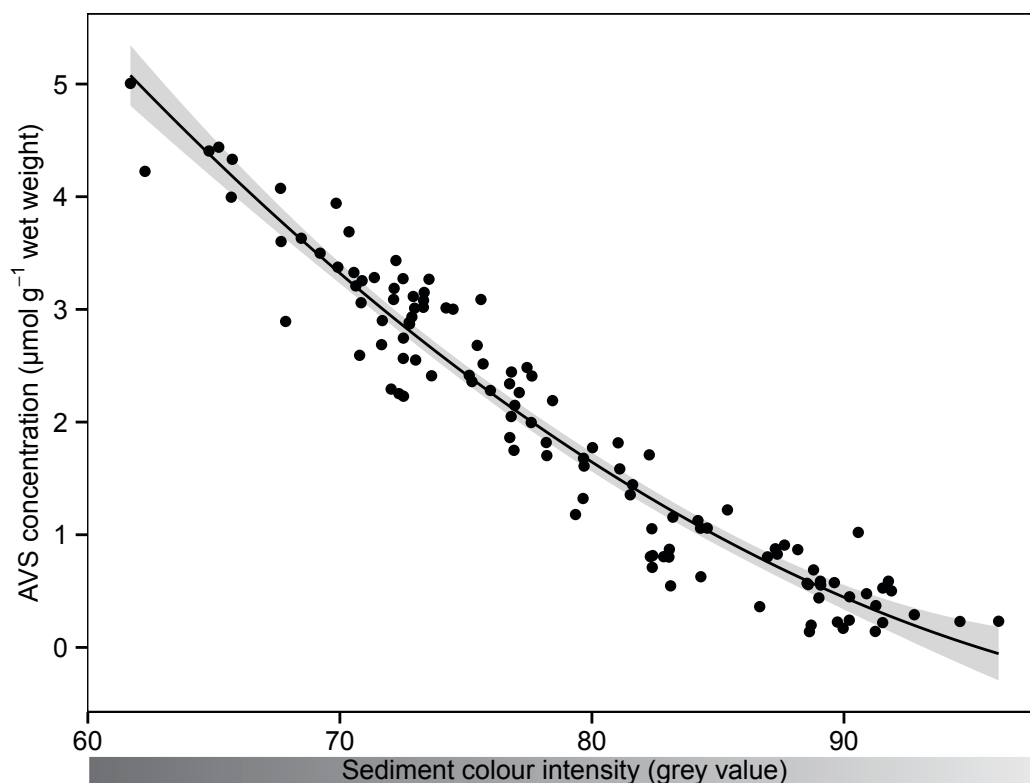


**Figure 2.6:** A scatter plot showing the relationship between the sediment AVS concentration ( $\mu\text{mol g}^{-1}$  wet weight) and the colour intensity of soft, subtidal sediment (upper 9 cm) collected from Awakiriapa Bay, Waiheke Island, New Zealand. A colour intensity of 0 is black, and that of 100 is white. The solid line is a quadratic fit through all points ( $[\text{AVS}] = 0.002 \times \text{GREY}^2 - 0.525 \times \text{GREY} + 28.392$ ,  $R^2 = 0.93$ ,  $n = 117$ ); the 95% confidence interval of the fit is denoted by the grey shaded area.

**Table 2.3:** Results of a linear and a quadratic model for the correlation between AVS concentration and sediment colour intensity. The BIC adds a penalty value for each parameter in the model and returns a log-likelihood value; a lower BIC value indicates a better fit.

Model	$x^2$	$x$	Intercept	$R^2$	BIC
Linear	—	−0.15	13.49	0.92	97.6
Quadratic	0.002	−0.52	28.39	0.93	74.9

### 2.3.2 Application: in situ SPI and analysis

I applied the established correlation between sediment AVS content and colour intensity to sediment profile images obtained as described above. The SPI-Scan imaged an area (including sediment and water column) of  $117 \times 216$  mm at a resolution of 300 dpi ( $0.08 \text{ mm pixel}^{-1}$ ) within 60 seconds.

I started the scan of the sediment profile immediately after the device was in place to exclude possible effects of the movement of the scan head inside the sediment on the sediment profile image. Such movement could result from the pull of the attached tether due to strong currents or boat drift.

The vertical AVS concentration profile derived from the sediment profile image in Figure 2.5A ranged from  $0.3 \mu\text{mol g}^{-1}$  in the upper sediment to  $9.5 \mu\text{mol g}^{-1}$  wet weight at a depth of 63 mm. Similarly, analysis of the sediment profile image in Figure 2.5C resulted in a vertical AVS concentration profile ranging from  $0.01 \mu\text{mol g}^{-1}$  wet weight in the upper sediment to  $1.3 \mu\text{mol g}^{-1}$  at a depth of 77 mm.

The process of creating an average vertical AVS concentration profile from a sediment profile image with the analySIS software was completed in  $\sim 1$  minute. This doesn't include the time required to average multiple rows and create an overlay as shown in Figure 2.5A and C. In contrast, producing one average AVS profile by sectioning a sediment core and extracting AVS with acid in the laboratory required  $\sim 2$  hours. The two-dimensional AVS distribution plots, shown in Figure 2.5B and D, were derived in  $\sim 1$  second, with no user intervention, by the previously described analySIS macro.



## 2.4 Discussion

I found a strong correlation ( $R^2 = 0.93$ , see Figure 2.6) between the AVS content of soft subtidal sediment and the sediment's colour intensity. Given the predictive power of this correlation and the simplicity of the procedure, I believe that estimating the distributions of AVS from sediment profile images can become a powerful tool in the routine assessment of subtidal organically enriched sediment, for example, sediments underneath and in the vicinity of marine farms, in ports, or polluted estuaries. The collection of sediment cores is only required for the initial calibration (AVS–colour intensity correlation); this makes large-scale AVS surveys possible. Furthermore, this approach enables the study of processes such as bioturbation and particle resuspension and their effects on the micro-scale distribution of AVS in the upper 20 cm of sediment.

The data were best described by a quadratic function ( $n = 117$ ,  $R^2 = 0.93$ ). This is at variance with the linear relationship ( $n = 40$ ,  $R^2 = 0.62$ ) published by Bull and Williamson (2001). Their data have a higher variance so this is not necessarily contradictory. A comparison of the data collected in this study and the data of Bull and Williamson (2001) are discussed in further detail later in this Chapter. Inspection of the model in Figure 2.6 revealed an increased slope at lower colour intensities, that is, the technique is less sensitive at higher AVS concentrations. One possible cause for this difference in sensitivity is the non-quantitative extraction of coloured sulfide minerals. The highest concentrations of AVS were obtained from dark coloured samples that likely contained a larger proportion of the minerals mackinawite and greigite, which are not quantitatively extracted.

Estimating AVS from sediment profile images relies on the assumptions that all AVS compounds are coloured and that all coloured AVS compounds are quantitatively extracted. Two pools do not comply with these assumptions. Firstly, the colourless dissolved sulfide species, of which the main contributors are  $\text{H}_2\text{S}$  and  $\text{HS}^-$ , are included in the acid extraction but impossible to detect using visible light. Secondly,

some coloured sulfide minerals are not extracted quantitatively, if at all. For example, cold 1 M HCl does not extract pyrite, and only extracts 40–67% of greigite and 92% of mackinawite (Cornwell & Morse, 1987). This non-quantitative extraction may render AVS concentration estimates inaccurate if the relative concentrations of these pools were to change either temporally or spatially. As pyrite is not extracted at all under standard extraction conditions, its presence could potentially introduce the most error into the correlation as it is highly coloured, but not an AVS component. The contribution by pyrite in organically enriched sediments may be minimal as Morse and Wang (1997) found that the formation of pyrite was inhibited in the presence of marine organic matter. Reduced formation of pyrite results in a larger proportion of sulfur species that, unlike pyrite, are both coloured and acid extractable. The contribution of colourless sulfides to AVS and incomplete extraction of some coloured sulfides is investigated in Chapter 4.

Another factor that can interfere with the estimation of AVS from image analysis is the presence of non-AVS components, such as organic debris, air-filled pockets, and burrows or tears, which may form from the shear stress of SPI-Scan penetrating the sediment. The sediment profile image in Figure 2.7 shows a large burrow, however, the rest of the image is suitable for analysis. When producing an average vertical AVS profile, user interaction is required to select the analysis area and such artefacts can be avoided. This is not the case for the automated two-dimensional AVS distribution analysis. This analysis uses the entire image, and any part of the image that falls within a certain colour intensity range is included in the analysis regardless of whether it is an AVS component or not. Tears or holes in the sediment are typically darker than the colour range that AVS compounds fall within, and for the most part, are excluded from the analysis. To avoid these types of artefacts completely, limits can be applied to ignore darker grey values, but this can result in the exclusion of high concentration AVS areas from the analysis.

Physical sediment characteristics are important parameters to consider when estimating AVS concentrations from a sediment profile image. The sediment at the test



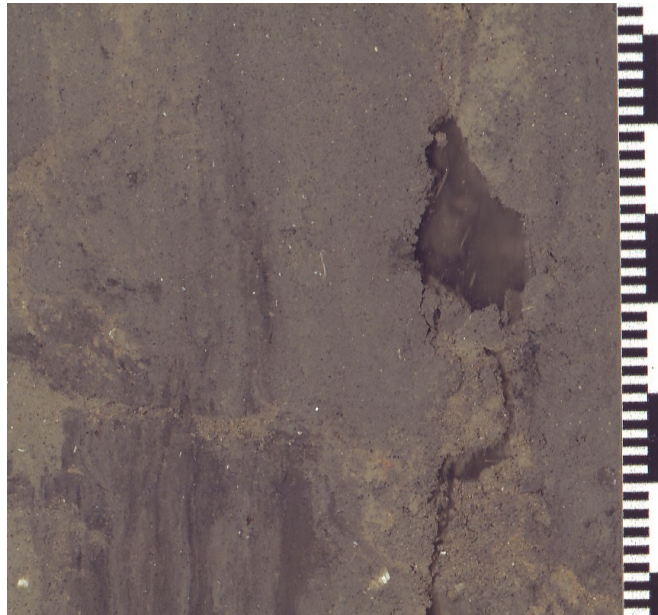


**Figure 2.7:** Cropped sediment profile image obtained with the SPI-Scan instrument from Awakiriapa Bay, Waiheke Island, New Zealand, in June 2013. This example shows a burrow that can invalidate automated image analysis. The small marks on the right hand scale are 1 mm, and the larger marks, 10 mm.

site in Awakiriapa Bay is a soft, cohesive mud. This type of sediment is easy for the SPI-Scan to penetrate and generally adheres well to the scanner tube while the image is being acquired. If the SPI-Scan is moved while in the sediment, or it doesn't enter the sediment perpendicular to the surface, contact between the scanner tube and the sediment can be broken. Such loss of contact allows other surficial sediments to fall in between the scanner tube and the sub-surface sediment; an example of this is shown in Figure 2.8A. The sediment that falls in does not adhere to the scanner tube surface and creates a rough surface that reflects light differently to the rest of the sediment. Analysing an image with this rough surface results in incorrectly high AVS concentrations in the derived AVS distribution image (Figure 2.8B). The colour intensity in these areas is affected by reflection, particles not adhering to the scanner tube, or voids where there are no sediment particles. Image anomalies such as these are not accounted for when establishing the correlation and so cannot be accounted for when analysing the image. A similar anomaly can occur at the sediment–water interface.

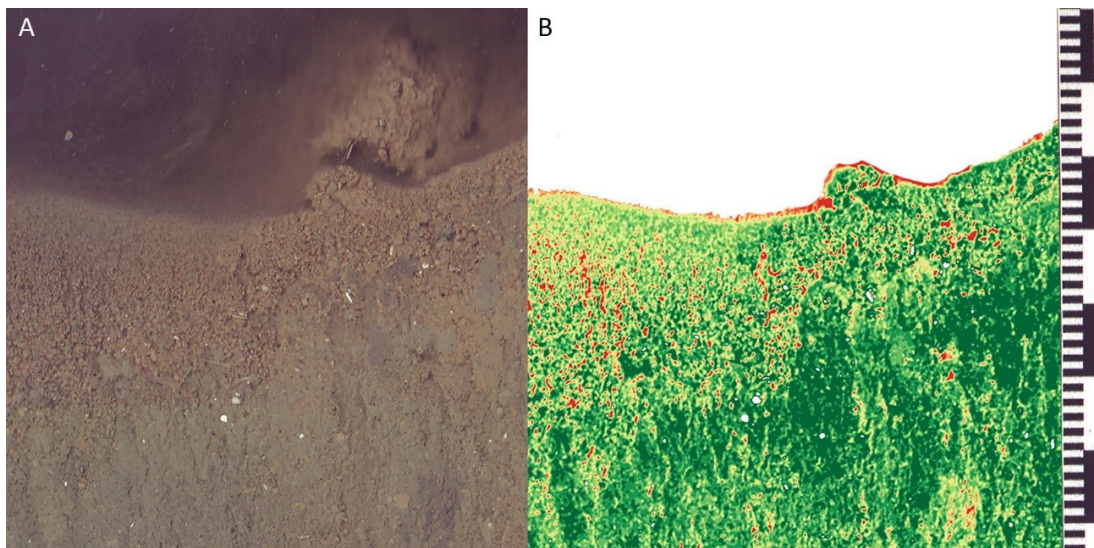


**Figure 2.8:** Cropped sediment profile image obtained with the SPI-Scan instrument from Awakiriapa Bay, Waiheke Island, New Zealand, in June 2013 and the derived false-colour AVS distribution image. This example shows the effects of the sediment surface losing contact with the scanner tube, allowing surficial sediment to fall in between the scanner tube and the sub-surface sediment, which invalidates image analysis. The small marks on the right hand scale are 1 mm, and the larger marks, 10 mm.

The sediment can lose contact with the scanner tube as the SPI-Scan penetrates the sediment (Figure 2.8). During penetration, some sediment compaction can occur and the upper few millimetres of sediment move away from the scanner tube. Sediment further away from the scanner tube surface appears darker in an image and the resulting derived image shows a high AVS concentration at the sediment–water interface. My recommendation for image analysis is to avoid the areas where sediment has lost contact with the scanner tube.

A sediment profile image can be analysed multiple ways to produce different representations of the sediment AVS content. Firstly, the average AVS concentration of the entire scanned sediment, or a defined area, such as a 4 cm band starting 1 cm beneath the sediment–water interface. A single value, such as this, could be a useful monitoring parameter as it would be easy to track spatial and temporal changes in the AVS content. This method also allows for the exclusion of previously mentioned image artefacts, maximising the number of usable images.

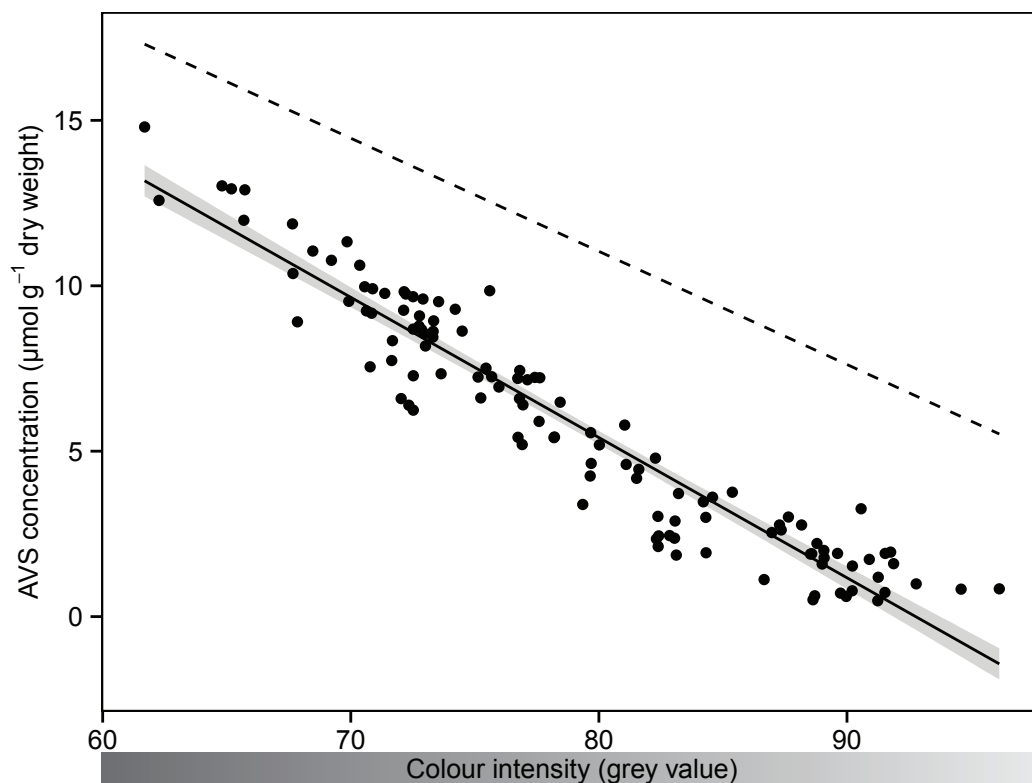
Secondly, vertical AVS concentration profiles; these require manual selection of the sediment area and time to process the results to make an overlay as shown in

Figure 2.5A and C. Vertical AVS concentration profiles provide the same information as an AVS concentration profile that can be produced using typical laboratory based, wet chemistry approaches or microelectrodes. Image analysis is faster than chemical approaches and capable of higher resolutions. At 300 dpi, it is possible to produce vertical AVS concentration profiles with increments of 80  $\mu\text{m}$ , which would be difficult to achieve with typical laboratory approaches.

Finally, the analyst can produce a two-dimensional, false colour AVS distribution plot using an automated procedure (Figure 2.5B and D). This analysis presents information that hasn't previously been obtained at high resolution. These false-colour images make it possible to observe the heterogeneity of sulfide distributions in the sediment. Monitoring the change in AVS distributions over time could enhance the understanding of animal-sediment relations, complimenting studies such as the study by Solan and Kennedy (2002).

To compare my AVS concentration estimates with that in Bull and Williamson (2001), I expressed the measured wet sediment AVS content per dry weight sediment and applied a linear fit to describe the relationship between this content and the corresponding grey values (Figure 2.9). To do so, I assumed that the pore water was free of sulfides and that the sediment water content decreased linearly from 75% wet weight in the surficial layer to 65% wet weight at a depth of 9 cm. The comparison revealed that AVS concentrations predicted with my correlation were  $5.6 \mu\text{mol g}^{-1}$  dry weight lower on average than the concentrations in Bull and Williamson (2001).

One reason for this difference could be the process of acquiring and quantifying sediment colour. I used a flatbed scanner in the laboratory to directly generate an RGB image; Bull and Williamson (2001), however, first photographed their sediment, developed the film, and then digitised the photograph to create an RGB image. Differences between these two processes may result in the same sediment colour being assigned a different value, resulting in a different correlation.



**Figure 2.9:** A scatter plot showing the linear relationship between the sediment AVS concentration ( $\mu\text{mol g}^{-1}$  dry weight) and the colour intensity of soft, subtidal sediment (upper 9 cm) collected from Awakiriapa Bay, Waiheke Island, New Zealand. A colour intensity of 0 is black, and that of 100 is white. The solid line is a linear fit through all points ( $[\text{AVS}] = -0.424 \times \text{GREY} + 39.32$ ,  $R^2 = 0.91$ ,  $n = 117$ ); the 95% confidence interval of the fit is denoted by the grey shaded area. The dashed line shows the fit for the data from Bull and Williamson (2001) with the equation  $[\text{AVS}] = -0.342 \times \text{GREY} + 38.4$ .

Another difference between our methods was that I measured AVS concentrations directly in the acid extractant using an amperometric  $\text{H}_2\text{S}$  microelectrode where Bull and Williamson (2001) trapped the  $\text{H}_2\text{S}$  gas evolved from acidifying the sediment in a buffer solution, which they then measured with an ion-specific electrode. There should be little difference between AVS concentrations measured using either method since the same concentration of  $\text{HCl}$  (1M) was used in both approaches to extract sulfide minerals from the sediment. The method use by Bull and Williamson (2001) assumes that all evolved  $\text{H}_2\text{S}$  gas is trapped in the buffer, so any differences would likely arise from the accuracy or sensitivity of the ion-selective electrode compared to the amperometric  $\text{H}_2\text{S}$  microelectrode.

Another reason for the difference in correlations could also be attributed to the particular sediment sources. Bull and Williamson (2001) collected subtidal sediment from an estuary, whereas I collected subtidal sediment from a coastal habitat. It may be possible to offset a correlation to work at a different location by subtracting the difference in the “background colour” of the sediment. That is, the colour of the sediment excluding AVS. For example, the average difference in grey value between Bull and Williamson (2001) and my correlation is 14 grey values, when estimating AVS concentrations between 5 and 15  $\mu\text{mol g}^{-1}$  dry weight. If I was to offset Bull and Williamson’s correlation by  $-14$  grey values, AVS concentrations predicted from an image using either correlation would be similar.

A second factor to consider when comparing the two correlations is the slope of the fit ( $-0.42$  in this study,  $-0.34$  in Bull and Williamson’s study). A difference in slopes could indicate different AVS mineral composition. For example, the colour intensity of sediment with a high mackinawite concentration may be different to sediment with a high greigite concentration, even though they may have the same total AVS concentration; this idea is explored further in Chapter 4. Despite the differences in sediment type, colour determination, and AVS quantification, the two AVS/colour correlations are surprisingly similar. This indicates that the correlation between AVS content and sediment colour intensity may be valid for a variety of sediment types in the Auckland region, one prerequisite for large-scale spatial surveys. I investigate whether this correlation holds for other subtidal, Hauraki Gulf sediments in the next chapter.

Bull and Williamson (2001) identified precise colour reproduction as their primary concern with their method. Their process of vertically slicing sediment cores in the laboratory, taking photographs under studio lighting using film photography, developing the film, and digitising the photographs introduced errors in the reproduction of sediment colour. I minimised oxidation of the sediment by horizontally slicing the sediment core so that only a small portion of the sediment was exposed to air for a short time ( $<3$  min). Using a flatbed scanner in the laboratory, I

could eliminate colour reproduction issues introduced by film photography and photo digitisation. The scanning hardware used in the laboratory and in situ used the same illumination technology, creating reproducible lighting conditions; individual scanning devices, however, may differ in their reproduction of colours. To account for such differences, I included a colour calibration strip in every image so that I could adjust colour properties before image analysis.

The key elements of this method are the correlation of sediment AVS content and sediment colour intensity in the laboratory, and the application of this correlation to in situ sediment profile images. Alternative instruments could be used to acquire in situ images and measure sediment colour in the laboratory to produce similar results, but it is essential that a colour measured in situ is assigned the same colour value in the laboratory. Colour calibration strips have been essential in this method for colour correction.

For the purpose of monitoring, accurately estimating the sediment content of dissolved colourless and non-extractable coloured minerals may not be as important as the ability to track temporal and spatial change in the coloured AVS content. One possible application for this technique is in the assessment of the effects of marine farms on benthic ecosystem function. In this example, two factors are of interest: first, temporal changes in the size of the affected area of seafloor, that is, the area at which the sediment AVS content is larger than that of the background. Time-series of sediment profile images taken along transects that intersect the farm will reveal such change. Second, changes over time in the intensity of organic matter deposition, that is, the maximum concentration of sedimentary AVS, can be revealed from the same time-series. The small size of SPI-Scan and the rapid scanning and image analysing procedure will ideally be suited to assess sediment underneath and in the vicinity of, for example, closely spaced long-lines or fish cages.

## Chapter 3

# Assessing the suitability of the sediment AVS/colour correlation at three sites in the Hauraki Gulf, New Zealand

### 3.1 Introduction

Monitoring techniques need to be rapid to promote regular assessment and be suitable for a range of locations. In Chapter 2, I described an improved correlation between sediment colour intensity and AVS concentration that was initially presented by Bull and Williamson (2001). I then used this correlation to develop a rapid technique for estimating the concentration of AVS in coastal marine sediments. Such technique is suited to assessing and monitoring the intensity of organic enrichment, however, it was only established and trialled in one location, Awakiriapa Bay, Waiheke Island, New Zealand.

The correlation between sediment colour intensity and AVS concentration was strong ( $R^2 = 0.93$ ) in Awakiriapa Bay, but differed to the correlation established by Bull and Williamson (2001) for a subtidal urban estuarine sediment in the Auckland region. The two correlations had similar slopes, but a horizontal offset; that is, a particular

grey value predicted a higher AVS concentration when using Bull and Williamson's correlation than when using my correlation.

Two possible explanations for these differences are: (1) the use of different methods to acquire sediment-profile images and measure the sediment AVS content, and (2) sediment at different locations differ in the relative contribution of the various sulfide species that comprise AVS. Such differences may cause the AVS/colour correlation at these locations to differ.

As discussed earlier, the dominant sulfide minerals, mackinawite and greigite, are not extracted quantitatively using 1 M HCl. Cold 1 M HCl, for example, extracts 93% mackinawite and 40–67% greigite from marine sediments (Cornwell & Morse, 1987). Therefore, if the AVS composition at one location comprised predominantly mackinawite and another location comprised predominantly greigite, the AVS/colour correlation at each location would differ.

Another important source of AVS in marine sediments are colourless dissolved porewater sulfides. Sediments with high water content may contain a higher concentration of dissolved porewater sulfides than sediments with low water content. The units of AVS can be expressed per gram wet sediment or per gram dry sediment. Conversion between these units for sediments with a significant contribution from dissolved porewater sulfides may be a factor that affects the AVS/colour correlation. The magnitude of this difference would be dependent on the water content of the sediment.

Another factor that is likely to influence the AVS/colour correlation is the concentration of pyrite. The colour of pyrite is dark brass and it is a non-AVS mineral, that is, it is not extracted using 1 M HCl. Pyrite will contribute to the dark colour of marine sediment but not to the AVS concentration. I discuss how I investigated pyrite in marine sediment and its contribution to sediment colour in Chapter 4.

To determine whether differences in the AVS/colour correlation arise from using alternative methods, I will use the same methodology at multiple locations in the



Hauraki Gulf, New Zealand. That is, I will determine sediment colour intensity and sediment AVS concentration at multiple locations using the same methods presented in Chapter 2.

After establishing an AVS/colour correlation at each location, I will investigate whether combining the sediment colour and AVS concentration data can produce a correlation suitable for estimating AVS concentrations from sediment colour intensity at multiple locations.

Furthermore, I will investigate the effect of presenting AVS concentration per gram wet weight and per gram dry weight on the shape and slope of the AVS/colour correlation.

## 3.2 Methods

### 3.2.1 Sediment collection

I collected eight cores of soft subtidal sediment using SCUBA from each of three sites around the Hauraki Gulf, New Zealand (Figure 3.1). I sampled Awakiriapa Bay in February 2013 and the other two sites, Wilson Bay and Te Kouma, in August 2013. At each site, I collected sediment approximately 50 m from the boundary of a mussel farm. I pushed tubes vertically into the sediment until two-thirds were filled with sediment and then sealed both ends of the tubes with stoppers. The sediment-filled tubes were transported in a refrigerated box to the laboratory. In the laboratory, I removed the upper lids and immersed the tubes gently in a plastic container ( $1,444 \text{ cm}^2 \times 54 \text{ cm}$ ) filled with 48 cm (78 L) seawater, which was aerated with a bubble stone.

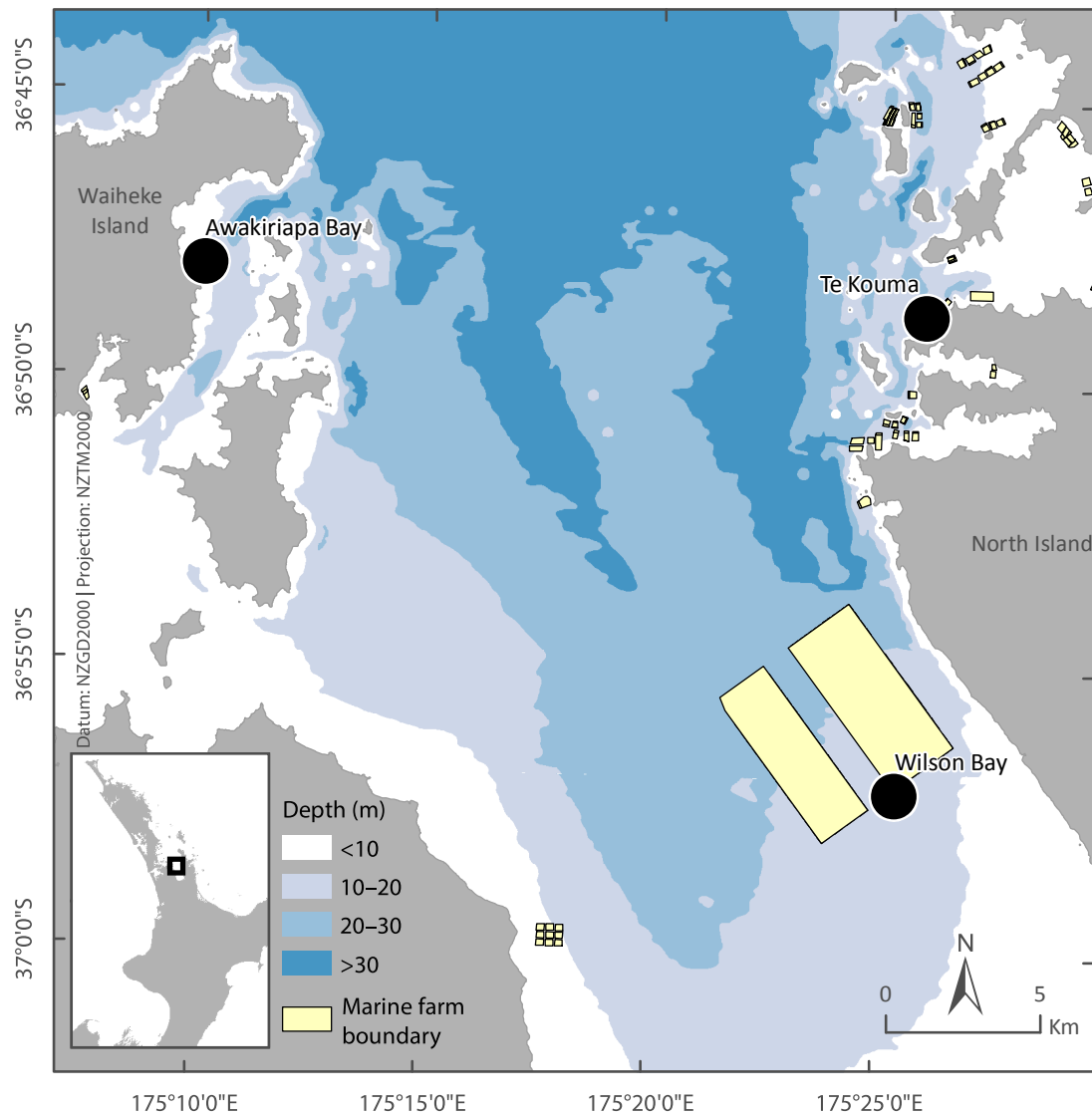


**Figure 3.1:** Locations of the three sediment-sampling sites in the Hauraki Gulf, New Zealand (black circles). The beige polygons indicate the boundaries of mussel farms in the region. Data from Land Information New Zealand and Waikato Regional Council.

### 3.2.2 Sediment analysis

Within one week of collection, I sectioned one sediment core at a time. I discarded the upper 1 cm of sediment as it was disturbed during sampling and transportation. I then took 2-cm thick samples from five depths ranging from 2–4 cm, following the scheme shown in Figure 3.2. I sliced the discarded layer immediately before sampling to minimise the sediment exposure to air.

I homogenised the freshly sliced sediment sample in an aluminium dish with a stainless steel spatula. From this dish, I removed  $4 \times \sim 1$  g of sediment for AVS

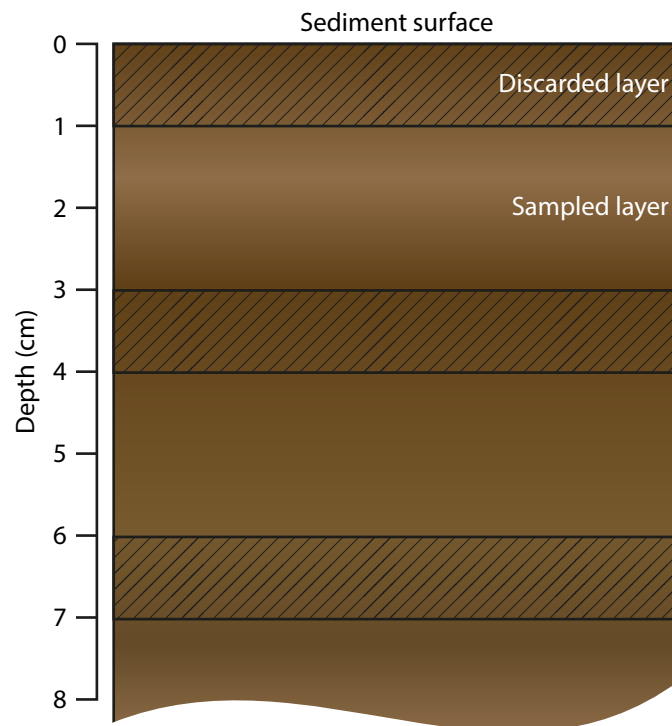


**Figure 3.2:** Scheme used sample subtidal marine sediments collected in acrylic tubes.

determination, the remaining sediment was divided between sediment colour analysis, water content, organic matter content, and particle size analyses. I processed each slice before cutting the next, keeping the air exposure of the sediment below 3 minutes.

Sediment water content was determined for each slice by weight loss after drying at 90 °C for 24 hours and organic content by weight loss after combusting in a 400 °C furnace for 6 h. These measurements of water content were used to convert AVS concentrations from  $\mu\text{mol L}^{-1}$  wet weight to  $\mu\text{mol L}^{-1}$  dry weight. A small subsample (approximately 0.1 g) was taken from each homogenised slice and combined to create one sample per site for particle size analysis, which was analysed on a laser-based particle analyser (Malvern Mastersizer 2000; Appendix A).

I determined the AVS concentration of each homogenised sample using the method described in Chapter 2 (Section 2.2.1, AVS determination). I added each of the four samples from a sediment slice (see above) into a 40 mL glass vial filled with 30 mL HCl ( $1 \text{ mol L}^{-1}$ , ACS grade) that was deoxygenated by purging with nitrogen for  $\geq 20$

minutes. The vial was closed with an airtight lid and briefly shaken. I weighed each HCl filled vial before and after adding sediment to determine the mass of sediment used in the extraction. I left the vials to stand while sectioning the remainder of the core. Sectioning one core was completed within 30 minutes. I waited for 30 minutes before measuring the concentration of AVS in the acid extract with an amperometric hydrogen sulfide microelectrode. The total sediment extraction time before measurement was one hour.

The microelectrode was calibrated with freshly prepared sulfide standards. To prepare the standards ranging from  $\sim 0\text{--}800\ \mu\text{mol S}^{2-}\ \text{L}^{-1}$ , I added 0, 50, 100, and 250  $\mu\text{L}$  aliquots of a stock solution of  $\text{Na}_2\text{S} \cdot 9\ \text{H}_2\text{O}$  (0.1 M) to 30 mL deoxygenated HCl (1 M). I measured the concentration of sulfide in the stock solution by iodometric titration using standard iodine (0.0125 M) and sodium thiosulfate (0.0125 M) solutions (Vogel, 1989).

I determined sediment colour by scanning the homogenised sediment on a flatbed scanner (CanoScan LiDE 100, Canon) at a resolution of 600 dpi. A colour calibration strip was scanned alongside the sediment so that colour calibration could be performed during image processing. The scanned image was then imported into the software *analySIS FIVE LS Research 3.3* (Olympus Soft Imaging Solutions) and processed in the same manner as described in Chapter 2 (Section 2.2.1, Colour analysis). Briefly: the intensity channel was extracted from the image as defined by the hue, saturation, and intensity (HSI) colour space. A  $4 \times 4$  pixel averaging filter was applied to minimise the effects of noise and anomalies in the image. The grey scale range was then adjusted to cover the maximum possible range, that is, the image was adjusted so that the black and white calibration squares were assigned grey values of 0 and 255 respectively. The brightest 2% and darkest 2% of the pixels were ignored during this step as some images contained artefacts that were brighter or darker than the calibration strip, voiding this step. I manually drew a polygon to select the area of sediment to obtain an average grey value. The polygon covered the maximum

sediment area possible without including colour artefacts from light leakage near the edge of the sediment and from air bubbles.

### 3.2.3 Statistical analyses

I correlated the sediment colour intensity and AVS concentration data for each site. For each correlation, I placed a linear and a quadratic fit through the data using ordinary least squares (OLS) regression, with grey value on the x-axis. I performed correlations with AVS concentrations expressed per gram wet sediment and per gram dry sediment separately. The best fit was determined by inspecting the  $R^2$  value and the Bayesian Information Criterion (BIC; Schwarz, 1978). The BIC adds a penalty value for each parameter in the model and returns a log-likelihood value; a lower BIC value indicates a better fit. For Awakirapa Bay and Wilson Bay, the fit that best described the data was quadratic, while at Te Kouma, the fit that best described the data was linear. To enable statistical comparison between the sites, I used a linear fit at all sites.

Before attempting to combine the data from the three locations, I first determined whether the data were normally distributed before proceeding with either an ANOVA if the data were normally distributed or a Kruskal–Wallis test if the data were not normally distributed to determine whether there were any statistically significant differences between the locations.

To assess the suitability of using one AVS/colour correlation to estimate the AVS concentration from sediment colour intensity at multiple sites, I pooled the data from each location to create one correlation.

### 3.3 Results

#### 3.3.1 Sediment characteristics

Particle size analysis revealed the sediment at all three sites to comprise predominantly of silt and clay (Table 3.1). Sediment at Te Kouma had the largest median particle size and the lowest water content and organic matter content. The rankings of sediment water and organic matter contents were inverse to that of the median grain size for all sites, that is, larger particle size was accompanied by lower water and organic matter content.

**Table 3.1:** Sediment particle sizes (% volume) and median size ( $\mu\text{m}$ ), as determined by laser particle size analysis from three sampled sites in the Hauraki Gulf, New Zealand. Water content and organic matter are the average values from 40 separately measured sediment subsamples with the standard error of the mean shown in parentheses. Particle size classifications are based on the Wentworth Scale. The site locations are shown in Figure 3.1

	Clay (%)	Silt (%)	Very fine sand (%)	Fine sand (%)	Medium sand (%)	Median size ( $\mu\text{m}$ )	Water content (%)	Organic matter (%)
Awakiriapa Bay	8.8	76.2	9.1	4.2	1.6	14.7	65.6 (0.6)	5.9 (0.1)
Wilson Bay	16.9	70.7	8.8	3.7	0	10.9	73.9 (0.1)	6.6 (0.1)
Te Kouma	11.9	46.1	15.8	23.8	2.4	36.1	50.5 (0.6)	3.7 (0.1)

#### 3.3.2 Site-specific AVS/colour correlations

The range of measured AVS concentrations differed at each site. Wilson Bay sediment had the largest AVS concentration range ( $0.2\text{--}7.0\ \mu\text{mol g}^{-1}$  wet weight; Figure 3.3).

The AVS concentrations, however, were not evenly distributed across the entire range and there was a break in the data between  $0.85\text{--}2.52\ \mu\text{mol g}^{-1}$ . The sediment AVS concentrations at Awakiriapa Bay and Te Kouma were lower than Wilson Bay, they also had a smaller range, and the data were more evenly distributed.

The correlation between sediment colour intensity and AVS concentration was strong ( $R^2 > 0.7$ ) at all sites (Figure 3.3, Table 3.2).

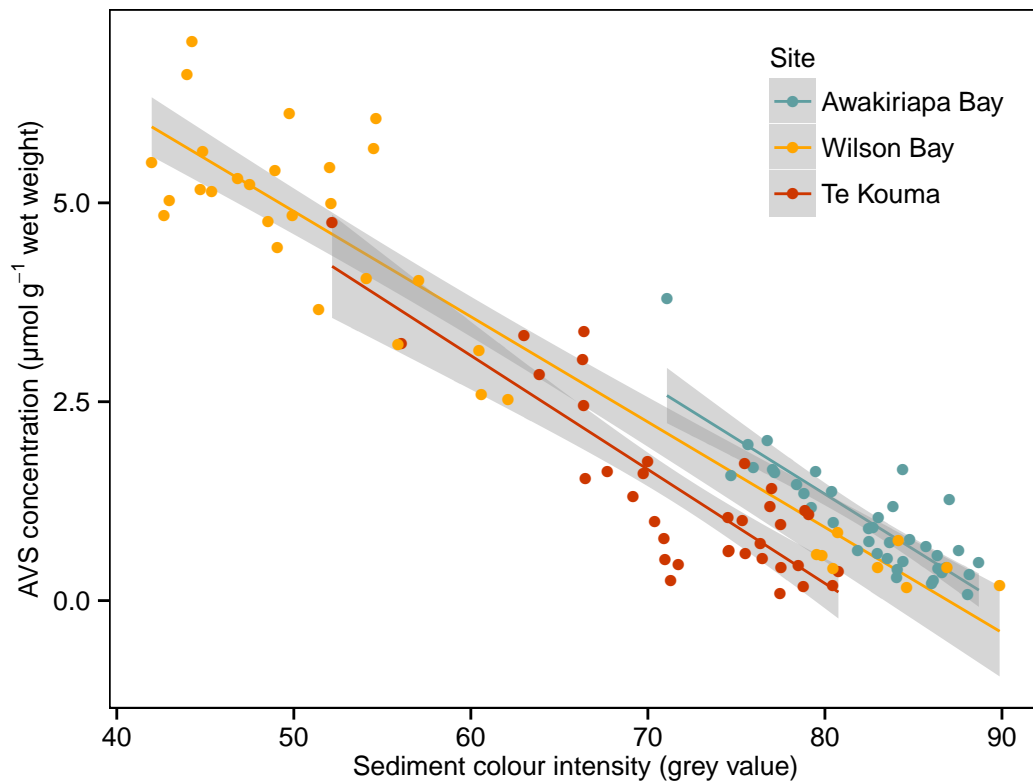


**Figure 3.3:** The relationship between acid volatile sulfide concentration (wet weight) and sediment colour intensity at three mussel farms in the Hauraki Gulf, New Zealand. A colour intensity of 0 is black, and that of 100 is white. Each solid line is a linear fit through that sites data points and the shaded area indicates the 95% confidence interval of the fit.

A Levene test indicated that the data were not normally distributed ( $F_{(2,117)} = 15.84$ ,  $p < 0.001$ ) which means that non-parametric analyses must be used on these data. The Kruskal–Wallis test revealed significant difference among AVS concentrations at the three locations ( $H_{(2)} = 28.39$ ,  $p < 0.001$ ). This indicates that the AVS/colour correlation is significantly different at each location.

**Table 3.2:** Equations for the linear fits that best describe the AVS/colour correlation for three sites in the Hauraki Gulf, New Zealand. AVS concentrations were presented per gram wet sediment. The data are presented in Figure 3.3.

	Slope	Intercept	$R^2$
Awakiriapa Bay	−0.139	12.45	0.72
Wilson Bay	−0.132	11.51	0.89
Te Kouma	−0.143	11.67	0.72

### 3.3.3 Pooled-data AVS/colour correlation

Despite significant statistical differences between the AVS concentrations at each site, I tentatively investigated whether it was possible to create a correlation that could be used to estimate AVS concentration from the sediment colour intensity at more than one site. I created such correlation by combining the data points from the three sampled sites, Awakiriapa Bay, Wilson Bay, and Te Kouma to create a pooled AVS/colour correlation, herein, pooled-data correlation (Figure 3.4).

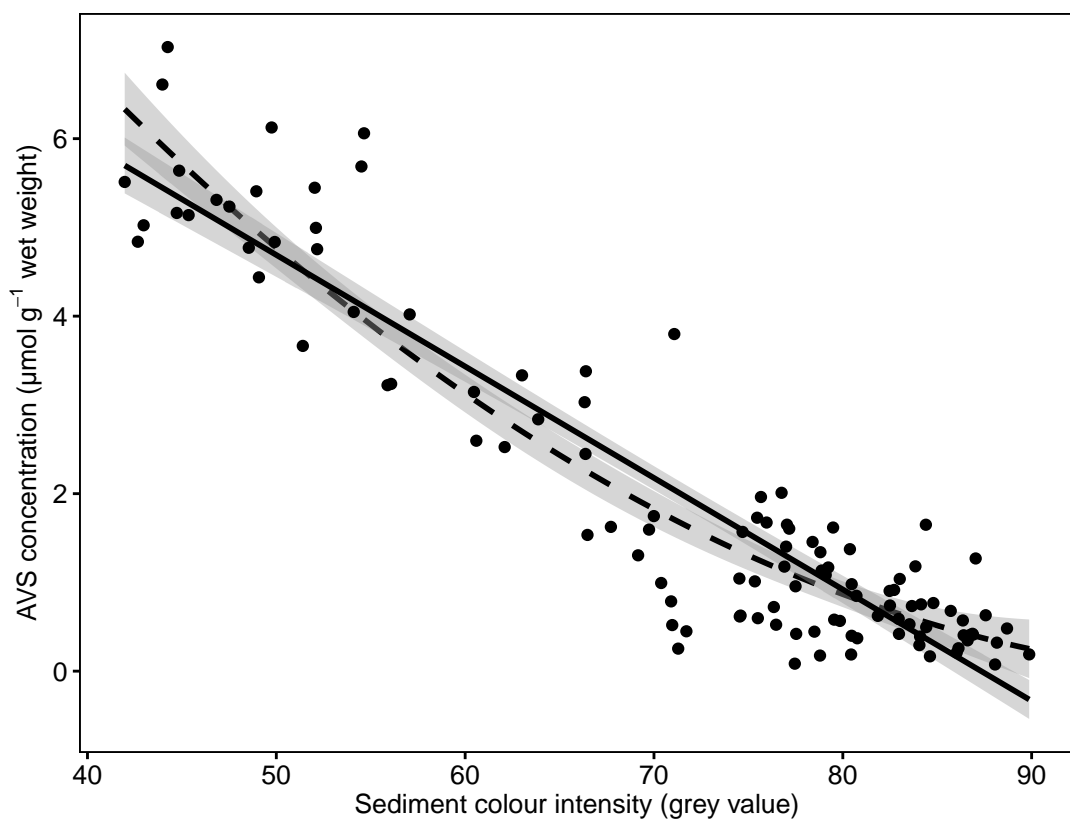


**Figure 3.4:** Pooled AVS concentration and sediment colour intensity data from three sampled sites — Awakiriapa Bay, Wilson Bay, and Te Kouma — in the Hauraki Gulf, New Zealand. AVS concentrations are presented per gram wet sediment. The solid black line denotes a linear fit through all data points and the dashed lined denotes a quadratic fit through all data points. The grey shaded area indicates the 95% confidence interval of each fit.

The pooled data were well described by both linear and quadratic fits (Figure 3.4; Table 3.3). The  $R^2$  values of both fits through the pooled data were higher than that of the  $R^2$  values for site-specific fits for Te Kouma and Awakiriapa Bay. This is likely just



an artefact of having more data points, rather than an indication that one correlation could be used for multiple sites.

**Table 3.3:** Equations for the linear and quadratic fits that describe the relationship between AVS concentration and sediment colour intensity. AVS concentrations were presented per gram wet sediment and per gram dry sediment. The BIC value in the final column indicates the maximum log-likelihood value of the model; a smaller value indicates a better fit.

	$x^2$	$x$	Intercept	$R^2$	BIC
Linear		-0.126	10.97	0.86	249
Quadratic	0.002	-0.351	18.07	0.88	236

Visual inspection of the fits that best described the pooled-data revealed that AVS concentrations would be overestimated in the middle of the plotted range using the pooled-data correlation equation (~60–70 grey values; Figure 3.4). The linear fit appears to describe the data more poorly than the quadratic fit over this range.

To estimate the accuracy of the pooled-data correlation, I used the equation of the linear fit that best described the pooled-data to estimate AVS concentration from sediment colour intensity at all three sites. I then compared the estimated AVS concentrations to the AVS concentrations measured in the laboratory (Figures 3.5 and 3.6).

The analysis revealed that the extent of the difference between the estimated AVS concentration and the measured AVS concentration differed between sites (Figure 3.6). The range AVS concentration differences for Wilson Bay and Te Kouma was  $\sim 2.5 \mu\text{mol g}^{-1}$ , which is large when compared to the total range of measured AVS concentrations ( $\sim 0\text{--}6 \mu\text{mol g}^{-1}$  wet weight).

The pooled-data correlation was most similar to the AVS/colour correlation for Wilson Bay. AVS concentrations estimated at Wilson Bay using the pooled-data correlation were on average  $0.14 \mu\text{mol g}^{-1}$  lower than the actual measured AVS concentration. The interquartile range of data from Awakiriapa Bay was positive, which indicates that the majority of AVS concentrations predicted at Awakiriapa Bay using the pooled-data correlation will be lower than their actual concentration.

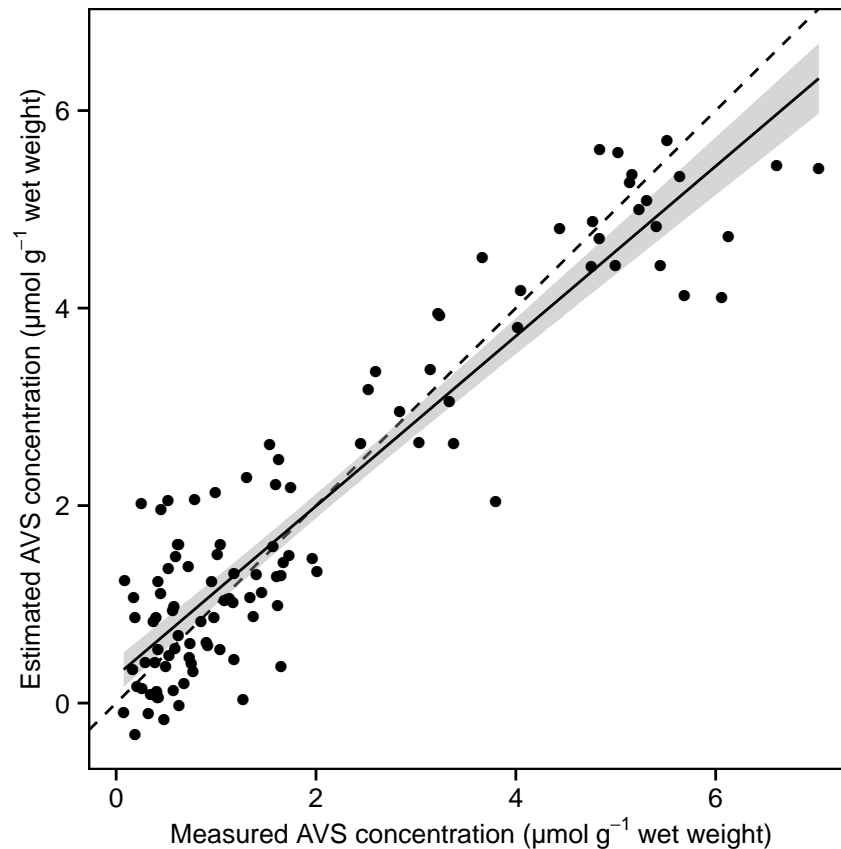


**Figure 3.5:** Comparison of AVS concentrations measured in sediment samples and AVS concentrations estimated from the sediment colour intensity of the samples using the pooled-data correlation equation. The black line indicates the line of best fit through the data ( $R^2 = 0.86$ ) and the grey shading denotes the 95% confidence interval of the fit. The dotted line denotes a 1:1 relationship, that is, where the estimated AVS concentration is equal to the measured AVS concentration.

Contrastingly, the interquartile range of data from Te Kouma was negative, and therefore, AVS concentrations estimated using the pooled-data correlation will be higher than their actual concentrations.

### 3.3.4 Converting AVS concentration units

To investigate the effect of sediment water content on the AVS/colour correlation I converted AVS concentration from  $\mu\text{mol g}^{-1}$  wet weight to  $\mu\text{mol g}^{-1}$  dry weight. After converting the AVS concentration units to per gram dry weight, the slope of the fits that best described the relationship between AVS concentration and sediment colour intensity differed between the sites (Figure 3.7). The statistical significant of this

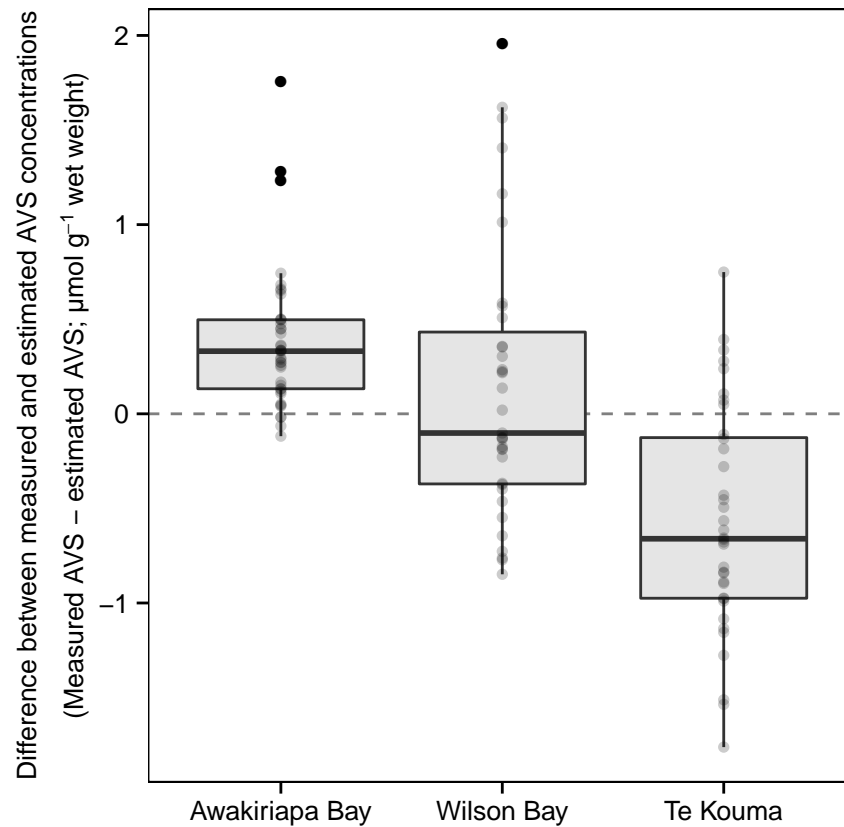


**Figure 3.6:** Difference between AVS concentrations measured in the laboratory and AVS concentrations estimated using the equation of the linear fit that best described the pooled-data (measured AVS concentration – estimated AVS concentration). A positive value indicates that the estimated AVS concentration is lower than the measured AVS concentration. A value of zero (indicated by the dashed horizontal line) indicates that the measured AVS concentration was the same as the AVS concentration estimated from sediment colour intensity. The grey box and black horizontal lines denote the lower, middle, and upper quartiles of the data. The range of values is indicated by the vertical lines. Individual values are overlaid as semi-transparent black circles. Outliers (deemed to be 1.5 times the interquartile range) are shown as black circles.

difference is indicated by the significant interaction between the Grey value and Site terms in the ANCOVA (Table 3.4). The difference in the slope of the line of best fit through the data of each location, when AVS concentration was presented per gram dry weight, was in contrast to the previously discussed results where the slopes were similar at each site when AVS concentration was presented per gram wet weight. Although the slopes of the fits were different at each site, the data were still well described by a linear fit ( $R^2 > 0.7$ ; Table 3.5).

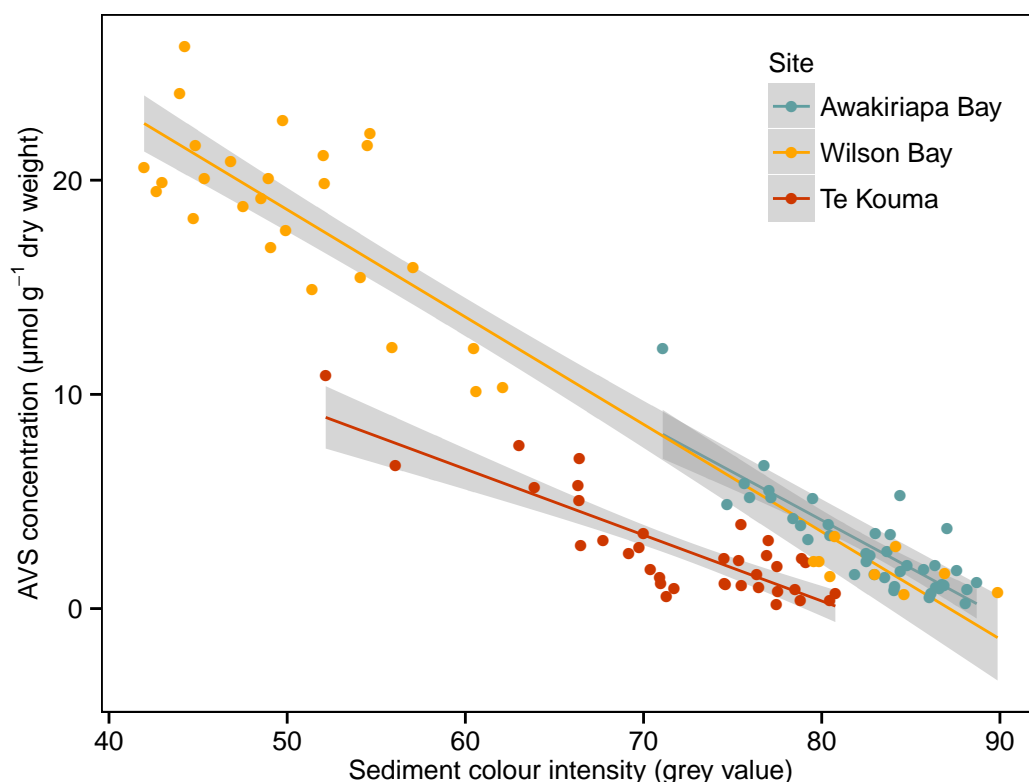


**Figure 3.7:** The relationship between acid volatile sulfide concentration (dry weight) and sediment colour intensity at three mussel farms in the Hauraki Gulf, New Zealand. The intensity of black is 0 and that of white is 100. Each solid line is a linear fit through the data points of one site and the shaded area indicates the 95% confidence interval of the fit.

**Table 3.4:** Full factorial ANCOVA to investigate difference in slopes of the fits that best describe the data presented in Figure 3.7. AVS concentration (dry weight) = Grey + Site,  $R^2 = 0.94$ .

	Df	Sum Sq	Mean Sq	F value	Pr(>F)
Grey	1	4774.4	4774.4	1489.92	<0.001
Site	2	640.0	320.0	99.86	<0.001
Grey:Site	2	48.4	24.2	7.55	<0.001
Residuals	105	336.5	3.2		

**Table 3.5:** Equation terms and  $R^2$  value for the fits through the data presented in Figure 3.7. AVS concentrations are presented per gram dry sediment.

	Slope	Intercept	$R^2$
Awakiriapa Bay	-0.449	40.03	0.71
Wilson Bay	-0.501	43.68	0.90
Te Kouma	-0.308	24.99	0.71

## 3.4 Discussion

### 3.4.1 Differences in the AVS/colour correlation at different locations

The slope of the fit that best described the relationship between sediment colour intensity and AVS concentration was similar at each of the three locations. The fits, however, were offset on the grey value scale. I noted a similar grey value offset between AVS/colour correlations with similar slopes in the comparison I made between the AVS/colour correlation I established in Awakiriapa Bay and the AVS/colour correlation Bull and Williamson (2001) established in an urban estuary (Chapter 2). I suggested two possible reasons for this grey value offset: (1) different methods for obtaining sediment colour may result in a different grey value for the same sediment, and (2) different sediment background colour, that is, the grey value of the sediment if it contained no iron sulfides and includes components such as clay and other minerals and metals.

Differing methodologies can be ruled out in this study as the same methods were used at each site to sample the sediment, measure the sediment colour, and measure the AVS concentration. Thus, the reason for the grey value offset between sites is likely a result of the background colour or composition of the sediment. Bull and Williamson (2001) list crystallinity, particle size, minor coloured phases, etc. as likely systematic sources of sediment colour change that introduce differences into the correlation between sediment colour intensity and AVS concentration.

Sediment characteristics, for example, its composition, particle size, and crystallinity will influence the colour and light reflecting properties of the sediment. The combination of these characteristics will determine the background colour intensity. An increase in the concentration of coloured AVS minerals will decrease the colour intensity of the sediment (darker sediment) from the background value. Assuming that the same proportion of coloured AVS minerals are present at each site (e.g.,

mackinawite and greigite), an increase of 1  $\mu\text{mol}$  of AVS minerals should have the same magnitude of effect on sediment colour intensity at every site. That is, the AVS/colour correlation slope is determined by the colour properties of the coloured AVS minerals and the offset of the correlation is determined by the background colour intensity of the sediment.

Contrastingly, when AVS concentration was converted to per gram dry sediment, the slope of the linear fit that best described the data differed significantly between sites (Figure 3.7). For example, sediment at Te Kouma had the lowest water content (51%), and subsequently, the lowest AVS/colour correlation slope when AVS concentration was presented per gram dry sediment; sediment at Wilson Bay had the highest water content (74%), and subsequently, the steepest AVS/colour correlation slope when AVS concentration was presented per gram dry sediment.

The difference in the AVS/correlation slope between sites is an artefact of converting the AVS concentration unit to per gram dry weight. All AVS measurements were conducted on wet sediment and the conversion to per gram dry sediment was calculated from the sample's water content. During this conversion process, the grey value of the sample remains the same but the AVS concentration increases. One gram of dry sediment has a higher AVS concentration than one gram of the same wet sediment, as illustrated in Figure 3.8. This AVS concentration increase results in the linear fit that best describes the data having a steeper slope. Sites with a higher water content will exhibit this effect the most. This is in agreement with the observation that the AVS/colour correlation with the steepest slope was established at Wilson Bay, which had the highest water content.

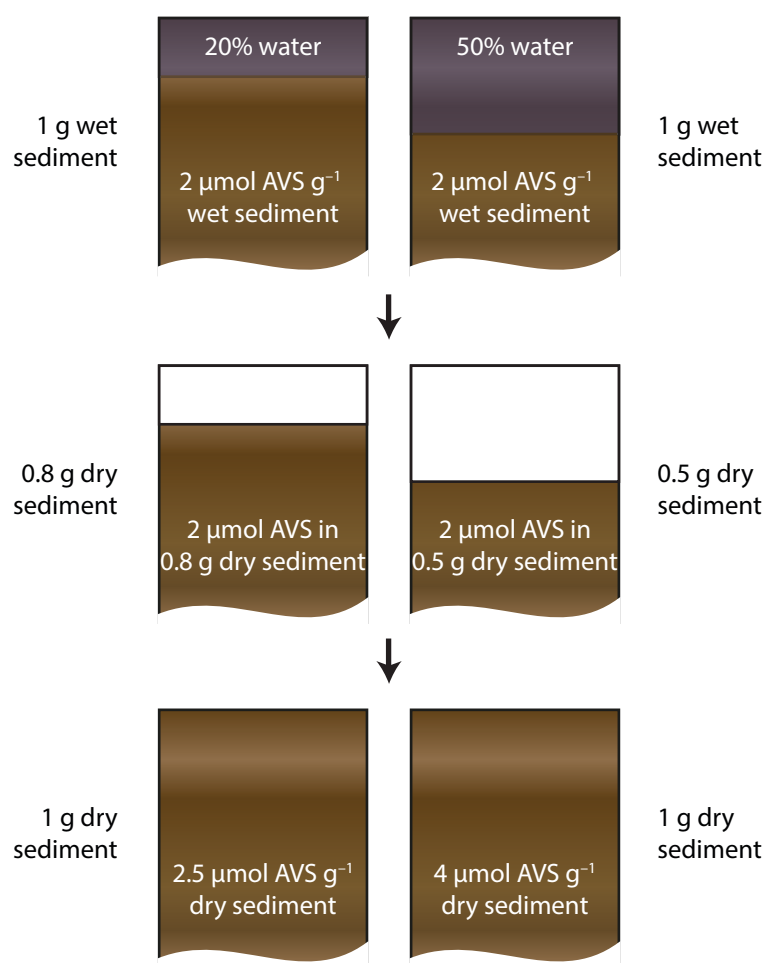


**Figure 3.8:** An illustration of the process for converting AVS concentration from  $\mu\text{mol g}^{-1}$  wet sediment to  $\mu\text{mol g}^{-1}$  dry sediment. The left hand column shows the process for sediment with 20% water content whereas the right hand column shows the process for sediment with 50% water content.

### 3.4.2 Assessing the suitability of an AVS/colour correlation established from multiple sites

Although the pooled-data from all three locations were well described by linear and quadratic fits ( $R^2 > 0.8$ ; Figure 3.4), the pooled-data correlation was a poor predictor of AVS concentrations across multiple sites.

The pooled-data correlation was biased toward the Wilson Bay data because the sediment from that location had the widest range of grey values. Furthermore, the fits that best described the data from Te Kouma and Awakiriapa Bay when AVS concentration was presented per gram wet sediment, were positioned approximately equal distance either side of the fit that best described data from Wilson Bay along the grey value axis. This similar but opposite difference ‘balances out’ when performing ordinary least squares regression, which may explain the good statistical fit, but poor AVS concentration prediction.

Assessing the suitability of a pooled-data AVS/colour correlation has confirmed the necessity of establishing a site-specific correlation to estimate AVS concentrations from sediment colour intensity. Even over relatively small areas, such as the Hauraki Gulf, the difference in background sediment colour between sites was large enough that a non-site specific correlation could not accurately predict the AVS concentration at all sites.

To be used in as a monitoring technique, the AVS/colour correlation should be established using sediment representative of the extent of the area being studied; this is to account for the natural spatial heterogeneity of the sediment. In this study, I collected sediment samples from a relatively small area near the boundary of the mussel farm. An improvement to this sampling approach is to collect sediment samples over a much larger area, ideally including beneath and further away from the mussel farm, or other organic matter source.



## Chapter 4

# Sediment sulfur chemistry

### 4.1 Introduction

In Chapter 2, I demonstrated how sediment acid volatile sulfide (AVS) concentration can be estimated from the colour intensity of a sediment profile image. Such estimation was possible after establishing a correlation between sediment colour intensity and AVS concentration. In Chapter 3, I demonstrated that the AVS/colour correlation was site-specific. One reason that necessitates a site-specific AVS/colour correlation is that sediments at different locations differ in their background colour, that is, the colour of the sediment excluding sulfide minerals. Another factor that may necessitate a site-specific AVS/colour correlation is the composition of the sedimentary sulfide pool, which consists of dissolved porewater sulfide, mackinawite, greigite, and pyrite.

In the context of establishing an AVS/colour correlation, sedimentary sulfides can be grouped into one of three pools: (1) colourless acid extractible sulfides. These are dissolved porewater sulfides,  $\text{H}_2\text{S}$ ,  $\text{HS}^-$ ,  $\text{S}^{2-}$ . These three species are present in the pH dependent equilibrium:  $\text{H}_2\text{S} \rightleftharpoons \text{HS}^- \rightleftharpoons \text{S}^{2-}$ . For example, at a typical seawater pH of 8.1, 9% of the total dissolved sulfide occurs in the form of  $\text{H}_2\text{S}$ , at pH 7.0  $[\text{H}_2\text{S}] \approx [\text{HS}^-]$ , and at pH 6.0, 91% occurs in the form of  $\text{H}_2\text{S}$ . (2) coloured sulfides that can be

fully or partially extracted with cold, 1 M HCl, including mackinawite and greigite, and (3) coloured sulfides that cannot be extracted with cold, 1 M HCl, including pyrite.

Sulfides can be extracted from marine sediments using sequential extraction techniques (Figure 4.1). To conduct such technique, an analyst initially extracts sediment with a weak or low concentration acid to remove sulfide minerals, such as mackinawite and greigite. The analyst then uses acids of increasing strength or concentration to extract sulfide minerals that are more difficult to extract, such as pyrite.

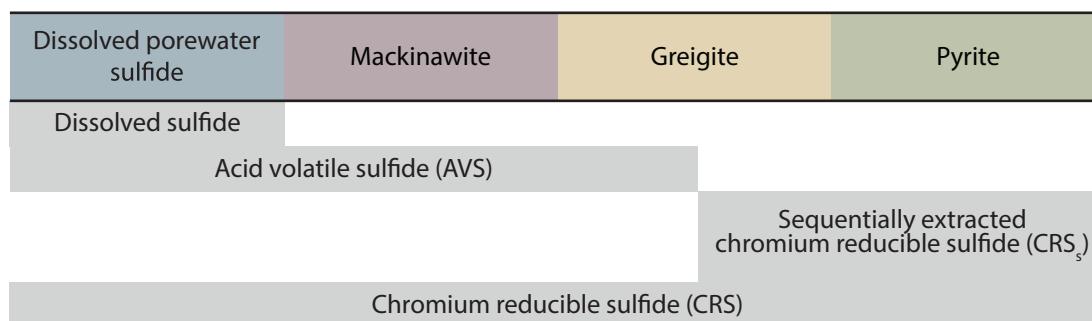


**Figure 4.1:** Visual representation of the sulfide components in marine sediment (top row). The grey shaded areas denote the sulfide pools as used in this study and the components that comprise each pool.

Dissolved porewater sulfides can be measured in the laboratory from collected sediment cores or samples, or they can be measured in situ using voltammetric (e.g., Brendel & Luther III, 1995) or amperometric (Jeroschewski, 1996; Kühl et al., 1998) electrodes.

The next pool, AVS, can be extracted under a variety of conditions. The composition of AVS is dependent on the extraction conditions because some sulfide minerals are more susceptible to acid extraction than others. Most marine sediment AVS extractions use HCl in concentrations ranging from 1–6 mol L<sup>-1</sup>; the acid can be hot (e.g., Berner, 1964b; Westrich, 1983; Wieder, Lang, & Granus, 1985), or cold (e.g., H. E. Allen et al., 1993; Cornwell & Morse, 1987; Jørgensen, 1977b; Westrich, 1983), and can also include SnCl<sub>2</sub> (e.g., Cornwell & Morse, 1987; Westrich, 1983) as a reducing agent to minimise interference from Fe<sup>3+</sup>. Cornwell and Morse (1987)

compared the extraction efficiencies of commonly used AVS extraction methods and showed that 1 M HCl extracted most mackinawite and some greigite from marine sediment (Table 4.1). Hot 6 M HCl quantitatively extracted mackinawite and greigite, however, some pyrite was also extracted.

**Table 4.1:** Extraction efficiencies of commonly used AVS extraction methods on synthetically prepared mackinawite, greigite, and pyrite, and mineral pyrite. Data from Cornwell and Morse (1987).

Method	% Mineral S extracted			
	Mackinawite	Greigite	Synthetic pyrite	Mineral pyrite
1 M HCl	92	40–67	0	0
6 M HCl + SnCl <sub>2</sub>	100–102	63–75	4–10	0
0.5 M H <sub>2</sub> SO <sub>4</sub> + TiCl <sub>2</sub>	101	96–100	48–82	0
Hot 6 M HCl + SnCl <sub>2</sub>	100–101	93–100	97–100	2

Rickard and Morse (2005) referred to AVS as a black-box measurement because the extraction techniques are non-selective, and most commonly, the relative proportion of the different sulfide forms are not known. The authors also suggested that it may be time to abandon the idea of the operational pool of AVS to focus more on the specific components of AVS. This suggestion likely arose from the widespread attribution of AVS solely to FeS. Meysman and Middelburg (2005), however, disagreed with such suggestion and justified continued use of the AVS operational pool by comparing it to the widely used organic carbon operational pool.

Sedimentary carbon is often placed into two operational pools, (1) acid volatile compounds (AVC, predominantly comprising carbonates) and non-acid volatile compounds (NAVC, typically referred to as organic matter). Meysman and Middelburg (2005) state how useful and widespread these two sedimentary carbon pools have been for developing the knowledge of marine sediments and how it is often difficult to identify specific components of such operational pools. Therefore, using operation pools has been the only choice available for studying marine sediments.

Reduced sulfide species remaining in the sediment following an AVS extraction can be removed using a chromium reduction as described by Zhabina and Volkov (1978).

This method selectively extracts reduced metal sulfides (e.g., iron, zinc, and cadmium sulfides) and elemental sulfur, whereas other forms of sulfur, such as those associated with amino acids, are not extracted, or only extracted in very small quantities.

Canfield et al. (1986) demonstrated the selectivity of this method by extracting a sample containing a range of sulfide sources, such as, barite as a source of acid-insoluble sulfate, gypsum as a source of acid-soluble sulfate, and amino acids to simulate a range of sulfur-containing organic compounds that may be present in marine sediments (Table 4.2).

**Table 4.2:** Sulfur recovery from various sulfur sources using a reduced chromic acid extraction technique (Canfield et al., 1986).

Sulfur phase	% recovery
Pyrite	95.9
Zinc blende	94.6
Cadmium sulfide	97.0
Elemental sulfur	92.0
Barite	0.0
Gypsum	0.0
Taurine	0.1
Methionine	0.0
Cysteine	2.0
Cystine	0.0
Egg Albumin	0.0

A reduced chromium extraction removes all sulfide minerals from the sediment, including the AVS fraction. In a sequential extraction, however, AVS is first extracted from a sample, and then the remaining sulfides are subsequently extracted from the same sample. Throughout this Chapter, I refer to the sequentially extracted chromium reducible sulfides as CRS<sub>s</sub> (Figure 4.1).

It is likely that sediment at different locations contain different proportions of dissolved sulfides and sulfide minerals. Differences in the sediment sulfide composition will affect the AVS/colour correlation. For example, sediment with a high mackinawite content and a low pyrite content would have a strong AVS/colour correlation because most of the change in sediment colour will be due to a change in AVS concentration. Contrastingly, sediment with a low mackinawite content and high

pyrite content would have a weaker AVS/colour correlation because a change in sediment colour from pyrite is not reflected by the equivalent change in AVS concentration. Furthermore, because CRS<sub>s</sub> takes longer to form than AVS, it is likely that the proportion of these two sulfide pools will change with sediment depth.

In this chapter, I investigate the relative concentrations of the three sulfide pools, dissolved porewater sulfide, AVS, and CRS<sub>s</sub> in marine sediment from three locations in the Hauraki Gulf, New Zealand using a sequential extraction technique. Such investigation may provide insight into some of the observed differences between the AVS/colour correlations at different locations, which were presented in Chapter 3. I will also investigate how the relative proportion of sulfide pools change with sediment depth and the effect that this has on the AVS/colour correlation. Additionally, because the AVS concentration of marine sediment is dependent on the type and concentration of acid, I will investigate how modifying the type and concentration of acid for extraction affects the shape of the AVS/colour correlation.

## 4.2 Methods

I used two approaches to investigate how the AVS/colour correlation changes as a function of sediment sulfide composition, and whether differences in the sediment sulfide composition could explain the differences in the slope of the AVS/colour correlation for different locations.

Firstly, I used a sequential extraction procedure to separately measure dissolved porewater sulfides, acid volatile sulfides (AVS) including porewater sulfides, and the remaining sequentially extracted chromium reducible sulfides (CRS<sub>s</sub>), from subtidal marine sediment (Figure 4.1).

Secondly, I extracted AVS from subtidal marine sediment under three different extraction conditions with reported extraction efficiencies, varying the acid and acid concentration.

### 4.2.1 Sediment collection

I collected eight cores of soft subtidal sediment using SCUBA close to a mussel farm at each of the following locations (Figure 3.1):

1. Awakiriapa Bay, Waiheke Island, New Zealand at a water depth of 12 m. The sample location was approximately 50 m north from the north-western boundary of the farm. This farm commenced production in 1980.
2. Wilson Bay, Hauraki Gulf, New Zealand at a water depth of 12 m. The sample location was approximately 50 m south from the southern end of the farming area boundary. This farming area commenced production in 1999.
3. Te Kouma, Hauraki Gulf, New Zealand at a water depth of 14 m. The sample location was approximately 50 m west of the western farm boundary. This farm commenced production in 1984.

At each site, I pushed acrylic tubes vertically into the sediment until two-thirds were filled with sediment. I then sealed the tubes with stoppers on both ends to minimise sediment disturbance. The sediment-filled tubes were transported in a refrigerated box to the laboratory. In the laboratory, I removed the upper lids and immersed the tubes gently in one of two plastic containers ( $1,444 \text{ cm}^2 \times 54 \text{ cm}$ ) each filled with 48 cm (78 L) seawater that was aerated with a bubble stone.

Within one week of collection, I sectioned one sediment core at a time following the scheme in Figure 3.2. Before sampling a sediment layer, a 1 cm thick slice was discarded to expose a freshly cut surface, which was immediately sampled. This procedure was adopted to minimise oxidation of the sampled sediment due to exposure to the atmosphere while processing the previous layer.

Sediment water content for each layer was determined by weight loss after drying at  $90^\circ\text{C}$  for 24 hours and organic content by weight loss after combusting in a  $400^\circ\text{C}$  furnace for 6 h. Granulometric analyses were performed on a laser-based particle analyser (Malvern Mastersizer 2000, Table 4.3). To prepare the samples for

granulometric analyses, I removed ~5 g sediment from the 1–3 and 4–5 cm layers from each of the eight cores per site and combined them to make a composite sample for each site.

**Table 4.3:** Granulometric analyses and mean sediment water and organic content. Mean diameters of sediment particles at the three sample sites by % volume. 10% of the distribution is below d(0.1), 50% of the distribution is below d(0.5), the median of the volume distribution, and 90% of the distribution is below d(0.9). The volume weighted mean (Mean) is the diameter of a sphere that has the same volume as the measured particle. Detailed results presented in Appendix A.

Site	d(0.1) ( $\mu\text{m}$ )	d(0.5) ( $\mu\text{m}$ )	d(0.9) ( $\mu\text{m}$ )	Mean ( $\mu\text{m}$ )	Water content (%)	Organic content (%)
Awakiriapa Bay	4.1	14.7	87.1	35.7	66	5.9
Wilson Bay	2.6	10.9	74.4	26.3	74	6.6
Te Kouma	3.3	36.1	192.6	73.0	50	3.7

## 4.2.2 Sequential extraction

### Dissolved sulfide measurement

I measured the concentration of dissolved porewater sulfide with an  $\text{H}_2\text{S}$  microelectrode (Unisense A/S, described in Chapter 2) inserted 1 cm into the freshly exposed surface of the sediment core.

The microelectrode detects the partial pressure of  $\text{H}_2\text{S}$  gas, which is only one component of the total dissolved sulfide concentration. Dissolved sulfide is present in a pH dependent equilibrium between  $\text{H}_2\text{S} \rightleftharpoons \text{HS}^- \rightleftharpoons \text{S}^{2-}$ . The total sulfide concentration can be calculated from the  $\text{H}_2\text{S}$  measurement using the following equation:

$$[\text{S}_{\text{tot}}^{2-}] = [\text{H}_2\text{S}] \times \left( 1 + \frac{K_1}{[\text{H}_3\text{O}^+]} \right) \quad (4.1)$$

where  $[\text{S}_{\text{tot}}^{2-}]$  is the total sulfide concentration,  $[\text{H}_2\text{S}]$  is the measured  $\text{H}_2\text{S}$  concentration,  $K_1$  is the dissociation constant of  $\text{H}_2\text{S}$  in seawater ( $10^{-\text{p}K_1}$ ), and  $[\text{H}_3\text{O}^+]$  is the concentration of hydrogen ions, i.e.  $10^{-\text{pH}}$  (Jeroschewski, 1996).

Millero, Plese, and Fernandez (1988) derived the following equation for calculating the  $pK_1$  of  $H_2S$  in seawater as a function of temperature ( $T$ , in Kelvin) and salinity ( $S$ , in parts per thousand):

$$pK_1 = -98.080 + \frac{5765.4}{T} + 15.04555 \times \log_e(T) + (-0.1570 \times S^{0.5}) + (0.0135 \times S) \quad (4.2)$$

I measured the porewater pH using a glass microelectrode that had a 50  $\mu m$  tip diameter (Unisense A/S) and an open-ended reference electrode containing Ag/AgCl in a gel-stabilized electrolyte (Unisense A/S). To avoid contaminating the tip of the reference electrode, I placed it in a beaker of tap water and connected it to the sediment by means of a salt bridge. I prepared a “U” shaped bridge by bending a 1 mm diameter glass capillary after heating over a flame. I then filled the bridge with a 3 M KCl solution containing 1% agarose to make a gel. The bridge was stored in a 3 M KCl solution when not in use.

### AVS measurement

Immediately after measuring the dissolved sulfide concentration, I sliced and homogenised a 2 cm section from the sediment core for AVS analysis. I took approximately 1 g of the homogenised sediment and added it to a 40 mL glass vial filled with 30 mL HCl (1 M, Ajax Finechem UNIVAR) that was deoxygenated by purging with nitrogen for  $\geq 20$  minutes. The vial was closed with an airtight lid and briefly shaken. I weighed the HCl filled vial before and after adding sediment to determine the mass of sediment used in the extraction. Four replicates were analysed for each sediment layer. I left the vials to stand while sectioning the remainder of the core. Sectioning one core was completed within one hour. I measured the concentration of  $H_2S$  in the acid extract using an  $H_2S$  microelectrode.

To prepare the sample for the next stage of analysis, I decanted as much of the HCl from each vial as possible without losing any of the sediment. I combined the four



replicates from each layer into a 50 mL plastic centrifuge tube, centrifuged the tubes at 1500 RPM for 5 minutes, decanted the liquid, and washed the samples with deionised water. I centrifuged and washed the samples with deionised water twice more and then centrifuged the samples before drying them in an oven overnight at 60 °C.

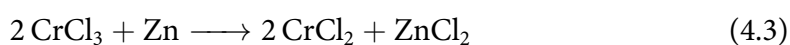
### Chromium reducible sulfide measurement

The final stage of the sequential extraction procedure was an acidic chromium reduction. I performed this extraction following the methods of Canfield et al. (1986). The extractant, chromium(II), is highly reducing with a reduction potential of  $-0.41$  V and extracts pyrite, elemental sulfur, and AVS but not organic sulfur or sulfate sulfur from marine sediments. Because I previously extracted AVS from this sediment, this extraction removed pyrite, elemental sulfur, and the remaining greigite (CRS<sub>s</sub>).

To extract CRS<sub>s</sub>, I added sediment to a round-bottomed flask containing the chromium(II) solution that had been deoxygenated with argon (Figure 4.2). The solution was heated to liberate sulfur as H<sub>2</sub>S gas, which was collected in a zinc acetate trapping solution.

A chromium(II) solution (CrCl<sub>2</sub>) can only be prepared by reducing a solution of CrCl<sub>3</sub>. The CrCl<sub>2</sub> solution is susceptible to oxidation and must be prepared fresh every 2–3 days.

I prepared the 1 M CrCl<sub>3</sub> solution by dissolving 42.63 g CrCl<sub>3</sub> · 6 H<sub>2</sub>O (Acros Organics) into cold HCl (160 mL, 0.5 M). Chromium(III) chloride (CrCl<sub>3</sub>, blue) was reduced to chromium(II) chloride (CrCl<sub>2</sub>, green) using a Jones reductor as described below, following the reaction in Equation 4.3.



I prepared the Jones reductor following the methods of Vogel (1989): I covered ~300 g of granulated zinc (20-mesh, ~800 µm particle size; Acros Organics) with 2% HgCl<sub>2</sub>

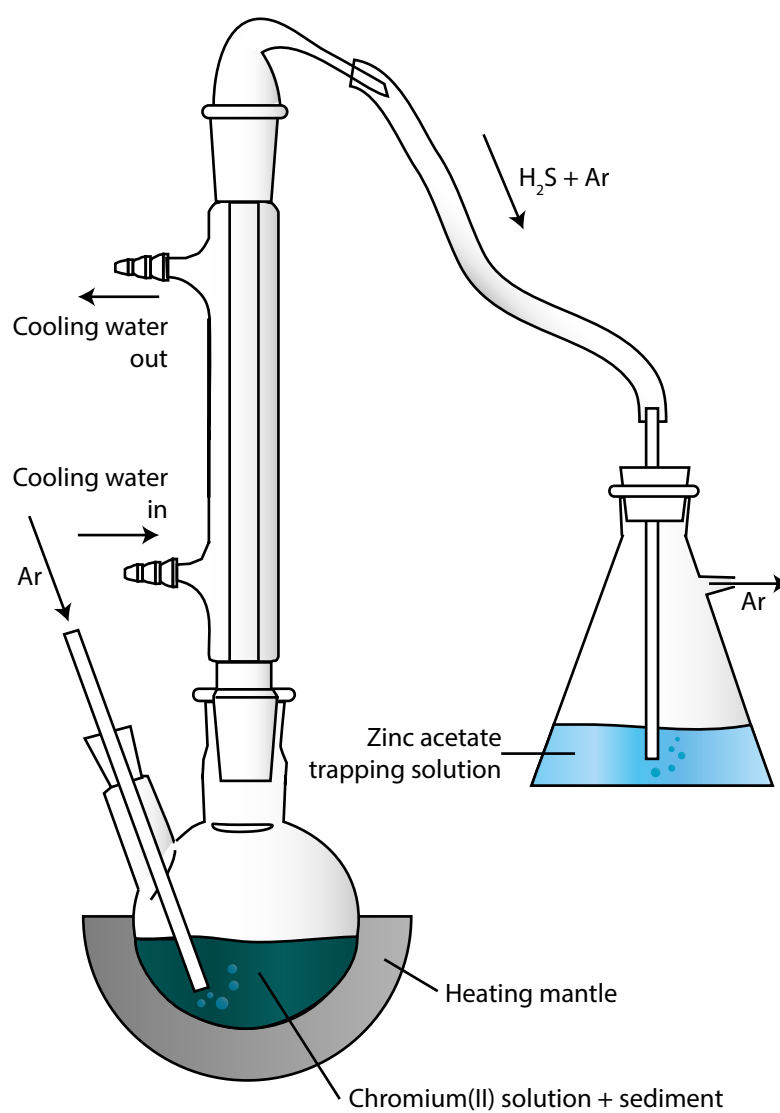


**Figure 4.2:** Schematic diagram showing the laboratory equipment setup for extracting chromium reducible sulfides from marine sediment. The acidic chromium(II) chloride solution converts sedimentary mineral sulfides into hydrogen sulfide gas (H<sub>2</sub>S), which is carried to the zinc acetate trapping solution by the carrier gas, argon (Ar).

(Ajax Finechem UNIVAR) solution in a beaker and stirred for 10 minutes. I decanted the  $\text{HgCl}_2$  solution and rinsed the remaining zinc three times with deionised water. The previously dull zinc had a bright silvery lustre, confirming the success of the amalgamation process.

To assemble the Jones reductor, I placed glass wool at the base of a 50 mL burette, and filled the burette with the amalgamated zinc, leaving an 8 cm space at the top (Figure 4.3). I then washed the zinc with 500 mL deionised water. Gentle suction was used to increase the flow speed for all solutions run through the burette at a speed less than  $100 \text{ mL min}^{-1}$ . The Jones reductor can be stored in this state, but the water level must remain above the zinc to avoid formation of basic salts by atmospheric oxidation, which corrode the reducing surface.

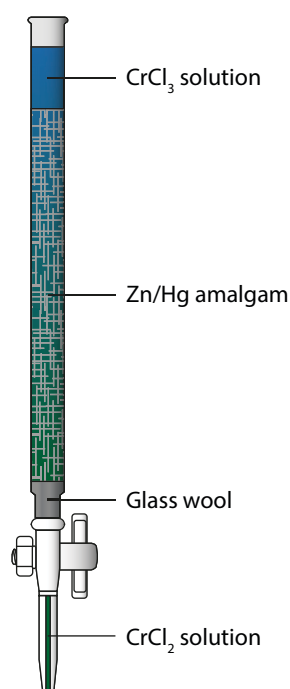


**Figure 4.3:** A Jones reductor made using a zinc/mercury amalgam in a burette to reduce chromium(III) chloride ( $\text{CrCl}_3$ , blue) to chromium(II) chloride ( $\text{CrCl}_2$ , green). The flow speed of the  $\text{CrCl}_2$  solution was increased using gentle suction and collected in a Büchner flask (not shown).

The zinc must be activated before use, this was achieved by flushing the burette with  $\text{HCl}$  (100 mL, 1 M), ensuring the zinc was always covered by some of the solution.

After activating the zinc, I added the  $\text{CrCl}_3$  solution to the burette. The reduction process was confirmed visually as the  $\text{CrCl}_3$  was blue, and  $\text{CrCl}_2$ , green. The reduced

$\text{CrCl}_2$  solution was collected in a Büchner flask and transferred to plastic 60 mL syringes to protect it from exposure to the atmosphere and allow accurate dispensing. To prepare the Jones reductor for storage, I flushed the burette with HCl (150 mL, 1 M) followed by deionised water (200 mL). The reductor was stored with the water level at least 3 cm above the layer of zinc.

I prepared the zinc acetate trapping solution by dissolving 40 g zinc acetate (dehydrate, Ajax Finechem UNIVAR) into 2 L deionised water. The pH of this solution was buffered by the addition of 0.5 mL glacial acetic acid.

I extracted  $\text{CRS}_s$  from the previously AVS extracted and dried marine sediment by adding ~0.5 g to a two-necked flask containing 5 mL 95% ethanol. After adding 10 mL of trapping solution to the Büchner flask, the assembled system (Figure 4.2) was then purged with argon for 20 minutes to remove oxygen. To the deoxygenated round-bottomed flask, I added 10 mL chromium(II) chloride solution and 5 mL concentrated HCl. I then heated the flask and left it to gently boil for 30 minutes; the total extraction time was 45 minutes. I had four replicate systems assembled, which allowed me to extract four samples simultaneously. During the extraction, the trapping solution turned milky white, indicating the formation of zinc sulfide.

There are many methods for analysing the trapped sulfide solution, including colorimetry, gravimetry, potentiometry, and photoionisation. A comparative study revealed that the colorimetric method by Cline (1969) was the preferred method because of its simplicity and high precision (Lasorsa & Casas, 1996). Low concentrations of sulfide are determined by the addition of a reagent that forms methylene blue in the presence of sulfur. The more sulfur that is present in the sample, the more intense the blue colour. I used a reagent containing N,N-dimethyl-*p*-phenylenediamine sulfate and ferric chloride ( $\text{FeCl}_3 \cdot 6 \text{H}_2\text{O}$ ); this is referred to as the mixed diamine reagent or MDR. The concentrations of the two components in the reagent are dependent on the sulfide concentration range being measured. I prepared three reagents, to cover three sulfide concentration ranges as

presented in Table 4.4, and stored them in dark glass-stoppered bottles in a refrigerator.

**Table 4.4:** Amount of N,N-dimethyl-*p*-phenylenediamine sulfate (diamine) and ferric chloride ( $\text{FeCl}_3 \cdot 6 \text{H}_2\text{O}$ ) dissolved into 500 mL of 50% HCl in deionised water (Cline, 1969). This mixed diamine reagent was used to determine the concentration of sulfide in the zinc acetate trapping solution from the reduced chromium extraction of marine sediment. The two higher concentration ranges require dilution of the sample after the colour has developed. A dilution factor of 2:25 means 2 mL of sample diluted with 23 mL deionised water.

Sulfide concentration range ( $\mu\text{mol L}^{-1}$ )	Diamine (g)	$\text{FeCl}_3 \cdot 6 \text{H}_2\text{O}$ (g)	Dilution factor
1–40	2	3	1:01
40–250	8	12	2:25
250–1000	20	30	1:50

I established a three-point calibration curve for the colorimetric method with freshly prepared sulfide standards for each concentration range. To prepare the standards ranging from 5–1000  $\mu\text{mol S}^{2-} \text{L}^{-1}$ , I added aliquots of a stock solution of  $\text{Na}_2\text{S} \cdot 9 \text{H}_2\text{O}$  (0.1 M) to 5 mL deoxygenated sulfide trapping solution. I determined the stock solution sulfide concentration by iodometric titration using standard iodine (0.0125 M) and sodium thiosulfate (0.0125 M) solutions (Vogel, 1989). I added 0.4 mL of the appropriate concentration range MDR to the standard and left it in the dark for 20 minutes to allow the colour to develop. The two higher concentration ranges require dilution of the sample after the colour development. If necessary, I diluted the colour-developed standard according to Table 4.4 and then transferred some of the diluted solution to a polycarbonate cuvette with a 1-cm path length. I determined the maximum absorption wavelength to be 666 nm by running a full wavelength scan from 400–800 nm in a UV-Visible spectrophotometer (Ultrospec 7000, GE Healthcare Life Sciences). All further analyses were single wavelengths scans at 666 nm. I established calibration curves for each of the three sulfide concentration ranges by correlating the concentration of the sample with the absorbance at 666 nm. Calibration was repeated monthly, or whenever a new MDR was prepared.

To determine which MDR range to use for the CRS extracted samples, I visually estimated the opacity of the trapping solution; samples were most commonly within the 250–1000  $\mu\text{mol L}^{-1}$  range. I added 0.4 mL of the appropriate range MDR solution to a beaker containing a 5 mL sample of the sulfide trapping solution. Samples were analysed in the same manner as the standards: after 20 minutes of colour development in the dark, I diluted the sample if necessary, transferred it to a polycarbonate cuvette (1 cm path length), and measured the absorbance at 666 nm. The concentration of the sample was then calculated from the previously established calibration curve.

If the measured sulfur concentration was outside of the previously estimated range, I repeated the above process with MDR for the correct concentration range.

### 4.2.3 AVS extraction conditions

I extracted marine sediments under three different conditions varying the acid used and the acid concentration to investigate whether a stronger extraction resulted in a more linear (less curved) correlation between sediment colour intensity and the AVS concentration. My rationale for this approach come from a discussion in Chapter 2 where I suggest that the curvature of the AVS/colour correlation is linked the non-quantitative AVS extraction procedure.

I prepared three cold acid extraction solutions: 1 M HCl, 6 M HCl with 15%  $\text{SnCl}_2$  as a reducing agent to reduce interference from  $\text{Fe}^{3+}$ , and 0.5 M  $\text{H}_2\text{SO}_4$  with 20%  $\text{TiCl}_3$  as a reducing agent to reduce interference from  $\text{Fe}^{3+}$ . The reducing agent was added to the deoxygenated acid immediately before use.

I collected eight sediment cores in March 2012 from the sampling site at Awakiriapa Bay, Waiheke Island, New Zealand (Figure 3.1). The cores were collected and stored in a laboratory in the same manner as previously described. I sectioned the cores one at a time following the scheme in Figure 3.2 to sample sediment from five different depths. I determined the sediment water content for each sampling depth by weight loss after drying at 90 °C for 24 hours.

I extracted AVS from the sediment as described above; briefly, I took ~1 g wet sediment and added it to a 40 mL glass vial containing 30 mL deoxygenated acid. The vial was weighed before and after addition of the sediment to accurately determine the mass of sediment used. This was repeated four times per slice, per method, to create pseudo-replicates, i.e.  $4 \times 3$  vials per sediment sample. After a one hour extraction, I determined the concentration of AVS in the acid extract using the previously described  $\text{H}_2\text{S}$  microelectrode.

#### 4.2.4 Statistical analyses

I calculated the mean sulfide concentration from the pseudo-replicate measurements for each sample. Outliers from replicates were identified using Grubb's outlier test and subsequently removed. The replicate mean values were used for all further statistical analyses. I performed all statistical analyses on both the wet weight and dry weight values using the software R (R Core Team, 2013). As  $\text{CRS}_s$  can only be presented in dry weight, all sulfide concentrations are presented in dry weight for consistency. All presented errors are the 95% confidence interval. I determined differences between means, sites, or methods using ANOVA or ANCOVA, and where suitable, posthoc Tukey contrasts.

When plotting AVS against sediment colour intensity, I placed colour intensity on the x-axis as the error associated with this measurement is very small; over 100,000 pixels are averaged to obtain the grey value, whereas only four measurements are averaged to obtain the AVS concentration. This configuration will produce the most representative regression using optimised least squares.

I fit linear and quadratic models through each data set to identify correlations. To determine which model was the best fit, I used the Bayesian Information Criterion (BIC; Schwarz, 1978). The BIC adds a penalty value for each parameter in the model and returns a log-likelihood value; a lower BIC value indicates a better fit.

## 4.3 Results

### 4.3.1 Sequential extraction

#### Dissolved porewater sulfide

I only detected porewater  $\text{H}_2\text{S}$  at the deepest measurement (80 mm) in cores 1 and 2. After converting the  $\text{H}_2\text{S}$  concentrations to total sulfide (Equation 4.1), their concentrations were 0.09 and 0.04  $\mu\text{mol S}^{2-}$  per gram of dry sediment, respectively.

#### Acid volatile sulfide (AVS)

The correlation between sediment colour intensity and AVS concentration measured using 1 M HCl at the three different sites in this study were strong and best described by quadratic fits (Figure 4.4, Table 4.5). The fit at each site had a significantly different slope as indicated by the significant interaction between the Grey and Site predictors (Table 4.6).

#### Sequentially extracted chromium reducible sulfide ( $\text{CRS}_s$ )

On average, 35 times more  $\text{CRS}_s$  was extracted from a sediment sample than AVS. Unlike the AVS extraction, however,  $\text{CRS}_s$  concentrations did not correlate strongly with the sediment colour intensity. Wilson Bay was the only site where sediment colour intensity correlated with  $\text{CRS}_s$  concentration ( $[\text{CRS}_{\text{WB}}] = -0.28 \times \text{Grey} + 62.63$ ,  $p = 0.03$ ,  $R^2 = 0.15$ ). The  $\text{CRS}_s$  extraction data are presented in Figure 4.5 in addition to the AVS extraction data for context.



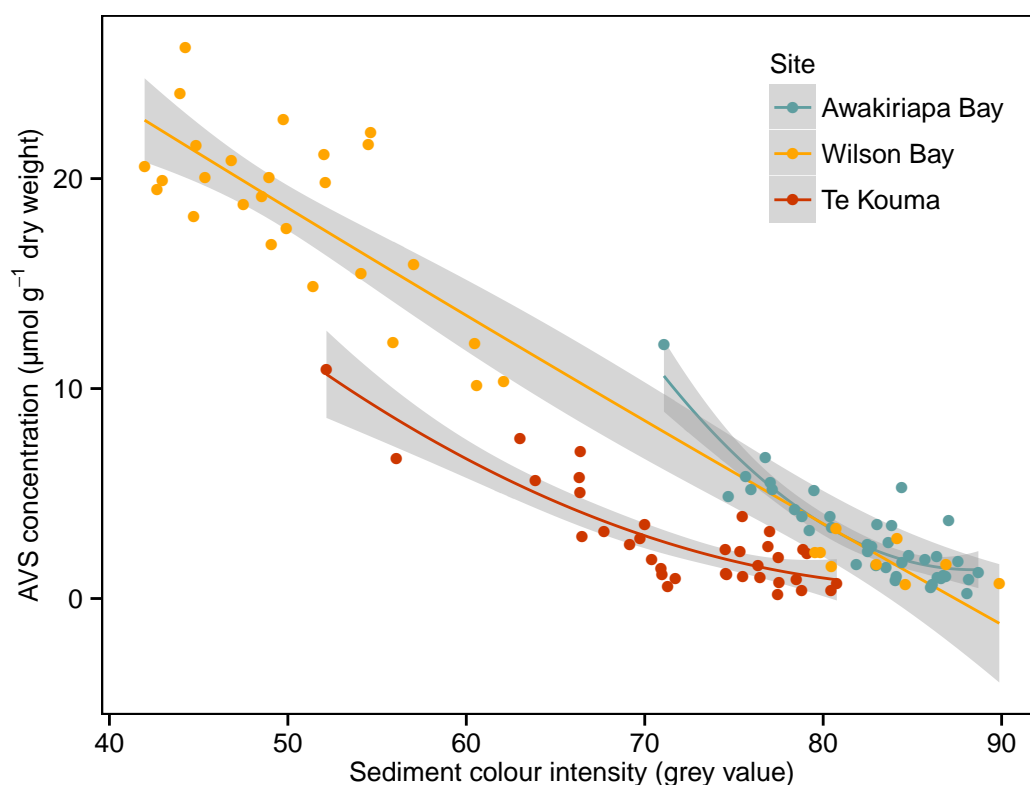


**Figure 4.4:** Sediment colour intensity–AVS concentration correlation at three sites in the Hauraki Gulf, New Zealand. AVS was extracted using 1 M HCl. The colour intensity of black is 0 and that of white is 100. Each coloured line is a quadratic fit that best describes the data for each site. The 95% confidence interval for each fit is shown by the grey shaded area.

**Table 4.5:** Terms for the quadratic fits that best describe the correlation between sediment colour intensity and AVS concentration at three sites in the Hauraki Gulf, New Zealand. The data and fits are displayed in Figure 4.4.

	$x^2$	$x$	Intercept	$R^2$
Awakiriapa Bay	−12.05	3.90	2.96	0.79
Wilson Bay	−44.73	1.87	13.89	0.91
Te Kouma	−11.68	2.92	2.68	0.74

**Table 4.6:** ANCOVA results to determine whether grey value (Grey) and the site (Site) are significant predictors for AVS concentration [AVS] from three locations in the Hauraki Gulf, New Zealand. Linear model:  $[AVS] = (Grey + Grey^2) + Site + (Grey + Grey^2):Site$ ;  $R^2 = 0.95$ .

	Df	Sum Sq	Mean Sq	F value	Pr(>F)
Grey (quadratic)	2	5107.43	2553.72	832.72	<0.001
Site	2	316.96	158.48	51.68	<0.001
Grey (quadratic):Site	4	62.06	15.51	5.06	<0.001
Residuals	102	312.81	3.07		

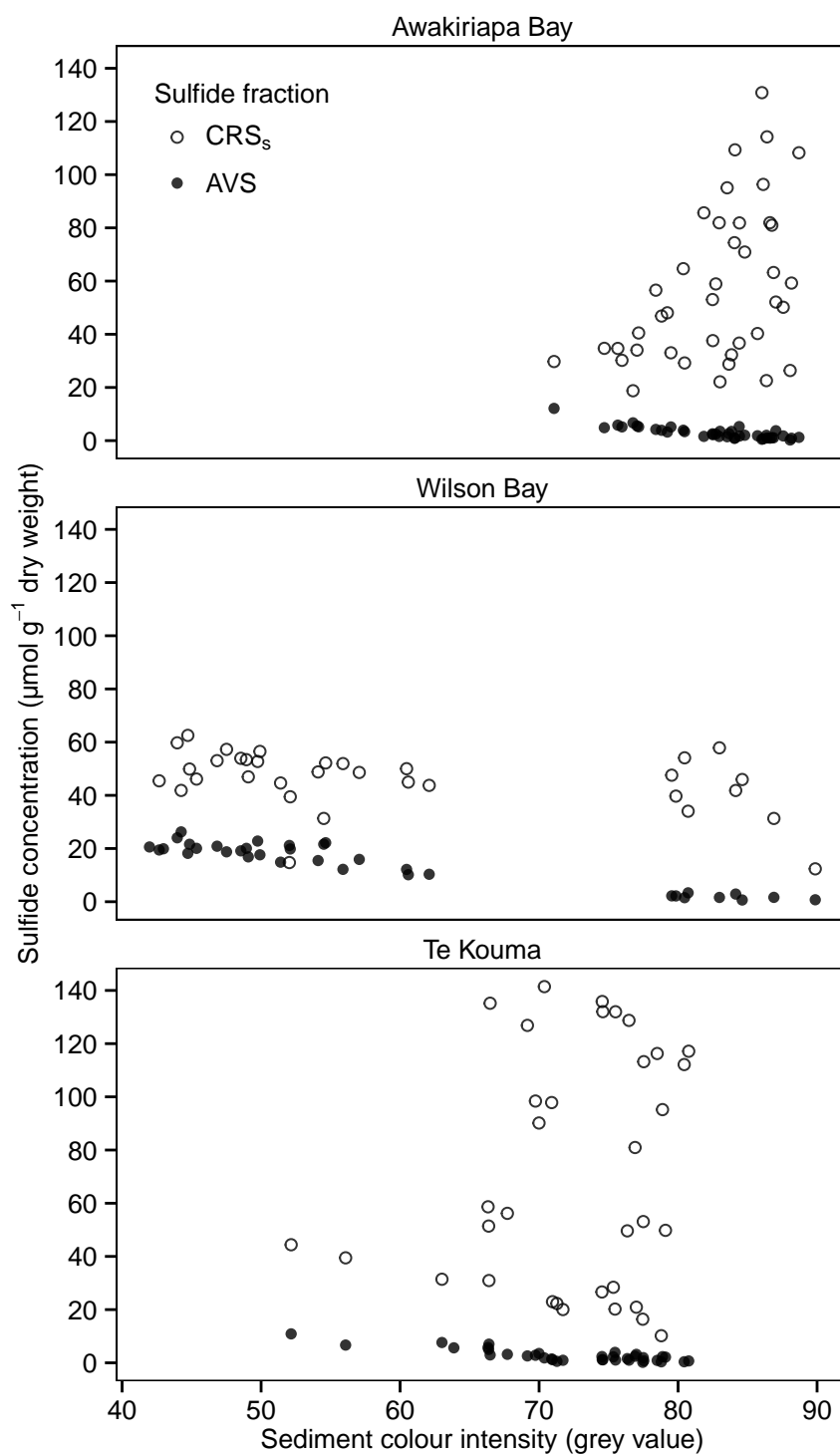


**Figure 4.5:** Relationships between sediment colour intensity and sulfide concentration for three sites in the Hauraki Gulf, New Zealand.

### Total reduced sulfide

I calculated total reduced sulfides as the sum of the AVS and CRS<sub>s</sub> fractions (Figure 4.6). The distribution of the sediment colour intensity–total reduced sulfide data points are very similar to that of the CRS<sub>s</sub> data points. This is because, on average, the AVS concentration was 35 times less than the corresponding CRS<sub>s</sub> value, and therefore, AVS didn't have a large influence on the total reduced sulfide concentration. Wilson Bay was the only site that had a significant total reduced sulfide/colour correlation,  $[TRS_{WB}] = -0.79 \times \text{Grey} + 107$ ,  $p < 0.001$ ,  $R^2 = 0.62$ .

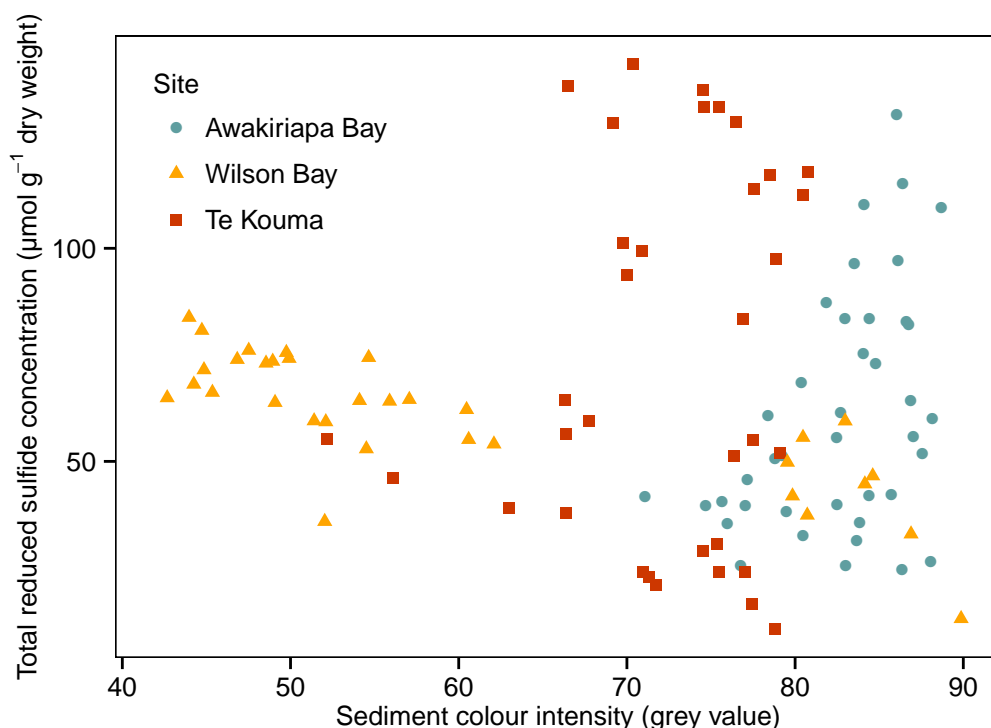


**Figure 4.6:** Relationship between sediment colour intensity and the total reduced sulfide concentration for three sites in the Hauraki Gulf, New Zealand. TRS is the sum of the acid volatile sulfide (AVS) and sequentially extracted chromium reducible sulfide (CRS<sub>s</sub>) fractions.

### Site differences in AVS and CRS<sub>s</sub> proportions

I investigated the differences in the AVS and CRS<sub>s</sub> concentrations at each site and found that the ranges of CRS<sub>s</sub> and AVS concentrations at Awakiriapa Bay and Te Kouma were similar but in contrast to those at Wilson Bay (Figure 4.7). The range of

CRS<sub>s</sub> concentrations at Awakiriapa Bay and Te Kouma were large, 112 and 131  $\mu\text{mol g}^{-1}$  respectively, whereas the range of CRS<sub>s</sub> concentrations at Wilson Bay was much smaller at 60  $\mu\text{mol g}^{-1}$ . This difference was reversed for AVS concentrations, that is, the AVS concentration range at Awakiriapa Bay and Te Kouma was small (12 and 11  $\mu\text{mol g}^{-1}$ , respectively) and the AVS concentration range at Wilson Bay was larger (26  $\mu\text{mol g}^{-1}$ ).

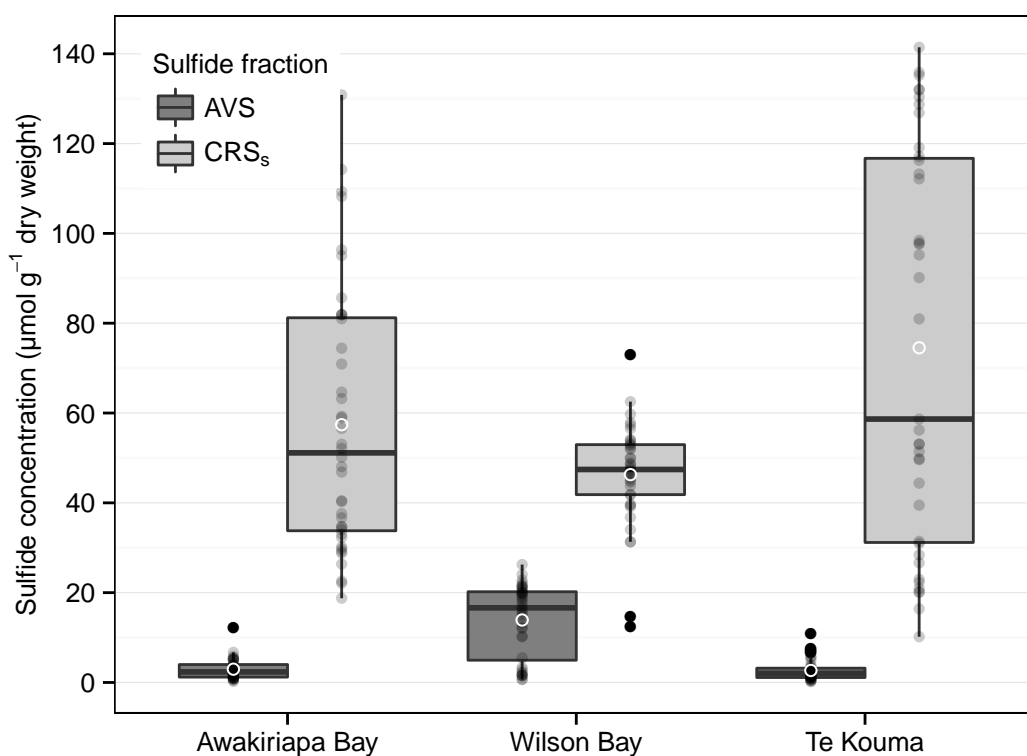


**Figure 4.7:** Sediment acid volatile sulfide (AVS) and sequentially extracted chromium reducible sulfide (CRS<sub>s</sub>) concentrations from three sampled sites in the Hauraki Gulf, New Zealand. The boxes show the upper, middle, and lower quartile of the data. Black vertical lines indicate the range of the data. Outliers (1.5 times the interquartile range) are plotted separately as black points. The overlaid semi-transparent points are the individual measured sulfide concentrations. The mean is indicated by the white circle.

I used ANOVA to determine whether the mean AVS and CRS<sub>s</sub> concentrations at each site were different to each other. This analysis revealed that the mean AVS concentration at Wilson Bay was higher than that of Awakiriapa Bay and Te Kouma (Tables 4.7 and 4.8).

**Table 4.7:** Summary of ANOVAs to determine differences in the AVS and CRS<sub>s</sub> concentrations between the sites Awakiriapa Bay (AB), Wilson Bay (WB), and Te Kouma (TK). Post-hoc Tukey contrasts are presented in the final column for  $p < 0.05$ .

	Df	Residuals	F Value	Pr(>F)	R <sup>2</sup>	Tukey
AVS	2	117	64.28	<0.001	0.52	WB > AB, TK
CRS <sub>s</sub>	2	114	7.99	<0.001	0.12	TK > AB, WB

**Table 4.8:** Mean AVS and CRS<sub>s</sub> concentrations and the mean AVS:CRS<sub>s</sub> ratios at three sites in the Hauraki Gulf, New Zealand. The 95% confidence interval of the mean is shown in parentheses;  $n = 40$ .

	AVS	CRS <sub>s</sub>	AVS:CRS <sub>s</sub> ratio
Awakiriapa Bay	3.0 (0.7)	57 (9)	0.05
Wilson Bay	13.9 (2.6)	46 (4)	0.30
Te Kouma	2.7 (0.7)	75 (14)	0.04

### Changes in the relative proportions of AVS and CRS<sub>s</sub> with sediment depth

To obtain sediment from each site with a range of colours, I exploited the natural vertical variation in the colour of the sediment column. That is, I sampled sediment at different depth in the sediment column. Such sampling scheme introduced sampling depth as an unintended additional parameter to the study and the effects of this can be seen in the depth profiles shown in Figure 4.8.

The depth profiles revealed that the mean AVS concentration at Awakiriapa Bay and Te Kouma slightly increased at 5 cm depth, and then decreased with increasing depth. The mean CRS<sub>s</sub> concentration at both of these sites increased with depth in the sediment. In contrast, the mean AVS concentration at Wilson Bay increased up to 11 cm and the mean CRS<sub>s</sub> concentration did not change to a depth of 11 cm but increased below this depth.

Because the AVS and CRS<sub>s</sub> profiles at Wilson Bay differ from the profiles at the two other sites, the proportion of AVS to CRS<sub>s</sub> (AVS:CRS<sub>s</sub>) also differed (Figure 4.9). All sites have an AVS:CRS<sub>s</sub> ratio of ~0.1 at 2 cm sampling depth. Deeper in the sediment, the AVS:CRS ratio at Wilson Bay is >0.25, whereas the ratio at Awakiriapa Bay and Te Kouma, after an initial increase at 5 cm, decreases to <0.01.

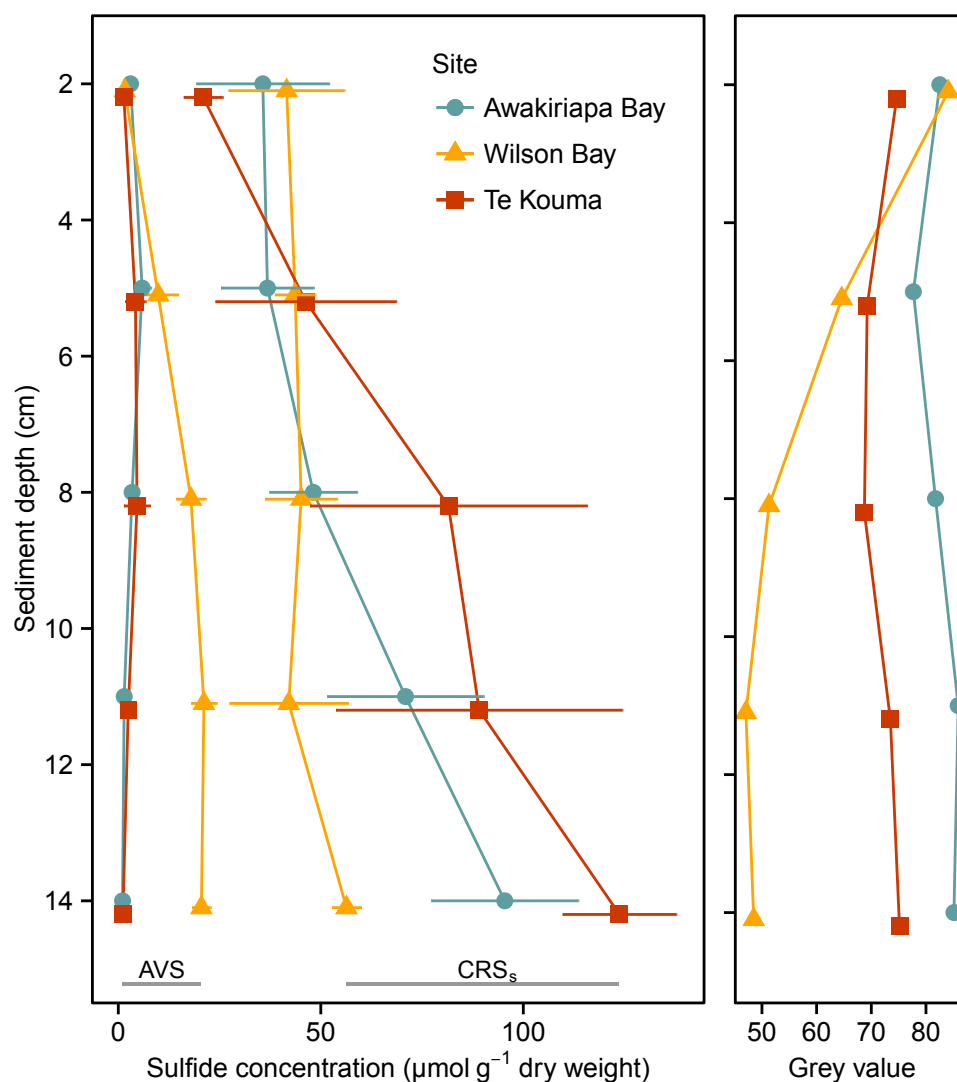


**Figure 4.8:** Mean sediment concentrations of acid volatile sulfide (AVS, left), chromium reducible sulfide (CRS<sub>s</sub>, middle), and grey value (right) by depth for three sampled sites in the Hauraki Gulf, New Zealand ( $n = 8$ ). Error bars show the 95% confidence interval of the mean.

### 4.3.2 Extraction methods

The choice of acid and its concentration had a significant effect on the concentration of AVS extracted from the sediment at Awakiriapa Bay (Figure 4.10, Table 4.9).

Although each method extracted a different AVS concentration from the sediment, the slope of the AVS/colour correlation for each method was the same. This is indicated by the non-significant interaction between the Grey and Method terms (Table 4.9). A quadratic fit best described the data for all methods (Table 4.10).

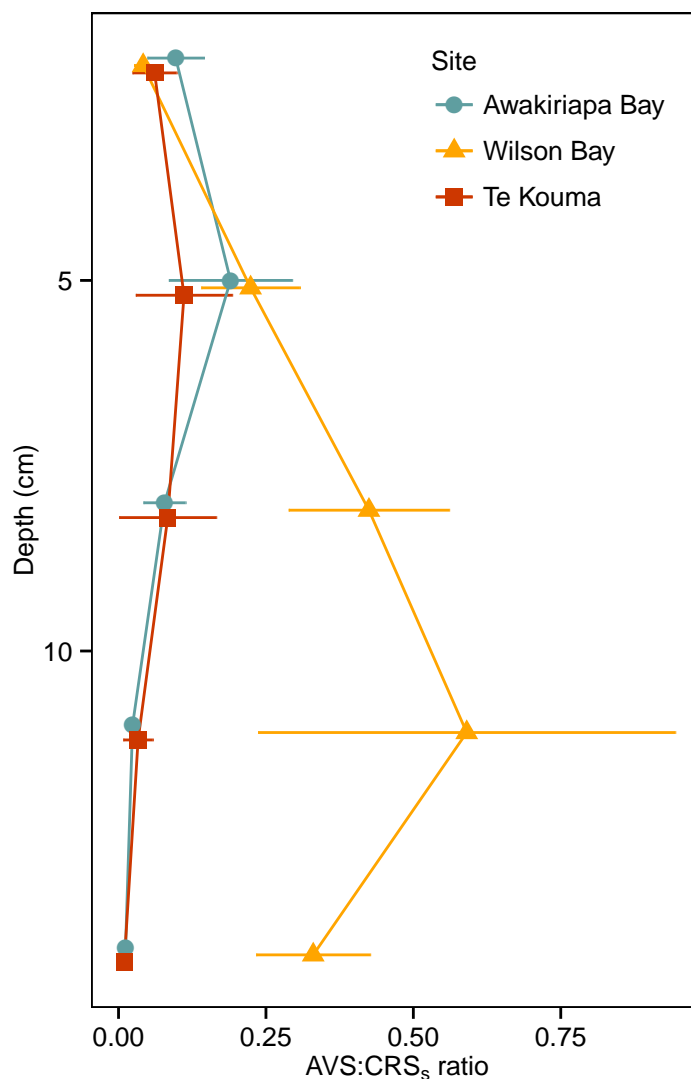


**Figure 4.9:** Mean ratio of acid volatile sulfide (AVS) to sequentially extracted chromium reducible sulfide (CRS<sub>s</sub>) concentration from three sites in the Hauraki Gulf, New Zealand ( $n = 8$ ). A low ratio indicates a greater proportion of CRS<sub>s</sub>. Sediment depth is the average depth of the analysed sediment slice. Error bars show the 95% confidence interval of the mean.

A post-hoc Tukey test revealed a significant difference between all methods, in the order  $6 \text{ M HCl} > 0.5 \text{ M H}_2\text{SO}_4 > 1 \text{ M HCl}$ , for  $p < 0.001$ . This is at variance with the sulfide mineral extraction efficiencies published by Cornwell and Morse (1987), which would have resulted in an order of  $0.5 \text{ M H}_2\text{SO}_4 > 6 \text{ M HCl} > 1 \text{ M HCl}$ .

To further investigate the differences between methods, I calculated the difference in AVS concentration after sediment extraction with  $6 \text{ M HCl}$  and  $1 \text{ M HCl}$ . There was a weak relationship between the grey value of the sediment and the difference in AVS concentration using the two methods (Figure 4.11). The AVS concentration difference

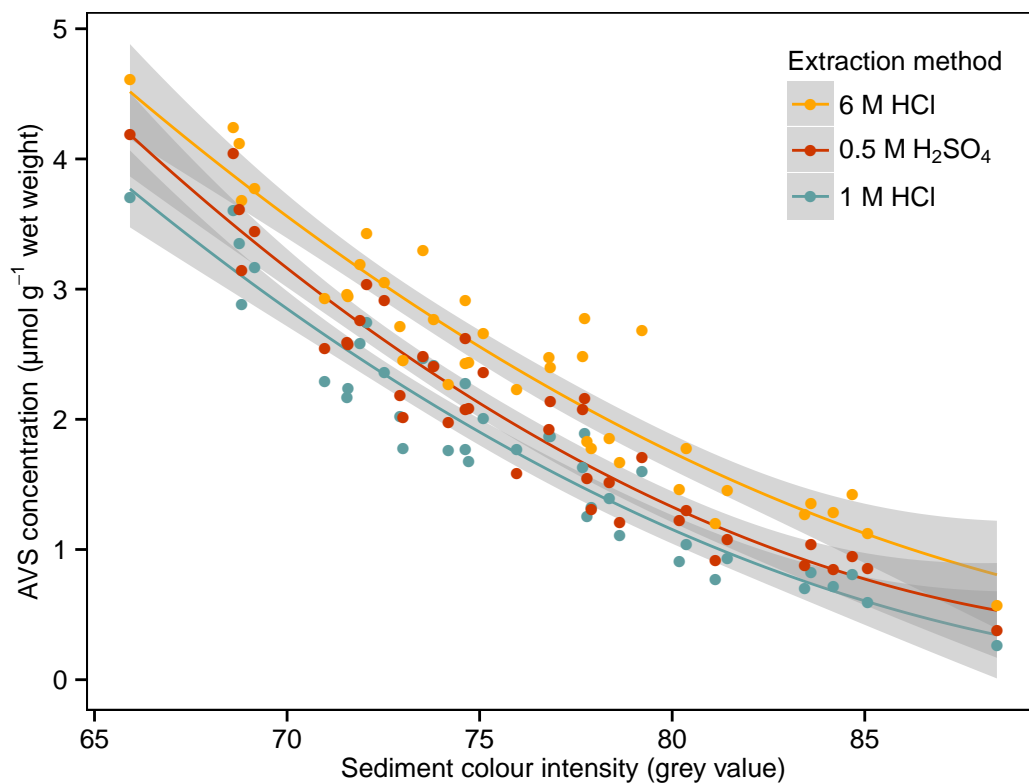


**Figure 4.10:** Correlations between sediment colour intensity and AVS concentration for three different acid extraction methods. Sediment from Awakiriapa Bay, Waiheke Island, New Zealand was extracted in 6 M HCl + SnCl<sub>2</sub>, 0.5 M H<sub>2</sub>SO<sub>4</sub> + TiCl<sub>3</sub>, or 1 M HCl. The best fit through the data for each method is denoted by the solid lines and the 95% confidence interval for each fit is shown by the grey shaded area.

between the two methods decreased with increasing grey value, i.e. decreasing AVS concentration. A decrease of 10 grey values resulted in an increase of 0.5 mol L<sup>-1</sup> difference between the two methods. The difference in extracted AVS concentration between the two methods was higher at higher AVS concentrations.



**Table 4.9:** Full factorial ANCOVA model used to determine whether different combinations of acids and concentrations (Method) extracted different amount of AVS from marine sediment (AVS concentration =  $[\text{Grey} + \text{Grey}^2] + \text{Method} + [\text{Grey} + \text{Grey}^2]:\text{Method}$ ). Grey value was used as the covariate. The  $R^2$  of the model was 0.93.

	Df	Sum Sq	Mean Sq	F value	Pr(>F)
Grey value (quadratic)	2	901.52	450.76	651.93	<0.001
Method	2	80.95	40.47	58.54	<0.001
Grey:Method	4	1.83	0.46	0.66	0.62
Residuals	111	76.75	0.69		

**Table 4.10:** Quadratic model terms and the  $R^2$  values for the fits that best describe the correlation between sediment colour intensity and AVS concentration for three different AVS extraction methods. The data and fits are displayed in Figure 4.10.

Method	$x^2$	$x$	Intercept	$R^2$
6 M HCl	0.015	−2.817	135.99	0.93
0.5 M H <sub>2</sub> SO <sub>4</sub>	0.018	−3.228	150.01	0.92
1 M HCl	0.014	−2.615	124.36	0.93

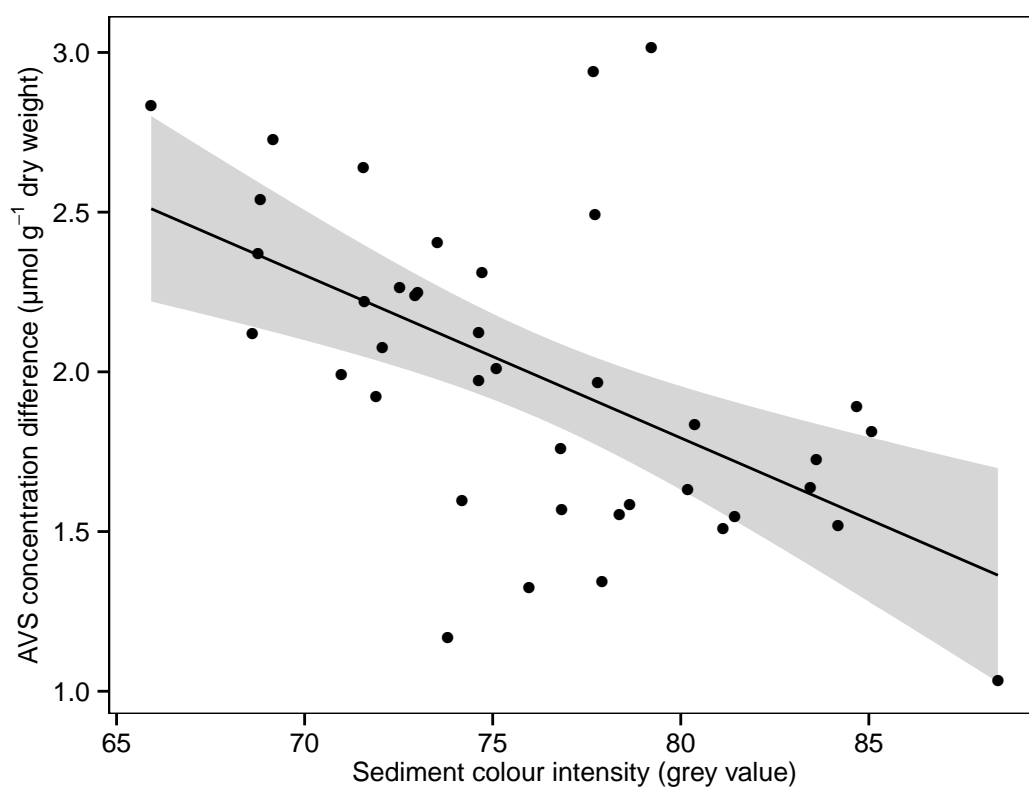


**Figure 4.11:** Difference in the amount of AVS extracted from marine sediment when using 6 M HCl and 1 M HCl. The line of best fit through the data is indicated by the black line and the 95% confidence interval of the fit is indicated by the grey shading. Difference =  $-0.05 \times \text{grey} + 5.87$ ,  $p < 0.001$ ,  $R^2 = 0.31$ .

## 4.4 Discussion

### 4.4.1 Relative proportion of sulfide pools at different locations and sediment depths

The most significant difference between the three sites was in the sediment AVS:CRS<sub>s</sub> ratio (Figure 4.7). The proportion of AVS:CRS<sub>s</sub> appears to be a function of the deposition environment and sediment depth.

This difference in AVS:CRS<sub>s</sub> can be most clearly observed in Wilson Bay sediment, which had high AVS:CRS<sub>s</sub> ratios at depths >5 cm (Figure 4.9). Unlike sediment in Awakiriapa Bay and Te Kouma, where the AVS:CRS<sub>s</sub> ratio decreased with depth, the ratio at Wilson Bay increased with depth. Samples with the highest measured CRS<sub>s</sub> concentration were collected from the greatest sediment depths. Despite their high sulfide concentration, they were not darkly coloured, that is, they did not have low colour intensities (Figure 4.5).

Such high AVS:CRS<sub>s</sub> ratios in Wilson Bay sediment, even at depth in the sediment, could indicate that the minerals mackinawite and greigite are not being, or have not yet been, converted to the more thermodynamically stable but kinetically slow to form mineral pyrite. Berner (1970) reported that the conversion of FeS to FeS<sub>2</sub> may take up to several years under ideal conditions, that is, in the presence of abundant H<sub>2</sub>S and elemental sulfur.

Multiple factors could be responsible for inhibiting the transformation of mackinawite and greigite into pyrite in the studied sediments, including the age of the overlying mussel farm, the rate of sediment deposition, sediment bioturbation by benthic macrofauna, and the conditions of the deposition environment.

The age of the overlying mussel farm may influence the relative proportion of pyrite as it will determine the length of time sediments have been exposed to elevated rates of organic matter deposition. It is likely that sediment beneath an old mussel farm would

have higher sulfide concentrations than sediment beneath a recently developed farm as more time would have passed for sulfide accumulation to occur. Following this logic, the sediment AVS:CRS<sub>s</sub> ratios should increase at each location in the order: Wilson Bay, Te Kouma, and Awakiriapa Bay, where the mussel farms at these locations were developed in 1999, 1984, and 1980 respectively. This order is not observed in this study as the expected order of Awakiriapa Bay and Te Kouma was reversed; their ratios, however, are similar (Table 4.8).

The rate of organic matter deposition on the sediment is another factor that will influence the AVS:CRS<sub>s</sub> ratio. For example, a sediment sample collected from 10 cm depth at a site with a high rate of organic matter deposition will be more recently deposited (younger) sediment than a sample collected at 10 cm depth from a site with a low rate of organic matter deposition. In addition, Aller (1982) summarised that particle reworking from benthic fauna typically extended up to 10 cm depth from the sediment surface in coastal marine soft sediments. The fauna typically responsible for particle reworking at these depths include crabs, heart urchins, brittle stars, polychaetes, and bivalves (Kristensen et al., 2012). Recently deposited sediment and sediment that has been reworked by macrofauna will likely have a higher AVS:CRS<sub>s</sub> ratio as there would have been insufficient time for pyrite transformation to occur.

The final factor that may influence the sediment AVS:CRS<sub>s</sub> ratio is the condition of the depositional environment. Chamberlain et al. (2001) observed differences in chemical and physical sediment characteristics beneath two mussel farms of similar ages in south-west Ireland and suggested such differences to be a factor of biodeposit dispersion, which is controlled by local current patterns and flow speeds. The Wilson Bay mussel farm is located in the eastern Firth of Thames, a large coastal embayment. Contrastingly, the Awakiriapa Bay and Te Kouma mussel farms are located in relatively sheltered bays. The current patterns and flow speeds will be higher energy in Wilson Bay than the other locations. As a result, the two greatest differences at Wilson Bay will be: (1) wider dispersal of faeces and pseudofaeces from the overlying mussel

farm, and (2) greater resuspension of deposited sediments. Both of these differences will result in an inhibition of the pyrite transformation process, and therefore, the sediment at this location will have a higher AVS:CRS<sub>s</sub> ratio, which is in agreement with the observation at Wilson Bay.

#### 4.4.2 Effects of CRS<sub>s</sub> on the AVS/colour correlation

CRS<sub>s</sub> was the largest reduced sulfide pool in all of the studied sediments. Pyrite, the primary component of CRS<sub>s</sub>, is black, and therefore, will contribute to sediment colour. This may interfere with estimating AVS concentration from sediment colour if the proportion of AVS:CRS<sub>s</sub> were to change after establishing the AVS/colour correlation.

CRS<sub>s</sub> did not correlate with sediment colour intensity at Awakiriapa Bay or Te Kouma, and correlated weakly at Wilson Bay (Figure 4.5). Because CRS<sub>s</sub> was the largest fraction of sulfide in these sediments, there was also no correlation between sediment colour intensity and the total reduced sulfide concentration, that is, the sum of dissolved porewater sulfides, AVS, and CRS<sub>s</sub> fractions (Figure 4.6).

Not all CRS<sub>s</sub> components are colourful and this results in some reduced sulfur components contributing to the CRS<sub>s</sub> sulfur pool, but not the colour intensity of the sediment. This consequently results in a poor correlation between sediment colour intensity and the CRS<sub>s</sub> and total reduced sulfide concentrations. Other sediment components that may weaken the AVS/colour correlation are non-iron metals, which can react with H<sub>2</sub>S to form metal sulfides. For example, zinc sulfide is white, cadmium sulfide is yellow, and manganese sulfide is red-brown. Such other metal sulfides are likely present in much lower concentrations than iron sulfide because of the proportionally lower abundance of the reactive metals (Morse & Luther III, 1999).

One of the main components that contributes to the CRS<sub>s</sub> concentration, but is not black, is elemental sulfur. The presence of elemental sulfur in sediments is essential for

the formation of pyrite. E. T. Allen, Crenshaw, Johnston, and Larsen (1912) elucidated that the reaction of  $\text{H}_2\text{S}$  and ferric iron does not form pyrite, but iron monosulfide (FeS). FeS only proceeded to form pyrite ( $\text{FeS}_2$ ) in the presence of elemental sulfur. Therefore, the concentration of  $\text{FeS}_2$  will be higher and that of FeS will be lower, when elemental sulfur is present in the sediment, than when it is not.

$\text{CRS}_s$  comprises a range of sulfide components, the main sources being greigite remaining after an AVS extraction, pyrite, and elemental sulfur. Quantifying these individual species, however, is difficult. Of these species, greigite is black, pyrite is a brassy colour, and elemental sulfur is yellow. The  $\text{CRS}_s$  components that will interfere with the AVS/colour correlation most strongly will be greigite, and then pyrite, and lastly elemental sulfur because of their decreasing contribution to sediment colour intensity. To account for each of these to establish a strong AVS correlation, one would have to measure each component separately, for example, using advanced X-ray diffraction techniques. For the purpose of monitoring, the use of such techniques is unlikely as they are laborious and expensive.

Predicting the contribution of different sulfide forms to the total sulfide content of marine sediment is complex and unlikely to be useful for establishing an AVS/colour correlation. This further supports the finding of Chapter 3: that a site-specific AVS/colour correlation is necessary to estimate sedimentary AVS concentrations from sediment colour intensity.

#### **4.4.3 Effect of increasing acid strength on the AVS/colour correlation**

The type and concentration of acid used for sediment extraction had no effect on the shape of the AVS/colour correlation. That is, a stronger sediment extraction method did not produce a more linear correlation (Figure 4.10). I suggested in Chapter 2 that the curvature of the AVS/colour correlation occurred because not all sulfide minerals are extracted quantitatively using 1 M HCl. My hypothesis was that increasing the acid

strength would extract a greater proportion of mackinawite and greigite from the sediment, and therefore, have a more linear relationship between the sediment colour and AVS concentration; however, the findings in this chapter do not support this idea.

An explanation for this observation is that the  $\text{CRS}_s$  pool, which includes pyrite, is much larger than the AVS pool. The relatively small increase in extracted mackinawite and greigite achieved using a stronger acid is negligible compared to the much larger unextracted  $\text{CRS}_s$  pool. Thus, the curvature in the AVS/colour correlation is likely a factor of the concentration of the  $\text{CRS}_s$  pool.

Furthermore, high AVS concentrations were typically measured deep in the sediment, which contained the highest concentrations of  $\text{CRS}_s$  (Figure 4.8). A low AVS: $\text{CRS}_s$  ratio would result in a steep AVS/colour correlation slope because a large change in sediment colour would be required for a relatively small change in AVS concentration; that is, the sensitivity of estimating AVS concentration from sediment colour decreases with a decreasing AVS: $\text{CRS}_s$  ratio.

Based on the sulfide mineral extraction efficiencies published by Cornwell and Morse (1987), 0.5 M  $\text{H}_2\text{SO}_4$  should have extracted a greater percentage of the sulfide minerals than 6 M HCl. However, in this study, 0.5 M  $\text{H}_2\text{SO}_4$  extracted less than the 6 M HCl. The reason for such difference is unknown. In the following, I will focus my discussion on the results of the 1 M and 6 M HCl sediment extractions.

The most notable effect of using a stronger acid for sediment extraction was an increase in the concentration of sulfide minerals extracted (Figure 4.10; Tables 4.9 and 4.10). This difference when using different acid concentration highlights the importance of stating the extraction conditions when presenting AVS concentrations.

A less noticeable effect of increasing the acid concentration for extracting sedimentary sulfides was that the difference in AVS concentration when extracted using 1 M and 6 M HCl varied with sediment grey value (Figure 4.11). The ability to detect this

difference using linear models was limited because the 95% confidence intervals for each fit overlapped each other. To investigate this line of enquiry, I used a more simplistic method. I subtracted the AVS concentration derived from the 6 M HCl extraction from that of the 1 M HCl extraction revealed (albeit, weakly) that the difference in AVS concentration between these methods increased at higher AVS concentrations (lower grey values; Figure 4.11).

An explanation for the greater difference between the two extractions at lower grey values (higher AVS concentration) is that each extraction removes a fixed percentage of sulfide minerals; for example, if 1 M HCl extracted 40% of the total sulfide, and 6 M HCl extracted 60% of the total sulfide, the difference between the two methods will be greater at higher AVS concentrations. Further investigation of the sulfide mineral composition in these types of sediments is necessary to confirm this explanation or to identify other possible causes.

## Chapter 5

# Assessing the sulfide footprint of mussel farms with sediment profile imagery: a New Zealand trial

### 5.1 Introduction

Global food production from marine farms has increased on average 6.2% per year since 2000, rising to 90.4 million tons in 2012 (FAO, 2014; Godfray et al., 2010). Of all marine-cultured species, bivalves contributed over 15 million tons. The introduction of new farms to the coast and increased stocking of existing farms necessitates the development of rapid and reliable techniques for the assessment of the effects that such farms have on coastal ecosystems.

Suspended bivalve farms can alter their ecosystems to various degrees depending on the farm's size, age, and stocking density, the seawater column depth and flow regimes, season, and climatic conditions (e.g., Crawford et al., 2003; Grant et al., 1995; Hartstein & Rowden, 2004; Mattsson & Lindén, 1983). Ecosystem effects may arise from mussel feeding habits, farm structures, and activities associated with mussel cultivation and harvest. Documented effects include changes in local hydrodynamics



(Plew, Stevens, Spigel, & Hartstein, 2005), phytoplankton depletion (Duarte, Labarta, & Fernández-Reiriz, 2008; Grant, Bacher, Cranford, Guyondet, & Carreau, 2008), the spread of invasive organisms (Hay, 1990), and the deposition of farm-derived organic matter (mussel faeces and pseudofaeces) (Keeley, Cromey, Goodwin, Gibbs, & Macleod, 2013). The latter can increase the sulfide and ammonium content of the sediment below mussel farms altering the structure and composition of benthic species assemblages (Dahlbäck & Gunnarsson, 1981; Grant et al., 1995; Kaspar, Gillespie, Boyer, & MacKenzie, 1985). Mattsson and Lindén (1983), for example, reported that the dominant heart urchin and brittle star had been replaced by opportunistic polychaetes 15 months after the introduction of a suspended mussel farm in ~15 m deep water of a sheltered bay on the Swedish west coast. Contrastingly, the benthic communities beneath some mussel farms remain relatively unaltered, such as a farm in the Hauraki Gulf, New Zealand where Wong and O'Shea (2010) found no clear difference between the number of opportunistic species identified outside and inside a mussel farm despite it being in the same location for more than 20 years. Other effects may result from the provision of additional hard substrate due to dropping shells: aggregation of sessile suspension feeder including ascidians, bryozoans, sponges, bivalves, and calcareous polychaete species. Such alterations increase the surface roughness and heterogeneity of the seafloor and create a reef-like habitat for a variety of mobile species including fish, crustaceans, and various echinoderms (Kaspar et al., 1985; Wong & O'Shea, 2011).

These and other alterations of the benthic environment are horizontally confined to an area beneath and possibly around the farm, which hereafter I refer to as the "footprint". In New Zealand, for the purpose of marine farm monitoring, environmental managers ask if and how this footprint changes over time. Once a new farm is fully operational its footprint may not change over time if the interaction of this farm with its surrounding environment reached a steady state. Alternatively, the extent and/or the intensity of the footprint may increase over time. To identify, and if existing, quantify such increase, marine farm monitoring should assess two variables: (1) the size of the

affected seafloor area, and (2) the degree to which the affected seafloor differs from the unaffected seafloor. Various approaches have been used worldwide to describe these variables, for example: detecting mussel debris with side scan sonar (Hartstein, 2005) or sediment grab samples (Wong & O'Shea, 2011), identifying genetic differences in sediment microbial communities (Castine, Bourne, Trott, & McKinnon, 2009), modelling biodeposit dispersion (Giles, Broekhuizen, Bryan, & Pilditch, 2009), and measuring the total free sulfide content of the sediment, the sediment redox potential, and water and organic matter contents (Cranford, Hargrave, & Doucette, 2009).

In recent years, environmental scientists have attempted to assess the footprint of mussel (Callier, McKindsey, & Desrosiers, 2008) and fish farms (Carroll, Cochrane, Fieler, Velvin, & White, 2003; Wildish et al., 2003) by measuring the depth of the apparent redox potential discontinuity (aRPD) with sediment profile imagery (SPI). SPI analyses can be supplemented with that of sediment surface images (Diaz & Schaffner, 1988) and other visual indicators, such as the presence or absence of fauna and their burrows, in addition to the depth of the aRPD. A combination of these parameters can be included in analyses to calculate benthic indices, for example, the organism–sediment index (OSI; Rhoads & Germano, 1982, 1986) and the benthic habitat quality index (BHQ; Nilsson & Rosenberg, 1997; O'Connor, Costelloe, Keegan, & Rhoads, 1989).

Bull and Williamson (2001) used sediment profile image analysis to quantify sedimentary minerals based on a relationship between a specific sediment colour property and the mineral concentration. The authors reported two linear correlations for the subtidal sediment of a New Zealand estuary: one between sediment colour intensity and acid volatile sulfide (AVS) concentration ( $R^2 = 0.67$ ), and the other between sediment colour saturation and iron oxyhydroxide ( $\text{FeO}(\text{OH})$ ) concentration ( $R^2 = 0.62$ ). Sediment colour intensity and AVS concentration are inversely related, such that a decrease in sediment colour intensity (darker sediment) accompanies an increase in AVS concentration. The authors established each correlation by slicing sediment cores vertically and photographing the exposed surface. They then analysed

subsamples of the sediment for AVS and FeO(OH) content, which were correlated with the corresponding colour property.

The correlation between sediment colour intensity and AVS concentration is of particular interest for assessing the environmental effect of marine farms because the sediment AVS concentration is a function of the organic matter deposition rate (Bagarinao, 1992; Berner, 1978; Brüchert, 1998; Cornwell & Sampou, 1995; Dahlbäck & Gunnarsson, 1981; Oenema, 1990; Y. I. Sorokin & Zakuskina, 2012; Thode-Andersen & Jørgensen, 1989). To the best of my knowledge, however, AVS measurements are not used in routine monitoring of marine farms presumably because of the laborious analytical process. As demonstrated in the previous chapters, estimating the AVS concentration from sediment profile images is rapid and could make AVS surveys a valuable supplement to existing benthic monitoring techniques.

In Chapter 2, I presented an AVS/colour correlation that was based on the approach of Bull and Williamson (2001). I then suggested to use this correlation in the monitoring of long-line mussel farms, that is, to investigate temporal changes in (a) the colour intensity of sediment underneath such farms and (b) the extent of the footprint, that is, the seafloor area of decreased sediment colour intensity (elevated sediment AVS content). The latter requires an approach to accurately detect the location of footprint's boundary.

Here, I demonstrate such an approach with a series of sediment profile images obtained along transects leading from inside to outside of a long-line mussel farm in Awakiriapa Bay, Waiheke Island, New Zealand.

## 5.2 Methods

### 5.2.1 In situ SPI survey

I acquired 182 profile images of soft subtidal sediment during three days in April 2013 and one day in June 2013 along three transects at the Awakiriapa Bay long-line mussel farm, Waiheke Island, New Zealand (S36°48.085', E175°10.022'; Figure 5.1). Scans were collected over two months due to technical issues with the scanner and logistical issues getting out on the boat. Ideally, scans would have been collected as closely together as possible. Each transect started approximately 50 m inside the farm boundary and extended north, ~200 m beyond the farm boundary. The farm boundary is defined as the position of the end buoy of the mussel line.

I acquired sediment profile images using SPI-Scan (see Chapter 1 for details). The sediment penetration depth of the instrument was adjusted using two approaches, (1) attaching 3–8 × 1 kg weights to the top of the device and (2) controlling the speed at which the instrument penetrated the sediment by either releasing the instrument approximately 2–3 m from the seafloor, or slowly lowering the instrument to the seafloor. I made such adjustments so that the sediment filled two-thirds of the image. Sediment profile scanning was started immediately after the device was in place.

The software (SPI-Scan) digitally embedded the GPS coordinates, date, and time of the acquired image in the metadata of each image. This information is also presented in the upper right-hand corner of the image (Figure 5.2).

A colour calibration strip was included on the right hand side of each profile-image. I used the calibration strip during image analysis to adjust the colour of the image so that the colour reproduction of each image was identical. Each profile image covered an area of 117 × 216 mm at a resolution of 300 dpi (0.08 mm pixel<sup>-1</sup>). Each scan took approximately 30 seconds to complete; this excludes the time required to lower the instrument from the boat or move the instrument, while underwater, to a new

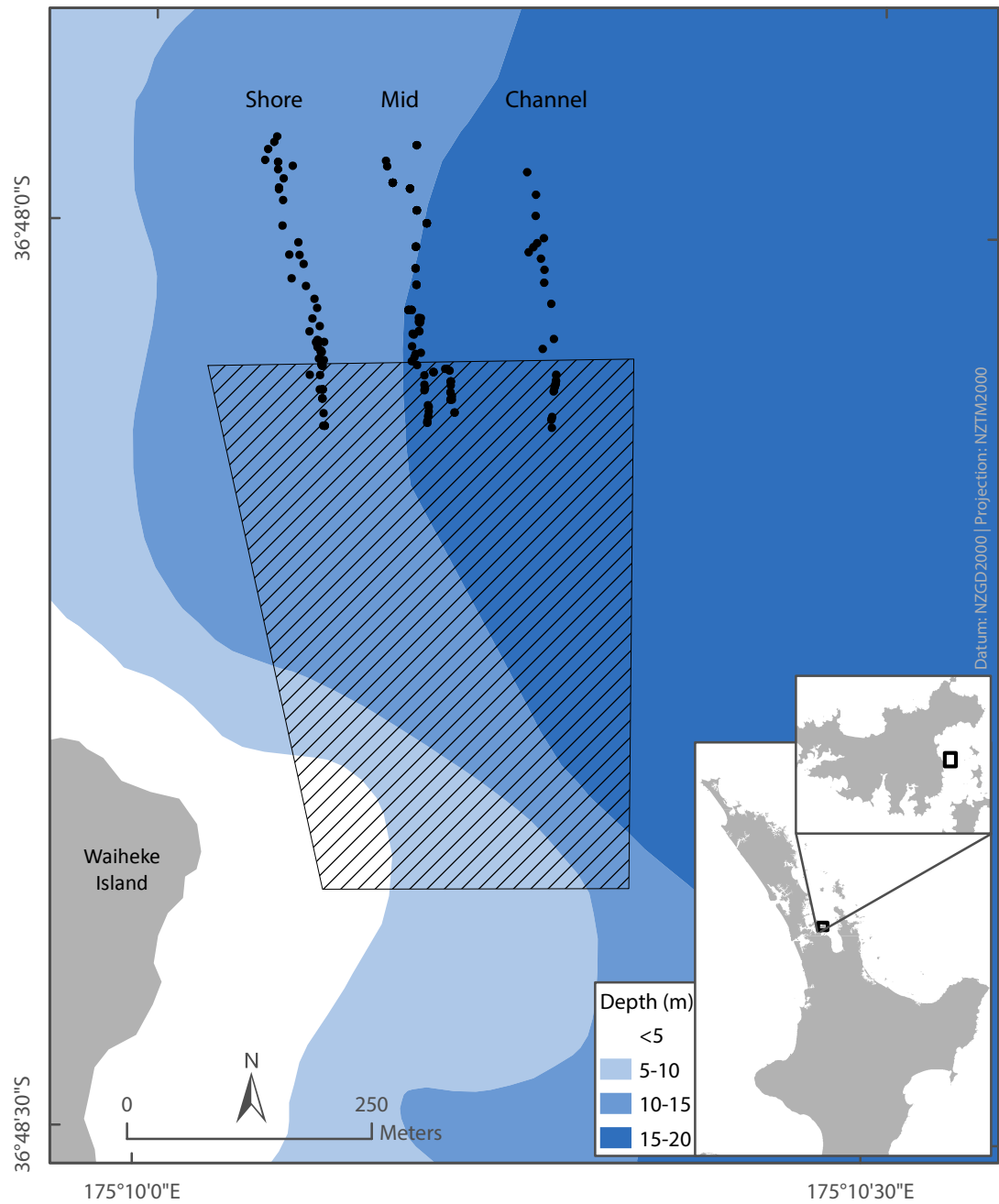


**Figure 5.1:** Location of the long-line mussel farm in Awakiriapa Bay, Waiheke Island, New Zealand. The hashed area indicates the long-line mussel farm. Each black symbol represents one sediment profile image taken along one of three transects.

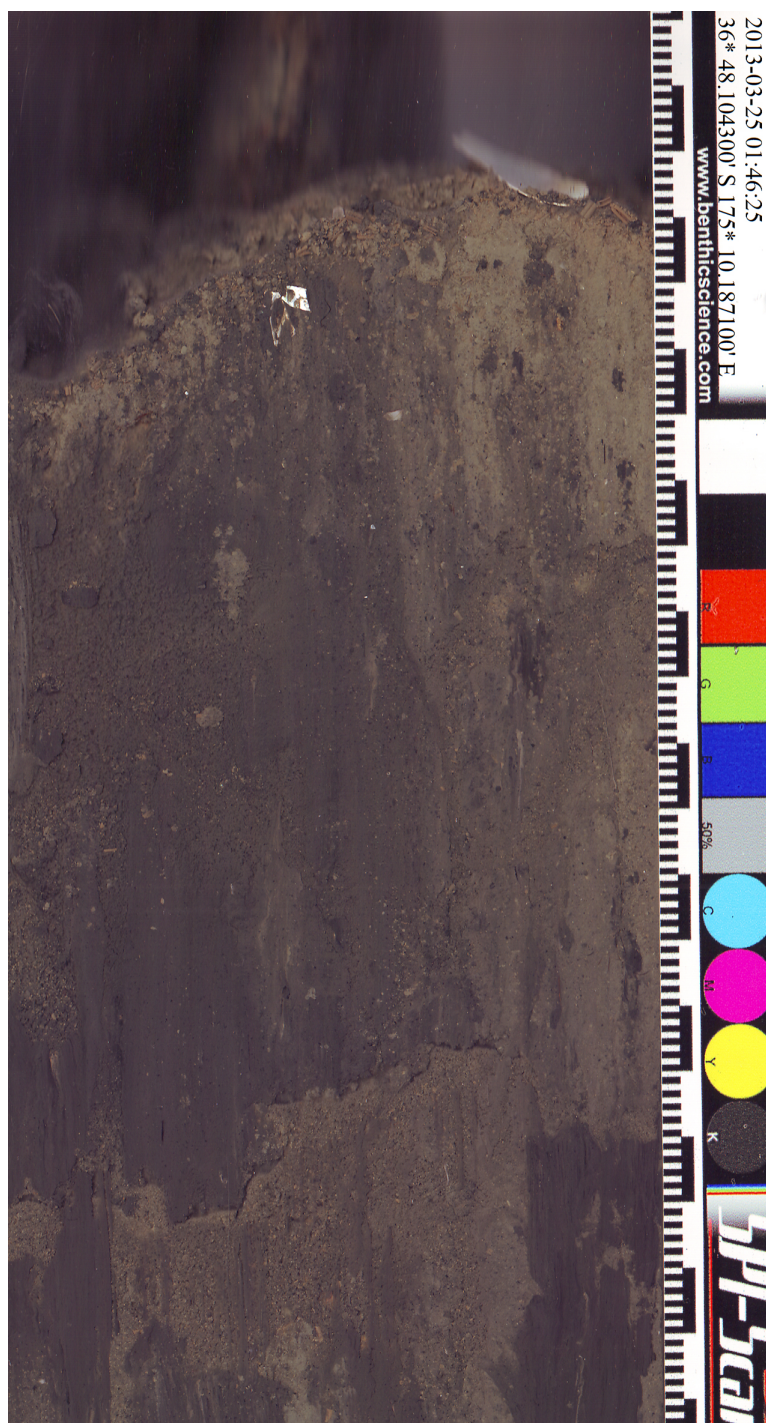


**Figure 5.2:** An example in situ profile image of sediment beneath the mussel farm in Awakiriapa Bay, Waiheke Island, New Zealand. The small and large black and white bars on the right hand side indicate 1 and 10 mm. Colour references are used for colour calibration of the digital image.

location. An example of the colour-range of imaged sediments is shown in Figure 5.3.



**Figure 5.3:** Example sediment profile images showing the range of sediment colours in Awakiriapa Bay, Waiheke Island, New Zealand. The left image was obtained outside the farm, 48 m north of the northern farm boundary, and the middle image and right images were obtained inside the farm, 35 and 57 m south of the northern farm boundary. The small and large black bars are 1 and 10 mm.

### 5.2.2 SPI analyses

To measure the colour intensity (grey value) of each sediment profile image, I first imported all images into the software *analySIS FIVE* (Olympus Soft Imaging Solutions, LS Research version 3.3). I then converted the colour image from the red, green, blue (RGB) colour space to the hue, saturation, intensity (HSI) colour space and measured the average grey value of the intensity channel of a defined area in the sediment profile image, as described below. I observed during image analysis that the sediment surface in the profile images was rarely horizontal and therefore trialled two different methods for selecting an area for image analysis, (1) a rectangle starting approximately 1 cm below the sediment surface that extended 4 cm down, and (2) a polygon that followed the contour of the sediment surface, starting 1 cm below the sediment surface and extending 4 cm down (Figure 5.4).

Because the mean grey values of the rectangular image area did not differ from those of the polygonal area (paired-samples t-test,  $t(174) = 0.49$ ,  $p = 0.62$ ), both methods



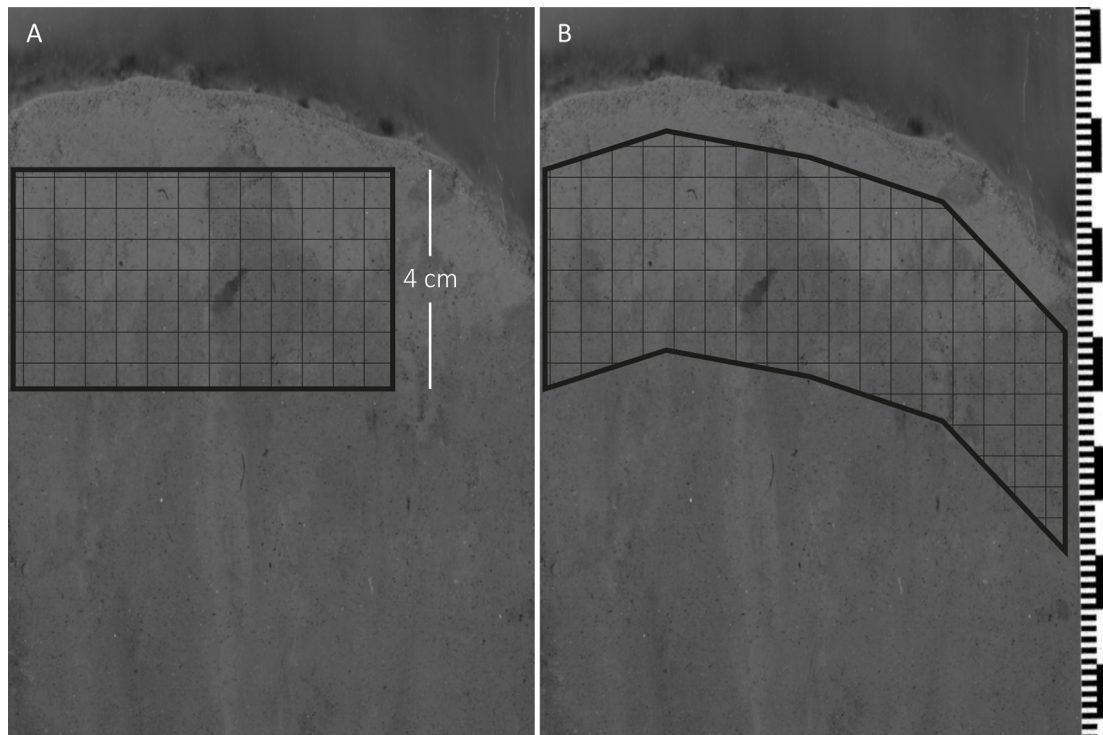


**Figure 5.4:** Two methods for selecting the area of interest for image analysis. The grey-scale images were derived from a full colour image by extracting the colour intensity channel in the HSI colour space. A, a rectangle starting approximately 1 cm from the sediment surface; B, a polygon that follows the contour of the sediment surface, starting approximately 1 cm below the sediment surface. The small and large black bars are 1 and 10 mm.

would have sufficed. In this study, however, I used the larger polygon (~400,000 versus ~260,000 pixels<sup>2</sup>) because the selection of this area was less ambiguous than that of a rectangular area.

Finally, I converted measured sediment colour intensities to sediment AVS concentrations using the previously established AVS/colour correlation for the Awakiriapa Bay long-line mussel farm:  $[AVS] = 0.0024 \times GREY^2 - 0.5249 \times GREY + 28.392$  (Chapter 2). Please note that not all measured grey values could be accurately converted to AVS concentrations because some were outside the range of grey values measured in Chapter 2 to establish this equation. For this reason, I conducted statistical analyses and footprint mapping using sediment colour intensity, rather than AVS concentrations.



### 5.2.3 Statistical analyses

I investigated whether there was any statistically significant difference between transects by analysing grey values inside the farm (distance from farm boundary  $<0$  m) outside the farm (distance from farm boundary  $>0$  m), and overall separately with ANCOVA. Where there was a significant difference, we additionally explored the effect of seawater depth, transect, and distance from the farm boundary on the grey value with a full factorial ANCOVA.

To identify the boundary of the colour intensity footprint, I performed a segmented regression analysis with the 'segmented' package in R (Muggeo, 2003; R Core Team, 2013). I performed this analysis for each of the three transects and on a dataset created by combining the data from all three transects. The analysis used an iterative procedure to fit two linear regressions and find a breakpoint in the data trend by minimising the sum of squares of the differences between observed and calculated variables. I constrained the slope of the second linear regression to zero because I was trying to identify a colour change from the unaffected sediment surrounding the farm (background). I assumed that although the colour intensity of this sediment will naturally vary, there would be no significant long-distance trend of increasing or decreasing colour intensity. I ran the segmented model using distance from the farm boundary as the predictor and a starting (psi) value of 100. I varied psi from 50 to 150 to ensure this value was not biasing the result.

### 5.2.4 Colour intensity mapping

I used marine farm location data (Land Information New Zealand) in ArcMap (ESRI ArcGIS, version 10.2) to determine the distance of each sampling point from the northern boundary of the mussel farm. To do so, I imported the GPS coordinates embedded in each sediment profile image and then calculated the distance from the image location to the northern edge of the mussel farm with the Generate Near Table tool in ArcMap. The depth information for each data point was extracted from a 20 m

resolution gridded bathymetric dataset (Mackay, Mackay, Neil, Mitchell, & Bardsley, 2012). I mapped the sediment colour intensity over an area extending from ~50 m inside the northern farm boundary to ~200 m north of the farm boundary with the polynomial interpolation model in ArcMap (Table 5.1). The model extrapolated the measured sediment colour intensities to cover this area.

**Table 5.1:** Parameters for the local polynomial interpolation model in ArcMap (ESRI ArcGIS, version 10.2). Measured sediment colour intensities along three transects running across the boundary of the mussel farm in Awakiriapa Bay, Waiheke Island, New Zealand were extrapolated over an area extending from ~50 m inside the northern farm boundary to ~200 m north of the farm boundary.

Parameter	Setting or value
Method	Local polynomial interpolation
Kernel function	Exponential
Output type	Prediction
Power	1
Bandwidth	166.62
Spatial condition number threshold	30
Exploratory trend surface analysis	20
Searching neighborhood	Standard
Neighbors to include	1000
Include at least	10
Sector type	Full
Major semiaxis	208.27
Minor semiaxis	208.27
Angle	0
Cell size	1.2 m

### 5.3 Results

Sediment colour intensities (grey values) were high and varied little ( $93 \pm 1$  grey values; mean  $\pm$  95% CI,  $n = 83$ ) at distances  $>50$  m north of the northern farm boundary. This defines the “background” sediment colour intensity in Awakiriapa Bay. The mean sediment colour intensity inside the farm, that is, south of the northern farm boundary, was almost one-third times lower (61 grey values) than the background colour intensity. This lower sediment colour intensity defines the AVS footprint of the farm.

Conversion of the measured sediment colour intensities to AVS concentrations following the methods in Chapter 2 revealed AVS concentrations far above the range of established AVS/colour correlation for nearly half of all profile images inside the farm, and negative concentrations for some profile images of sediment outside the farm (Figure 5.5). The latter concentrations were all within the margin of error of the AVS/colour calibrations if the actual AVS concentrations were at or near  $0 \mu\text{mol g}^{-1}$  wet weight; the mean 95% individual CI of the AVS/colour calibration was  $0.5 \mu\text{mol g}^{-1}$  wet weight.

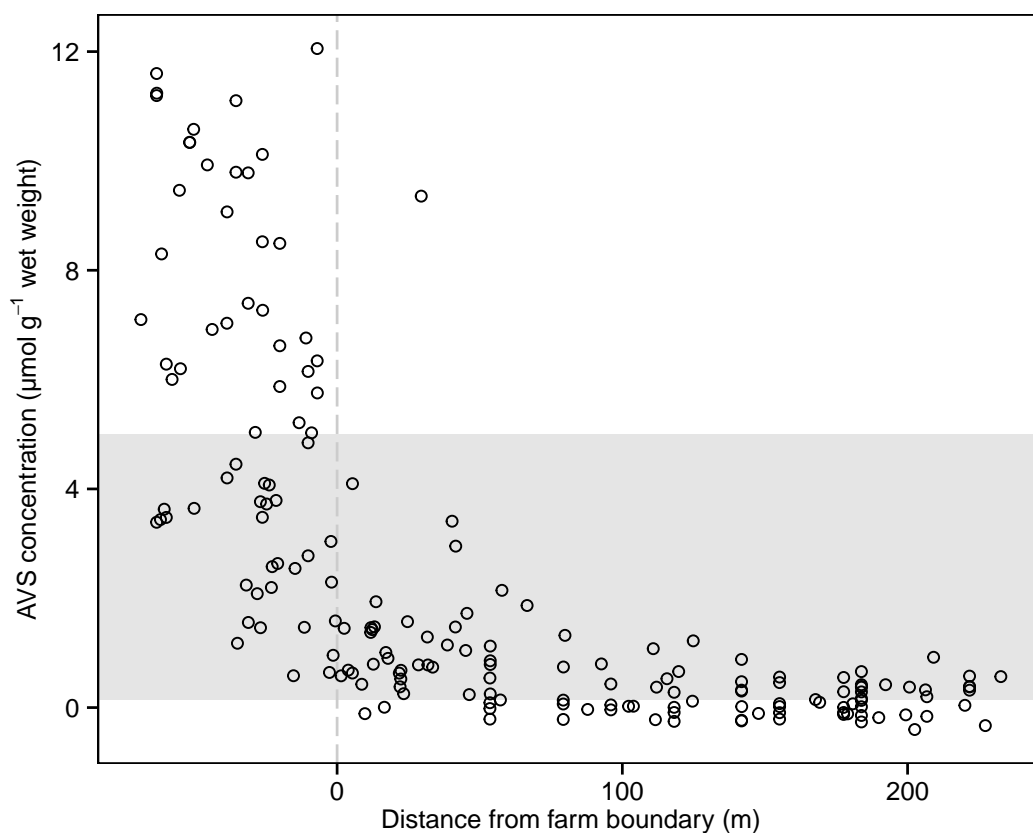


**Figure 5.5:** Sediment AVS concentrations along three transects crossing the northern boundary of a mussel farm in Awakiriapa Bay, Waiheke Island, New Zealand. AVS concentrations were predicted from measured sediment colour intensities using the previously established AVS/colour correlation (Chapter 2). AVS concentrations inside the grey area were derived from grey values within the range of grey values included in the AVS/colour intensity correlation; AVS concentrations outside of this grey area were extrapolated using the correlation equation.

In the following I locate the position of the AVS footprint boundary using colour intensity data instead of AVS data to avoid uncertainty from extrapolating the AVS/colour calibration. Segmented regression analysis of the colour intensity data

from all transects located the northern boundary of the footprint at  $56 \pm 13$  m ( $\pm 95\%$  confidence interval of the breakpoint) outside and north of the mussel farm (Fig. 6A). Furthermore, segmented regression analysis on individual transects revealed that the footprint extended 35 m less on the shore side than it did in the middle of the farm (Figures 5.6B–D, Table 5.2).

**Table 5.2:** Extent of the Awakiriapa Bay mussel farm colour intensity footprint. The extent of the mussel farm footprint was determined by segmented regression analysis for each transect individually, and for the combined set of sediment colour intensity data.

Transect	Footprint extent (m)	95% CI	$R^2$	$N$
All	56	13	0.69	182
Shore	35	11	0.81	57
Mid	71	21	0.70	97
Channel	19	27	0.76	28

The mean sediment colour intensity inside the farm was lower (darker sediment) along the Shore and Mid transects than it was along the Channel transect (Table 5.3).

**Table 5.3:** ANCOVA used to investigate differences in the colour intensity of sediment along three transects across the Awakiriapa Bay mussel farm boundary, Waiheke Island, New Zealand. Overall includes all data points for each transect, Inside farm and Outside farm include data points for distances  $<0$  and  $>0$  m from the northern farm boundary. Where the result was significant ( $p > 0.05$ ), I used a Tukey posthoc contrast to determine ranking. The model equation was: Grey = Distance + Transect.

	Df	Residuals	$F$	$p$	$R^2$	Tukey contrast
Overall	2	178	1.13	0.324	0.56	
Inside farm	2	61	6.84	0.002	0.33	Shore, Mid < Channel
Outside farm	2	113	0.59	0.558	0.25	

To elucidate the increase in intensity of the footprint towards the shore side of the farm, I investigated how the variables Depth, Distance from the farm boundary, and Transect influenced sediment colour intensities inside the mussel farm and found that all three variables, and some interactions between these variables, had a significant effect (Table 5.4). The Shore transect was closest to the shore and in seawater two meters shallower than that of the other two transects (Table 5.5).

The colour intensity footprint map in Figure 5.7 supports the results of the segmented regression analysis: sediment colour intensities were  $>80$  grey values at distances

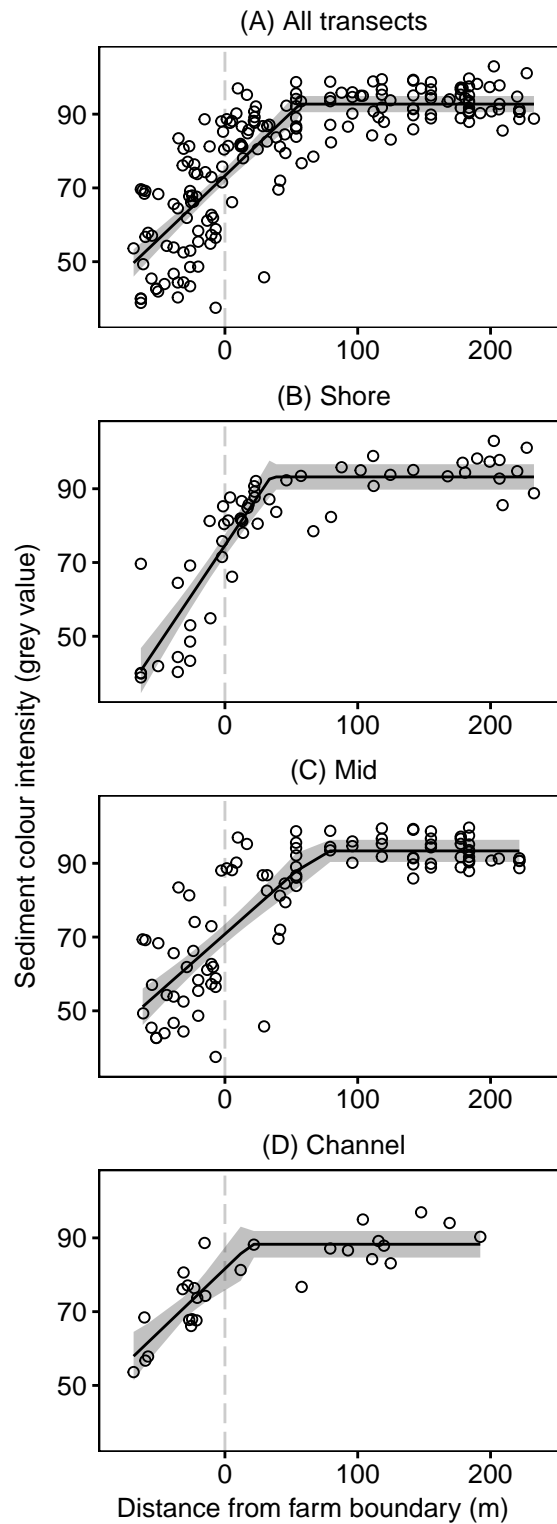


**Figure 5.6:** Segmented regression analysis. A segmented regression model identified the distance from the northern farm boundary at which the colour intensities of the sediment in Awakiriapa Bay, Waiheke Island, New Zealand started to decrease when heading towards the farm. The analysis was performed on data combined from the three transects (A) and separately for each transect (B–D). The grey shaded area shows the 95% confidence interval of the model and the vertical grey dashed line denotes the mussel farm boundary. Negative distances indicate points within the farm, that is, south of the northern farm boundary.

**Table 5.4:** Full factorial ANCOVA used to investigate the effect of Distance from the farm boundary, Transect, and Depth on the colour intensity of the sediment inside the farm (distance <0 m from the farm boundary).

Inside ( $R^2 = 0.56$ )	Df	Sum Sq	Mean Sq	F value	Pr(>F)
Distance	1	2274.9	2274.9	22.3	<0.001
Transect	2	1849.1	924.5	9.1	<0.001
Depth	1	442.7	442.7	4.3	0.042
Distance:Transect	2	639.6	319.8	3.1	0.051
Distance:Depth	1	89.8	89.8	0.9	0.352
Transect:Depth	2	973.2	486.6	4.8	0.012
Distance:Transect:Depth	2	701.7	350.9	3.4	0.039
Residuals	53	5398.4	101.9		

**Table 5.5:** Mean water depth and mean sediment colour intensity for each of three transects within the mussel farm. The final column indicates the number of samples that were averaged.

	Depth (m)	95% CI	Colour intensity (grey value)	95% CI	N
Shore	13.6	0.04	58	8	18
Mid	15.3	0.03	59	5	32
Channel	15.7	0.003	70	5	15

greater than 50 m from the farm boundary and <77.5 grey values at distances less than 50 m from the farm boundary. This map also indicated that the colour intensity footprint didn't extend as far on the western side of the farm as it did on the eastern side.

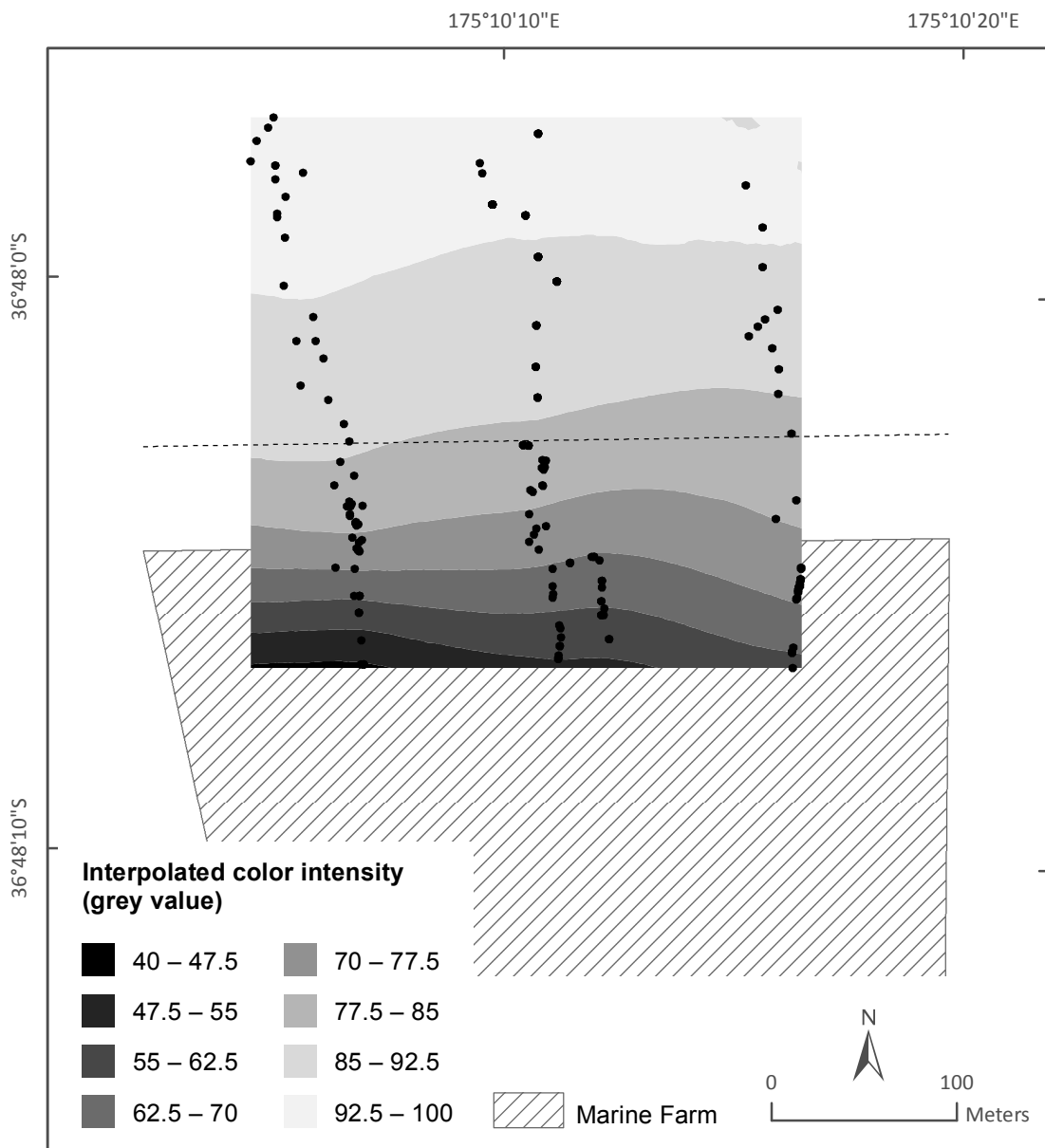


**Figure 5.7:** Sediment colour intensity footprint of the Awakiriapa Bay mussel farm, Waiheke Island, New Zealand. A local polynomial interpolation model (ArcMap) extrapolated the colour intensity of the sediment imaged along three transects (black symbols) to map the sediment colour intensity in the shaded area. Sediment colour intensity is correlated to AVS concentration (Bull and Williamson (2001), Chapter 2). The hashed area denotes the mussel farm. The dashed line 56 m north of the northern farm boundary denotes the edge of the mussel farm AVS footprint, as identified from segmented regression analysis of sediment colour intensity data.

## 5.4 Discussion

I demonstrated the use of in situ SPI to assess the sediment colour intensity footprint of a long-line mussel farm. Two variables were of interest, the intensity of the footprint, that is, the magnitude of the difference between the colour intensity of the sediment underneath the farm and that of the surrounding unaffected sediment, and the size or spatial extent of the footprint. For the trial mussel farm, I determined the latter with segmented regression analysis of our colour intensity data (Figure 5.6, Table 5.2); the footprint extended approximately 50 m beyond the northern boundary of the mussel farm. This distance lies within the range of numerical model predictions of the dispersion and erosion of faeces and pseudofaeces at a nearby mussel farm, 25 km southeast of Awakiriapa Bay. Here, Giles et al. (2009) found that mussel faeces released by this farm, into a 10 m deep seawater column were deposited up to 60 m away from the mussel farm boundary. Incorporating resuspension by erosion into their model increased this distance to 130 m. Clearly, the deposition of small amounts of faeces and pseudofaeces away from the farm does not necessarily result in a detectable decrease of sediment colour intensity, but such deposition modelling can inform the design of future AVS and colour intensity footprint surveys. In particular, it will help to ensure that survey transects extend far enough from the mussel farm boundary to include the unaffected seafloor.

Two advantages of this SPI analysis technique are that it is rapid and it does not require in-depth training and experience of the operator to measure and adequately interpret the ecological significance of image parameters. The operator simply uses software routines to measure one property of the sediment, its colour intensity. Selecting an image area to determine this property is the only step in my routine that requires the operator to make a decision. I believe that its simplicity and automation make this method suitable to complement other types of assessments of the effects of organic enrichment of sediments underneath mussel or fish farms on the soft-sediment ecosystem because it will ensure that data acquisition remains consistent over the



lifetime of a monitoring program. The placement of colour intensity survey transects at the onset of such program must consider local differences in seawater depth and current speed — two variables that affect the dilution and dispersion of faeces and pseudofaeces after release (Chamberlain et al., 2001; Giles & Pilditch, 2004).

For the trial mussel farm, differences in the sediment colour intensities between the three transects and the sediment colour intensity map in Figure 5.7 indicate that the farm AVS footprint did not extend as far beyond the farm boundary close to the shore as it did close to the channel, logically because the seafloor underneath the shore side farm blocks is less deep and thus biodeposits would not disperse as far. Hartstein and Stevens (2005) support this reasoning; their sediment trap measurements and dispersal model revealed that because particles released from a farm in shallower seawater spend less time in the water column they deposit over a smaller area of seafloor than particles released in deeper seawater. Consequently, deposition in shallow seawater will elevate the sediment organic matter content more than deposition in deeper seawater. Differences in water depth cannot explain the differences in the sediment mean colour intensity between the Mid and Channel transects within the farm as their depths did not differ significantly. I suggest that this difference likely resulted from a higher flow speed along the Channel transect, which has the a similar effect as a greater water depth, increasing the dispersion of suspended particles from the mussel farm.

Over half of the sediment colour intensities measured inside the mussel farm were outside the range of those colour intensities included in the strong AVS/colour intensity correlation that was established in Chapter 2. Clearly, a new calibration covering a wider range of sediment colour intensities is required to accurately predict the entire range of AVS concentrations and any conclusions made from the extrapolated AVS concentrations should be conservative. Many of the AVS concentrations derived for the sediment in the area between the farm boundary and the AVS footprint boundary, however, are within the calibrated range and so suitable for comparison with future measurements. Such measurements outside the farm

boundary may reveal that the sediment colour intensities have decreased over time and this will indicate that the intensity and extent of the AVS footprint of this farm has increased. Environmental managers may use such trend to request more detailed investigations of the effects of organic matter deposition on benthic ecosystem functioning.

I mapped sediment colour intensities to visually represent the two-dimensional colour intensity footprint. Such representation may simplify any assessment of the shape of the footprint but it cannot provide any more detailed information than the three transect measurements from which it was derived. The availability of resources for mussel farm monitoring often limit the number of sites, measured parameters, and the frequency at which measurements are conducted. If so, I recommend focusing data acquisition to produce sufficient sediment profile images along one transect rather than aiming for greater spatial coverage. The minimum number of scans will depend on local conditions and this should be investigated with a trial before commencing monitoring. In this study, segmented regression identified the footprint boundary along the Channel transect with as few as 28 data points. Segmented regression analyses of, for example, annual data sets will then allow investigators to assess if the position of the footprint boundary in the direction of this transect or the intensity of the footprint, that is, the AVS content of the sediment underneath the farm change over time. If the shape of the footprint and local differences in its extent are of interest, however, the sampling design should ensure sufficient spatial coverage to produce colour intensity maps as shown in Figure 5.7.

Deposition of farm-derived organic matter alters both the redox chemistry of the receiving soft-sediment seafloor and the composition of its benthic species assemblages (Callier, Richard, McKindsey, Archambault, & Desrosiers, 2009; McKindsey, Archambault, Callier, & Olivier, 2011; Robert, McKindsey, Chaillou, & Archambault, 2013). Changes in these two variables are linked; soft sediment with elevated organic matter often supports assemblages dominated by few opportunistic species. The seafloor underneath mussel farms, however, accumulates hard substrate

in the form of dropped mussel shells and this accumulation can lead to contrasting results. In a previous study of the trial mussel farm in Awakiriapa Bay, for example, Wong and O'Shea (2011) demonstrated that species richness and diversity of the macrofaunal assemblage were higher beneath than outside the mussel farm. The authors suggested that the boundary of the farm footprint (based on attributes of the benthic macrofaunal assemblage) was marked by the outer limit of benthic clumps of mussel shells, which extended 30 m past the boundary of the mussel farm. Here, instead of using clumps of dropped mussel shells as an indicator, I used a property of the soft-sediment ecosystem that is linked with the deposition of farm-derived organic matter and demonstrated that the footprint of this farm extended beyond 30 m.

## Chapter 6

### Conclusion

I have provided evidence and discussion throughout this thesis that sediment profile images are suitable for assessing the enrichment of soft, subtidal sediment with organic matter. To provide this, I further developed a correlation presented by Bull and Williamson (2001) between sediment colour intensity and the sediment content of acid volatile sulfide (AVS), a product of the microbial degradation of organic matter. Using this correlation, I estimated AVS concentrations from a sediment-profile image and produced high-resolution vertical AVS concentration profiles, or two-dimensional false colour images representing the distribution of AVS in the sediment (Chapter 2).

It is important to note that the AVS/colour correlation is site specific. I first noted this when I compared the AVS/colour correlation I established for the sediment in Awakiriapa Bay with that previously established for the sediment of an Auckland estuary by Bull and Williamson (2001) (Chapter 2). The two correlations had similar slopes but were offset on the grey value axis. Further investigation revealed similar differences between three sites in the Hauraki Gulf, New Zealand (Chapter 3).

By investigating the speciation of reduced sulfur in the sediment of three different locations in the Hauraki Gulf (Chapter 4), I was able to determine that sediment age influences the relationship between sediment colour intensity and AVS content. To

include a wide range of sediment colour intensity and AVS concentrations in my analyses, I sampled the sediment column vertically to a depth of 14 cm. In doing so, I also sampled sediment of different ages.

My analyses revealed that the relative proportions of sulfide mineral pools (dissolved porewater sulfide, AVS, and sequentially extracted chromium reducible sulfide, CRS<sub>s</sub>; Chapter 4) were a function of sediment depth. The concentration of dissolved porewater sulfides was negligible at all sites. Deeper sediment contained a higher proportion of CRS<sub>s</sub>, a sulfide pool that predominantly comprises the black mineral pyrite and does not contribute to the measured AVS concentration. Pyrite is thermodynamically stable but kinetically slow to form and may take up to several years to form from its precursors. Contrastingly, the minerals that comprise AVS (predominantly mackinawite and greigite) form over hours or days. Thus, high and low proportions of CRS<sub>s</sub> indicate older and younger sediment.

The age of sediment at a particular depth in the sediment column will depend on site-specific factors, such as the rate of organic matter deposition, the intensity of bioturbation, sediment mixing by resuspension, and cycles of particle erosion and settling at the site. In other words, sediments collected from the same depth in the sediment columns of different locations are unlikely of the same age, and therefore, their relative contents of AVS and CRS<sub>s</sub> will differ. Such differences may explain the observed differences between the AVS/colour correlations at the three study locations and the failure of a correlation of pooled AVS/colour data (three locations) to accurately predict the sediment AVS content at these locations. This finding reinforces the need to establish a site-specific AVS/colour correlation.

The presence of a vertical sulfur mineral composition gradient may also explain why the function that best described the relationship between sediment colour intensity and AVS concentration was quadratic rather than linear. To investigate factors that influence the shape of the AVS/colour correlation, I extracted AVS with different acid concentrations. The reason for using different acid concentrations was that a strong

extraction removes a greater proportion of AVS minerals. Based on the findings from Cornwell and Morse (1987), none of the extractions, however, would have removed any pyrite from the sediments. The only effect observed with these extractions was that high-concentration acid removed more AVS from the sediment than low-concentration acid; the shape of the AVS/colour correlation, however, was not affected by acid concentration.

Sediment deeper in the sediment column usually contained more  $\text{CRS}_s$  than subsurface or surface sediment. Thus, if an AVS/colour correlation was established using deep sediment, the slope of the fit that described this correlation would be less steep because a large proportion of the sediment colour intensity will be due to pyrite, rather than AVS minerals. Conversely, the fit describing an AVS/colour correlation for subsurface or well-mixed sediment will have a steep slope because a large proportion of the sediment colour intensity will be due to AVS minerals.

The finding that  $\text{CRS}_s$  concentrations were higher in deeper sediment is consistent with the study of Berner (1970), for example, who reported that the formation of pyrite, one of the main components of  $\text{CRS}_s$ , may take up to several years under ideal conditions. The formation of pyrite is kinetically very slow although it is one of the most thermodynamically stable forms of iron sulfide (Berner, 1964a). It may be possible to exploit this process and investigate historic rates of organic matter degradation when including more accurate measurements of sediment age.

Interpreting sediment processes using pyrite concentrations may be more complex than they first seem. Rickard and Morse (2005) explain that mackinawite and greigite are not necessarily precursors to pyrite. This is because pyrite forms from dissolved phases, which may come from mackinawite and greigite but they are not required. Removing the direct link between mackinawite and greigite concentrations and pyrite concentrations may limit the amount of information that can be gained by assessing these three different minerals. It may prove beneficial to identify pyrite concentrations, since they will contribute to sediment colour but not the AVS

concentration, so corrections can be made to the AVS/colour correlation; research efforts, however, should be focused towards understanding sediment processes using the AVS concentrations estimated from a sediment profile image, which have a stronger link to sediment organic matter degradation.

I applied the developed technique to assess the intensity and extent of elevated sediment AVS from a long-line mussel farm in Awakiriapa Bay, Waiheke Island, New Zealand. In this study, the range of grey values measured from sediment-profile images was greater than the range of grey values used to establish the site-specific AVS/colour correlation. In this situation, I demonstrated that the area of sediment beneath and surrounding the mussel farm that was affected by organic enrichment (the farm footprint) could still be detected by analysing the sediment colour intensity, rather than the AVS concentration.

I used a robust statistical analysis to identify a breakpoint in the trend of increasing grey value with increasing distance from the long-line mussel farm. The distance of this breakpoint identified the extent of the farm's colour intensity footprint. Including such analyses into a monitoring scheme will enable coastal managers to assess whether such extent is increasing or decreasing over time. Importantly, acquiring in situ sediment-profile images was rapid and facilitated a large number of samples. Many samples are required to identify clear patterns from otherwise 'noisy' environmental data.

Additionally, I mapped the sediment colour intensity to produce a visual footprint of the farm. It is important to state, however, that the spatial mapping cannot provide any further information than the measured transects provide. Such visual footprint, however, is a powerful tool for communicating information to non-technical audiences and visualising local patterns, such as on-shore–off-shore gradients in the footprint extent.

The breakpoint analysis and visual mapping of sediment colour intensity to identify the farm footprint area are both derived from sediment profile image analysis. For this

reason, these techniques could be used to supplement SPI studies that employ benthic indices such as OSI or BHQ without additional field work. Germano et al. (2011) commented on the complexity of interpreting SPI images and the need to gain as much information as possible from these images to interpret them correctly.

For example, Rhoads and Germano (1986) developed the OSI to identify the state of the environment from sediment profile images based on benthic succession along organic enrichment gradients as described by Johnson (1972) and Pearson and Rosenberg (1978). This assessment will reveal information on the current benthic state, but it can be difficult to interpret the rate or direction of change of the state, that is, whether conditions are ‘improving’ or ‘declining’. This may be partly due to the resilience of some organisms or a lag between chemical changes in the sediment and changes to the benthic community composition. Including additional information such as the AVS concentration may provide some context for these findings; for example, sediments with high AVS concentrations but OSI scores that indicate a ‘good’ state may be an indication that the current state could decline. Further investigation and development would be required to test this line of thinking. More simply, the current implementation of benthic indices derived from SPI provide a snapshot of the current state, supplementing this information with estimated AVS concentrations may provide some indication on whether the state is likely to improve, remain the same, or decline.

The sediment content of AVS is a suitable indicator of organic enrichment in coastal sediments. Its use in routine monitoring, however, has been limited because of its laborious measurement. The technique I have presented in this thesis makes AVS an assessable parameter to coastal managers and scientists for routine assessment of coastal soft sediments. Such technique is ideally suited for assessing organic enrichment of sediments with organic matter from sources such as mussel and fish farms, two industries that are developing rapidly to feed our continually growing population.



## 6.1 Recommendations for further work

### *Sampling approach*

In response to the findings of Chapter 4 where I identified that the proportion of AVS:CRS<sub>s</sub> changed with sediment depth, I recommend that future AVS/colour calibrations are established using sediment sampled from the same depth from cores that are collected along a horizontal gradient. Assuming similar depositional environments, this is the best approach to try and sample sediment that is all of a similar age.

To obtain a wide range of sediment colour intensities, samples should be collected along a gradient extending from beneath or near a source of organic enrichment to a distance away from the source, rather than exploiting the natural variation with sediment depth that I used in this study. This approach should allow the AVS/colour calibration to be established without the added uncertainty of the changing composition of sulfide minerals that naturally occur over time (i.e., increasing sediment depth). It is possible that such an approach may result in a more linear relationship between AVS concentration and sediment colour intensity.

### *Investigate effects of sediment age on sulfide mineral composition*

Another line of enquiry that I recommend based on the findings of Chapter 4 is investigating the effect of sediment age on the sulfide mineral composition. Specifically, use techniques such as carbon dating to identify any patterns between sediment age (depth) and the concentration of pyrite. Such line of enquiry may provide clues on how this technique could be used to assess the current effects of organic enrichment on the sediment by using the upper sediment layers, whereas, using deeper sediment, it may be possible to see how rates of organic matter degradation may have changed over time based on the relative proportion of the slowly forming pyrite.

*Further characterise sediment sulfide species*

In order to better understand the factors that influence the relationship between AVS concentration and sediment colour intensity, it is important to have a good understanding of the species that are, or are not present. I assumed, for example, that the concentration of polysulfides were negligible in this study based on previous publications. Within this study, however, I did not isolate or measure their concentration in the sediment. Furthermore, I didn't section sediment cores under anoxic conditions, which has been reported to result in higher concentrations of polysulfides than would have been found in the sediment naturally. Analysing specifically for polysulfides would provide further certainty about the sulfide composition in these sediments.

Similarly, further efforts could be made to identify sulfide mineral composition using complimentary techniques such as X-ray diffraction (XRD). Such technique may provide information that could be used to better understand the relative proportions of mackinawite, greigite, and pyrite, the three dominant reduced sulfide minerals. This may provide further understanding of how the AVS/colour correlation may change under different extraction conditions or when analysing sediment of different ages (depths).

Particles sizes can be characterised down to the nm scale using scanning electron microscopy (SEM). With regard to pyrite particle size, this approach may be able to indicate the amount of pyrite that is likely to be extracted during a one hour extraction using 1 M HCl, since fine particles will be extracted faster than large particles. It is possible that the pyrite in the sediments analysed in this study were of a size that they would not be extracted in detectable amounts during a one hour extraction.

*Identify non-sulfide coloured species*

Throughout this thesis, I referred to the 'background' colour of the sediment, that is, the colour of the sediment excluding the extracted AVS components. There are many other components and sediment characteristics that likely contribute towards the

sediment colour that I have not identified in this study. Bull and Williamson (2001) briefly mentioned some of these components, including particle size, crystallinity, and the presence of coloured metals.

Sediment containing high concentrations of non-AVS coloured components may reduce the sensitivity of the technique as it would be more difficult to detect small changes in the sediment colour as a result of a change in the AVS concentration. For this reason, I recommend that further work be conducted to identify some of the more strongly coloured components, particularly those that contribute substantially to the colour intensity. It may be possible to correct for these components and increase the sensitivity of the technique. Furthermore, correcting for the sediment background may be a step towards identifying a way to use one AVS/colour correlation at multiple sites or sediment types.

*Explore relationships between sediment properties and sediment colour using other colour spaces*

In Chapter 2, I presented some of the colour spaces that are used to describe sediment colour. Although there are many different colour spaces, I chose to use HSI to be consistent with the methods of Bull and Williamson (2001). In doing so, I ruled out exploring the possibility of using other colour spaces to estimate the AVS concentrations from a sediment profile image.

It is possible that other colour spaces may also be useful for estimating the concentration of AVS from a sediment profile image. I recommend exploring other colour spaces, such as RGB, Munsell and CIE Lab, to see whether any are more sensitive to changes in AVS concentration than HSI. This may be achieved by using one channel of the colour space, such as the intensity channel used in this study, or a combination of channels. Some colour spaces may be less susceptible to noise or effects from the 'background' colour of the sediment or result in a more linear relationship between AVS concentration the sediment colour intensity.

## References

- Allen, E. T., Crenshaw, J. L., Johnston, J., & Larsen, E. S. (1912). The mineral sulphides of iron. *American Journal of Science*, 33(195), 169–236. doi: 10.2475/ajs.s4-33.195.169
- Allen, H. E., Fu, G. M., & Deng, B. L. (1993). Analysis of acid-volatile sulfide (AVS) and simultaneously extracted metals (SEM) for the estimation of potential toxicity in aquatic sediments. *Environmental Toxicology and Chemistry*, 12(8), 1441–1453. doi: 10.1002/etc.5620120812
- Aller, R. C. (1980). Relationships of tube-dwelling benthos with sediment and overlying water chemistry. In K. R. Tenore & B. C. Coull (Eds.), *Marine benthic dynamics* (pp. 285–308). Columbia: University of South Carolina Press.
- Aller, R. C. (1982). The effects of macrobenthos on chemical properties of marine sediment and overlying water. In P. L. McCall & M. J. S. Tevesz (Eds.), *Animal-sediment relations* (Vol. 100, pp. 53–102). Springer US. doi: 10.1007/978-1-4757-1317-6\_2
- Aller, R. C. (1994). Bioturbation and remineralization of sedimentary organic matter: effects of redox oscillation. *Chemical Geology*, 114(3-4), 331–345. doi: 10.1016/0009-2541(94)90062-0
- Ankley, G. T. (1996). Evaluation of metal/acid-volatile sulfide relationships in the prediction of metal bioaccumulation by benthic macroinvertebrates. *Environmental Toxicology and Chemistry*, 15(12), 2138–2146. doi: 10.1002/etc.5620151209
- Bagarinao, T. (1992). Sulfide as an environmental factor and toxicant: Tolerance and adaptations in aquatic organisms. *Aquatic Toxicology*, 24(1-2), 21–62. doi: 10.1016/0166-445X(92)90015-F
- Balsam, W. L., Deaton, B. C., & Damuth, J. E. (1999). Evaluating optical lightness as a proxy for carbonate content in marine sediment cores. *Marine Geology*, 161(2-4), 141–153. doi: 10.1016/s0025-3227(99)00037-7
- Berner, R. A. (1964a). Distribution and diagenesis of sulfur in some sediments from the Gulf of California. *Marine Geology*, 1(2), 117–140. doi: 10.1016/0025-3227(64)90011-8
- Berner, R. A. (1964b). An idealized model of dissolved sulfate distribution in recent sediments. *Geochimica et Cosmochimica Acta*, 28(9), 1497–1503. doi: 10.1016/0016-7037(64)90164-4
- Berner, R. A. (1964c). Iron sulfides formed from aqueous solution at low temperatures and atmospheric pressure. *Journal of Geology*, 72(3), 293–306.
- Berner, R. A. (1970). Sedimentary pyrite formation. *American Journal of Science*, 268(1), 1–23. doi: 10.2475/ajs.268.1.1
- Berner, R. A. (1978). Sulfate reduction and the rate of deposition of marine sediments.

- Earth and Planetary Science Letters*, 37(3), 492–498. doi: 10.1016/0012-821X(78)90065-1
- Berner, R. A. (1982). Burial of organic carbon and pyrite sulfur in the modern ocean: its geochemical and environmental significance. *American Journal of Science*, 282(4), 451–473. doi: 10.2475/ajs.282.4.451
- Berner, R. A. (1984). Sedimentary pyrite formation: An update. *Geochimica et Cosmochimica Acta*, 48(4), 605–615. doi: 10.1016/0016-7037(84)90089-9
- Blanpain, O., du Bois, P. B., Cugier, P., Lafite, R., Lunven, M., Dupont, J., ... Pichavant, P. (2009). Dynamic sediment profile imaging (DySPI): A new field method for the study of dynamic processes at the sediment–water interface. *Limnology and Oceanography: Methods*, 7, 8–20. doi: 10.4319/lom.2009.7.8
- Boudreau, B. P., & Westrich, J. T. (1984). The dependence of bacterial sulfate reduction on sulfate concentration in marine sediments. *Geochimica et Cosmochimica Acta*, 48(12), 2503–2516. doi: 10.1016/0016-7037(84)90301-6
- Brendel, P. J., & Luther III, G. W. (1995). Development of a gold amalgam voltammetric microelectrode for the determination of dissolved Fe, Mn, O<sub>2</sub>, and S(-II) in porewaters of marine and freshwater sediments. *Environmental Science and Technology*, 29(3), 751–761. doi: 10.1021/es00003a024
- Brostigen, G., & Kjekshus, A. (1969). Redetermined crystal structure of FeS<sub>2</sub> (pyrite). *Acta Chemica Scandinavica*, 23, 2186–2188. doi: 10.3891/acta.chem.scand.23-2186
- Brown, J. R., Gowen, R. J., & McLusky, D. S. (1987). The effect of salmon farming on the benthos of a Scottish sea loch. *Journal of Experimental Marine Biology and Ecology*, 109(1), 39–51. doi: 10.1016/0022-0981(87)90184-5
- Brüchert, V. (1998). Early diagenesis of sulfur in estuarine sediments: The role of sedimentary humic and fulvic acids. *Geochimica et Cosmochimica Acta*, 62(9), 1567–1586. doi: 10.1016/S0016-7037(98)00089-1
- Bull, D. C., & Williamson, R. B. (2001). Prediction of principal metal-binding solid phases in estuarine sediments from color image analysis. *Environmental Science and Technology*, 35, 1658–1662. doi: 10.1021/es0015646
- Butler, I. B., Böttcher, M. E., Rickard, D., & Oldroyd, A. (2004). Sulfur isotope partitioning during experimental formation of pyrite via the polysulfide and hydrogen sulfide pathways: implications for the interpretation of sedimentary and hydrothermal pyrite isotope records. *Earth and Planetary Science Letters*, 228(3–4), 495–509. doi: 10.1016/j.epsl.2004.10.005
- Butler, I. B., & Rickard, D. (2000). Framboidal pyrite formation via the oxidation of iron (II) monosulfide by hydrogen sulphide. *Geochimica et Cosmochimica Acta*, 64(15), 2665–2672. doi: 10.1016/S0016-7037(00)00387-2
- Cahoon, L. B., Beretich, G. B., Thomas, C. J., & McDonald, A. M. (1993). Benthic microalgal production at Stellwagen Bank, Massachusetts Bay, USA. *Marine Ecology Progress Series*, 102, 179–185.
- Cahoon, L. B., & Cooke, J. E. (1992). Benthic microalgal production in Onslow Bay North Carolina, USA. *Marine Ecology Progress Series*, 84, 185–196.
- Callier, M. D., McKindsey, C. W., & Desrosiers, G. (2007). Multi-scale spatial variations in benthic sediment geochemistry and macrofaunal communities under a suspended mussel culture. *Marine Ecology Progress Series*, 348, 103–115. doi: 10.3354/meps07034
- Callier, M. D., McKindsey, C. W., & Desrosiers, G. (2008). Evaluation of indicators

- used to detect mussel farm influence on the benthos: Two case studies in the Magdalen Islands, Eastern Canada. *Aquaculture*, 278, 77–88. doi: 10.1016/j.aquaculture.2008.03.026
- Callier, M. D., Richard, M., McKindsey, C. W., Archambault, P., & Desrosiers, G. (2009). Responses of benthic macrofauna and biogeochemical fluxes to various levels of mussel biodeposition: An *in situ* “benthocosm” experiment. *Marine Pollution Bulletin*, 58(10), 1544–1553. doi: 10.1016/j.marpolbul.2009.05.010
- Canfield, D. E., Jørgensen, B. B., Fossing, H., Glud, R., Gundersen, J., Ramsing, N. B., ... Hall, P. O. J. (1993). Pathways of organic carbon oxidation in three continental margin sediments. *Marine Geology*, 113(1-2), 27–40. doi: 10.1016/0025-3227(93)90147-n
- Canfield, D. E., Raiswell, R., Westrich, J. T., Reaves, C. M., & Berner, R. A. (1986). The use of chromium reduction in the analysis of reduced inorganic sulfur in sediments and shales. *Chemical Geology*, 54(1-2), 149–155. doi: 10.1016/0009-2541(86)90078-1
- Canfield, D. E., Thamdrup, B., & Hansen, J. W. (1993). The anaerobic degradation of organic matter in Danish coastal sediments: Iron reduction, manganese reduction, and sulfate reduction. *Geochimica et Cosmochimica Acta*, 57(16), 3867–3883. doi: 10.1016/0016-7037(93)90340-3
- Carroll, M. L., Cochrane, S., Fieler, R., Velvin, R., & White, P. (2003). Organic enrichment of sediments from salmon farming in Norway: Environmental factors, management practices, and monitoring techniques. *Aquaculture*, 226(1-4), 165–180. doi: 10.1016/S0044-8486(03)00475-7
- Castine, S. A., Bourne, D. G., Trott, L. A., & McKinnon, D. A. (2009). Sediment microbial community analysis: Establishing impacts of aquaculture on a tropical mangrove ecosystem. *Aquaculture*, 297(1-4), 91–98. doi: 10.1016/j.aquaculture.2009.09.013
- Chamberlain, J., Fernandes, T. F., Read, P., Nickell, T. D., & Davies, I. M. (2001). Impacts of biodeposits from suspended mussel (*Mytilus edulis* L.) culture on the surrounding surficial sediments. *ICES Journal of Marine Science*, 58, 411–416. doi: 10.1006/jmsc.2000.1037
- Cicchetti, G., Latimer, J. S., Rego, S. A., Nelson, W. G., Bergen, B. J., & Coiro, L. L. (2006). Relationships between near-bottom dissolved oxygen and sediment profile camera measures. *Journal of Marine Systems*, 62(3-4), 124–141. doi: 10.1016/j.jmarsys.2006.03.005
- Cline, J. D. (1969). Spectrophotometric determination of hydrogen sulfide in natural waters. *Limnology and Oceanography*, 14(3), 454–458. doi: 10.4319/lo.1969.14.3.0454
- Cloern, J. E. (2001). Our evolving conceptual model of the coastal eutrophication problem. *Marine Ecology Progress Series*, 210(2001), 223–253. doi: 10.3354/meps210223
- Cooper, D. C., & Morse, J. W. (1998). Extractability of metal sulfide minerals in acidic solutions: Application to environmental studies of trace metal contamination within anoxic sediments. *Environmental Science and Technology*, 32(8), 1076–1078. doi: 10.1021/es970415t
- Cornwell, J. C., & Morse, J. W. (1987). The characterization of iron sulfide minerals in anoxic marine sediments. *Marine Chemistry*, 22(2-4), 193–206. doi: 10.1016/0304-4203(87)90008-9

- Cornwell, J. C., & Sampou, P. A. (1995). Environmental controls on iron sulfide mineral formation in a coastal plain estuary. In M. A. Viaravamurthy & M. A. A. Schoonen (Eds.), *Geochemical transformations of sedimentary sulfur* (pp. 224–242). Washington DC: ACS Symposium, 612. doi: 10.1021/bk-1995-0612.ch012
- Cranford, P. J., Hargrave, B. T., & Doucette, L. I. (2009). Benthic organic enrichment from suspended mussel (*Mytilus edulis*) culture in Prince Edward Island, Canada. *Aquaculture*, 292, 189–196. doi: 10.1016/j.aquaculture.2009.04.039
- Crawford, C. M., Macleod, C. K. A., & Mitchell, I. M. (2003). Effects of shellfish farming on the benthic environment. *Aquaculture*, 224(1-4), 117–140. doi: 10.1016/S0044-8486(03)00210-2
- Cypionka, H. (1994). Novel metabolic capacities of sulfate-reducing bacteria, and their activities in microbial mats. In L. J. Stal & P. Caumette (Eds.), *Microbial mats* (Vol. 35, pp. 367–376). Springer Berlin Heidelberg. doi: 10.1007/978-3-642-78991-5\_38
- Dahlbäck, B., & Gunnarsson, L. Å. H. (1981). Sedimentation and sulfate reduction under a mussel culture. *Marine Biology*, 63(3), 269–275. doi: 10.1007/BF00395996
- Danovaro, R., Corinaldesi, C., La Rosa, T., Luna, G. M., Mazzola, A., Mirto, S., ... Fabiano, M. (2003). Aquaculture impact on benthic microbes and organic matter cycling in coastal Mediterranean sediments: a synthesis. *Chemistry and Ecology*, 19, 59–65. doi: 10.1080/0275754031000084392
- Danovaro, R., Gambi, C., Luna, G. M., & Mirto, S. (2004). Sustainable impact of mussel farming in the Adriatic Sea (Mediterranean Sea): Evidence from biochemical, microbial and meiofaunal indicators. *Marine Pollution Bulletin*, 49, 325–333. doi: 10.1016/j.marpolbul.2004.02.038
- Diaz, R. J., & Rosenberg, R. (1995). Marine benthic hypoxia: A review of its ecological effects and the behavioural responses of benthic macrofauna. *Oceanography and Marine Biology: An Annual Review*, 33, 245–303.
- Diaz, R. J., & Schaffner, L. C. (1988). Comparison of sediment landscapes in the Chesapeake Bay as seen by surface and profile imaging. In M. P. Lynch & E. C. Krome (Eds.), *Understanding the estuary: Advances in Chesapeake Bay research* (Vol. 129, pp. 222–240). Chesapeake Research Consortium.
- Diaz, R. J., & Trefry, J. H. (2006). Comparison of sediment profile image data with profiles of oxygen and Eh from sediment cores. *Journal of Marine Systems*, 62, 164–172. doi: 10.1016/j.jmarsys.2006.01.009
- Di Toro, D. M., Mahony, J. D., Hansen, D. J., Scott, K. J., Carlson, A. R., & Ankley, G. T. (1992). Acid volatile sulfide predicts the acute toxicity of cadmium and nickel in sediments. *Environmental Science and Technology*, 26(1), 96–101. doi: 10.1021/es00025a009
- Di Toro, D. M., Mahony, J. D., Hansen, D. J., Scott, K. J., Hicks, M. B., Mayr, S. M., & Redmond, M. S. (1990). Toxicity of cadmium in sediments: The role of acid volatile sulfide. *Environmental Toxicology and Chemistry*, 9(12), 1487–1502. doi: 10.1002/etc.5620091208
- Downs, R. T., & Hall-Wallace, M. (2003). The American mineralogist crystal structure database. *American Mineralogist*, 88, 247–250.
- Duarte, P., Labarta, U., & Fernández-Reiriz, M. J. (2008). Modelling local food depletion effects in mussel rafts of Galician Rias. *Aquaculture*, 274(2), 300–312.

- FAO. (2014). *The state of world fisheries and aquaculture* (Tech. Rep.). Food and Agriculture Organization of the United Nations.
- Fenchel, T. (1996). Worm burrows and oxic microniches in marine sediments. 1. spatial and temporal scales. *Marine Biology*, 127(2), 289–295. doi: 10.1007/bf00942114
- Fenchel, T., King, G. M., & Blackburn, T. H. (2012). *Bacterial biogeochemistry: The ecophysiology of mineral cycling* (3rd ed.). London: Academic Press.
- Fichez, R. (1990). Absence of redox potential discontinuity in dark submarine cave sediments as evidence of oligotrophic conditions. *Estuarine, Coastal and Shelf Science*, 31(6), 875–881. doi: 10.1016/0272-7714(90)90089-A
- Froelich, P. N., Klinkhammer, G. P., Bender, M. L., Luedtke, N. A., Heath, G. R., Cullen, D., ... Maynard, V. (1979). Early oxidation of organic matter in pelagic sediments of the eastern equatorial Atlantic: suboxic diagenesis. *Geochimica et Cosmochimica Acta*, 43(7), 1075–1090. doi: 10.1016/0016-7037(79)90095-4
- Gagnon, C., Mucci, A., & Pelletier, É. (1995). Anomalous accumulation of acid-volatile sulphides (AVS) in a coastal marine sediment, Saguenay Fjord, Canada. *Geochimica et Cosmochimica Acta*, 59(13), 2663–2675. doi: 10.1016/0016-7037(95)00163-T
- Geider, R., & Roche, J. L. (2002). Redfield revisited: variability of c:n:p in marine microalgae and its biochemical basis. *European Journal of Phycology*, 37(1), 1–17. Retrieved from <http://dx.doi.org/10.1017/S0967026201003456> doi: 10.1017/S0967026201003456
- Germano, J. D., Rhoads, D. C., Valente, R. M., Carey, D. A., & Solan, M. (2011). The use of sediment profile imaging (SPI) for environmental impact assessments and monitoring studies: lessons learned from the past four decades. In R. N. Gibson, R. J. A. Atkinson, & J. D. M. Gordon (Eds.), *Oceanography and marine biology: an annual review* (Vol. 49, pp. 235–297). Boca Raton, Florida: Taylor & Francis.
- Gerwing, T. G., Gerwing, A. M. A., Drolet, D., Hamilton, D. J., & Barbeau, M. A. (2013). Comparison of two methods of measuring the depth of the redox potential discontinuity in intertidal mudflat sediments. *Marine Ecology Progress Series*, 487, 7–13. doi: 10.3354/Meps10407
- Giles, H., Broekhuizen, N., Bryan, K. R., & Pilditch, C. A. (2009). Modelling the dispersal of biodeposits from mussel farms: The importance of simulating biodeposit erosion and decay. *Aquaculture*, 291(3-4), 168–178. doi: 10.1016/j.aquaculture.2009.03.010
- Giles, H., & Pilditch, C. A. (2004). Effects of diet on sinking rates and erosion thresholds of mussel *Perna canaliculus* biodeposits. *Marine Ecology Progress Series*, 282, 205–219. doi: 10.3354/Meps282205
- Glud, R. N., Gundersen, J. K., Jørgensen, B. B., Revsbech, N. P., & Schulz, H. D. (1994). Diffusive and total oxygen uptake of deep-sea sediments in the eastern South Atlantic Ocean: *in situ* and laboratory measurements. *Deep Sea Research Part I: Oceanographic Research Papers*, 41(11-12), 1767–1788. doi: 10.1016/0967-0637(94)90072-8
- Glud, R. N., Tengberg, A., Kühl, M., Hall, P. O. J., & Klimant, I. (2001). An *in situ* instrument for planar O<sub>2</sub> optode measurements at benthic interfaces. *Limnology and Oceanography*, 46(8), 2073–2080. doi: 10.4319/lo.2001.46.8.2073
- Godfray, H. C. J., Beddington, J. R., Crute, I. R., Haddad, L., Lawrence, D., Muir, J. F., ... Toulmin, C. (2010). Food security: The challenge of feeding 9 billion people.



- Science*, 327(5967), 812–818. doi: 10.1126/science.1185383
- Goldhaber, M. B., & Kaplan, I. R. (1980). Mechanisms of sulfur incorporation and isotope fractionation during early diagenesis in sediments of the Gulf of California. *Marine Chemistry*, 9(2), 95–143.
- Grant, J., Bacher, C., Cranford, P. J., Guyondet, T., & Carreau, M. (2008). A spatially explicit ecosystem model of seston depletion in dense mussel culture. *Journal of Marine Systems*, 73(1–2), 155–168. doi: 10.1016/j.jmarsys.2007.10.007
- Grant, J., Hatcher, A., Scott, D. B., Pocklington, P., Schafer, C. T., & Winters, G. V. (1995). A multidisciplinary approach to evaluating impacts of shellfish aquaculture on benthic communities. *Estuaries*, 18(1 A), 124–144. doi: 10.2307/1352288
- Gray, J. S., Wu, R. S.-S., & Or, Y. Y. (2002). Effects of hypoxia and organic enrichment on the coastal marine environment. *Marine Ecology Progress Series*, 238, 249–279. doi: 10.3354/meps238249
- Gražulis, S., Chateigner, D., Downs, R. T., Yokochi, A. F. T., Quirós, M., Lutterotti, L., ... Le Bail, A. (2009). Crystallography Open Database — an open-access collection of crystal structures. *Journal of Applied Crystallography*, 42(4), 726–729. doi: 10.1107/S0021889809016690
- Gražulis, S., Daškevic, A., Merkys, A., Chateigner, D., Lutterotti, L., Quirós, M., ... Le Bail, A. (2012). Crystallography Open Database (COD): an open-access collection of crystal structures and platform for world-wide collaboration. *Nucleic Acids Research*, 40(D1), D420–D427. doi: 10.1093/nar/gkr900
- Grizzle, R. E., & Penniman, C. A. (1991). Effects of organic enrichment on estuarine macrofaunal benthos: a comparison of sediment profile imaging and traditional methods. *Marine Ecology Progress Series*, 74(2-3), 249–262. doi: 10.3354/Meps074249
- Hansen, M. H., Ingvorsen, K., & Jørgensen, B. B. (1978). Mechanisms of hydrogen sulfide release from coastal marine sediments to the atmosphere. *Limnology and Oceanography*, 23(1), 68–76. doi: 10.4319/lo.1978.23.1.0068
- Hartstein, N. D. (2005). Acoustical and sedimentological characterization of substrates in and around sheltered and open-ocean mussel aquaculture sites and its bearing on the dispersal of mussel debris. *IEEE Journal of Oceanic Engineering*, 30(1), 85–94. doi: 10.1109/JOE.2004.841388
- Hartstein, N. D., & Rowden, A. A. (2004). Effect of biodeposits from mussel culture on macroinvertebrate assemblages at sites of different hydrodynamic regime. *Marine Environmental Research*, 57(5), 339–357. doi: 10.1016/j.marenvres.2003.11.003
- Hartstein, N. D., & Stevens, C. L. (2005). Deposition beneath long-line mussel farms. *Aquacultural Engineering*, 33(3), 192–213. doi: 10.1016/j.aquaeng.2005.01.002
- Hay, C. H. (1990). The dispersal of sporophytes of *Undaria pinnatifida* by coastal shipping in New Zealand, and implications for further dispersal of *Undaria* in France. *British Phycological Journal*, 25(4), 301–313. doi: 10.1080/00071619000650331
- Hedges, J. I., Clark, W. A., & Cowie, G. L. (1988). Fluxes and reactivities of organic matter in a coastal marine bay. *Limnology and Oceanography*, 33(5), 1137–1152. doi: 10.4319/lo.1988.33.5.1137
- Hoehler, T. M., Alperin, M. J., Albert, D. B., & Martens, C. S. (1998). Thermodynamic control on hydrogen concentrations in anoxic sediments. *Geochimica et*

- Cosmochimica Acta*, 62(10), 1745–1756. doi: 10.1016/S0016-7037(98)00106-9
- Holmer, M., & Kristensen, E. (1994). Organic matter mineralization in an organic-rich sediment: Experimental stimulation of sulfate reduction by fish food pellets. *FEMS Microbiology Ecology*, 14(1), 33–44. doi: 10.1111/j.1574-6941.1994.tb00088.x
- Huntsman, S. A., & Barber, R. T. (1977). Primary production off northwest Africa: the relationship to wind and nutrient conditions. *Deep Sea Research*, 24(1), 25–33. doi: 10.1016/0146-6291(77)90538-0
- Jakobsson, M., Løvlie, R., Al-Hanbali, H., Arnold, E., Backman, J., & Mörrth, M. (2000). Manganese and color cycles in Arctic Ocean sediments constrain Pleistocene chronology. *Geology*, 28(1), 23. doi: 10.1130/0091-7613(2000)28<23:maccia>2.0.co;2
- Jeroschewski, P. (1996). An amperometric microsensor for the determination of H<sub>2</sub>S in aquatic environments. *Analytical Chemistry*, 68(24), 4351–4357. doi: 10.1021/ac960091b
- Johnson, R. G. (1972). Conceptual models of benthic marine communities. In T. J. M. Schopf (Ed.), *Models in paleobiology* (pp. 149–159). San Francisco: Freeman, Cooper & Co.
- Joint, I. R. (1978). Microbial production of an estuarine mudflat. *Estuarine and Coastal Marine Science*, 7, 185–95.
- Jones, G. A., & Kaiteris, P. (1983). A vacuum-gasometric technique for rapid and precise analysis of calcium carbonate in sediments and soils. *Journal of Sedimentary Research*, 53(2), 655–660.
- Jørgensen, B. B. (1977a). Bacterial sulfate reduction within reduced microniches of oxidized marine sediments. *Marine Biology*, 41(1), 7–17. doi: 10.1007/BF00390576
- Jørgensen, B. B. (1977b). The sulfur cycle of a coastal marine sediment (Limfjorden, Denmark). *Limnology and Oceanography*, 22(5), 814–832. doi: 10.4319/lo.1977.22.5.0814
- Jørgensen, B. B. (1982). Mineralization of organic matter in the sea bed—the role of sulphate reduction. *Nature*, 296, 643–645. doi: 10.1038/296643a0
- Jørgensen, B. B. (2006). Bacteria and marine biogeochemistry. In H. D. Schulz & M. Zabel (Eds.), *Marine geochemistry* (pp. 169–206). Springer Berlin Heidelberg. doi: 10.1007/3-540-32144-6\_5
- Jørgensen, B. B., & Bak, F. (1991). Pathways and microbiology of thiosulfate transformations and sulfate reduction in a marine sediment (Kattegat, Denmark). *Applied and Environmental Microbiology*, 57(3), 847–856.
- Jørgensen, B. B., Isaksen, M. F., & Jannasch, H. W. (1992). Bacterial sulfate reduction above 100°C in deep-sea hydrothermal vent sediments. *Science*, 258(5089), 1756–1757. doi: 10.1126/science.258.5089.1756
- Jørgensen, B. B., & Kasten, S. (2006). Sulfur cycling and methane oxidation. In H. D. Schulz & M. Zabel (Eds.), *Marine geochemistry* (pp. 271–308). Berlin: Springer.
- Kaspar, H. F., Gillespie, P. A., Boyer, I. C., & MacKenzie, A. L. (1985). Effects of mussel aquaculture on the nitrogen cycle and benthic communities in Kenepuru Sound, Marlborough Sounds, New Zealand. *Marine Biology*, 85(2), 127–136. doi: 10.1007/BF00397431
- Keeley, N. B., Cromey, C. J., Goodwin, E. O., Gibbs, M. T., & Macleod, C. M. (2013).

- Predictive depositional modelling (depomod) of the interactive effect of current flow and resuspension on ecological impacts beneath salmon farms. *Aquaculture Environment Interactions*, 3(3), 275–291. doi: 10.3354/aei00068
- Kirk, J. T. O. (1994). *Light and photosynthesis in aquatic ecosystems* (2nd ed.). Cambridge University Press. doi: 10.1017/CBO9780511623370
- Klausmeier, C. A., Litchman, E., Daufresne, T., & Levin, S. A. (2004). Optimal nitrogen-to-phosphorus stoichiometry of phytoplankton. *Nature*, 429(6988), 171–174. doi: 10.1038/nature02454
- Knoblauch, C., Sahm, K., & Jørgensen, B. B. (1999). Psychrophilic sulfate-reducing bacteria isolated from permanently cold arctic marine sediments: description of *Desulfofrigus oceanense* gen. nov., sp. nov., *Desulfofrigus fragile* sp. nov., *Desulfotalea gelida* gen. nov., sp. nov., *Desulfotalea psychrophila* gen. nov., sp. nov. and *Desulfotalea arctica* sp. nov. *International Journal of Systematic and Evolutionary Microbiology*, 49(4), 1631–1643.
- Kristensen, E. (1984). Effect of natural concentrations on nutrient exchange between a polychaete burrow in estuarine sediment and the overlying water. *Journal of Experimental Marine Biology and Ecology*, 75(2), 171–190. doi: 10.1016/0022-0981(84)90179-5
- Kristensen, E. (2000). Organic matter diagenesis at the oxic/anoxic interface in coastal marine sediments, with emphasis on the role of burrowing animals. *Hydrobiologia*, 426(1), 1–24. doi: 10.1023/A:1003980226194
- Kristensen, E., Penha-Lopes, G., Delefosse, M., Valdemarsen, T., Quintana, C. O., & Banta, G. T. (2012). What is bioturbation? The need for a precise definition for fauna in aquatic sciences. *Marine Ecology Progress Series*, 446, 285–302. doi: 10.3354/meps09506
- Kuehni, R. G. (2003). *Color space and its divisions*. Hoboken, New Jersey: John Wiley & Sons. doi: 10.1002/0471432261
- Kühl, M., Steuckart, C., Eickert, G., & Jeroschewski, P. (1998). A H<sub>2</sub>S microsensor for profiling biofilms and sediments: Application in an acidic lake sediment. *Aquatic Microbial Ecology*, 15(2), 201–209. doi: 10.3354/ame015201
- Lasorsa, B., & Casas, A. (1996). A comparison of sample handling and analytical methods for determination of acid volatile sulfides in sediment. *Marine Chemistry*, 52(3-4), 211–220. doi: 10.1016/0304-4203(95)00074-7
- Lennie, A. R., Redfern, S. A. T., Champness, P. E., Stoddart, C. P., Schofield, P. F., & Vaughan, D. J. (1997). Transformation of mackinawite to greigite: An in situ X-ray powder diffraction and transmission electron microscope study. *American Mineralogist*, 82(3-4), 302–309.
- Lennie, A. R., Redfern, S. A. T., Schofield, B., & Vaughan, D. J. (1995). Synthesis and rietveld crystal structure refinement of mackinawite, tetragonal FeS. *Mineralogical Magazine*, 59(4), 677–683.
- Libes, S. M. (2009). *Introduction to marine biogeochemistry* (2nd ed.). New York: Academic Press.
- Lluch-Cota, S.-E. (2000). Coastal upwelling in the eastern Gulf of California. *Oceanologica Acta*, 23(6), 731–740. doi: 10.1016/S0399-1784(00)00121-3
- Loring, D. H., & Rantala, R. T. T. (1992). Manual for the geochemical analyses of marine sediments and suspended particulate matter. *Earth-Science Reviews*, 32(4), 235–283. doi: 10.1016/0012-8252(92)90001-A
- Luther III, G. W. (1991). Pyrite synthesis via polysulfide compounds. *Geochimica et*

- Cosmochimica Acta*, 55(10), 2839–2849. doi: 10.1016/0016-7037(91)90449-F
- Luther III, G. W. (2005). Acid volatile sulfide — a comment. *Marine Chemistry*, 97(3-4), 198–205. doi: 10.1016/j.marchem.2005.08.001
- Lyle, M. (1983). The brown–green color transition in marine sediments: A marker of the Fe(III)–Fe(II) redox boundary. *Limnology and Oceanography*, 28, 1026–1033. doi: 10.4319/lo.1983.28.5.1026
- MacIntyre, H. L., & Cullen, J. J. (1996). Primary production by suspended and benthic microalgae in a turbid estuary: time-scales of variability in San Antonio Bay, Texas. *Marine Ecology Progress Series*, 145, 245–268.
- Mackay, K., Mackay, E., Neil, H., Mitchell, J., & Bardsley, S. (2012). *Hauraki Gulf. NIWA chart, miscellaneous series 91*. National Institute of Water & Atmospheric Research Ltd.
- Mattsson, J., & Lindén, O. (1983). Benthic macrofauna succession under mussels, *Mytilus edulis* L. (Bivalvia), cultured on hanging long-lines. *Sarsia*, 68(2), 97–102. doi: 10.1080/00364827.1983.10420561
- McKindsey, C. W., Archambault, P., Callier, M. D., & Olivier, F. (2011). Influence of suspended and off-bottom mussel culture on the sea bottom and benthic habitats: a review. *Canadian Journal of Zoology*, 89(7), 622–646. doi: 10.1139/z11-037
- Meysman, F. J. R., & Middelburg, J. J. (2005). Acid-volatile sulfide (AVS) — a comment. *Marine Chemistry*, 97(3-4), 206–212. doi: 10.1016/j.marchem.2005.08.005
- Millero, F. J., Plese, T., & Fernandez, M. (1988). The dissociation of hydrogen sulfide in seawater. *Limnology and Oceanography*, 33(2), 269–274. doi: 10.4319/lo.1988.33.2.0269
- Morse, J. W., & Berner, R. A. (1995). What determines sedimentary C/S ratios? *Geochimica et Cosmochimica Acta*, 59(6), 1073–1077. doi: 10.1016/0016-7037(95)00024-t
- Morse, J. W., & Cornwell, J. C. (1987). Analysis and distribution of iron sulfide minerals in recent anoxic marine sediments. *Marine Chemistry*, 22(1), 55–69. doi: 10.1016/0304-4203(87)90048-X
- Morse, J. W., & Luther III, G. W. (1999). Chemical influences on trace metal-sulfide interactions in anoxic sediments. *Geochimica et Cosmochimica Acta*, 63(19-20), 3373–3378. doi: 10.1016/S0016-7037(99)00258-6
- Morse, J. W., Millero, F. J., Cornwell, J. C., & Rickard, D. (1987). The chemistry of the hydrogen sulfide and iron sulfide systems in natural waters. *Earth-Science Reviews*, 24(1), 1–42. doi: 10.1016/0012-8252(87)90046-8
- Morse, J. W., & Rickard, D. (2004). Chemical dynamics of sedimentary acid volatile sulfide. *Environmental Science and Technology*, 38(7), 131A–136A. doi: 10.1021/es040447y
- Morse, J. W., & Wang, Q. (1997). Pyrite formation under conditions approximating those in anoxic sediments: II. influence of precursor iron minerals and organic matter. *Marine Chemistry*, 57(3-4), 187–193. doi: 10.1016/S0304-4203(97)00050-9
- Muggeo, V. M. R. (2003). Estimating regression models with unknown break-points. *Statistics in Medicine*, 22, 3055–3071. doi: 10.1002/sim.1545
- Mulsow, S., Krieger, Y., & Kennedy, R. (2006). Sediment profile imaging (SPI) and micro-electrode technologies in impact assessment studies: Example from two

- fjords in Southern Chile used for fish farming. *Journal of Marine Systems*, 62, 152–163. doi: 10.1016/j.jmarsys.2005.09.012
- Newhall, S. M., Nickerson, D., & Judd, D. B. (1943). Final report of the O.S.A. subcommittee on the spacing of the Munsell colors. *Journal of the Optical Society of America*, 33(7), 385–411. doi: 10.1364/JOSA.33.000385
- Nilsson, H. C., & Rosenberg, R. (1997). Benthic habitat quality assessment of an oxygen stressed fjord by surface and sediment profile images. *Journal of Marine Systems*, 11(3–4), 249–264. doi: 10.1016/S0924-7963(96)00111-X
- Nilsson, H. C., & Rosenberg, R. (2000). Succession in marine benthic habitats and fauna in response to oxygen deficiency: Analysed by sediment profile-imaging and by grab samples. *Marine Ecology Progress Series*, 197, 139–149. doi: 10.3354/meps197139
- Nixon, S. W. (1995). Coastal marine eutrophication: a definition, social causes, and future concerns. *Ophelia*, 41, 199–219.
- O'Connor, B. D. S., Costelloe, J., Keegan, B. F., & Rhoads, D. C. (1989). The use of REMOTS® technology in monitoring coastal enrichment resulting from mariculture. *Marine Pollution Bulletin*, 20(8), 384–390. doi: 10.1016/0025-326x(89)90316-0
- Oenema, O. (1990). Sulfate reduction in fine-grained sediments in the Eastern Scheldt, southwest Netherlands. *Biogeochemistry*, 9(1), 53–74. doi: 10.1007/BF00002717
- Paavo, B. L. (2007). *Soft-sediment benthos of Aramoana and Blueskin Bay (Otago, New Zealand) and effects of dredge-spoil disposal* (Unpublished doctoral dissertation). Department of Marine Science, University of Otago, New Zealand.
- Patterson, A., Kennedy, R., O'Reilly, R., & Keegan, B. F. (2006). Field test of a novel, low-cost, scanner-based sediment profile imaging camera. *Limnology and Oceanography: Methods*, 4, 30–37. doi: 10.4319/lom.2006.4.30
- Pearson, T. H., & Rosenberg, R. (1978). Macrobenthic succession in relation to organic enrichment and pollution of the marine environment. *Oceanography and Marine Biology: An Annual Review*, 16, 229–311.
- Pinto, R., Patrício, J., Baeta, A., Fath, B. D., Neto, J. M., & Marques, J. C. (2009). Review and evaluation of estuarine biotic indices to assess benthic condition. *Ecological Indicators*, 9(1), 1–25. doi: 10.1016/j.ecolind.2008.01.005
- Plew, D. R., Stevens, C. L., Spigel, R. H., & Hartstein, N. D. (2005). Hydrodynamic implications of large offshore mussel farms. *IEEE Journal of Oceanic Engineering*, 30(1), 95–108. doi: 10.1109/JOE.2004.841387
- Prahl, F. G., Ertel, J. R., Goni, M. A., Sparrow, M. A., & Eversmeyer, B. (1994). Terrestrial organic carbon contributions to sediments on the Washington margin. *Geochimica et Cosmochimica Acta*, 58(14), 3035–3048. doi: 10.1016/0016-7037(94)90177-5
- Quigg, A., Finkel, Z. V., Irwin, A. J., Rosenthal, Y., Ho, T.-Y., Reinfelder, J. R., ... Falkowski, P. G. (2003). The evolutionary inheritance of elemental stoichiometry in marine phytoplankton. *Nature*, 425(6955), 291–294. doi: 10.1038/nature01953
- R Core Team. (2013). *R: A language and environment for statistical computing*. Vienna, Austria, URL <http://www.R-project.org>.
- Rabus, R., Hansen, T. A., & Widdel, F. (2013). Dissimilatory sulfate- and sulfur-reducing prokaryotes. In E. Rosenberg, E. F. DeLong, S. Lory,

- E. Stackebrandt, & F. Thompson (Eds.), *The prokaryotes* (pp. 309–404). Springer Berlin Heidelberg. doi: 10.1007/978-3-642-30141-4\_70
- Raftery, A. E. (1995). Bayesian model selection in social research. *Sociological Methodology*, 25, 111–163.
- Raiswell, R., & Berner, R. A. (1985). Pyrite formation in euxinic and semi-euxinic sediments. *American Journal of Science*, 285(8), 710–724. doi: 10.2475/ajs.285.8.710
- Redfield, A. C. (1934). On the proportions of organic derivatives in sea water and their relation to the composition of plankton. In R. J. Daniel (Ed.), *James Johnstone memorial volume* (pp. 177–192). University Press of Liverpool.
- Reeburgh, W. S. (1983). Rates of biogeochemical processes in anoxic sediments. *Annual Review of Earth and Planetary Sciences*, 11(1), 269–298. doi: 10.1146/annurev.ea.11.050183.001413
- Revsbech, N. P., Jørgensen, B. B., & Blackburn, T. H. (1980). Oxygen in the sea bottom measured with a microelectrode. *Science*, 207(4437), 1355–1356. doi: 10.1126/science.207.4437.1355
- Rhoads, D. C., & Boyer, L. F. (1982). The effects of marine benthos on physical properties of sediments. In P. L. McCall & M. J. S. Tevesz (Eds.), *Animal–sediment relations* (pp. 3–52). Springer US. doi: 10.1007/978-1-4757-1317-6\_1
- Rhoads, D. C., & Cande, S. (1971). Sediment profile camera for *in situ* study of organism–sediment relations. *Limnology and Oceanography*, 16, 110–114. doi: 10.4319/lo.1971.16.1.0110
- Rhoads, D. C., & Germano, J. D. (1982). Characterization of organism–sediment relations using sediment profile imaging: an efficient method of remote ecological monitoring of the seafloor (Remots™ system). *Marine Ecology Progress Series*, 8, 115–128.
- Rhoads, D. C., & Germano, J. D. (1986). Interpreting long-term changes in benthic community structure: a new protocol. *Hydrobiologia*, 142(1), 291–308. doi: 10.1007/bf00026766
- Rhoads, D. C., McCall, P. L., & Yingst, J. Y. (1978). Disturbance and production on the estuarine seafloor. *American Scientist*, 66(5), 577–586.
- Rhoads, D. C., & Young, D. K. (1970). The influence of deposit-feeding organisms on sediment stability and community trophic structure. *Journal of Marine Research*, 28(2), 150–178.
- Richardson, K., & Jørgensen, B. B. (2013). Eutrophication: Definition, history and effects. In *Eutrophication in coastal marine ecosystems* (pp. 1–19). American Geophysical Union. doi: 10.1029/CE052p0001
- Rickard, D. (1975). Kinetics and mechanism of pyrite formation at low-temperatures. *American Journal of Science*, 275(6), 636–652. doi: 10.2475/ajs.275.6.636
- Rickard, D. (1995). Kinetics of FeS precipitation: Part 1. competing reaction mechanisms. *Geochimica et Cosmochimica Acta*, 59(21), 4367–4379. doi: 10.1016/0016-7037(95)00251-T
- Rickard, D. (1997). Kinetics of pyrite formation by the H<sub>2</sub>S oxidation of iron (II) monosulfide in aqueous solutions between 25 and 125°C: The rate equation. *Geochimica et Cosmochimica Acta*, 61(1), 115–132. doi: 10.1016/S0016-7037(96)00321-3
- Rickard, D., & Luther III, G. W. (1997). Kinetics of pyrite formation by the H<sub>2</sub>S

- oxidation of iron (II) monosulfide in aqueous solutions between 25 and 125°C: The mechanism. *Geochimica et Cosmochimica Acta*, 61(1), 135–147. doi: 10.1016/S0016-7037(96)00322-5
- Rickard, D., & Luther III, G. W. (2007). Chemistry of iron sulfides. *Chemical Reviews*, 107(2), 514–562. doi: 10.1021/cr0503658
- Rickard, D., & Morse, J. W. (2005). Acid volatile sulfide (AVS). *Marine Chemistry*, 97(3–4), 141–197. doi: 10.1016/j.marchem.2005.08.004
- Robert, P., McKindsey, C. W., Chaillou, G., & Archambault, P. (2013). Dose-dependent response of a benthic system to biodeposition from suspended blue mussel (*Mytilus edulis*) culture. *Marine Pollution Bulletin*, 66(1), 92–104. doi: 10.1016/j.marpolbul.2012.11.003
- Romero-Ramirez, A., Grémare, A., Desmalades, M., & Duchêne, J. C. (2013). Semi-automatic analysis and interpretation of sediment profile images. *Environmental Modelling & Software*, 47, 42–54. doi: 10.1016/j.envsoft.2013.04.008
- Rosenberg, R., Magnusson, M., & Nilsson, H. C. (2009). Temporal and spatial changes in marine benthic habitats in relation to the EU Water Framework Directive: The use of sediment profile imagery. *Marine Pollution Bulletin*, 58, 565–572. doi: 10.1016/j.marpolbul.2008.11.023
- Rosenberg, R., Nilsson, H. C., & Diaz, R. J. (2001). Response of benthic fauna and changing sediment redox profiles over a hypoxic gradient. *Estuarine, Coastal and Shelf Science*, 53(3), 343–350. doi: 10.1006/ecss.2001.0810
- Schulz, H. D., & Zabel, M. (2006). *Marine geochemistry*. Springer Berlin Heidelberg. doi: 10.1007/3-540-32144-6
- Schwarz, G. (1978). Estimating the dimension of a model. *The Annals of Statistics*, 6(2), 461–464. doi: 10.2307/2958889
- Sikes, E. L., Uhle, M. E., Nodder, S. D., & Howard, M. E. (2009). Sources of organic matter in a coastal marine environment: Evidence from n-alkanes and their <sup>13</sup>C distributions in the hauraki gulf, New Zealand. *Marine Chemistry*, 113(3–4), 149–163. doi: 10.1016/j.marchem.2008.12.003
- Skinner, B. J., Erd, R. C., & Grimaldi, F. S. (1964). Greigite, the thio-spinel of iron; a new mineral. *The American Mineralogist*, 49, 543–555.
- Solan, M., Germano, J. D., Rhoads, D. C., Smith, C., Michaud, E., Parry, D., ... Rosenberg, R. (2003). Towards a greater understanding of pattern, scale and process in marine benthic systems: A picture is worth a thousand worms. *Journal of Experimental Marine Biology and Ecology*, 285–286, 313–338. doi: 10.1016/S0022-0981(02)00535-X
- Solan, M., & Kennedy, B. (2002). Observation and quantification of *in situ* animal–sediment relations using time-lapse sediment profile imagery (t-SPI). *Marine Ecology Progress Series*, 228, 179–191. doi: 10.3354/meps228179
- Solan, M., Wigham, B. D., Hudson, I. R., Kennedy, R., Coulon, C. H., Norling, K., ... Rosenberg, R. (2004). In situ quantification of bioturbation using time-lapse fluorescent sediment profile imaging (f-SPI), luminophore tracers and model simulation. *Marine Ecology Progress Series*, 271, 1–12. doi: 10.3354/meps271001
- Sorokin, I. I., Giovanardi, O., Pranovi, F., & Sorokin, P. I. (1999). Need for restricting bivalve culture in the southern basin of the Lagoon of Venice. *Hydrobiologia*, 400, 141–148. doi: 10.1023/A:1003707231839

- Sorokin, Y. I., & Zakuskina, O. Y. (2012). Acid-labile sulfides in shallow marine bottom sediments: A review of the impact on ecosystems in the Azov Sea, the NE Black Sea shelf and NW Adriatic lagoons. *Estuarine, Coastal and Shelf Science*, 98, 42–48. doi: 10.1016/j.ecss.2011.11.020
- Steinacher, M., Joos, F., Frölicher, T. L., Bopp, L., Cadule, P., Cocco, V., ... Segschneider, J. (2010). Projected 21st century decrease in marine productivity: a multi-model analysis. *Biogeosciences*, 7(3), 979–1005. doi: 10.5194/bg-7-979-2010
- Stenton-Dozey, J., Probyn, T., & Busby, A. (2001). Impact of mussel (*Mytilus galloprovincialis*) raft-culture on benthic macrofauna, in situ oxygen uptake, and nutrient fluxes in Saldanha Bay, South Africa. *Canadian Journal of Fisheries and Aquatic Sciences*, 58, 1021–1031. doi: 10.1139/cjfas-58-5-1021
- Teal, L. R., Parker, R., Fones, G., & Solan, M. (2009). Simultaneous determination of in situ vertical transitions of color, pore-water metals, and visualization of infaunal activity in marine sediments. *Limnology and Oceanography*, 54, 1801–1810. doi: 10.4319/lo.2009.54.5.1801
- Theberge, S. M., & Luther III, G. W. (1997). Determination of the electrochemical properties of a soluble aqueous FeS species present in sulfidic solutions. *Aquatic Geochemistry*, 3(3), 191–211. doi: 10.1023/a:1009648026806
- Thode-Andersen, S., & Jørgensen, B. B. (1989). Sulfate reduction and the formation of  $^{35}\text{S}$ -labeled FeS, FeS<sub>2</sub>, and S<sup>0</sup> in coastal marine sediments. *Limnology and Oceanography*, 34(5), 793–806. doi: 10.4319/lo.1989.34.5.0793
- Van Duyl, F. C., Kop, A. J., Kok, A., & Sandee, A. J. J. (1992). The impact of organic matter and macrozoobenthos on bacterial and oxygen variables in marine sediment boxcosms. *Netherlands Journal of Sea Research*, 29(4), 343–355.
- van Griethuysen, C., Gillissen, F., & Koelmans, A. A. (2002). Measuring acid volatile sulphide in floodplain lake sediments: Effect of reaction time, sample size and aeration. *Chemosphere*, 47(4), 395–400. doi: 10.1016/S0045-6535(01)00314-9
- Varela, M., & Penas, E. (1985). Primary production of benthic microalgae in an intertidal sand flat of the Ria de Arosa, NW Spain. *Marine Ecology Progress Series*, 25, 111–119.
- Vogel, A. I. (1989). *Vogel's textbook of quantitative chemical analysis* (5th ed.). New York: Revised by G. H. Jeffery et al. John Wiley & Sons, Inc.
- Vopel, K., & Funnell, G. (2006). *Wilson Bay sediment profile imaging: 1. instrument test* (Technical Report No. 2006/09). Environment Waikato.
- Vopel, K., Giles, H., Budd, R., & Hart, C. (2007). *Wilson Bay sediment profile imaging: 2. pilot study* (NIWA Client Report No. HAM2007-080). NIWA Hamilton.
- Wenzhöfer, F., & Glud, R. N. (2002). Benthic carbon mineralization in the Atlantic: a synthesis based on in situ data from the last decade. *Deep Sea Research Part I: Oceanographic Research Papers*, 49(7), 1255–1279. doi: 10.1016/S0967-0637(02)00025-0
- Westrich, J. T. (1983). *The consequences and controls of bacterial sulfate reduction in marine sediments* (Unpublished doctoral dissertation). Yale University.
- Westrich, J. T., & Berner, R. A. (1984). The role of sedimentary organic matter in bacterial sulfate reduction: The G model tested. *Limnology and Oceanography*, 29(2), 236–249. doi: 10.4319/lo.1984.29.2.0236
- Wieder, R. K., Lang, G. E., & Granus, V. A. (1985). An evaluation of wet chemical methods for quantifying sulfur fractions in freshwater wetland peat. *Limnology*



- and Oceanography*, 30(5), 1109–1115. doi: 10.4319/lo.1985.30.5.1109
- Wildish, D. J., Hargrave, B. T., MacLeod, C., & Crawford, C. (2003). Detection of organic enrichment near finfish net-pens by sediment profile imaging at SCUBA-accessible depths. *Journal of Experimental Marine Biology and Ecology*, 285–286, 403–413. doi: 10.1016/S0022-0981(02)00540-3
- Williamson, R. B., Wilcock, R. J., Wise, B. E., & Pickmere, S. E. (1999). Effect of burrowing by the crab *Helice crassa* on chemistry of intertidal muddy sediments. *Environmental Toxicology and Chemistry*, 18, 2078–2086. doi: 10.1897/1551-5028(1999)018<2078:EOBBTC>2.3.CO;2
- Wong, K. L. C., & O'Shea, S. (2010). Sediment macrobenthos off eastern Waiheke Island, Hauraki Gulf, New Zealand. *New Zealand Journal of Marine and Freshwater Research*, 44(3), 149–165. doi: 10.1080/00288330.2010.498088
- Wong, K. L. C., & O'Shea, S. (2011). The effects of a mussel farm on benthic macrofaunal communities in Hauraki Gulf, New Zealand. *New Zealand Journal of Marine and Freshwater Research*, 45(2), 187–212. doi: 10.1080/00288330.2010.550628
- Ye, L.-X., Ritz, D. A., Fenton, G. E., & Lewis, M. E. (1991). Tracing the influence on sediments of organic waste from a salmonid farm using stable isotope analysis. *Journal of Experimental Marine Biology and Ecology*, 145(2), 161–174. doi: 10.1016/0022-0981(91)90173-t
- Zhabina, N. N., & Volkov, I. I. (1978). A method of determination of various sulfur compounds in sea sediments and rocks. In W. E. Krumbein (Ed.), *Environmental biogeochemistry; methods, metals and assessment* (Vol. 3, pp. 735–745). Ann Arbor, Michigan: Ann Arbor Science Publishers.

# Appendix A

## Sediment particle size analyses

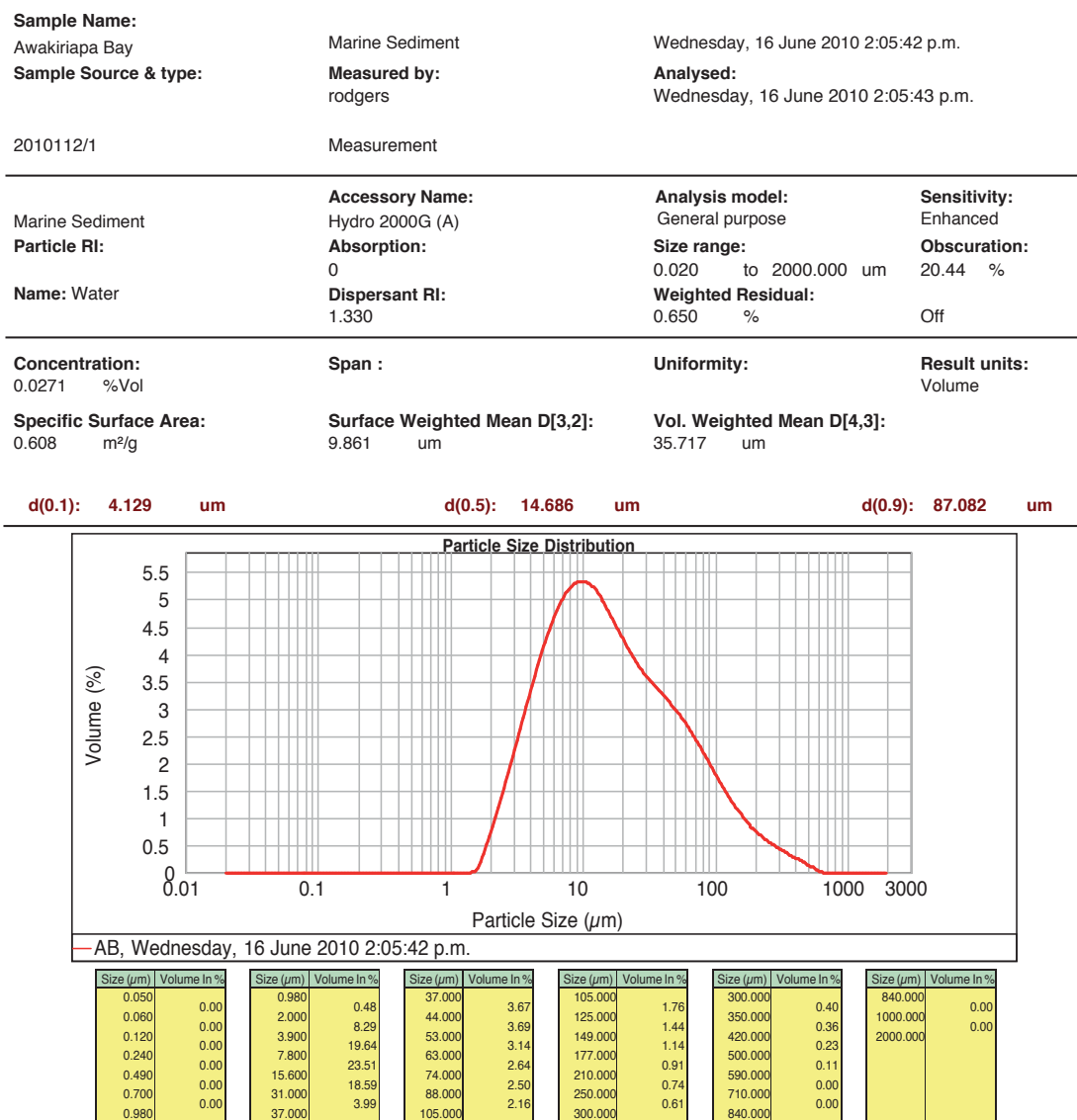


**Figure A.1:** Laser particle size analysis (Malvern Mastersizer 2000) of the upper 4 cm sediment at Awakiriapa Bay, Hauraki Gulf, New Zealand.

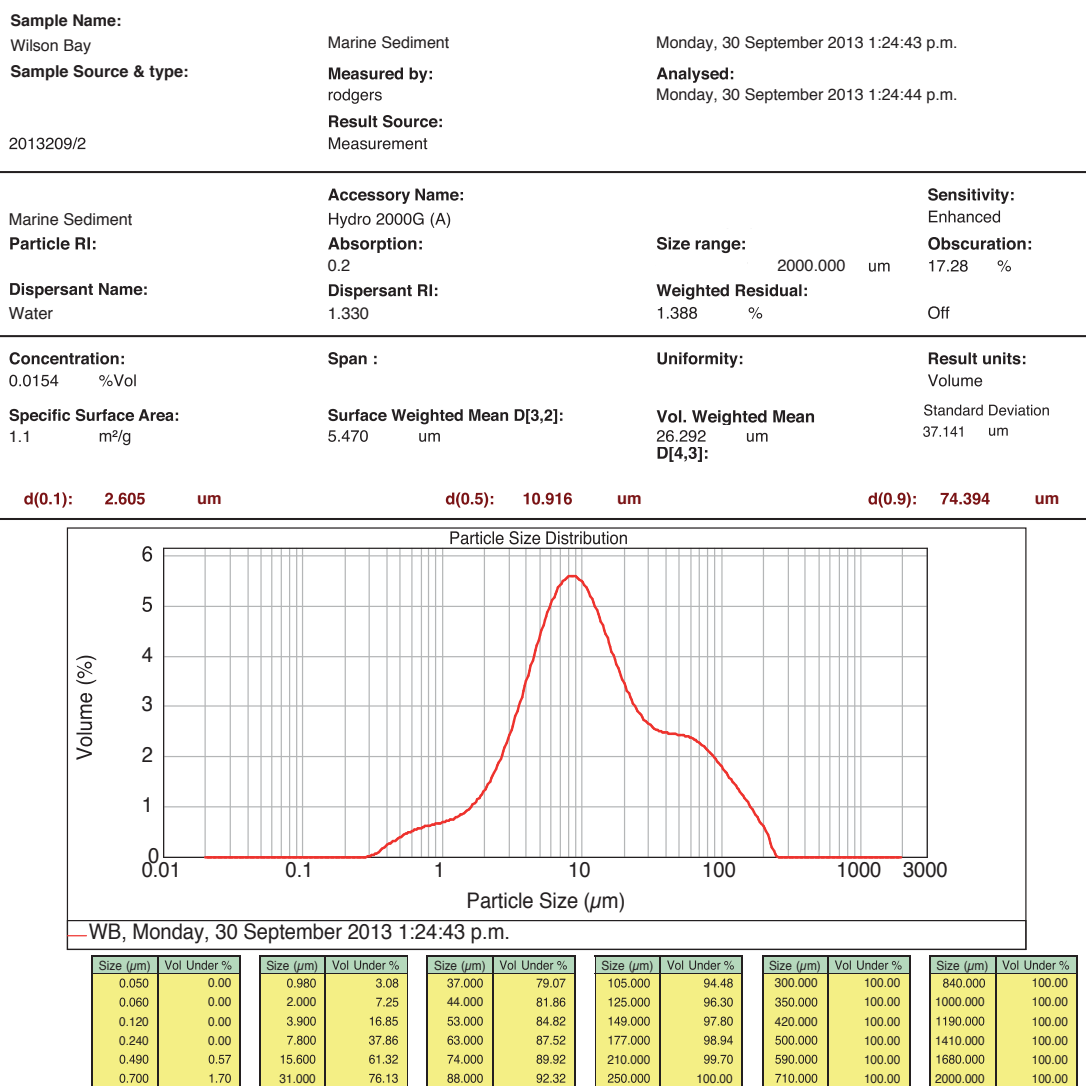


**Figure A.2:** Laser particle size analysis (Malvern Mastersizer 2000) of the upper 4 cm sediment at Wilson Bay, Hauraki Gulf, New Zealand.

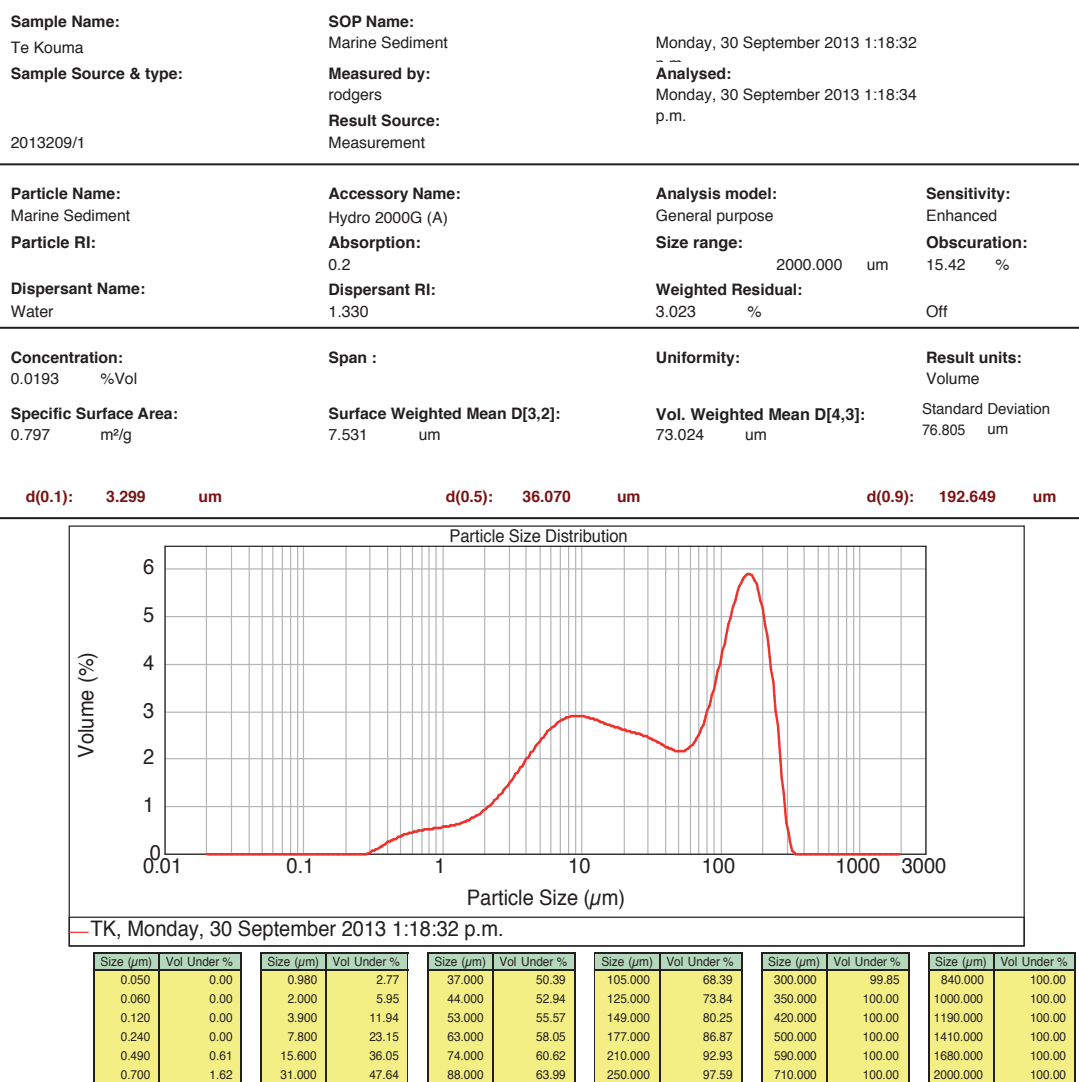


**Figure A.3:** Laser particle size analysis (Malvern Mastersizer 2000) of the upper 4 cm sediment at Te Kouma, Hauraki Gulf, New Zealand.

## Appendix B

### AVS/colour correlation data

**Table B.1:** Data used to create the AVS/colour correlation in Chapter 1 that was sampled from Awakiriapa Bay, Waiheke Island, New Zealand. Depth: depth sampled from the sediment core; Grey value: Mean sediment colour intensity of the homogenised sample; AVS: concentration of acid volatile sulfide (AVS) as extracted with 1 M HCl; % water content: calculated as weight difference after drying at 90°C for 24 hours.

Sample	Depth (cm)	Grey value	AVS ( $\mu\text{mol g}^{-1} \text{ ww}$ )	Water content(%)
A1	1.0	113.96	0.17	71.55
A2	1.5	111.27	0.55	70.08
A3	2.0	109.12	0.87	69.20
A4	2.5	106.20	1.16	68.28
A5	3.0	102.27	1.70	69.02
A6	3.5	98.38	2.26	68.58
A7	4.0	93.71	3.01	68.20
A8		— Sample dropped —		
A9	5.0	86.47	3.63	67.70
A10	5.5	87.50	4.00	67.73
A11	6.0	85.92	4.41	66.83
A12	6.5	86.01	4.33	66.52
A13	7.0	88.16	4.07	66.81
A14	7.5	89.31	3.69	65.31
A15	8.0	91.56	3.37	65.14
A16	8.5	93.05	3.15	65.94
A17	9.0	93.88	3.08	65.11
B1	1.0	113.32	0.14	71.55
B2	1.5	111.99	0.45	70.08
B3	2.0	107.46	0.91	69.20
B4	2.5	104.76	1.32	68.28
B5	3.0	101.11	1.82	69.02
B6	3.5	93.64	2.87	68.58
B7	4.0	90.44	3.19	68.20
B8	4.5	89.93	3.50	67.97
B9	5.0	91.86	3.25	67.70
B10	5.5	92.97	3.06	67.73
B11	6.0	92.05	3.27	66.83
B12	6.5	93.06	3.28	66.52
B13	7.0	92.85	3.27	66.81
B14	7.5	92.16	3.21	65.31

continued over page...

Sample	Depth (cm)	Grey value	AVS ( $\mu\text{mol g}^{-1} \text{ ww}$ )	Water content(%)
B15	8.0	92.55	3.00	65.14
B16	8.5	93.81	3.01	65.94
B17	9.0	94.98	2.68	65.11
C1	1.0	113.23	0.44	71.55
C2	1.5	107.99	1.06	70.08
C3	2.0	101.79	1.68	69.20
C4	2.5	97.70	2.05	68.28
C5	3.0	94.30	3.09	69.02
C6	3.5	91.19	2.75	68.58
C7	4.0	88.41	3.11	68.20
C8	4.5	89.17	2.89	67.97
C9	5.0	92.30	2.88	67.70
C10	5.5	96.07	2.41	67.73
C11	6.0	99.14	2.19	66.83
C12	6.5	100.55	2.15	66.52
C13	7.0	96.66	2.48	66.81
C14	7.5	94.73	2.69	65.31
C15	8.0	93.46	2.90	65.14
C16	8.5	95.77	2.56	65.94
C17	9.0	98.14	2.36	65.11
D1	1.0	121.35	0.23	71.55
D2	1.5	119.71	0.29	70.08
D3	2.0	118.09	0.59	69.20
D4	2.5	117.37	0.37	68.28
D5	3.0	115.34	0.50	69.02
D6	3.5	111.62	0.83	68.58
D7	4.0	107.37	1.35	68.20
D8	4.5	99.17	2.34	67.97
D9	5.0	95.65	2.41	67.70
D10	5.5	98.26	2.41	67.73
D11	6.0	99.98	2.00	66.83
D12	6.5	101.59	1.82	66.52
D13	7.0	100.47	1.86	66.81
D14	7.5	100.08	1.75	65.31
D15	8.0	101.73	1.61	65.14
D16	8.5	103.22	1.77	65.94
D17	9.0	104.04	1.71	65.11
E1	1.0	121.24	0.23	71.55
E2	1.5	120.45	0.14	70.08
E3	2.0	119.40	0.22	69.20
E4	2.5	118.66	0.24	68.28
E5	3.0	118.02	0.20	69.02
E6	3.5	117.12	0.23	68.58
E7	4.0	115.90	0.36	68.20
E8	4.5	111.84	0.63	67.97
E9	5.0	109.38	0.81	67.70
E10	5.5	107.47	0.82	67.73
E11	6.0	108.10	0.80	66.83
E12	6.5	108.69	0.71	66.52
E13	7.0	108.58	0.81	66.81
E14	7.5	105.73	1.05	65.31
E15	8.0	105.03	1.18	65.14
E16	8.5	105.67	1.06	65.94
F1	1.0	121.37	0.48	71.55
F2	1.5	118.60	0.59	70.08

*continued over page...*

Sample	Depth (cm)	Grey value	AVS ( $\mu\text{mol g}^{-1} \text{ ww}$ )	Water content(%)
F3	2.0	117.83	0.58	69.20
F4	2.5	116.68	0.69	68.28
F5	3.0	115.71	1.02	69.02
F6	3.5	114.49	0.88	68.58
F7	4.0	111.62	1.22	68.20
F8	4.5	106.59	1.58	67.97
F9	5.0	99.16	2.28	67.70
F10	5.5	94.74	3.09	67.73
F11	6.0	94.89	2.93	66.83
F12	6.5	94.80	2.55	66.52
F13	7.0	91.99	2.59	66.81
F14	7.5	94.75	2.52	65.31
F15	8.0	94.76	2.29	65.14
F16	8.5	95.53	2.25	65.94
F17	9.0	96.39	2.23	65.11
G1	1.0	117.97	0.53	71.55
G2	1.5	117.54	0.56	70.08
G3	2.0	117.59	0.57	69.20
G4	2.5	117.10	0.55	68.28
G5	3.0	115.82	0.87	69.02
G6	3.5	113.79	0.80	68.58
G7	4.0	111.25	1.13	68.20
G8	4.5	107.54	1.44	67.97
G9	5.0	100.62	2.44	67.70
G10	5.5	90.87	3.33	67.73
G11	6.0	81.35	5.01	66.83
G12	6.5	82.10	4.22	66.52
G13	7.0	85.84	4.44	66.81
G14	7.5	87.94	3.60	65.31
G15	8.0	91.25	3.94	65.14
G16	8.5	92.18	3.43	65.94
G17	9.0	95.23	3.02	65.11

## Appendix C

### Sediment AVS and CRS analyses

**Table C.1:** Sediment acid volatile sulfide (AVS) and chromium reducible sulfide (CRS) analyses sampled at various depths from sediment cores collected at Awakiriapa Bay (AB), Wilson Bay (WB), and Te Kouma (TK), Hauraki Gulf, New Zealand. Water content was determined by weight difference after drying at 90°C for 24 hours and organic matter at 400°C for 6 hours.

Sample	Site	Depth (cm)	Grey value	AVS ( $\mu\text{mol g}^{-1} \text{ ww}$ )	CRS ( $\mu\text{mol g}^{-1} \text{ dw}$ )	Water content (%)	Organic matter (%)
AB1a	AB	2	77.16	1.61	40.48	69.06	6.28
AB1b	AB	5	78.81	1.34	46.85	65.49	6.34
AB1c	AB	8	82.48	0.90	53.05	64.73	5.75
AB1d	AB	11	86.74	0.41	81.00	62.93	5.63
AB1e	AB	14	86.03	0.21	130.84	59.83	5.63
AB2a	AB	2	80.47	0.98	29.21	71.08	6.28
AB2b	AB	5	79.48	1.62	33.03	68.57	6.34
AB2c	AB	8	79.23	1.17	48.07	63.79	5.75
AB2d	AB	11	85.72	0.68	40.27	63.07	5.63
AB2e	AB	14	86.87	0.42	63.22	60.56	5.63
AB3a	AB	2	83.02	1.04	22.12	70.34	6.28
AB3b	AB	5	71.08	3.80	29.75	68.65	6.34
AB3c	AB	8	83.84	1.18	32.28	65.92	5.75
AB3d	AB	11	88.16	0.32	59.24	64.50	5.63
AB3e	AB	14	86.61	0.35	81.94	62.98	5.63
AB4a	AB	2	77.04	1.65	34.04	70.16	6.28
AB4b	AB	5	80.38	1.37	64.65	64.88	6.34
AB4c	AB	8	84.80	0.77	70.91	62.20	5.75
AB4d	AB	11	88.70	0.48	108.24	61.00	5.63
AB4e	AB	14	86.40	0.40	114.22	58.93	5.63
AB5a	AB	2	84.42	0.50	81.85	71.08	6.28
AB5b	AB	5	74.69	1.57	34.71	67.73	6.34
AB5c	AB	8	82.50	0.74	37.60	66.64	5.75
AB5d	AB	11	84.06	0.29	74.43	65.07	5.63
AB5e	AB	14	86.13	0.26	96.34	61.98	5.63
AB6a	AB	2	88.06	0.08	26.37	67.88	6.28
AB6b	AB	5	75.96	1.67	30.20	67.60	6.34
AB6c	AB	8	78.40	1.46	56.58	65.48	5.75
AB6d	AB	11	83.53	0.53	95.06	64.09	5.63
AB6e	AB	14	81.86	0.62	85.65	60.95	5.63
AB7a	AB	2	83.66	0.73	28.77	72.25	6.28

*continued over page...*



Sample	Site	Depth (cm)	Grey value	AVS ( $\mu\text{mol g}^{-1} \text{ ww}$ )	CRS ( $\mu\text{mol g}^{-1} \text{ dw}$ )	Water content (%)	Organic matter (%)
AB7b	AB	5	76.76	2.01	18.76	70.00	6.34
AB7c	AB	8	75.66	1.96	34.67	66.28	5.75
AB7d	AB	11	82.72	0.92	58.93	63.13	5.63
AB7e	AB	14	82.96	0.59	81.91	62.39	5.63
AB8a	AB	2	86.36	0.57	22.57	71.44	6.28
AB8b	AB	5	84.40	1.65	36.68	68.80	6.34
AB8c	AB	8	87.04	1.27	52.11	65.90	5.75
AB8d	AB	11	87.57	0.63	50.15	64.33	5.63
AB8e	AB	14	84.09	0.39	109.34	61.90	5.63
TK1a	TK	2	75.34	1.01	28.40	54.76	4.07
TK1b	TK	5	63.87	2.84	—	49.64	2.70
TK1c	TK	8	69.74	1.60	98.42	43.76	2.79
TK1d	TK	11	74.59	0.63	132.02	44.18	4.10
TK1e	TK	14	75.50	0.60	131.99	43.43	3.93
TK2a	TK	2	70.97	0.52	22.98	55.31	4.21
TK2b	TK	5	56.08	3.24	39.47	51.47	3.81
TK2c	TK	8	66.33	3.03	58.66	47.39	3.00
TK2d	TK	11	66.48	1.54	135.20	48.14	4.38
TK2e	TK	14	—	0.90	130.44	45.59	3.05
TK3a	TK	2	74.52	1.04	26.63	55.58	4.42
TK3b	TK	5	67.72	1.63	56.20	49.03	3.63
TK3c	TK	8	69.16	1.31	126.86	49.61	4.00
TK3d	TK	11	77.50	0.96	53.10	50.76	3.48
TK3e	TK	14	70.91	0.79	97.85	45.82	2.69
TK4a	TK	2	77.00	1.40	20.92	55.88	3.24
TK4b	TK	5	76.90	1.18	80.95	52.30	3.97
TK4c	TK	8	78.88	1.13	95.19	50.98	3.23
TK4d	TK	11	79.09	1.08	49.81	49.46	3.93
TK4e	TK	14	80.76	0.37	117.14	47.21	3.93
TK5a	TK	2	71.72	0.45	20.03	52.68	3.76
TK5b	TK	5	63.01	3.33	31.42	56.33	4.67
TK5c	TK	8	52.16	4.75	44.39	56.31	4.86
TK5d	TK	11	69.99	1.75	90.16	50.29	3.49
TK5e	TK	14	70.38	0.99	141.44	45.96	3.16
TK6a	TK	2	71.28	0.25	22.30	54.33	3.70
TK6b	TK	5	—	1.40	53.04	49.46	3.94
TK6c	TK	8	—	0.77	97.59	49.99	2.81
TK6d	TK	11	—	0.90	119.11	49.14	3.81
TK6e	TK	14	74.54	0.62	135.84	47.95	3.49
TK7a	TK	2	78.79	0.18	10.19	52.70	4.11
TK7b	TK	5	75.46	1.73	20.20	55.88	3.94
TK7c	TK	8	66.39	3.38	30.93	51.87	3.16
TK7d	TK	11	66.37	2.45	51.41	51.31	4.10
TK7e	TK	14	76.47	0.52	128.74	47.48	3.17
TK8a	TK	2	77.46	0.08	16.40	53.10	4.10
TK8b	TK	5	76.35	0.72	49.62	53.93	3.92
TK8c	TK	8	78.50	0.45	116.29	50.97	2.84
TK8d	TK	11	80.44	0.19	112.14	52.75	4.04
TK8e	TK	14	77.53	0.42	113.22	45.88	3.98
WB1a	WB	2	80.47	0.40	54.10	73.69	6.30
WB1b	WB	5	60.47	3.15	50.01	74.09	5.60
WB1c	WB	8	54.10	4.05	48.80	73.85	6.43
WB1d	WB	11	44.85	5.64	49.89	73.89	5.75
WB1e	WB	14	44.73	5.16	62.54	71.62	6.75

continued over page...

Sample	Site	Depth (cm)	Grey value	AVS ( $\mu\text{mol g}^{-1} \text{ ww}$ )	CRS ( $\mu\text{mol g}^{-1} \text{ dw}$ )	Water content (%)	Organic matter (%)
WB2a	WB	2	—	0.38	39.13	74.19	6.39
WB2b	WB	5	—	3.58	48.14	72.85	8.09
WB2c	WB	8	—	4.37	36.78	73.29	7.89
WB2d	WB	11	—	5.40	47.28	74.57	7.58
WB2e	WB	14	49.75	6.13	52.73	73.14	6.65
WB3a	WB	2	84.15	0.75	41.82	73.85	6.78
WB3b	WB	5	60.59	2.60	44.98	74.41	6.44
WB3c	WB	8	52.10	4.99	39.46	74.81	6.79
WB3d	WB	11	44.25	7.03	41.84	73.22	7.85
WB3e	WB	14	—	5.50	72.93	—	—
WB4a	WB	2	89.87	0.19	12.36	74.19	5.59
WB4b	WB	5	80.72	0.85	34.04	74.57	6.59
WB4c	WB	8	54.51	5.69	31.31	73.70	7.16
WB4d	WB	11	52.03	5.45	14.73	74.26	6.85
WB4e	WB	14	54.65	6.06	52.18	72.67	6.50
WB5a	WB	2	86.89	0.41	31.31	74.94	7.29
WB5b	WB	5	79.84	0.57	39.70	74.01	6.53
WB5c	WB	8	55.89	3.22	51.94	73.53	7.36
WB5d	WB	11	49.08	4.44	46.96	73.69	6.41
WB5e	WB	14	49.92	4.84	56.51	72.59	5.81
WB6a	WB	2	79.54	0.58	47.58	73.70	5.20
WB6b	WB	5	51.40	3.66	44.63	75.36	6.81
WB6c	WB	8	42.97	5.02	—	74.76	6.81
WB6d	WB	11	41.97	5.51	—	73.22	9.98
WB6e	WB	14	47.52	5.23	57.29	72.10	6.43
WB7a	WB	2	82.98	0.42	57.86	73.90	5.45
WB7b	WB	5	57.06	4.02	48.61	74.74	7.29
WB7c	WB	8	48.54	4.77	53.92	75.05	6.96
WB7d	WB	11	46.83	5.31	53.04	74.56	6.07
WB7e	WB	14	48.94	5.41	53.42	73.05	5.96
WB8a	WB	2	84.61	0.17	45.95	74.28	4.96
WB8b	WB	5	62.09	2.53	43.74	75.54	6.67
WB8c	WB	8	42.67	4.84	45.46	75.14	6.42
WB8d	WB	11	45.36	5.14	46.12	74.40	4.97
WB8e	WB	14	43.97	6.61	59.75	72.50	6.45

## Appendix D

### Awakiriapa Bay image analysis

**Table D.1:** Details of the in situ images acquired using SPI-Scan along three transect (West, Mid, and East) from Awakiriapa Bay, Waiheke Island, New Zealand. I measured the mean sediment colour intensity (grey value) of the upper 4 cm of the sediment-profile image using image analysis and then derived the AVS concentration with the formula  $[AVS] = 0.0024GREY^2 - 0.5249GREY + 28.392$ .

Image name	Latitude	Longitude	Transect	Grey value	AVS ( $\mu\text{mol g}^{-1} \text{ ww}$ )
MoW20130320-0004	-36.7995	175.1693	M	90.75	0.37
MoW20130320-0005	-36.7994	175.1692	M	91.30	0.32
MoW20130320-0006	-36.7993	175.1696	M	90.71	0.38
MoW20130320-0008	-36.7993	175.1696	M	88.68	0.58
MoW20130320-0010	-36.7993	175.1696	M	90.63	0.39
MoW20130320-0011	-36.7993	175.1696	M	91.37	0.32
MoW20130320-0012	-36.7996	175.1693	M	90.28	0.42
MoW20130320-0013	-36.7996	175.1693	M	90.63	0.39
MoW20130320-0014	-36.7996	175.1693	M	91.71	0.29
MoW20130320-0015	-36.7996	175.1693	M	87.89	0.66
MoW20130320-0016	-36.7996	175.1693	M	93.13	0.17
MoW20130320-0017	-36.7996	175.1693	M	93.58	0.13
MoW20130320-0018	-36.7996	175.1693	M	97.53	0.00
MoW20130320-0019	-36.7996	175.1693	M	95.11	0.02
MoW20130320-0020	-36.7996	175.1693	M	90.76	0.37
MoW20130320-0021	-36.7996	175.1693	M	99.67	0.00
MoW20130320-0022	-36.7997	175.1695	M	91.68	0.29
MoW20130320-0023	-36.7997	175.1695	M	96.66	0.00
MoW20130320-0024	-36.7997	175.1695	M	88.93	0.55
MoW20130320-0025	-36.7997	175.1695	M	95.28	0.00
MoW20130320-0026	-36.7997	175.1695	M	97.22	0.00
MoW20130320-0027	-36.7998	175.1696	M	95.08	0.02
MoW20130320-0028	-36.7998	175.1696	M	88.86	0.56
MoW20130320-0029	-36.7998	175.1696	M	96.71	0.00
MoW20130320-0030	-36.7998	175.1696	M	94.34	0.07
MoW20130320-0031	-36.7998	175.1696	M	98.69	0.00
MoW20130320-0032	-36.7998	175.1696	M	89.88	0.46
MoW20130320-0033	-36.8000	175.1697	M	99.08	0.00
MoW20130320-0034	-36.8000	175.1697	M	85.89	0.88
MoW20130320-0035	-36.8000	175.1697	M	91.55	0.30
MoW20130320-0036	-36.8000	175.1697	M	91.35	0.32
MoW20130320-0037	-36.8000	175.1697	M	89.71	0.47

*continued over page...*

Image name	Latitude	Longitude	Transect	Grey value	AVS ( $\mu\text{mol g}^{-1} \text{ ww}$ )
MoW20130320-0038	-36.8000	175.1697	M	99.31	0.00
MoW20130320-0039	-36.8002	175.1696	M	99.47	0.00
MoW20130320-0040	-36.8002	175.1696	M	96.66	0.00
MoW20130320-0041	-36.8002	175.1696	M	95.26	0.01
MoW20130320-0042	-36.8002	175.1696	M	91.80	0.28
MoW20130320-0044	-36.8004	175.1696	M	94.65	0.05
MoW20130320-0045	-36.8004	175.1696	M	90.14	0.43
MoW20130320-0047	-36.8004	175.1696	M	95.93	0.00
MoW20130320-0048	-36.8005	175.1696	M	93.51	0.14
MoW20130320-0049	-36.8005	175.1696	M	98.80	0.00
MoW20130320-0050	-36.8005	175.1696	M	94.43	0.07
MoW20130320-0051	-36.8008	175.1696	M	98.69	0.00
MoW20130320-0052	-36.8008	175.1696	M	94.13	0.09
MoW20130320-0053	-36.8008	175.1696	M	95.59	0.00
MoW20130320-0054	-36.8008	175.1696	M	89.03	0.54
MoW20130320-0055	-36.8008	175.1695	M	86.10	0.86
MoW20130320-0056	-36.8008	175.1695	M	92.14	0.25
MoW20130320-0057	-36.8008	175.1695	M	83.86	1.12
MoW20130320-0058	-36.8008	175.1695	M	86.70	0.79
MoW20130320-0060	-36.8010	175.1696	M	45.78	9.36
MoW20130320-0062	-36.8013	175.1698	M	62.71	4.84
MoW20130320-0063	-36.8013	175.1698	M	57.25	6.15
MoW20130320-0064	-36.8013	175.1698	M	72.95	2.78
MoW20130321-0000	-36.8017	175.1701	M	42.64	10.34
MoW20130321-0001	-36.8017	175.1701	M	42.65	10.34
MoW20130321-0003	-36.8016	175.1701	M	53.86	7.03
MoW20130321-0004	-36.8016	175.1700	M	65.64	4.20
MoW20130321-0006	-36.8016	175.1700	M	46.72	9.07
MoW20130321-0007	-36.8015	175.1701	M	83.45	1.18
MoW20130321-0010	-36.8015	175.1700	M	52.52	7.40
MoW20130321-0011	-36.8015	175.1700	M	44.40	9.78
MoW20130321-0012	-36.8015	175.1700	M	66.25	4.07
MoW20130321-0013	-36.8014	175.1700	M	58.36	5.87
MoW20130321-0014	-36.8014	175.1700	M	55.42	6.62
MoW20130321-0015	-36.8014	175.1700	M	48.66	8.49
MoW20130321-0016	-36.8013	175.1700	M	61.91	5.03
MoW20130321-0017	-36.8013	175.1700	M	56.49	6.34
MoW20130321-0018	-36.8013	175.1700	M	37.51	12.06
MoW20130321-0019	-36.8013	175.1700	M	58.83	5.76
MoW20130321-0020	-36.8019	175.1686	W	40.04	11.20
MoW20130321-0021	-36.8019	175.1686	W	38.84	11.60
MoW20130321-0022	-36.8019	175.1686	W	69.64	3.39
MoW20130321-0025	-36.8019	175.1686	W	39.91	11.24
MoW20130321-0026	-36.8017	175.1686	W	41.91	10.58
MoW20130321-0029	-36.8016	175.1686	W	40.32	11.10
MoW20130321-0030	-36.8016	175.1686	W	64.47	4.45
MoW20130321-0031	-36.8016	175.1686	W	44.37	9.79
MoW20130321-0032	-36.8015	175.1685	W	52.98	7.27
MoW20130321-0034	-36.8015	175.1686	W	69.18	3.48
MoW20130321-0035	-36.8015	175.1686	W	48.56	8.52
MoW20130321-0036	-36.8015	175.1686	W	43.33	10.12
MoW20130321-0040	-36.8014	175.1684	W	54.88	6.76
MoW20130321-0041	-36.8011	175.1685	W	90.69	0.38
MoW20130321-0042	-36.8012	175.1685	W	66.14	4.10
MoW20130321-0043	-36.8009	175.1685	W	83.71	1.14

continued over page...

Image name	Latitude	Longitude	Transect	Grey value	AVS ( $\mu\text{mol g}^{-1} \text{ ww}$ )
MoW20130321-0045	-36.8010	175.1684	W	87.14	0.74
MoW20130321-0046	-36.8009	175.1684	W	92.29	0.24
MoW20130321-0047	-36.8006	175.1684	W	82.34	1.32
MoW20130321-0048	-36.8008	175.1685	W	93.48	0.14
MoW20130321-0049	-36.8007	175.1685	W	78.49	1.87
MoW20130321-0051	-36.8005	175.1682	W	95.82	0.00
MoW20130321-0052	-36.8004	175.1683	W	95.00	0.02
MoW20130321-0053	-36.8003	175.1683	W	98.88	0.00
MoW20130321-0054	-36.8002	175.1683	W	93.76	0.12
MoW20130321-0055	-36.8000	175.1681	W	95.07	0.02
MoW20130321-0057	-36.8003	175.1682	W	90.76	0.37
MoW20130321-0058	-36.7997	175.1680	W	97.05	0.00
MoW20130321-0059	-36.7998	175.1681	W	93.38	0.15
MoW20130321-0060	-36.7996	175.1681	W	98.20	0.00
MoW20130321-0061	-36.7997	175.1680	W	94.38	0.07
MoW20130321-0062	-36.7994	175.1678	W	85.55	0.92
MoW20130321-0063	-36.7995	175.1680	W	97.35	0.00
MoW20130321-0064	-36.7994	175.1680	W	97.80	0.00
MoW20130321-0065	-36.7994	175.1680	W	92.75	0.20
MoW20130321-0066	-36.7995	175.1682	W	102.96	0.00
MoW20130321-0068	-36.7993	175.1679	W	94.76	0.04
MoW20130321-0069	-36.7993	175.1679	W	101.11	0.00
MoW20130321-0070	-36.7992	175.1680	W	88.77	0.57
MoW20130325-0002	-36.8018	175.1712	E	53.61	7.10
MoW20130325-0006	-36.8017	175.1712	E	68.42	3.63
MoW20130325-0007	-36.8017	175.1712	E	56.72	6.28
MoW20130325-0010	-36.8017	175.1712	E	57.83	6.00
MoW20130325-0019	-36.8015	175.1712	E	76.11	2.24
MoW20130325-0020	-36.8015	175.1712	E	80.62	1.56
MoW20130325-0022	-36.8015	175.1712	E	77.09	2.08
MoW20130325-0023	-36.8014	175.1712	E	67.74	3.77
MoW20130325-0024	-36.8014	175.1712	E	66.11	4.10
MoW20130325-0025	-36.8014	175.1712	E	67.95	3.72
MoW20130325-0026	-36.8014	175.1712	E	76.38	2.20
MoW20130325-0027	-36.8014	175.1712	E	67.63	3.79
MoW20130325-0028	-36.8014	175.1712	E	73.76	2.64
MoW20130325-0031	-36.8013	175.1712	E	88.62	0.58
MoW20130325-0032	-36.8013	175.1712	E	74.28	2.55
MoW20130325-0036	-36.8011	175.1711	E	81.29	1.46
MoW20130325-0037	-36.8010	175.1712	E	88.16	0.63
MoW20130325-0041	-36.8007	175.1712	E	76.70	2.14
MoW20130325-0043	-36.8005	175.1711	E	87.11	0.74
MoW20130325-0044	-36.8004	175.1711	E	86.61	0.80
MoW20130325-0045	-36.8003	175.1710	E	94.98	0.03
MoW20130325-0046	-36.8001	175.1711	E	83.11	1.22
MoW20130325-0047	-36.8001	175.1710	E	87.88	0.66
MoW20130325-0048	-36.8002	175.1709	E	84.24	1.08
MoW20130325-0049	-36.8002	175.1709	E	89.15	0.53
MoW20130325-0051	-36.7999	175.1710	E	96.93	0.00
MoW20130325-0052	-36.7997	175.1710	E	94.04	0.10
MoW20130325-0053	-36.7995	175.1708	E	90.28	0.42
MoW20130325-0054	-36.8018	175.1698	M	69.39	3.44
MoW20130325-0055	-36.8018	175.1698	M	49.32	8.30
MoW20130325-0056	-36.8018	175.1698	M	69.19	3.48
MoW20130325-0059	-36.8017	175.1698	M	45.43	9.46

continued over page...

Image name	Latitude	Longitude	Transect	Grey value	AVS ( $\mu\text{mol g}^{-1} \text{ ww}$ )
MoW20130325-0060	-36.8017	175.1698	M	57.05	6.20
MoW20130325-0061	-36.8017	175.1698	M	68.34	3.64
MoW20130325-0066	-36.8017	175.1698	M	43.94	9.93
MoW20130325-0067	-36.8016	175.1698	M	54.29	6.92
MoW20130325-0075	-36.8015	175.1697	M	61.87	5.03
MoW20130325-0076	-36.8015	175.1697	M	81.31	1.46
MoW20130325-0079	-36.8015	175.1697	M	74.09	2.58
MoW20130325-0085	-36.8014	175.1697	M	61.11	5.21
MoW20130625-0000	-36.8011	175.1685	W	84.81	1.01
MoW20130625-0002	-36.8011	175.1685	W	85.72	0.90
MoW20130625-0003	-36.8012	175.1685	W	81.19	1.48
MoW20130625-0005	-36.8012	175.1685	W	81.94	1.37
MoW20130625-0006	-36.8013	175.1686	W	81.39	1.45
MoW20130625-0008	-36.8012	175.1686	W	87.64	0.68
MoW20130625-0009	-36.8013	175.1685	W	80.42	1.58
MoW20130625-0010	-36.8013	175.1686	W	85.24	0.96
MoW20130625-0011	-36.8013	175.1686	W	71.50	3.04
MoW20130625-0012	-36.8013	175.1686	W	75.78	2.29
MoW20130625-0013	-36.8014	175.1685	W	81.25	1.47
MoW20130625-0017	-36.8012	175.1685	W	81.56	1.43
MoW20130625-0018	-36.8012	175.1685	W	86.65	0.79
MoW20130625-0019	-36.8012	175.1685	W	78.04	1.94
MoW20130625-0020	-36.8011	175.1686	W	87.67	0.68
MoW20130625-0021	-36.8011	175.1685	W	92.09	0.25
MoW20130625-0022	-36.8011	175.1685	W	80.51	1.57
MoW20130625-0023	-36.8011	175.1685	W	89.21	0.52
MoW20130625-0024	-36.8008	175.1697	M	84.51	1.04
MoW20130625-0025	-36.8008	175.1697	M	79.46	1.72
MoW20130625-0028	-36.8009	175.1697	M	71.97	2.95
MoW20130625-0029	-36.8009	175.1697	M	81.21	1.47
MoW20130625-0032	-36.8009	175.1697	M	69.54	3.41
MoW20130625-0033	-36.8010	175.1697	M	86.78	0.78
MoW20130625-0034	-36.8010	175.1697	M	82.57	1.29
MoW20130625-0035	-36.8010	175.1696	M	86.76	0.78
MoW20130625-0037	-36.8012	175.1697	M	96.99	0.00
MoW20130625-0042	-36.8012	175.1696	M	90.19	0.43
MoW20130625-0043	-36.8012	175.1696	M	88.14	0.63
MoW20130625-0046	-36.8013	175.1696	M	88.04	0.64
MoW20130625-0047	-36.8011	175.1696	M	95.24	0.01
MoW20130625-0049	-36.8012	175.1696	M	88.64	0.58

## Appendix E

### Vertical pH profiles

**Table E.1:** Results from measuring vertical pH profiles in subtidal marine sediment cores collected from Awakirapa Bay, Waiheke Island, New Zealand. A negative depth indicates that the measurement was made in the water overlying the sediment surface. Core 1 was measured in 0.5 mm increments and the remaining cores were measured at 1 mm increments.

Depth (mm)	pH					
	Core 1	Core 2	Core 3	Core 4	Core 5	Core 6
−10	—	8.148	8.078	—	—	—
−9	—	8.119	8.081	—	—	—
−8	—	8.105	8.080	—	—	—
−7	—	8.098	8.080	8.112	—	—
−6	—	8.094	8.079	8.107	8.052	—
−5	—	8.073	8.080	8.098	8.050	—
−4	—	8.084	8.074	8.097	8.089	8.038
−3	—	8.084	8.072	8.098	8.021	8.036
−2.5	8.045	—	—	—	—	—
−2	8.045	8.086	8.068	8.103	8.045	8.042
−1.5	8.049	—	—	—	—	—
−1	8.050	8.079	8.072	8.101	8.034	8.043
−0.5	8.051	—	—	—	—	—
0	8.049	8.066	8.073	8.048	8.055	8.038
0.5	8.016	—	—	—	—	—
1	7.953	7.961	8.042	7.941	7.983	7.945
1.5	7.847	—	—	—	—	—
2	7.723	7.753	7.978	7.741	7.792	7.743
2.5	7.614	—	—	—	—	—
3	7.502	7.576	7.856	7.568	7.599	7.550
3.5	7.419	—	—	—	—	—
4	7.361	7.462	7.693	7.456	7.449	7.420
4.5	7.319	—	—	—	—	—
5	7.292	7.416	7.561	7.387	7.318	7.341
5.5	7.275	—	—	—	—	—
6	7.261	7.398	7.475	7.346	7.244	7.285
6.5	7.246	—	—	—	—	—
7	7.224	7.400	7.427	7.328	7.218	7.258
7.5	7.213	—	—	—	—	—
8	7.203	7.400	7.431	7.312	7.203	7.245
8.5	7.195	—	—	—	—	—

*continued over page...*

Depth (mm)	pH					
	Core 1	Core 2	Core 3	Core 4	Core 5	Core 6
9	7.190	7.397	7.428	7.314	7.174	7.229
9.5	7.186	—	—	—	—	—
10	7.183	7.391	7.424	7.310	7.152	7.226
10.5	7.179	—	—	—	—	—
11	7.173	7.387	7.418	7.317	7.135	7.233
11.5	7.173	—	—	—	—	—
12	7.170	7.383	7.411	7.283	7.121	7.238
12.5	7.166	—	—	—	—	—
13	7.163	7.369	7.404	7.262	7.112	7.244
13.5	7.160	—	—	—	—	—
14	7.157	7.363	7.410	7.244	7.115	7.25
14.5	7.154	—	—	—	—	—
15	7.151	7.358	7.416	7.226	7.118	7.254
15.5	7.149	—	—	—	—	—
16	7.146	7.348	7.43 0	7.220	7.127	7.259
16.5	7.143	—	—	—	—	—
17	7.140	7.335	7.435	7.207	7.136	7.276
17.5	7.136	—	—	—	—	—
18	7.133	7.287	7.445	7.213	7.154	7.265
18.5	7.129	—	—	—	—	—
19	7.126	7.313	7.451	7.212	7.177	7.266
19.5	7.123	—	—	—	—	—
20	7.120	7.328	7.448	7.211	7.185	7.271
20.5	7.117	—	—	—	—	—
21	7.114	7.324	7.441	7.211	7.193	7.271
21.5	7.112	—	—	—	—	—
22	7.109	7.316	7.424	7.231	7.198	7.268
22.5	7.107	—	—	—	—	—
23	7.105	7.303	7.417	7.232	7.138	7.266
23.5	7.103	—	—	—	—	—
24	7.102	7.290	7.400	7.233	7.159	7.265
24.5	7.102	—	—	—	—	—
25	7.102	7.276	7.379	7.237	7.182	7.259
25.5	7.103	—	—	—	—	—
26	7.104	7.264	7.369	7.213	7.193	7.258
26.5	7.108	—	—	—	—	—
27	7.113	7.251	7.351	7.210	7.194	7.260
27.5	7.121	—	—	—	—	—
28	7.129	7.238	7.334	7.207	7.204	7.251
28.5	7.134	—	—	—	—	—
29	7.143	7.223	7.322	7.208	7.196	7.251
29.5	7.148	—	—	—	—	—
30	7.155	7.207	7.315	7.211	7.195	7.251
30.5	7.161	—	—	—	—	—
31	7.166	7.195	7.308	7.211	7.200	7.251
31.5	7.175	—	—	—	—	—
32	7.180	7.186	7.299	7.216	7.197	7.253
32.5	7.185	—	—	—	—	—
33	7.187	7.175	7.288	7.224	7.186	7.255
33.5	7.190	—	—	—	—	—
34	7.195	7.176	7.28	7.230	7.165	7.255
34.5	7.196	—	—	—	—	—
35	7.199	7.186	7.277	7.235	7.168	7.255
35.5	7.201	—	—	—	—	—

continued over page...



Depth (mm)	pH					
	Core 1	Core 2	Core 3	Core 4	Core 5	Core 6
36	7.203	7.197	7.270	7.239	7.175	7.252
36.5	7.205	—	—	—	—	—
37	7.206	7.207	7.264	7.257	7.164	7.245
37.5	7.209	—	—	—	—	—
38	7.210	7.217	7.252	7.284	7.156	7.236
38.5	7.211	—	—	—	—	—
39	7.211	7.227	7.257	7.266	7.158	7.230
39.5	7.210	—	—	—	—	—
40	7.212	7.235	7.257	7.298	7.159	7.218
40.5	7.213	—	—	—	—	—
41	7.213	7.246	7.259	7.309	7.158	7.211
41.5	7.213	—	—	—	—	—
42	7.212	7.257	7.262	7.321	7.140	7.202
42.5	7.211	—	—	—	—	—
43	7.212	7.263	7.269	7.321	7.141	7.195
43.5	7.211	—	—	—	—	—
44	7.210	7.266	7.282	7.316	7.134	7.187
44.5	7.210	—	—	—	—	—
45	7.209	7.270	7.301	7.307	7.125	7.178
45.5	7.207	—	—	—	—	—
46	7.208	7.276	7.336	7.300	7.118	7.164
46.5	7.207	—	—	—	—	—
47	7.207	7.285	7.411	7.294	7.112	7.162
47.5	7.206	—	—	—	—	—
48	7.203	7.291	7.588	7.287	7.118	7.156
48.5	7.205	—	—	—	—	—
49	7.204	7.292	7.731	7.277	7.105	7.152
49.5	7.204	—	—	—	—	—
50	7.205	7.293	7.769	7.262	7.095	7.144
50.5	7.205	—	—	—	—	—
51	7.206	7.293	7.736	7.246	7.094	7.136
51.5	7.206	—	—	—	—	—
52	7.207	7.295	7.666	7.226	7.081	7.131
52.5	7.207	—	—	—	—	—
53	7.207	7.293	7.586	7.208	7.119	7.127
53.5	7.206	—	—	—	—	—
54	7.202	7.286	7.523	7.190	7.032	7.121
54.5	7.202	—	—	—	—	—
55	7.199	7.280	7.471	7.178	7.010	7.116
55.5	7.197	—	—	—	—	—
56	7.194	7.274	7.427	7.167	7.007	7.111
56.5	7.188	—	—	—	—	—
57	7.186	7.269	7.389	7.158	7.007	7.104
57.5	7.182	—	—	—	—	—
58	7.178	7.265	7.355	7.149	7.006	7.108
58.5	7.174	—	—	—	—	—
59	7.170	7.260	7.326	7.142	7.005	7.098
59.5	7.166	—	—	—	—	—
60	7.162	7.254	7.297	7.138	6.996	7.089
60.5	7.159	—	—	—	—	—
61	7.157	7.248	7.277	7.136	6.994	7.089
61.5	7.154	—	—	—	—	—
62	7.152	7.245	7.239	7.135	6.990	7.082
62.5	7.148	—	—	—	—	—

continued over page...

Depth (mm)	pH					
	Core 1	Core 2	Core 3	Core 4	Core 5	Core 6
63	7.148	7.243	7.225	7.136	6.991	7.079
63.5	7.147	—	—	—	—	—
64	7.147	7.240	7.216	7.135	6.989	7.078
64.5	7.146	—	—	—	—	—
65	7.146	7.239	7.229	7.136	6.982	7.074
65.5	7.145	—	—	—	—	—
66	7.145	7.238	7.242	7.136	6.981	7.072
66.5	7.144	—	—	—	—	—
67	7.144	7.235	7.248	7.136	6.987	7.066
67.5	7.144	—	—	—	—	—
68	7.144	7.233	7.254	7.140	6.972	7.063
68.5	7.142	—	—	—	—	—
69	7.145	—	7.262	7.136	6.997	7.064
69.5	7.145	—	—	—	—	—
70	7.146	—	—	7.127	6.978	7.059
70.5	7.145	—	—	—	—	—
71	—	—	—	7.128	6.969	7.060
72	—	—	—	7.126	6.968	7.059
73	—	—	—	7.121	6.974	7.059
74	—	—	—	—	6.973	7.062
75	—	—	—	—	—	6.951
76	—	—	—	—	—	7.010